PhD-FSTM-2025-138
Faculty of Science, Technology and Medicine

DISSERTATION

Defence held on 01/12/2025 in Esch-sur-Alzette

to obtain the degree of

DOCTEUR DE L'UNIVERSITÉ DU LUXEMBOURG
EN *SCIENCE EXACTES ET NATURELLES*
by

João MALLMANN

Born on 10 July 1995 in Santa Rosa, Brazil

PROTECTIVE Co_3O_4 COATINGS FOR SOEC INTERCONNECTS SYNTHESIZED BY ATMOSPHERIC PRESSURE PECVD: OXIDATION AND ELECTRICAL PERFORMANCE

Dissertation defence committee

Dr Patrick Choquet, dissertation supervisor
Doctor, Luxembourg Institute of Science and Technology

Dr Nicolas Boscher, dissertation co-supervisor
Doctor, Luxembourg Institute of Science and Technology

Dr Maël Guennou, chairman
Professor, Université du Luxembourg

Dr Fabio Palumbo, external reviewer
Doctor, CNR Nanotech & University of Bari

Pr Fernando Pedraza Diaz, external reviewer
Professor, Université de la Rochelle

Dr Fabien Rouillard, expert in advisory capacity
Doctor, CEA Saclay & Université Paris Saclay

“Wisdom begins in wonder”

Plato

Acknowledgments

First of all, I would like to thank my supervisors, Patrick, Nicolas, and Fabien, for giving me the opportunity to work on this topic, which I came to be deeply passionate about. I consider myself extremely lucky to have had the chance to work with three excellent scientists.

Special thanks go to Fabien Rouillard for seeing the potential in me after a short-term internship and by offering me the opportunity to develop as a scientist. Moreover, the many scientific discussions throughout this PhD. I have always appreciated that, for you, the understanding was more important than the results itself. These discussions and the sometimes too direct corrections were fundamental to make me grow both as a person and as a researcher.

I would also like to thank Nicolas Boscher, who carried out the close supervision after the retirement of Patrick Choquet. Thank you for keeping me on track and making sure I did not deviate from the topic. You were also fundamental in helping me improve my scientific writing and in understanding the importance of the bigger picture in research.

I would also like to acknowledge Patrick Choquet for the valuable insights during our weekly meetings and for continuing the supervision despite the retirement period. I hope it was fun and that I offered a good transition between the research and retirement.

A big thank you as well to JB for always being very helpful in the lab with several experiments, and for teaching me how to use the plasma deposition machine.

Beyond the scientific work and my supervising team itself, this PhD has been defined by the people I met along the way. As it is often said, it is not about the destination, but about the journey, and during this journey, I had the chance to meet amazing people.

From CEA, Mathilde Bouvier tremendously helped with my PhD work by conducting several experiments (TGA and ASR), performing SEM analyses, and through many valuable discussions. I am also grateful to Kevin Ginestar for being very helpful with trainings and characterisations techniques. My colleague Sergio Diez helped me with the sequential isotopic tracer experiments and was, along with Clément Pierre, a good friend every time I was visiting the lab in Saclay. I would also like to acknowledge Romain Malac for sharing the office when I was back at CEA. To all the other people I met in Building 458, thank you—I always felt very welcome.

From my stay in Luxembourg, I carry many meaningful relationships with me. First, I am grateful to have worked with the Plasma Chimbas (Camilo, François, Kamal, and Rodolphe). I learned a lot from you, and you made the lab work very pleasant. From office 4510, I am glad to have met amazing people who made the daily work much lighter, either during coffee breaks, lunches, and in afterworks (Marek, Drialys, Dominique, Manon, Hadi, Emut, Marta, Ingrid, Jonathan, Aitor, Jordi and Sara). Special thanks to Thiago, Awais, and Marko for accompanying me throughout the entire PhD journey. It was great to simply discuss science with you, crack some jokes (sometimes too many), and for always being there for me. To all the other members of the PLAVA group, it was always a pleasure to be part of the team.

To all the other people I met during this PhD, particularly outside of work, Ernesto, Marco, Silvia, Thiago R., Alberto Vinicius, and Wilhiam, you were equally fundamental to this journey. To my football teammates, thank you as well for providing moments to decompress and disconnect from work.

I am also grateful to the platform teams who collaborated with me on XPS (Jérôme and Christèle), ToF-SIMS (Jérôme B.), and SIMS (Jérémy and Nathalie). Special thanks to Yves Flemming for his great attention to detail during XRD analyses, and to Adrian-Marie for the TEM analyses and the long discussions in front of the microscope.

I would also like to acknowledge my long-term friends who supported me from Brazil (Felipe and Gabriel) and here in Europe (Lucas L., Lucas R., and William), always providing advice and encouragement.

I am deeply grateful for the family I have. Obrigado, seu Dalcio e dona Ironi. I also want to thank my sister, Camila, and my brother-in-law, Arnaud, for being the scientific examples in the family. I truly look up to you, maninha. A big thank you as well to the Kreshpaj family, whom I have come to consider my own. Thank you for your support.

Finally, I would like to express my deepest gratitude to my partner, Anxhela, for being there for me throughout this PhD journey, especially during these last months of writing. You were fundamental in keeping me going.

Abstract

This PhD work investigates the use of Atmospheric Plasma-Enhanced Chemical Vapor Deposition (AP-PECVD) to produce Co_3O_4 protective coatings on AISI 441 interconnects for Solid Oxide Electrolyzer Cells (SOECs).

The first part of the manuscript is dedicated on the understanding of the growth mechanisms of Co_3O_4 coatings by AP-PECVD. The effects of deposition parameters (*e.g.*, temperature, gas composition and atmosphere) on the coating morphology, stoichiometry, and composition are analyzed. Plasma energetic species, notably reactive oxygen-nitrogen species (produced after interaction with air), governed the film composition and crystallinity. The AP-PECVD technique enables the formation of pure, dense Co_3O_4 coatings with excellent substrate adhesion and minimal carbon contamination.

In the second part of the manuscript, the oxidation and electrical performances of the Co_3O_4 coated AISI 441 substrates are investigated under SOEC operating conditions (700 – 850 °C). Two AP-PECVD procedures were evaluated: fast *vs.* slow plasma nozzle displacement speed. Fast displacement speed promoted the formation of more homogeneous Co_3O_4 coatings, which significantly reduce the oxidation kinetics (factor 2 on the parabolic rate constant) and the Cr volatilization rate (by one order of magnitude) compared to uncoated AISI 441 substrates.

The oxide scale growth mechanism was examined using sequential oxidation test with labelled O_2 molecules and short and long-term oxidation tests in air at 800 and 850 °C up to 5000 h of exposure. $Co_{3-x}Mn_xO_4$ grows outwardly by Mn oxidation and diffusion into the Co_3O_4 coating. Simultaneously, a Cr_2O_3 layer grows below it and a Cr-rich Reactive Layer (RL) is formed between Cr_2O_3 and the external Co-Mn spinel. It is demonstrated that the Cr_2O_3 and RL presented competitive growth, strongly correlated to the Mn/Co concentration ratio of the external Co-Mn spinel layer. Such behaviour is discussed.

Finally, *in-situ* Area Specific Resistance (ASR) measurements are conducted to investigate the electrical performance time evolution of the coated AISI 441 substrates. The Co_3O_4 coatings improve the electrical performance in comparison to uncoated AISI 441 substrate by exhibiting lower ASR values after long-term exposure and reduced ASR increasing rate. Such improvement is due to the lower growth rate of Cr-rich oxide layer and the drastic decrease of the volatilization rate of Cr. Several initial Co_3O_4 coating thicknesses (400-2000 nm) are assessed during this work. The 2000 nm-Co_3O_4 coating shows the best electrical performance, with a predicted lifetime below the maximum accepted ASR value (50 $m\Omega\cdot cm^2$) of 5.8 years, higher than the minimum 4.5 years required.

Glossary

GHG – GreenHouse gases

IPCC - Intergovernmental Panel on Climate Change

CCS - Carbon Capture and Storage

SMR - Steam Methane Reforming

CCUS - Carbon Capture, Utilization, and Storage

PEM - Proton Exchange Membrane

TPB - Triple Phase Boundary

TGA – ThermoGravimetric Analysis

CFSE – Crystal field Stabilization Energy

OSPE – Octahedral Site Preference Energy

MCO – Manganese Cobalt Oxide ($Co_{3-x}Mn_xO_4$)

CeCo – Metallic coatings deposited by PVD (10 nm Ce, 640 nm Co)

RL – Reactive Layer

ASR - Area Specific Resistance

SOC – Solid Oxide Cell

SOEC - Solid Oxide Electrolysis Cell

SOFC - Solid Oxide Fuel Cell

TEC – Thermal Expansion Coefficient

AISI – American Iron Steel Institute

AP-PECVD – Atmospheric Pressure Plasma Enhanced Chemical Vapour Deposition

CVD – Chemical Vapour Deposition

PVD – Physical Vapour Deposition

DBD – Dielectric Barrier Discharge

RONS - Reactive Oxygen and Nitrogen Species

ROS – Reactive Oxygen Species

UV – Ultra Violet

LTE – Local Thermodynamic Equilibrium

Non-LTE – Non-Local Thermodynamic Equilibrium

AC – Alternative Current

DC – Direct Current

SIE – Specific Input Energy

EEDF – Electron Energy Distribution Function

OES – Optical Emission Spectroscopy

AZO – Aluminum Zinc Oxide

TTIP – Titanium Tetra Iso Propoxide

PMMA – PolyMethylMethAcrylate

HMDSO – HexaMethylDiSilOxane

ToF-SIMS – Time of Flight Secondary Ion Mass Spectroscopy

SEM – Scanning Electron Microscopy

XPS – X-ray Photoelectron Spectroscopy

YSZ – Yttria-Stabilized Zirconia

CGO – Cerium Gadolinium Oxide

OER – Oxygen Evolution Reaction

LSM – Lanthanum Strontium Manganate

LSF - Lanthanum Strontium Ferrite

LSC - Lanthanum Strontium Cobaltite

FSS - Ferritic Stainless Steels

JT – Jahn-Teller

FIB – Focused Ion Beam

TEM – Transmission Electron Microscopy

SIMS – Secondary Ion Mass Spectroscopy

XRD – X-Ray Diffraction

FTIR – Fourier Transformed InfraRed

SAED – Single Area Electron Diffraction

FFT – Fast Fourier Transformed

GD-OES – Glow Discharge – Optical Emission Spectroscopy

FWHM – Full Width at a Half Maximum

ΔH – Enthalpy

ΔG – Gibbs free energy

T – temperature

th – thickness

ΔS – Entropy

t – Time

σ – Electrical Conductivity ($S\cdot cm^{-1}$)

ρ – Density ($g\cdot cm^{-3}$)

R – Universal Gas Constant

D – Diffusion Coefficient

E_a – Activation Energy

E_s – Strain energy

E_p – Energy Potential between Tetrahedral and Octahedral Field

Table of contents

Acknowledgments i

Abstract vii

Glossary ix

Introduction 2

I – State of the art 6

1. Solid oxide electrolysis cell (SOEC) 6

1.1. Global warming 6

1.2. H_2 production as part of the solution 7

1.3. Low carbon-emitting H_2 production 8

1.4. Solid Oxide Electrolysis Cell (SOEC) 9

1.5. Choice of materials 11

1.5.1. Electrolyte 11

1.5.2. Electrode Materials 12

1.6. Interconnect 13

1.7. Degradation Mechanisms in SOEC technology: Current understanding 15

1.7.1. Thermodynamics of oxidation 15

1.7.2. Kinetics of oxidation 17

1.7.3. Interconnect oxidation 19

1.7.4. Cr-evaporation 21

1.8. Protective Coatings 24

1.8.1. Perovskites 25

1.8.2. Spinels 25

1.8.3. Structure 25

1.8.4. Cation distribution 28

1.9. Performance - Oxidation 30

1.9.1. Oxidation rate 30

1.9.2. Reactive layer 32
1.9.3. Electrical performance 34
1.9.4. Thermal expansion coefficient 38
1.10. Coating processes and impact on properties 39
2.Atmospheric Pressure Plasma Enhanced Chemical Vapor Deposition (AP-PECVD) 41
2.1. Plasma generation 42
2.2. Plasma jets 44
2.3. Precursor Injection 46
2.4. Precursor injection Systems for Plasma Processing 48
2.5. AP-PECVD drawbacks 49
2.6. Thin film growth – Mechanisms involved 50
2.6.1. Plasma role (species) 51
2.6.2. Plasma – precursor interactions 55
2.6.3. Precursor Activation 56
2.6.4. Powder formation 58
2.6.5. Oxidation (Thin film and contaminants) 59
2.6.6. Growth rate increase 60
2.7. Choice of precursor 61
3.Summary and Strategy 63
Chapter II - Experimental section 66
1. .... Substrates 66
2.AP-PECVD setup 67
2.1. Precursor solution preparation 69
2.2. Influence of the surrounding gas environment 70
2.3. Plasma characterisation 71

3.Oxidation experiments 72
3.1. Thermogravimetric experiments 72
3.2. Isothermal oxidation experiments 73
3.3. Cr-evaporation measurements 74
3.4. Electrical measurements 77
3.5. $^{16}O/^{18}O$ experiments 79
4.Thin film characterisation 82
4.1. Morphology 82
4.1.1. Scanning electron microscopy (SEM) 82
4.1.2. Focused Ion Beam (FIB) 82
4.1.3. Confocal microscope 82
4.2. Chemical composition 83
4.2.1. Raman spectroscopy 83
4.2.2. Fourier Transform Infrared Spectroscopy (FTIR) 83
4.2.3. X-ray Photoelectron spectroscopy (XPS) 83
4.2.4. Time of Flight Secondary Ion Mass Spectroscopy (ToF-SIMS) 84
4.2.5. SIMS/NanoSIMS 84
4.2.6. Glow Discharge–Optical Emission Spectroscopy (GD-OES) 84
4.3. Structural characterisation 85
4.3.1. X-ray diffractograms (XRD) 85
4.3.2. Transmission electron microscopy (TEM) 85
Chapter III - Synthesis of Co_3O_4 by AP-PECVD technique: Growth Mechanisms 86
1. .... Introduction 86
2. .... Methodology 87

3. .... Results 90

3.1. Precursor solution selection and injection (Optimization) 90

3.1.1. Precursor solution selection 90

3.1.2. Precursor solution injection 91

3.2. Plasma deposition parameters 93

3.3. Influence of O_2 addition in the carrier gas 95

3.4. Substrate heating temperature 98

3.5. Plasma temperature 103

3.6. Plasma-substrate distance 105

3.7. Plasma chemistry 107

3.7.1. Plasma-precursor and plasma-air interactions 107

3.7.2. Influence of the surrounding environment (non-oxidizing atmosphere) 110

4.Main takeaways 115

Chapter IV – Performance of Co_3O_4 Thin Films under SOEC Operating Conditions 116

1. .... Introduction 116

2. .... **Methodology** 116

3. .... **Results** 119

3.1. Description of the “as-deposited” coatings 119

3.2. Oxidation performance of B1-700 nm sample 123

3.2.1. Oxidation kinetics at 800 and 850 °C 123

3.2.2. Characterization of the oxide scale at 800 °C 125

3.2.3. Characterization of the oxide scale at 850 °C 127

3.2.4. Mn-diffusion in the external spinel oxide at 800 and 850 °C 130

3.2.5. Coating influence on Mn and Cr oxidation rate at 850 °C 132

3.2.6. Formation of a Co-Mn-Cr Reactive layer (RL) between Cr_2O_3 and the Co-Mn spinel layer 133

3.2.7. Long-term exposure of B1-700 nm coatings 135

3.2.8. Preliminary discussion 139

3.3. Oxidation performance of B2 coated samples 139

3.3.1. Oxidation kinetics 139

3.3.2. Influence of the coating thickness on the short-term oxidation behaviour 141

3.3.3. Influence of the coating thickness on the long-term oxidation behaviour 143

3.3.4. Extensive study of the spinel layer formed on B1 and B2 coated samples by Raman spectroscopy : link between Raman shift and chemical composition 147

3.3.5. Chromium evaporation 150

3.4. Sequential Isotopic Tracer Experiment 152

4. .... Discussion 155

4.1. Oxide scale growth mechanism 155

4.1.1. Comparison of the Reaction Layer formation formed on growing oxide scale with results from diffusion couple experiments in literature 158

4.2. Competitive growth of Cr_2O_3 and Reaction Layer 159

4.3. Impact of the Mn/Co concentration ratio in the outer spinel layer 160

4.3.1. Influence on the oxide scale formation 160

4.3.2. Prediction of the long-term Mn/Co concentration ratio in the outer spinel layer from initial coating thickness 163

4.4. Co_3O_4 coating influence on AISI 441 oxidation kinetics 165

4.4.1. Influence of the atmospheric pressure plasma procedure on the oxidation performance 165

4.4.2. Coating thickness influence 167

4.4.3. Expected influence of coatings to the electrical performance from our previous observations 167

4.5. Influence of additional LSM coating on the oxidation kinetics of Co_3O_4 coated samples and effect on oxide scale composition 168

5.Main takeaways 171

Chapter V – Electrical performance of the Co_3O_4 coated and uncoated AISI 441 substrates 174

1. ..... Introduction 174

2. ..... Results 176

2.1. Electrical performance of the uncoated and B1-700 nm coated AISI 441 substrates 176

2.1.1. Area Specific Resistance (ASR) 176

2.1.2. Current inversion 178

2.2. Electrical performance of the uncoated, B2-400 nm and B2-2000 nm coated AISI 441 substrates 180

2.2.1. ASR (experiment 2) 180

2.2.2. Current inversion 183

2.3. Activation energy 183

2.4. Microstructural characterization of the oxide scale 185

2.5. Chromium poisoning 188

3. ..... Discussion 191

3.1. Uncoated AISI 441 192

3.2. B1 and B2 coated AISI 441 195

3.3. Long-term electrical performance prediction 196

3.4. Cr evaporation 198

4.Main takeaways 201

Conclusions 204

Outlook 206

List of Appendices 246

Appendix I – State of the art 246

Appendix III – Synthesis of Co_3O_4 by AP-PECVD technique: Growth Mechanisms 248

Appendix IV - Performance of Co_3O_4 Thin Films under SOEC Operating Conditions 249

Appendix V - Electrical performance of the Co_3O_4 coated and uncoated AISI 441 substrates 252

List of Figures

Figure I. 1 - a) Greenhouse gas emissions in CO_2 equivalent per year. The values are based on real measurements up to the year 2023, and on estimation thereafter based on three different scenarios[24]. b) Evolution of H_2 demand with time and by sector. Adapted from Carbone4 report[2]. 7

Figure I. 2 – Comparison of carbon footprint of the production of H2 for different methods[2]. 8

Figure I. 3 - Thermodynamic requirements for the water splitting reaction in function of the temperature[6]. 9

Figure I. 4 - Electrolysis cell illustrating the hydrogen and oxygen porous electrodes and the electrolyte. The triple phase boundary (TPB) points are indicated by the red dots. Reprinted from Liu et al.[5] 10

Figure I. 5 - The repeating unit, formed by the electrodes and electrolyte, is connected by interconnects[35]. 11

Figure I. 6 – Ellingham-Richardson diagram showing the Gibbs free energy for oxide formation in function of the temperature. Cr_2O_3 dissociation pressure at 800 °C is obtained from the red dotted line.[11] 17

Figure I. 7 - Oxidation behaviour based on the oxidation kinetics [Adapted from Reddy[39]].18

Figure I. 8 – Schematic of the scale formation following the Wagner's model[51]. 19

Figure I. 9 - Vapor pressure of two Cr-oxide species ($CrO_2(OH)_2$ and Cr_2O_3) as a function of temperature. [from Fergus[73]]. 22

Figure I. 10 - a) Scheme illustrating the interconnect/O_2 electrode/electrolyte cross section. The scheme highlights the passage of O_2 gas through the porous electrode to react with Cr_2O_3, which forms gaseous species (CrO_3). Adapted from Dejob[16]. b) Scheme highlights the Cr-poisoning effect produced by the Cr-volatile species on SOEC mode[84]. 24

Figure I. 11 - AB_2O_4 spinel structure where the lattice surroundings and nearest neighbours are represented as (a) the tetrahedral A-site, (b) the octahedral B-site, and (c) the tetrahedral anion X-site[94]. 26

Figure I. 12 - Bond length distance between the O-O bonds in the tetrahedral edge (a) and shared (b) and unshared (c) octahedral edge in function of oxygen parameter (u) and the lattice parameter (a). The polyhedron volume is also plotted in function of u (d). Adapted from Sickafus [94]........ 27

Figure I. 13 - a) Octahedral site preference energy (OSPE) for various cations from transition metals[96,107,114,115]. b) Co-Mn-O phase diagram[116]. 29

Figure I. 14 – Parabolic rate constants obtained from literature of uncoated (red) and coated (black) alloys annealed at 800 and 850 °C. Values were obtained for AISI 430, AISI 441 and Crofer 22 APU[48,62,83,119,124,126–132]. Coating type (from the Co-Mn spinel spectrum) and experimental conditions (laboratory air, dry O_2 and air + H_2O) are given in Appendix I.1. .. 31

Figure I. 15 - Scheme indicating the diffusion mechanisms behind the formation of a reactive layer between Co-Mn spinels and the chromia layer at high temperatures[121]. 33

Figure I. 16 - Scheme highlighting the various layers that should be considered for the area specific resistance (ASR) measurements for interconnect materials. [Adapted from Zhu[14]]. 35

Figure I. 17 - ASR values obtained for five different alloys after 3000 h annealing at 800 °C for Ce-CO coated substrates[48]. 38

Figure I. 18 - Representation of the chemical reaction happening in CVD and plasma-driven CVD. A, B and C represent the typical CVD reaction while A*, B* and C* the plasma process. The activation energy Y is smaller than the activation energy X from CVD process[167]. (a) Electron energy distribution function (EEDF) represents the typical distribution of electron energy in plasma. Here, it follows Maxwellian-Boltzmann shape while it may vary at atmospheric pressure. Average energy is below 2 eV and above that, inelastic process may happen (b)[21]........ 41

Figure I. 19 - Gas (T_g) and electron (T_e) temperature in function of the pressure. Adapted from Merche et al.[19] 43

Figure I. 20 - Classification of plasma jets using the specific input energy (SIE), defined by the plasma power dissipated by the dilution gas volume, in $J \cdot L^{-1}$. Each box defines a plasma jet configuration. Red triangle represents the configuration used in the present work. Adapted from Winter et al.[174] 45

Figure I. 21 - Scheme of a plasma jet configuration. Definition of three regions: A refers to the plasma discharge, B to the downstream region in a separate chamber to the discharge and C to the afterglow after the outlet exit. The right arrow indicates that the reactive species and gas temperature decreases downstream. Adapted from Fanelli et al. (2017) and Bardos et al. (1988). 48

Figure I. 22 – Schematic representing a typical vapour deposition reactor with the specific conditions. Reprinted from Sun et al.[185]. 50

Figure I. 23 - Energy level diagram of N_2 molecules. On the right side, a comparison with Ar and He metastable states. Reprinted from do Nascimento[190]........ 52

Figure I. 24 - Timescale of the typical processes happening in plasma deposition. Reprinted from Park et al. [200]........ 55

Figure II. 1 – Photos of the coated samples with different dimensions (described above) for each experiment. An uncoated sample is given for comparison. 66

Figure II. 2 - AP-PECVD schematic illustration describing the configuration system. 67

Figure II. 3 - Plasma jet connected to the 6-axes robotic arm. 68

Figure II. 4 - Schematic of the AISI 441 substrates support to hold the samples during deposition. 69

Figure II. 5 - Experimental setup for the test under inert N_2 atmosphere. The plasma jet was placed in an acrylic box. The O_2 detector was placed inside the box to measure the O_2 concentration (yellow arrow). Prior to performing the deposition, N_2 was purged to ensure low O_2 concentration. 70

Figure II. 6 - OES spectra of (Exp.) the real experiment in light green and (Sim.) the simulated spectrum from the LIFBASE software. The simulated spectrum considers only the NO species, thus the slight difference between spectra. 71

Figure II. 7 - Schematic illustration of the Cr-evaporation experiments. The furnace is shown in a) in which the isotherm region is highlighted by the red dotted square. The quartz crucibles (b) containing the substrates are positioned in the isotherm. The samples are placed inside the quartz crucible above four support points to avoid direct contact with the LSM powder. Holes were performed on top of the box to maintain a constant air flow [Adapted from Dejob[16]]. 74

Figure II. 8 - a) Quartz crucible for the Cr-evaporation experiment. b) Crucible filled with LSM powder. c) Crucible filled with LSM powder and coated AISI 441 substrate. 75

Figure II. 9 - Calibration curve of Co and Cr elements for the ICP-OES measurements. ... 76

Figure II. 10 - Illustration of the ASR system showing a schematic of the ASR sample (a) with its dimensions where the region of interest is highlighted in yellow, and the coated ASR sample (c). b) indicates the cross-section of the ASR stack. The samples are placed in-between two Pt electrode, which have the same shape as the samples. The Co_3O_4 coating is present on both sides of the samples as the LSM (50 µm) coating. The voltage is measured in each one of the strips. The current flow determines the SOC mode. 77

Figure II. 11 - Scheme of the ASR experiment (a) showing a stack with various samples and electrodes placed inside a reactor with a constant air flow. A 5 kg (0.5 MPa) weight was placed above the reactor. b) Assembly of samples/Pt electrodes compressed between alumina rods in the tubular quartz sample holder. c) Setup before insertion into the quartz reactor. Yellow arrow indicates the 5 kg weight. 78

Figure II. 12 – Schematic representation of the experimental setup used for the sequential $^{16}O_2/^{18}O_2$ isotopic tracer experiment. Adapted from Diez-Mayo et al. [unpublished work]. 79

Figure II. 13 - Experimental setup showing gas valves and pumping system (a), quartz reactor (b), substrate in the isothermal region (c), and portable oven (d)........................ 80

Figure II. 14 - MS spectrum of the output gas composition during second oxidation step (isotopic $^{18}O_2$). 81

Figure III. 1 - Raman spectra of the thin films comparing the injection rate (a) and $Co(acac)_3$ precursor-solvent system (b) variation. The Co_3O_4 standard is shown in magenta and the $Co(acac)_3$ precursor in black for reference. 91

Figure III. 2 - Co-based coatings deposited by AP-PECVD using (a) 10 mM, (b) 15 mM, (c) 20 mM and (d) 40 mM $Co(acac)_3$ concentration in the solution. The yellow dotted squares indicate the region covered by the plasma jet.. 91

Figure III. 3 - SEM top-view images of Co_3O_4 thin films produced by AP-PECVD under open-air conditions at 250 °C and 40% O_2 addition to the carrier gas. The micrographs indicate four distinct regions of the same Co_3O_4 thin film, two at 50 k magnification (a, b) and two at 100 k magnification (c, d). 93

Figure III. 4 - SEM cross-section images showing the thin films produced at 250 °C and 0% O_2 (a), 40% O_2 (b) and 60% O_2 (c), the films produced using 40% O_2 without heating using ethanol as the solvent (d) and acetone (e). (f) 300 °C substrate heating and 40% O_2 and (g) shows the thin film produced in non-oxidizing atmosphere.. 94

Figure III. 5 - TEM observations of the Co_3O_4 thin film prepared by AP-PECVD of $Co(acac)_3$ under open-air conditions, and a substrate heating temperature of 300 °C. The gas flow comprised a N_2 gas mixed with 40% O_2 for cobalt precursor injection: (a) Cross-section image of the Co_3O_4 thin film using bright-field TEM. (b) High resolution TEM micrograph at the substrate/coating interface. (c) Enlarged region obtained from image b (within green solid squares). (d) Identification of the lattice planes by Fast Fourier transform (FFT) performed from image (c)... 95

Figure III. 6 - Raman spectra (left) of thin films produced at 250 °C (substrate heating) and varied O_2 concentrations in the carrier gas. Standard Co_3O_4 is shown for reference (magenta). High-resolution X-ray photoelectron spectroscopy (HR-XPS) of Co 2p for the film produced with 40% O_2.. 96

Figure III. 7 - ToF-SIMS profile of the thin films prepared by AP-PECVD under open-air conditions at 250 °C and 0% O_2 in the carrier gas (left), and at 300 °C with 40% O_2 in the carrier gas. The thin film/SiO_2 native layer interface was identified by the variation of the inflection point from the different elements observed in the profile. 98

Figure III. 8 - Comparison of ToF-SIMS intensity ratios of O^-/CO^- (a) and O^-/Co^+ (b) for four films produced under open-air (different tones of blue) and non-oxidizing atmosphere (red). 99

Figure III. 9 - Raman spectra of thin films produced at different substrate heating temperatures and 40 % O_2 concentrations in the carrier gas (different tones of blue). Co(acac)$_3$ precursor (black) and standard Co_3O_4 is shown for reference (magenta)....... 100

Figure III. 10 - X-ray Diffractograms of the samples produced with no additional heating, at 250°C and 300°C with 40% O_2 concentration in the carrier gas (a). Variation of $\sin^2\theta$ versus $(h^2+k^2+l^2)$ for the Co_3O_4 thin films prepared without additional heating system (light blue), at 250°C (blue) and at 300°C (dark blue). The slope of the linear fit (A) was applied in equation ($A = \lambda/4a^2$) to determine the lattice parameter 8.080 Å, 8.078 Å, and 8.074 Å, for the sample prepared without external heating, 250°C and 300°C,respectively (b). Williamson-Hall plot of the sample produced at 250°C with 40% O_2 concentration in the carrier gas (c)........ 101

Figure III. 11 - OES measurements were performed without a heating plate and with 40% O_2 gas mixture in the carrier gas. (a) OES spectra were measured at different distances from the plasma torch outlet. (b) Temperature profile obtained from the OES (red circles) and thermocouple (black squares) measurements at different distances from the outlet nozzle. Thermocouple (T) measurements were also performed in a controlled atmosphere, either a nonoxidizing environment (magenta spheres) or an environment simulating the open-air (80% N_2/20% O_2, defined by blue squares). 104

Figure III. 12 - FTIR (a) and Raman (b) spectra of the thin films produced by increasing the plasma torch outlet-precursor injection distance from 15 to 40 mm. The Co(acac)$_3$ precursor is provided for comparison. 105

Figure III. 13 - (a) OES measurements with only plasma (black), plasma and acetone (magenta), and plasma and the precursor solution (blue). (b) OES measurements comparing various O_2 concentrations in the carrier gas. 108

Figure III. 14 - Plasma colour variation on the open-air (left) and inert atmosphere (right). The colour change highlights the lack of O_2 in the non-oxidizing atmosphere 110

Figure III. 15 - a) Raman spectra of the thin films prepared by AP-PECVD under open-air conditions at 250°C and 40% O_2 in the carrier gas (Co_3O_4 thin film - blue) and in non-oxidizing atmosphere (Cobalt-based thin film - red). The Raman spectra of the reference Co_3O_4 sample (Co_3O_4 reference - magenta), fabricated from the oxidation of a pure metallic cobalt sample, and the raw cobalt precursor (Co(acac)$_3$ precursor - black) are provided for comparison. b) X-ray diffractograms of the cobalt-based thin films prepared by AP-PECVD under open-air conditions at 250°C and 40% O_2 (Co_3O_4 thin film - blue) and under non-oxidizing atmosphere (Cobalt-based thin film - red). The Co_3O_4 reference (magenta) No. 00-042-1467 from the JCPDS database is provided for comparison. 111

Figure III. 16 - ToF-SIMS profile of the thin films prepared by AP-PECVD under open-air conditions at 250°C (Co_3O_4 thin film) in a) and under non-oxidizing atmosphere (Cobalt-based thin film) in b) without addition of O_2 in the carrier gas. The interface thin film/SiO_2 native layer was identified by the variation of the inflection point from the different elements observed in the profile. 112

Figure III. 17 - Relative atomic composition of the Co_3O_4 thin films produced by AP-PECVD under open-air conditions (250°C and 40% O_2) and the cobalt-based thin film produced by AP-PECVD under non-oxidizing atmosphere conditions. XPS measurements were performed at the surface of the samples, after 900 s of Ar_{1000}^+ cluster sputtering and after 900 s of Ar^+ sputtering. 113

Figure IV. 1 – Scheme indicating the side view (a) and top view (b) of the AP-PECVD deposition on the AISI 441 substrates. 118

Figure IV. 2 – SEM top-view images from Co_3O_4 coatings produced following batch 1 (a, b and c) and batch 2 (d, e and f). The micrographs were obtained at a magnification of 1000x (a and d), 5000x (b and e) and 10000x (c and f). For a better comparison, the same coating thickness (700 nm) was prepared. 120

Figure IV. 3 – Surface topography images obtained for B1 (a and b) and B2 (c and d) coatings. The z scale was homogenized in all cases irrespective of the magnification. 121

Figure IV. 4 – FIB-SEM cross-section from B1 (a) and B2 (b) 700 nm thick coatings......... 122

Figure IV. 5 – Raman spectra of coatings produced at 0.05 $mm\cdot s^{-1}$ (Chapter III, black), 0.5 $mm\cdot s^{-1}$ (B1, red) and 5 $mm\cdot s^{-1}$ (B2, violet). The FWHM of the A1g peak of each condition is displayed in the graph. 122

Figure IV. 6 - Evolution of the mass gain per area unit as a function of time for uncoated and coated samples at 800 and 850 °C. At 800 °C, the values were obtained using thermogravimetric (TGA) measurements under dry air while at 850 °C, discontinuous mass gain experiments were carried out under laboratory air. 124

Figure IV. 7 – Uncoated AISI 441 sample oxidized under dry air for 530 h at 800 °C. a) FIB-SEM cross-sectional micrograph highlighting the duplex layer formed atop the AISI 441 substrate and additional features observed after oxidation. b) SEM cross-sectional micrograph. Orange line illustrates the zone analyzed by EDS profiling (c). 126

Figure IV. 8 – Co_3O_4 coated AISI 441 sample oxidized under dry air for 500 h at 800 °C. a) Top-view image showing the polyhedral shape of the scale grains. SEM (b) and FIB-SEM (c) cross-sectional micrographs show the various features observed in the micrographs at low and high magnification, respectively. Orange line illustrates the zone analyzed by EDS profiling (d). 127

Figure IV. 9 - SEM cross-sectional micrographs showing uncoated (a, c and e) and B1 coated (b, d, f) AISI 441 substrates oxidized for 24 h (a and b), 48 h (c and d) and 120 h (e and f). EDS profiles from uncoated (g) and B1 coated (h) samples after 120 h of exposure at 850 °C are shown. 128

Figure IV. 10 – STEM-EDS mapping from B1 samples oxidized under laboratory air for 120 h at 850 °C.......... 129

Figure IV. 11 - Raman spectra from uncoated (a) and B1 coated (b) samples at various oxidation conditions. Samples were compared with a Cr_2O_3 reference spectrum (a) and with the as-coated sample (b). Reference lines were used to highlight the peak positions from the Cr_2O_3 reference (a) and F_2g (1) and A_1g lines from the initial Co_3O_4 spinel. Dotted red lines show the peak shift and the red arrow, the broadening of the peaks. 131

Figure IV. 12 - a) Amount of oxidized Cr (sphere) and Mn (star) over time, in $mol\cdot cm^{-2}$, for the uncoated (red) and coated (black) samples oxidized at 850 °C under laboratory air. b) The square thickness of the layers showing a Cr-rich phase for the uncoated (red) and coated (black) samples. 133

Figure IV. 13 - NanoSIMS analysis of the cross-section of B1 coated AISI 441 substrate annealed at 850 °C for 120 hours. Elemental mapping is shown for Mn (a), Cr (b) and Co (c). The elemental profile is shown in (d). 134

Figure IV. 14 – TEM analysis of the B1 coated sample annealed at 850 °C for 120 hours. a) STEM cross section showing the chromia scale (down) and Co-Mn spinel (up). The red rectangle indicates the region analyzed by EDS (b). c) Represents the elemental mapping of Cr (d), Co (e), and Mn (f) altogether. 135

Figure IV. 15 – SEM cross-sections (a,c) and EDS profiles (b,d) of B1 coated samples annealed at 800 °C for 2500 h under laboratory air (a,b) and 5000 h (c,d) under an O_2 atmosphere. The dotted lines are used to highlight each layer of the chemical profile. The small-dotted line separates the Cr-rich sublayer (indicated by the region where Cr content is higher than Mn) and the Mn-rich sublayer (higher Mn content). 136

Figure IV. 16 – XPS analysis (a) and Raman spectra (b) of the B1 coated samples annealed at 800 °C for 2500 h under laboratory air. XPS analysis shows the relative atomic concentration of Mn, Co and Cr over the sputtering time. The XPS profile is performed from the surface to the oxide Oxygen was not considered in the measurements. The Raman spectrum of the B1 coated sample (blue) is compared to an unoxidized Co_3O_4 reference sample (black) and oxidized AISI 441 (magenta). 137

Figure IV. 17 - – Mass gain per unit area in function of time at 800 °C. The thermogravimetric experiments were conducted in dry air for 200 h for coated samples and 530 h for uncoated AISI 441. From these experiments, k_p values were calculated, and mass gain values were extrapolated to 2000 h. Discontinuous experiments were performed for 2000 h at 800 °C under laboratory air. Empty symbols refer to values corrected for Cr evaporation. 140

Figure IV. 18 - SEM cross-sections (a,b,c) and EDS profiles (d,e,f) of B2 coated samples annealed at 800 °C for 200 h under dry air. Figures (a) and (d) represent the sample B2-400 nm, (b) and (e) the sample B2-1000 nm, and (c) and (f) the sample B2-2000 nm. The dotted lines are used to highlight each layer of the chemical profile. 142

Figure IV. 19 - SEM cross-section (a) and EDS profiles (b) of B2-400 nm sample, annealed at 800 °C for 2000 h under laboratory air. The dotted lines are used to highlight each layer of the chemical profile. The small-dotted line separates the Cr-rich sublayer (indicated by the region where Cr content is higher than Mn) and the Mn-rich sublayer (higher Mn content). 144

Figure IV. 20 - TEM bright field cross-section of the B2-1000 nm sample (a). Yellow arrow indicates the region where the EDS profile (b) was taken, and the red circle indicates the region where SAED analysis was performed. 146

Figure IV. 21 - TEM bright field cross-section of the B2-2000 nm sample, showing the Co-Mn spinel layer (a), and the chromia layer (b). Yellow arrows indicate the regions where the EDS profiles (c,d) were taken, and the red circles indicate the regions where SAED analyses were performed. From (g), a STEM-EDS mapping was performed, showing Mn (h), Si (i) and Cr (j). 147

Figure IV. 22 - Raman model developed for the F_2g (1) (a) and the A_1g (b) vibration modes using data obtained by EDS analyses for various samples. Peak position (black) and broadening (red) are presented in function of Mn content in the Co-Mn spinel. 149

Figure IV. 23 – Schematic description of the two possible scenarios for the formation of the oxide scale. The scheme highlights the initial as-deposited material, and the oxide formed after the first oxidation step using $^{16}O_2$, hypothesizing on the formation of a chromia oxide and Mn-enrichment to the spinel. The two scenarios relate to the second oxidation step using $^{86}O_2$, and the layers grown during this stage are shown in purple. 153

Figure IV. 24 – SIMS intensity profiles of uncoated (a) and B2-1000 nm coated (b) AISI 441 in function of sputtering time. The right axis indicates the intensity fraction of ^{18}O over the total oxygen intensity (^{16}O+^{18}O). The dotted lines indicate the spinel/chromia and chromia/alloy interfaces. 154

Figure IV. 25 – Evolution of the oxide scale with the oxidation time. a) Schematic representation of the oxide scale at the early oxidation stages: Mn diffusion into Co-spinel and Cr_2O_3 formation. b) Initial diffusion of Cr into the external spinel oxide resulting in the formation of the Reactive Layer (RL). The Co-Mn spinel grows outwards. c) Continuous Cr diffusion leads to Cr-enrichment of RL and thus formation of Cr_2O_3. All oxide layers grow outwards. 156

Figure IV. 26 – Schematic representation of the influence of Mn/Co concentration ratio on the growth rate of chromia and the RL. 160

Figure IV. 27 - Thermodynamic calculations of the (a) cation distribution at 800 °C and (b) phase diagram for $Co_{3-x}Mn_xO_4$ spinels obtained using the software Thermo-Calc[306]. Data was obtained from Golikov et al.[311] 162

Figure IV. 28 - a) Amount of oxidized Mn in function of time at 800 °C. Red empty and black stars represent coated and uncoated samples respectively. The horizontal line represents the maximum amount of Mn in the AISI 441 alloy, calculated from equation IV.4. The dotted line is a guide to the eye, representing the amount of Mn oxidized over time. Pink squares indicate coated samples with an extra LSM layer. b) Mn content in the Co-Mn spinel, calculated from equation IV.5, in function of the initial Co_3O_4 coating thickness. The dotted lines correspond to the Co_3O_4 initial coating thicknesses used in this work (400, 700, 1000 and 2000 nm). 164

Figure IV. 29 - a) Mass gain over time for B1-700 nm coated samples with the addition of a LSM layer using TGA measurements. Samples were oxidized at 700, 800 and 850 °C for 500, 450 and 170 h, respectively. The k_p values are highlighted in (b) 169

Figure IV. 30 – SEM cross-sections and EDS chemical profiles of the B1-700 nm coated samples with the addition of a LSM layer oxidized at 700 (a,b,c), 800 (d,e,f) and 850 °C (g,h,i). 170

Figure V. 1 - Heating profiles (Experiments 1 & 2) for the evaluation of the ASR values of the uncoated AISI substate (Experiments 1 & 2) and the B1-700 nm (Experiment 1), B2-400 nm (Experiment 2) and B2-2000 nm (Experiment 2) coated AISI substates. 175

Figure V. 2 - (a) Area Specific Resistance (ASR) experiment evolution as a function of time. The experiment was conducted under 5 $L \cdot h^{-1}$ flow of synthetic air at 700 °C for 333 h, 800 °C for 320 h and 850 °C for 890 h. The average ASR values of uncoated AISI 441 sample (black) and the ASR values of the B1-700 nm under SOFC (red) and SOEC (blue) mode were followed. Current inversion periods (magenta spheres) were conducted during the experiment. The third current inversion period is highlighted in (b) for SOEC/SOFC modes of the B1-700 nm sample. At the end of the experiment, short additional isotherms were conducted at 800 and 700 °C, zoom in (c). 177

Figure V. 3 - (a) Area specific resistance (ASR) experiment evolution in function of time. The experiment was conducted under 5 L·h^{-1} flow of synthetic air at 700 °C for 330 h, 800 °C for 330 h and 850 °C for approximately 2400 h. The average ASR values of uncoated (black), B2-400 nm (blue) and B2-2000 nm (red) AISI 441 substrates were followed. Current inversion periods (magenta spheres) were conducted during the experiment. At the end of the experiment, short additional isotherms were conducted at 800, 750 and 700 °C (b)...... 181

Figure V. 4 – ASR values in function of temperature determined during stepwise cooling at the end of experiment 2.. 184

Figure V. 5 – SEM cross-section (a) and EDS analysis (b) of the uncoated sample after the ASR experiment 1. The orange arrow highlights the position of the EDS measurement. . 185

Figure V. 6 - SEM cross-section (a) and EDS analysis (b) of the B1-700 nm sample after the ASR experiment. The measurement. 186

Figure V. 7 - SEM cross-sections (a, c and e) and EDS analyses (b, d and f) of the uncoated (a, b), B2-400 nm (c, d) and B2-2000 nm (e, f) samples after the ASR experiment. The orange arrow highlights the position of the EDS measurement. 188

Figure V. 8 - SEM cross-sections of the uncoated (a) and B1-700 nm coated (b) samples after the ASR experiment. The yellow circles indicate regions with higher Cr concentration highlighted by the chemical contrast on the measurement. In (a), the Cr chemical mapping is shown for comparison. In (b), the square represents the region in the yellow circle close to the Pt electrode. The EDS analysis are shown in Table V.5. 189

Figure V. 9 - SEM cross-section (a) of the B2-2000 nm AISI 441 substrate after the ASR experiment working in SOEC mode. The yellow rectangles highlight the region where the EDS measurements were performed. 12 regions in the LSM layer were analyzed, with region 1 representing the region closer to the oxide and 12, the region closer to the Pt electrode. (b) Atomic concentration of Cr (star) and Co (square) are presented in function of the measurement (distance from the oxide) within the LSM layer. 191

Figure V. 10 – Calculated ASR values in function of the layer thickness (µm). The ASR values were calculated from equation V.2, and the electrical conductivity data was obtained from Liu et al.[118] for the Co-Mn spinels with different Cr contents ($MC_{3-x}Cr_xO_4$), while the chromia values were obtained from the lower[151] and upper[144,145] chromia conductivity values in literature, and from the values obtained in our work (hexagon filled in the upper part). .. 194

Appendix I. 1 - Parabolic rate constants (kp) obtained in the literature for coated and uncoated AISI 441, Crofer H, Crofer 22 APU and AISI 430. Coatings used, annealing temperature and conditions used are shown. 246

Appendix III. 1 - TEM cross section of the Co_3O_4 thin film (a). Selected area electron diffraction (SAED) image (b) corresponding to the region highlighted in the orange dotted circle. The SAED analysis confirms the formation of crystalline Co_3O_4. Peak positions are the same as found in XRD. There is a slight deviation from the theoretical value for Co_3O_4. 248

Appendix III. 2 - Peak positions, FWHM for the peaks F_2g (1) and A_1g, which refers to Co^{2+} and Co^{3+} respectively, and the peak ratio based on the intensity of these two peaks. Data was acquired from the Raman spectrum for all conditions and FWHM was calculated using a Lorentzian deconvolution from Origin software. The data was compared to a reference from literature (Hadjiev et al.[14]) and to a Co_3O_4 standard produced in the laboratory. 248

Appendix IV. 1 - SIMS profile of the uncoated (a) and B1 coated (b) samples annealed at 850 °C for 48 hours. 249

Appendix IV. 2 - GD-OES analysis of the uncoated (a, c) and coated (b, d) samples annealed at 850 °C for 120 hours. The (c) and (d) represent a zoomed region of the (a) and (b) images to highlight elements in minor concentration. 249

Appendix IV. 3 – NanoSIMS analysis with elemental mapping of Cr, Mn and Co. A Mn-Cr layer is observed between alloy and Cr_2O_3. 250

Appendix IV. 4 – Cross-section micrograph of the uncoated AISI 441 substrate after 2000 h of exposure at 800 °C. Average Cr-rich oxide layer thickness is 4.5 µm......................... 250

Appendix IV. 5 – X-ray diffraction analysis of B2-1000 nm after 2000 h of exposure at 800 °C. Shoulder peaks were referenced to the tetragonal phase. 251

Appendix V. 1 - (a) ASR evolution as a function of time for the B1-700 nm sample operated in SOFC (red) and SOEC (blue) modes. (b) ASR evolution during heating and cooling at the end stage of the ASR experiment. 252

Appendix V. 2 - SEM cross-sections (a, c) and EDS analyses (b, d) of the B1-700 nm sample under SOEC (a, b) and SOFC (c, d) modes after the ASR experiment 3. The orange arrow highlights the position of the EDS measurement. 254

Appendix V. 3 - Chromia electrical conductivity calculated for coated samples from experiments 1-3. ASR values were taken from the values at the end of the experiment at 700 °C, and from the average values from SOC modes in experiment 3. The average chromia thickness was considered. 255

List of Tables

Table I. 1 - Chemical composition of some of the current alloys used as interconnect materials. 14

Table I. 2 – Summary of the degradation issues observed in SOEC technologies and the main mitigation strategies. [Reprinted from Liu et al.[5]]. 15

Table I. 3 - Electrical conductivity and thermal expansion coefficient (TEC) for several compounds that may be present after the oxidation of an interconnect. 37

Table I. 4 – Main deposition techniques reported in literature for the synthesis of Co-Mn spinel oxides. Reprinted from Zhu et al.[14] 39

Table I. 5 - Internal energy of several molecular species available in AP-PECVD using a N_2 plasma gas under open-air conditions. Values were obtained from Huber et al.[199] and Liu et al.[179]. 54

Table I. 6 – Main Co-based precursors observed in the literature. 62

Table II. 1 - AISI 441 chemical composition from GDMS analysis in %wt. * :the carbon concentration was measured by combustion analysis coupled with infrared detection. 67

Table III. 1 - Experimental parameters evaluated for the AP-PECVD experiments. 89

Table III. 2 - Chemical composition of the thin films obtained using various O_2 concentrations in the carrier gas. Results shown here were obtained by HR-XPS after a cluster Ar sputtering (Ar_{1000}^+) for 900 s. 97

Table III. 3 - Chemical composition of thin films obtained using various substrate heating temperatures and 40% O_2 concentration in the carrier gas. Results shown here were obtained by HRXPS after a cluster Ar sputtering (Ar_{1000}^+) for 900 s, and from the survey spectra in the bulk after Ar+ sputtering for 900 s. 99

Table III. 4 - FTIR organic signatures obtained from[259–261]. The Y_w shows a strong decrease in signal compared to the precursor peak. 106

Table IV. 1 – Deposition conditions used for the two batches B1 and B2 used for the oxidation experiments. 117

Table IV. 2 – Description of the experiments performed for each set of conditions. 119

Table IV. 3 - Parabolic rate constant (k_p) of uncoated and coated AISI 441 substrates at 800 and 850 °C. The k_p values of the AISI 441 substrates oxidized at 800 °C (TGA measurements) were also evaluated in the last 100 h. 125

Table IV. 4 – Chemical composition of the inner and external layer formed during oxidation at 800 and 850 °C of coated and uncoated AISI 441 substrates. The thickness (ImageJ) and the chemical composition (EDS) of the chromia and spinel layers were obtained from the average measurements performed on at least five micrographs. 130

Table IV. 5 – Thickness values of the chromia and spinel layers and the composition of the spinel sublayers for B1 coated samples at 800 °C for 2500 and 5000 h. The ratio of each sublayer is also displayed. 138

Table IV. 6 – Parabolic rate constant (k_p) values obtained from thermogravimetric experiments for 200 h for B2 coated samples and 530 h for uncoated AISI 441. B1-700 nm k_p is shown for comparison. 140

Table IV. 7 – Chemical composition of the spinel layer for each of the coated samples obtained by EDS analysis, and the thickness values for the chromia and spinel oxide layers. Samples were annealed at 800 °C for 200 h under dry air. 142

Table IV. 8 - Chemical composition of the spinel sublayers of the B2-400 nm coated AISI 441 substrate obtained by EDS analysis, and the thickness values for the chromia and spinel oxide layers. Samples were annealed for 2000 h at 800 °C under laboratory air. 144

Table IV. 9 - Chemical composition of the total external spinel layer for each of the coated samples obtained by EDS analysis, and the thickness values for the chromia and spinel oxide layers. Samples were annealed for 2000 h at 800 °C under laboratory air. 145

Table IV. 10 - Comparison of Chromium evaporation rates of coated and uncoated AISI 441 substrates (this work) after exposure in laboratory air at 800 °C for 2000 h. Values for various ferritic stainless steels (FSS) exposed at 800 °C for different times and atmospheric conditions found in literature are added (italic). 151

Table IV. 11 – Thickness evolution of Cr_2O_3 and RL over time for B2 coated samples. 159

Table IV. 12 – Thickness evolution of Cr_2O_3 and RL over time for B2 coated samples 160

Table V. 1 – ASR values for the B1-700 nm (both SOC modes) and uncoated (average) AISI 441 substrates at the end of the experiment at 700, 800 and 850 °C. The increasing rate was obtained from the linear regression during the isotherm at 850 °C. The values in parenthesis for uncoated sample highlights the increasing rate during the steep ASR rise occurring from 1200 h of exposure. 178

Table V. 2 – Average ASR values for the B2-2000 nm, B2-400 nm and uncoated samples at the end of the experiment at 700, 800 and 850 °C. The increasing rate was obtained from the linear regression during the isotherm at 850 °C. Values obtained from 1600 to 2120 h are shown in the left, and from 2200 to 3100 h are shown in the right. The values in right for uncoated sample highlight the increasing rate during the steep ASR rise (2750-2900 h). Values from experiment 1 are given for comparison (orange). Values in parentheses represent the SOFC mode while the SOEC values are shown on the right for B1-700 nm sample. 182

Table V. 3 – Activation energy values obtained from the small polaron hopping conduction equation for samples from experiments 1 and 2 (bold). The activation energies from SOFC (left) and SOEC (right) were calculated for the B1-700 nm sample. Average value is shown in parenthesis. The activation energy shown here is the average value from the activation energy obtained during a cooling and a heating step. 184

Table V. 4 - Average thickness of chromia and spinel layers from experiment 1 (highlighted in orange) and 2 obtained from five micrographs and measured using the software imageJ. The chemical composition from the spinel layer was obtained from the average of five EDS analysis. 186

Table V. 5 – Chemical composition (% at.) of regions 1 and 2 highlighted by the yellow squares in Figure V.8b. The other element is oxygen. 189

Table V. 6 - XPS measurements obtained at the LSM and Pt side of the surface of the uncoated and B1-700 nm coated samples working in SOFC mode. After the experiment, the cell was disassembled, separating the alloy/LSM couple from the Pt electrode. The measurements were conducted at the LSM and Pt electrode surfaces. 190

Table V. 7 – Calculated ASR values for the spinel phase using the spinel thickness measured and the electrical conductivity values from literature[118]. 196

Table V. 8 – Chromia electrical conductivity values calculated from the ASR values and Cr_2O_3 thickness for coated and uncoated samples at 800 °C. 196

Table V. 9 – Predicted lifetime values at 850 °C for coated AISI 441 samples estimated from equation V.3. 198

Table V. 10 – Calculated required thickness for the Cr-rich oxide redeposited at the Pt/electrode interface. The thickness values were calculated using the chromia conductivity values from literature and from this work, and the ASR obtained at the end of experiment 1 at 800 °C. 199

Introduction

Hydrogen is currently widely employed in numerous chemical processes, most notably in ammonia synthesis for fertilizers and methanol production, as well as in the steel industry for the reduction of iron ore. Beyond these established uses, hydrogen also holds significant potential for emerging applications such as synthetic fuel production (for aviation, maritime transport, and heavy-duty road vehicles) and energy storage solutions for intermittent renewable energy sources [1–4].

Although hydrogen is produced naturally when underground water encounters iron-rich rocks, called "geologic", natural or white hydrogen, its commercial extraction is still in the early stage and most hydrogen must be produced. Current hydrogen production processes are predominantly carbon-intensive, relying mainly on methane steam reforming or coal gasification[2]. In 2018, global hydrogen production reached approximately 115 million tonnes (including about 1 million tonnes in France), resulting in greenhouse gas emissions equivalent to around 3% of global emissions, comparable to those from the entire aviation sector[2,3].

Consequently, decarbonizing hydrogen production has become a crucial challenge in achieving carbon neutrality targets by 2050. Among the various production pathways, water electrolysis powered by low-carbon electricity is currently considered the most promising solution[3,5].

Among electrolytic methods, the Solid Oxide Electrolysis Cell (SOEC), operating at 700 – 800 °C, stands out for its high efficiency through combined electrical and thermal energy inputs[6,7]. SOECs rely on a stack of multiple electrolysis cells to reach high H_2 output. The electrolysis cells are connected by means of interconnects (ferritic stainless steel), which ensure efficient electrical conduction while simultaneously separating the gas streams passing through the cathode (H_2/H_2O) and anode (O_2)[5,6,8–10]. The interconnects must maintain good electrical performance and chemical stability during the whole SOEC lifetime, determined to be at least 40,000 h (ca. 4.5 years)[11]. The high temperatures (700 – 800 °C) generally used during SOEC operation is responsible for the formation of a protective Cr-rich oxide scale. However, this protective Cr-rich oxide presents low electrical conductivity, which detrimentally increase the resistance over the stack with the oxide scale thickening. In addition, the oxide may further oxidize in O_2/H_2O environments, producing gaseous Cr-species, which poison other components of the cell by blocking active sites.[5,12,13]

Protective coatings are critical to limit degradation of the interconnects and enhance their lifetime. The main coating strategies involve spinels from the Co-Mn system and their variations[14]. Currently, the main coating technique commercially used is Physical Vapor Deposition (PVD) but slurry deposition and ElectroPhoretic Deposition (EPD) also offer promising solutions [14,15]. Despite being technologically mature, these techniques present a few drawbacks, such as the requirement of energy-consuming pumping systems for PVD and/or a series of reduction/oxidation pretreatments steps for the densification of the coatings for slurry or EPD [14]. These features can increase cost (PVD) or degrades the initial conductivity of the interconnect by forming Cr rich oxide scale during the pre-treatment annealing step (Slurry and EPD).

The present PhD work aims at studying a new method for the deposition of protective coatings: Atmospheric Plasma-Enhanced Chemical Vapor Deposition (AP-PECVD). The AP-PECVD process is part of the numerous coating synthesis and deposition processes evaluated by CEA for SOEC interconnects. In the framework of these activities, several PhD projects[16,17] are funded by the *Transversal Materials & Processes Skills Program* (*Programme Transversal de Compétences Matériaux & Procédés*). AP-PECVD offers the benefit of working at atmospheric pressure, similar to slurry deposition and EPD, but may not require additional heat treatment steps to achieve dense coatings. In addition, thickness-controlled coatings, *i.e.*, several hundreds of nanometres to a few microns, can be formed in AP-PECVD while EPD or slurry deposition produce thicker coatings, *i.e.*, tens of microns[18,19]. Finally, AP-PECVD, which enables the growth of high-purity oxides related to the presence of plasma reactive species[20,21], allows localized coating synthesis and is easily scalable for industrial applications.

The objectives of this PhD work are twofold.

The first objective of the present PhD work is to understand the AP-PECVD mechanisms enabling the growth of dense Co_3O_4 coating. Several deposition parameters were studied and their impact on the film growth mechanism and coating properties (e.g. stoichiometry, morphology and impurities) was elucidated.

The second objective of the present PhD work is to develop a deep understanding of the oxidation behaviour, the Cr volatilization rate, diffusion mechanisms, and the electrical performances of Co_3O_4 coated AISI 441 substrates under SOEC operating conditions (air at 700 – 850 °C). The performances, compared to the ones of uncoated AISI 441 substrates, are correlated to the AP-PECVD process parameters and coating characteristics.

The present PhD manuscript is organized into five chapters.

- The first chapter, "State of the art", presents the context and motivation for this work. The fundamentals of oxidation, and the current knowledge on interconnect protection for SOCs technologies are analyzed. The main techniques used for coating deposition are briefly reviewed, while plasma deposition processes are described with more details. Finally, the approach and objectives of the present PhD work are explained.
- The second chapter, "Experimental section", reports in detail the experimental setup used for the coating deposition, and for the evaluation of the coating performance under operating conditions. The different analytical techniques and conditions used to characterize the plasma phase and composition, morphology and structure of the coatings are reported.
- The third chapter, "Synthesis of Co_3O_4 by AP-PECVD technique: Growth mechanisms", focuses on the understanding of plasma-precursor interactions and the thin film growth mechanisms.
- The fourth chapter, "Performance of Co_3O_4 coated AISI 441 substrate under SOEC Operating Conditions", studies the oxidation behaviour, the Cr volatilization rate, diffusion mechanisms of AISI 441 substrates coated with the Co_3O_4 coatings previously developed in chapter III. The influence of the Co_3O_4 coating thickness on the oxidation of the AISI 441 substrate and on the oxide scale growth is notably assessed.
- Finally, in the fifth chapter, "Electrical performances of the Co_3O_4 coated and uncoated AISI 441 substrates", *in-situ* Area Specific Resistance (ASR) experiments are used to study the electrical performance of the Co_3O_4 coatings prepared from different AP-PECVD procedures and different thicknesses.
- The conclusions of this work and the outlooks for future research endeavours are presented in the final section.

I – State of the art

1. Solid oxide electrolysis cell (SOEC)

1.1. Global warming

Greenhouse gas (GHG) emissions have been steadily rising since the onset of the Industrial Revolution in the XVIII century, with the discovery of the potential of fossil fuels to generate energy. The technological development and population increase requested higher amounts of energy production, which were followed by rising GHG emissions[22,23]. Figure I.1a highlights the exponential rise in CO_2 emissions. The relation of GHG emission and global warming is well known. Currently CO_2 concentrations reached 425 ppm compared to 280 ppm of pre-industrial levels[24]. According to the Intergovernmental Panel on Climate Change (IPCC), CO_2 concentrations should remain below 450 ppm to avoid a global temperature rise of 1.5 °C above pre-industrial levels within the next few decades[24]. This threshold is associated with severe climate impacts, including more frequent and intense heatwaves, rising sea levels, and ecosystem disruption[22]. To mitigate these effects, it is imperative that global GHG emissions stabilize within the next few years and decline sharply thereafter (Figure I.1a). The reduction in fossil fuel dependency should be compensated by increased deployment of low carbon-emitting sources, such as nuclear power, renewable energies, and other low-carbon sources[25].

Current efforts should also focus on tackling processes emitting large amounts of CO_2. Therefore, many governmental policies consider hydrogen to be fundamental to further reduce CO_2 emissions. Hydrogen is extensively used in oil refining, ammonia production for fertilizers, and methanol synthesis in refining processes, with its demand steadily increasing in recent years (Figure I.1b). However, the main challenge lies in the carbon-intensive origin of this hydrogen. At present, around 99% of global hydrogen production is derived from fossil fuels[4], primarily through steam methane reforming and coal gasification, generating approximately 920 million tonnes of CO_2 annually[3,26]. This amount is equivalent to about 2–3% of total global greenhouse gas emissions, similar to the CO_2 emitted from aviation, globally[2].

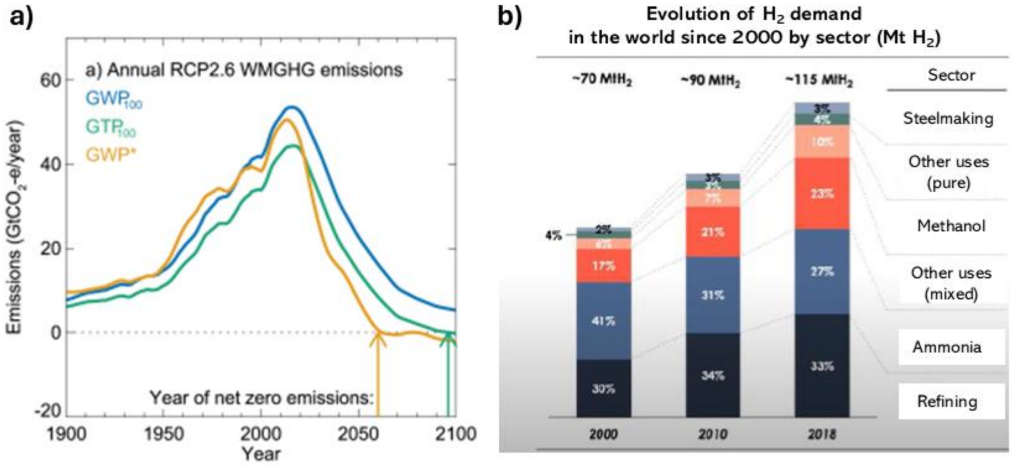

Figure I. 1 - a) Greenhouse gas emissions in CO_2 equivalent per year. The values are based on real measurements up to the year 2023, and on estimation thereafter based on three different scenarios[24]. b) Evolution of H_2 demand with time and by sector. Adapted from Carbone4 report[2].

1.2. H_2 production as part of the solution

Hydrogen is typically produced via steam methane reforming (SMR), emitting 10–13 kg of CO_2 per kg of hydrogen. Coal gasification, another conventional route, is even more carbon-intensive[2]. Another alternative relies on coupling these processes with carbon capture, utilization, and storage (CCUS) to reduce emissions, which can theoretically capture up to 90% of CO_2 emissions. However, the widespread deployment of CCUS is limited by high capital costs, energy penalties, and technological challenges[3,27]. Figure I.2 compares the CO_2 emissions of these high carbon emitting processes with low carbon-emitting sources. Producing H_2 via water electrolysis powered by low CO_2 emitting energy sources (e.g., renewables and nuclear) exhibits great potential for cutting CO_2 emissions.

Therefore, transitioning to green hydrogen, produced using low-carbon emitting electricity (e.g., nuclear, renewables), offers a major opportunity to decarbonize existing H_2-dependent industries (shown in Figure I.1b). Secondarily, H_2 could be an alternative to decarbonize new sectors, particularly the ones that are hard-to-abate with current technologies[28]. These new usages are expected to correspond to approximately 40 % of H_2 demand by 2030[26]. Highly pollutant process, such as steelmaking, heavy industry, and long-distance transport may profit from using H_2 to decarbonize the sector. Hydrogen-based direct reduction in steel production could reduce emissions by up to 90%, while fuel cell vehicles eliminate tailpipe emissions entirely. In aviation and maritime sectors, where electrification is challenging, hydrogen-derived synthetic fuels offer a promising alternative[3,27,29–31]. Such potential solutions should drive the global hydrogen demand to triple by 2050.

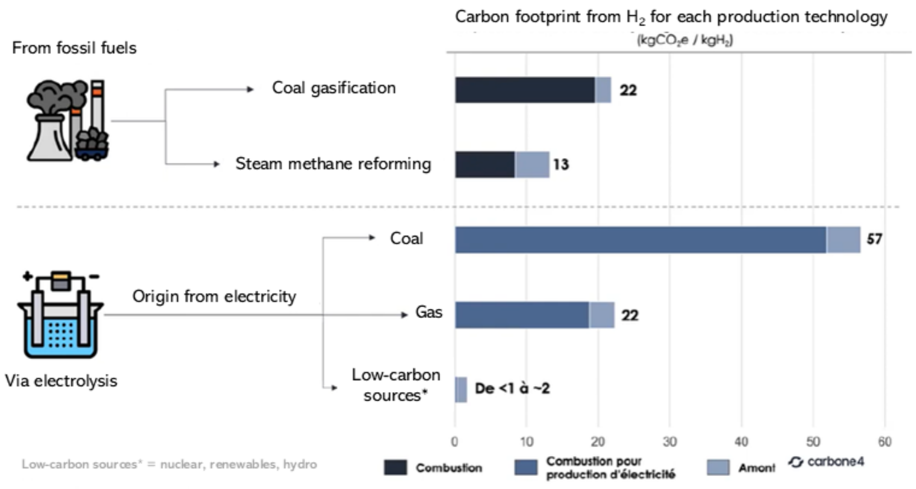

Figure I. 2 – Comparison of carbon footprint of the production of H2 for different methods[2].

1.3. Low carbon-emitting H_2 production

Low carbon emitting hydrogen, generated via the water electrolysis powered by low polluting sources (e.g., renewables and nuclear), offers a near-zero-emission alternative. Despite its environmental advantages, low carbon emitting hydrogen currently constitutes less than 1% of global production due to high energy requirements and elevated costs[4]. Electrolysis involves splitting water into hydrogen and oxygen using an electric current, typically consuming around 50 kWh per kilogram of hydrogen produced[3], with current electrolyzers operating at 70% efficiency[5].

Three main electrolysis technologies are under development or deployment: alkaline electrolyzers, proton exchange membrane (PEM) electrolyzers, and solid oxide electrolyzer cells (SOECs). Alkaline electrolyzers are commercially mature and cost-effective but have limited dynamic response to variable renewable energy input. PEM electrolyzers provide high-purity hydrogen and fast response times but rely on scarce and expensive materials such as platinum and iridium[3,5]. SOECs operate at elevated temperatures (700–800 °C), allowing for higher electrical efficiency by integrating waste heat, although their commercialization is hindered by material degradation and high system costs[32]. While alkaline and PEM technologies are already deployed at scale, SOECs represent a promising next-generation pathway for reducing the energy intensity of low carbon emitting hydrogen production[6].

Advances in electrolyzer efficiency, cost reduction through economies of scale, and increased policy-driven investment are expected to enable the large-scale deployment of low carbon emitting hydrogen as a key component of a decarbonized global system[5,32].

1.4. Solid Oxide Electrolysis Cell (SOEC)

Solid Oxide Electrolysis Cells (SOECs) stand out as an advanced and promising technology for hydrogen production and energy conversion due to their ability to operate at high temperatures, typically 700-800 °C[6]. In SOECs, water vapor reacts at the cathode (fuel electrode) with electrons from external power sources. It renders the production of H_2 and oxygen ions, which are transported to the anode (oxygen electrode), via an ion-conducting, gas-tight membrane, where the oxygen ions recombine, and liberate the e^- again[5,6,33].

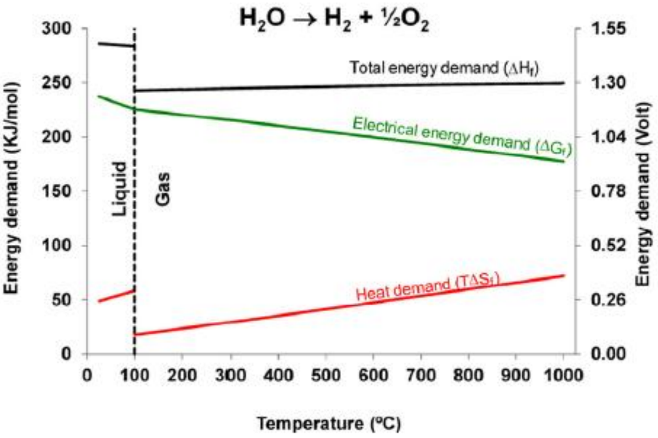

Figure I. 3 - Thermodynamic requirements for the water splitting reaction in function of the temperature[6].

The main advantage of SOECs compared to water electrolysis processes relies on the use of high temperature. This high temperature translates into significantly higher thermal energy provided to the system. This thermal energy input reduces the electrical energy requirements, which can be explained in terms of thermodynamics. The water splitting process is endothermic (ΔH_{1023K} = + 248.3 kJ/mol)[9,34]. The enthalpy reaction consists of:

$$\Delta H = \Delta G + T \times \Delta S$$

where ΔH is the enthalpy (total energy demand), ΔG the Gibbs free energy (electrical energy demand), T is the temperature and ΔS the entropy. While ΔG term represents the electrical energy requirements, the T×ΔS term comprehends the heat demand. Thus, higher temperatures translate in stronger contribution from the T×ΔS term. Figure I.3 highlights this dependency, with a reduction in electrical energy input of 18% between electrolysis at 80 and at 800 °C[6]. Even higher temperatures could lead to further energy demands reduction. However, material limitations, particularly corrosion and degradation at elevated temperatures, restrain practical operation to the 700-800 °C range, which offers a balance between efficiency and durability[5,6].

Two other factors are critical to enable the clean production of H_2: the electricity and heat sources. In general, SOECs are foreseen to work with low emitting energy sources (renewables and nuclear surplus) and using waste heat sources. The heat energy can be supplied externally (e.g., from nuclear, solar, or exothermic chemical sources) or internally via Joule heating from resistive losses within the stack[32,34]. SOECs are well-suited to integrate waste heat from industrial processes, aligning with energy efficiency and circular economy principles. Industries such as steel, cement, and power generation are ideal candidates for coupling with SOECs[34]. Moreover, SOECs can co-electrolyze steam and CO_2 to generate syngas, a valuable feedstock for synthetic fuels and chemicals[6]. This versatility makes SOECs a promising solution for decarbonizing hard-to-electrify sectors and expanding the role of electrolysis in sustainable energy systems.

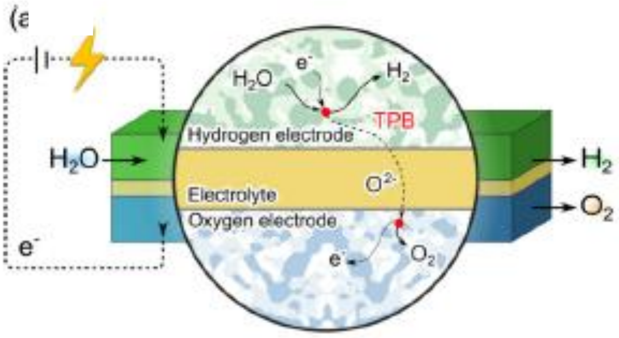

Figure I. 4 - Electrolysis cell illustrating the hydrogen and oxygen porous electrodes and the electrolyte. The triple phase boundary (TPB) points are indicated by the red dots. Reprinted from Liu et al.[5]

Figure I.4 describe an electrolysis unit cell, composed of a cathode, anode and electrolyte. During electrolysis the water vapor enters through the cathode side, where the molecules will be first adsorbed at the cathode's surface and reacting as follows:

$$H_2O_{(g)} + 2\,e^- \rightarrow H_{2\,(g)} + O^{2-}$$

The O^{2-} anion will be transported through the electrolyte until reaching the anode where:

$$O^{2-} \rightarrow \frac{1}{2} O_{2\,(g)} + 2\,e^{-}$$

With a general reaction:

$$H_2O_{(g)} \rightarrow H_{2\,(g)} + \frac{1}{2} O_{2\,(g)}$$

These reactions require the simultaneous presence of a gaseous phase (H_2O/H_2 and O_2), an electron conducting environment (electrodes), and an ion conducting environment (electrolyte). The point where these reactions happen is called the Triple Phase Boundary (TPB) which is highlighted by the red dots in Figure I.4[5]. The TPB is reached using porous electrodes enabling gaseous species to reach the electrolyte. Each unit cell is combined in series by means of an interconnect, which ensures proper gas separation (H_2O/H_2 and O_2 sides) and efficient electrical contact between cells[5,6]. Figure I.5 illustrates the SOEC components to produce a stack with multiple unit cells.

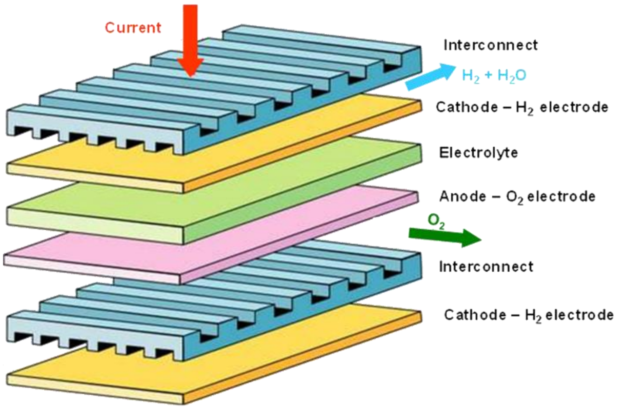

Figure I. 5 - The repeating unit, formed by the electrodes and electrolyte, is connected by interconnects[35].

1.5. Choice of materials

1.5.1. Electrolyte

The SOEC electrolyte must ensure the passage of O^{2-} anions without the passage of gases or other compounds. Therefore, the electrolyte must be dense, and the materials used must ensure high oxygen ion conductivity, minimal electronic conductivity, gas impermeability, and chemical and thermal stability under both oxidizing and reducing conditions[5,36]. In addition, the thermal expansion coefficient (TEC) must be compatible with other cell components to prevent mechanical stress during operation[11,36]. Yttria-stabilized zirconia

(YSZ), typically doped with 8–10 mol% Y_2O_3, is the reference electrolyte due to its excellent mechanical strength, chemical inertness, and reliable ionic conductivity at high temperatures (~ 800–1000 °C). Cerium gadolinium oxide (CGO), with ~ 20 mol% Gd_2O_3, offers significantly higher ionic conductivity at intermediate temperatures (< 800 °C), but suffers from increased electronic conductivity under reducing conditions. Currently, YSZ remains the standard due to its proven long-term stability and compatibility with SOEC operating environments[9,36].

1.5.2. Electrode Materials

In SOECs, electrode materials must be porous to allow gas diffusion, while also exhibiting both ionic and electronic conductivity to facilitate electrochemical reactions[37]. High catalytic activity is essential to enhance reaction rates and minimize polarization losses. Composite electrodes combining materials with complementary conductivities are commonly used, often with graded interfaces to reduce thermal stress from mismatched thermal expansion coefficients[11,36,37]. Stability in highly reducing (fuel electrode) or oxidizing (oxygen electrode) environments is critical, as is chemical compatibility with adjacent components. The porous structure also maximizes the triple-phase boundary, improving gas transport and electrochemical performance[5,36].

1.5.2.1. Cathode

Cathode materials must maintain chemical and structural stability at high operating temperatures and across a wide range of oxygen partial pressures, which fluctuate due to varying H_2O/H_2 concentrations during operation. To ensure long-term durability and high efficiency, cathode materials must support strong electrochemical activity, promote gas transport, and resist degradation under reducing conditions. Metal and metal-ceramic composites are commonly used to meet these demanding requirements. The state-of-the-art cathode is typically a porous cermet composed of nickel and electrolyte material (YSZ), offering good adhesion and thermal expansion compatibility. This composite structure also provides high electronic and ionic conductivity, along with sufficient porosity to facilitate gas diffusion and redox reactions[36–38].

1.5.2.2. Anode

The anode must exhibit high catalytic activity for the oxygen evolution reaction (OER) and maintain stability in oxidizing environments at elevated temperatures. Due to cost constraints, noble metals are avoided, and mixed metal oxides are preferred. The most widely used anode material is Lanthanum strontium manganate (LSM), valued for its stability and compatibility. However, LSM has limited oxygen ion conductivity, which restricts the triple-phase boundary (TPB) area. This limitation can be mitigated by incorporating YSZ to form a composite anode. Alternative materials such as $La_{1-x}Sr_xCo_{1-y}Fe_yO_3$ (LSCF) or $La_{1-x}Sr_xCoO_3$ (LSC) offer higher electronic conductivity and are promising candidates for intermediate-temperature SOECs due to their enhanced electrochemical performance.[5,36,37]

1.6. Interconnect

Interconnects functions are to electrically connect individual electrolysis cells within a stack while maintaining gas separation between the oxidizing (O_2 electrode) and reducing (H_2/H_2O) environments[5,35,36]. These components are among the most expensive in the stack, representing (along with cell/paste slurries), approximately 80% of the total cost[5]. Their fabrication involves several processing steps, such as etching and machining, making material selection critical for cost reduction and manufacturing efficiency.

Interconnect materials must satisfy the following requirements[11,39,40]:

1. High electronic conductivity to ensure efficient current transport between adjacent cells and to the external circuit.
2. Thermal expansion coefficient compatible with other SOEC components (typically $10–11 \times 10^{-6}\ K^{-1}$).
3. Chemical stability under both oxidizing (cathode) and reducing (anode) atmospheres, and across the oxygen partial pressure gradient.
4. Chemical compatibility with adjacent electrode materials.
5. High density and low gas permeability to prevent fuel and oxidant mixing.
6. Adequate thermal conductivity ($>5\ W \cdot m^{-1} \cdot K^{-1}$) to facilitate heat transfer from the cathode to the anode.
7. Cost-effectiveness in terms of raw materials and manufacturability, particularly for planar SOEC designs where interconnects are the largest components.

A wide range of materials has been explored for SOEC interconnects. Early candidates included ceramic materials such as lanthanum chromates, which presented semiconducting properties and chemical stability. However, their poor sinterability, high operating temperatures (~1000 °C), and elevated costs have limited their practical use, especially in large-scale applications.

Metallic interconnects, particularly Ferritic Stainless Steels (FSS), have become the preferred choice due to their high electrical conductivity, thermal compatibility, and cost-effectiveness. Chromium-based FSS produce a protective chromia (Cr_2O_3) layer during operation. These chromia-forming alloys offer a good compromise between oxidation resistance and electrical conductivity. In comparison, alloys forming SiO_2 or Al_2O_3 scales provide better oxidation resistance but suffer from significantly lower conductivity[11,36].

Among FSS, tailor-made alloys such as Crofer 22 APU, Crofer 22 H, Sanergy HT, and ZMG232 G10 are widely used. These steels typically contain ~ 22% Cr to form a protective chromia scale, minor Mn additions to promote $(Cr,Mn)_3O_4$ spinel formation, and reactive elements (i.e., La, Ce) to enhance scale adhesion and reduce oxidation rates[41–46]. Silicon content is minimized during steel preparation or chemically bound (i.e., via Laves phase formation) to prevent the formation of insulating SiO_2 subscales. Despite their improved performance, these alloys remain costly due to complex processing and low production volumes.

More economical alternatives, such as AISI 430, AISI 441 and AISI 444, are also considered. These steels contain higher levels of silicon, which can lead to the formation of detrimental SiO_2 layers. Elements like Nb and Mo are added to promote the formation of Laves phases that immobilize silicon[47,48]. Table I.1 summarizes the chemical compositions, in weight, of the most studied FSS grades.

Table I. 1 - Chemical composition of some of the current alloys used as interconnect materials.

Alloy*	Cr	Mn	Si	Nb	Ti	C	Other	Fe
AISI 430[48]	16.2	0.49	0.34	-		<0.2	-	Bal.
AISI 441[48]	17.6	0.35	0.6	0.39	0.17	<0.03	-	Bal.
AISI 444[48]	19.0	0.35	0.4	0.6	<0.01	<0.03	1.9 Mo	Bal.
Crofer 22 APU[48]	22.92	0.38	0.01	-	0.06	<0.01	0.07 La	Bal.
Crofer 22 H[11]	20-24	0.8	0.1-0.6	0.2-1	<0.2	<0.03	0.04-0.2 RE, 1-3 W	Bal.

* The steel composition may slightly vary depending on manufacturer

1.7. Degradation Mechanisms in SOEC technology: Current understanding

SOEC operate under harsh conditions, including elevated temperatures, H_2-containing atmospheres, and oxidizing environments, which pose significant challenges for material selection. Damage to electrode materials or their interfaces inevitably results in performance degradation[5]. Such degradation is typically manifested by increased overvoltage, leading to a gradual rise in the SOEC's operating voltage over time. In severe cases, this can ultimately result in system failure. Currently, a voltage increase rate ranging from 0.6% to 1.5% per 1,000 hours of operation is commonly observed[49].

Table I.2 summarizes the main degradation issues currently encountered on SOECs and that can limit the SOEC performance[5]. In the current study, we will focus on the degradation phenomena happening on the metallic interconnects. Despite their many advantages, Ferritic Stainless Steels (FSS) are prone to oxidation under SOEC operating conditions, high temperatures and oxidizing environments (in air or H_2/H_2O gas mixtures). This oxidation leads to the formation of protective but poorly conducting oxide scales (chromia and Cr-Mn spinels, i.e., $MnCr_2O_4$). Over time, these scales grow, increasing overall resistance, which translates into poor electrical performance and reduced durability of the SOECs[5,11,39].

Table I. 2 – Summary of the degradation issues observed in SOEC technologies and the main mitigation strategies. [Reprinted from Liu et al.[5]].

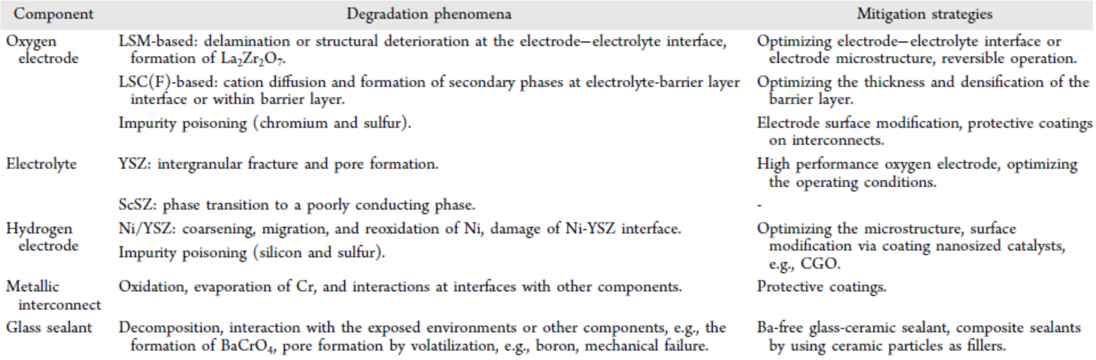

Component	Degradation phenomena	Mitigation strategies
Oxygen electrode	LSM-based: delamination or structural deterioration at the electrode–electrolyte interface, formation of $La_2Zr_2O_7$.	Optimizing electrode–electrolyte interface or electrode microstructure, reversible operation.
	LSC(F)-based: cation diffusion and formation of secondary phases at electrolyte-barrier layer interface or within barrier layer.	Optimizing the thickness and densification of the barrier layer.
	Impurity poisoning (chromium and sulfur).	Electrode surface modification, protective coatings on interconnects.
Electrolyte	YSZ: intergranular fracture and pore formation.	High performance oxygen electrode, optimizing the operating conditions.
	ScSZ: phase transition to a poorly conducting phase.	-
Hydrogen electrode	Ni/YSZ: coarsening, migration, and reoxidation of Ni, damage of Ni-YSZ interface. Impurity poisoning (silicon and sulfur).	Optimizing the microstructure, surface modification via coating nanosized catalysts, e.g., CGO.
Metallic interconnect	Oxidation, evaporation of Cr, and interactions at interfaces with other components.	Protective coatings.
Glass sealant	Decomposition, interaction with the exposed environments or other components, e.g., the formation of $BaCrO_4$, pore formation by volatilization, e.g., boron, mechanical failure.	Ba-free glass-ceramic sealant, composite sealants by using ceramic particles as fillers.

1.7.1. Thermodynamics of oxidation

To better understand the oxidation behaviour of these materials, it is essential to examine thermodynamic and kinetic principles govern oxide formation[50]. Thermodynamically, the oxidation of a metal (M) in the presence of oxygen can be described by the general reaction:

$$aM_{(s)} + \frac{b}{2} O_{2\,(g)} \rightarrow M_aO_{b\,(s)}$$

The feasibility of this reaction is determined by the Gibbs free energy change ($\Delta G = \Delta H - T\Delta S$), where a negative value indicates a thermodynamically favourable process[50]. ΔH is the enthalpy change, T is the temperature in Kelvin and ΔS is the entropy change of the reaction. The Gibbs free energy can also be written as:

$$\Delta G = \Delta G^{\circ} + RTln\left(\frac{a_{M_aO_b}}{a_M^a \times a_{O_2}^{b/2}}\right)$$

Where ΔG° is the standard Gibbs free energy, R is the universal gas constant, and a stand for the activity of the components. Generally, the a is set to 1 for pure solids. Here, we considered M as a pure metal (for alloys, the activity is determined by its concentration)[50]. Finally, for gas-solid reactions, the Gibbs free energy can be expressed as a function of the oxygen partial pressure (p_{O_2}) in bar and with p^0 being the reference standard pressure at 25 °C equal to 1 bar:

$$\Delta G = \Delta G^{\circ} + \frac{b}{2}RTln\,(\frac{p_{O_2}}{p^0})$$

At equilibrium ($\Delta G = 0$), the oxygen partial pressure per mol of O_2 required to maintain the metal-oxide balance can be calculated using the following expression:

$$p_{O_2\,(\Delta G=0)} = exp\left(\frac{\Delta G^{\circ}}{RT}\right)$$

The p_{O_2} value, known as the dissociation pressure, defines the threshold below which the oxide becomes unstable and may begin to decompose.

Figure I.6 shows the Ellingham-Richardson diagram for various metal oxides. It graphically represents the standard Gibbs free energy of oxide formation (ΔG°) as a function of temperature. Assuming constant enthalpy and entropy over a temperature range, the ΔG° vs. T relationship appears as a straight line. From the diagram, one can obtain the dissociation pressure, which is highlighted for Cr_2O_3 at 800 °C in Figure I.6[50,51]. It is about 10^{-28} bar. In this diagram, the oxides which are located in the lower part are the most stables oxides. For example, SiO_2 and Cr_2O_3 are more thermodynamically stable than Fe_2O_3 As temperature increases, the thermodynamic stability of all oxides decreases, meaning that higher oxygen partial pressures are required to sustain oxidation. The Ellingham-Richardson diagram represents a good base for indicating which oxide is more stable and will be formed. However, thermodynamics is not the sole factor dominating oxidation.

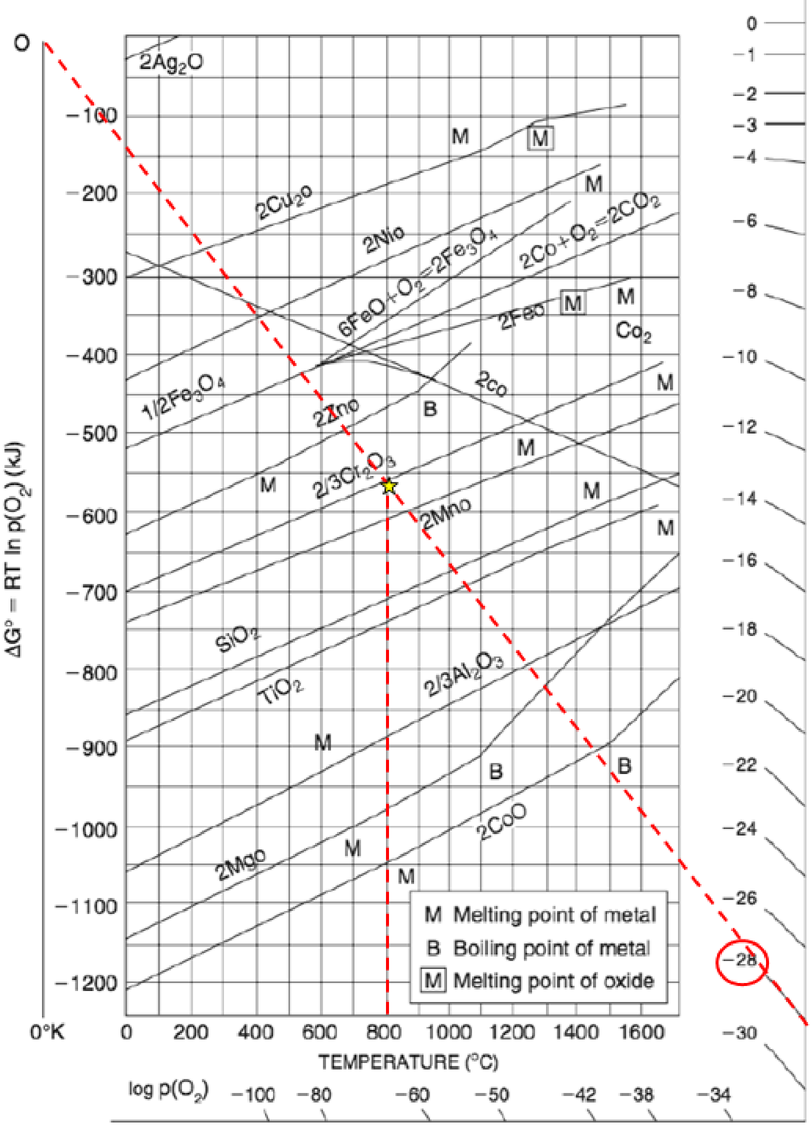

Figure I. 6 – Ellingham-Richardson diagram showing the Gibbs free energy for oxide formation in function of the temperature. Cr_2O_3 dissociation pressure at 800 °C is obtained from the red dotted line.[11].

1.7.2. Kinetics of oxidation

While thermodynamics determines whether oxidation is feasible, the oxidation rate is governed by kinetics. The oxidation kinetics of the material will determine how fast the oxidation will occur.

First, the oxidation relies on the oxygen adsorption, oxide nucleation and growth, which occurs fast[50]. These initial stages finish with the formation of a continuous scale. Over time, the oxidation rate varies with the nature of the oxide scale: whether it is dense and protective, or porous and non-protective[51,52]. The nature of the oxide will determine the limiting factors for the reactions.

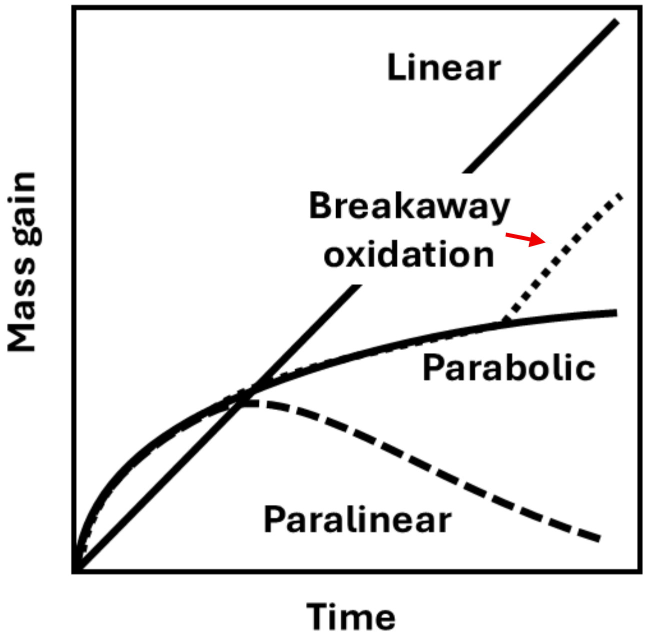

Figure I. 7 - Oxidation behaviour based on the oxidation kinetics [Adapted from Reddy[39]].

Figure I.7 illustrates some of the behaviour types of experienced during oxidation. In porous scales, for instance, O_2 diffuses freely along the scale, accelerating the oxidation process. Thus, the process is governed by surface chemical reactions, and the reaction rate is linear. The oxidation rate is defined by

$$\frac{\Delta m}{A} = k_l \times t + C$$

where $\frac{\Delta m}{A}$ represents the mass gain per unit of area, k_l is the linear rate constant, t is the time and C the constant of integration. On the other hand, if the oxide is dense and protective, the process will be governed by the diffusion of the species along the scale. These species are either the cations, i.e., Cr or the oxygen anion. In this case, a parabolic behaviour is followed, defined by a fast initial diffusion, but reduced with increasing thickness[50,53]. The parabolic behaviour is typically measured by the thickness variation, or the mass gain of the samples and is defined by

$$\frac{\Delta m^2}{A} = k_p \times t + C$$

Where k_p is the parabolic rate constant. Wagner developed a theoretical framework in 1933 to explain the parabolic oxidation behaviour observed in many metals at high temperatures[54,55]. His model assumes that the oxide scale formed during oxidation is dense and well-adherent, and that the rate-limiting step is the lattice diffusion of ions and electrons through this scale (Figure I.8). The oxidation process is driven by a chemical potential gradient, which arises from the difference in oxygen partial pressure across the oxide layer. Wagner also assumed that at the metal/oxide and oxide/gas interfaces local thermodynamic equilibrium is reached and that reactions at these interfaces occur rapidly. Additionally, the solubility of oxygen in the metal is considered negligible. Since diffusion is highly sensitive to the defect chemistry of the oxide, doping can significantly influence the oxidation rate. As the oxide layer thickens, the diffusion path length increases, leading to a decrease in the oxidation rate over time, characteristic of parabolic kinetics[51,52,54,55].

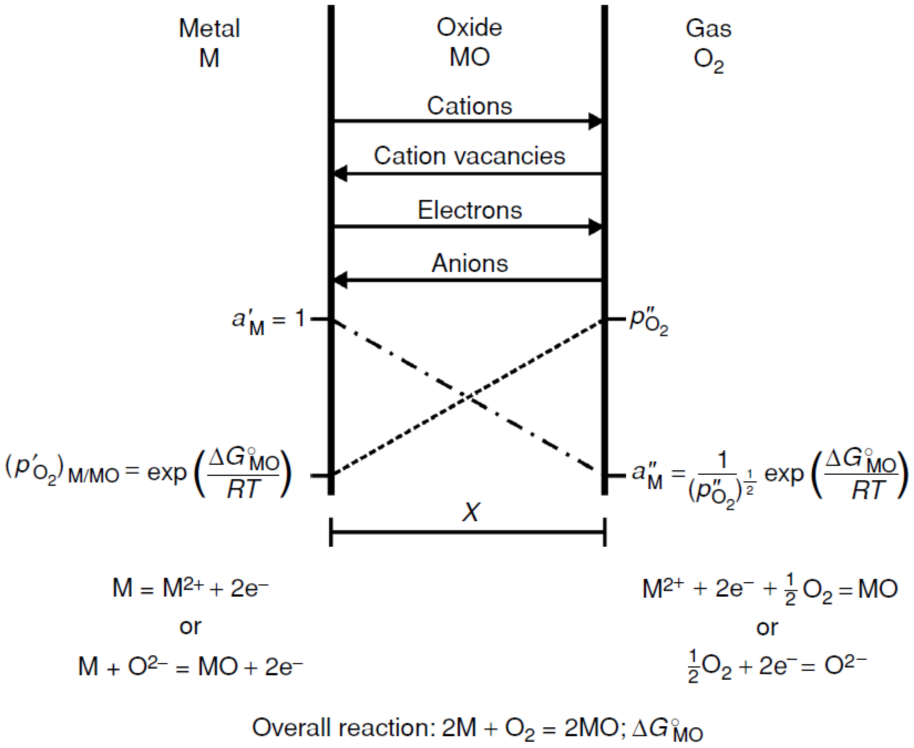

Figure I. 8 – Schematic of the scale formation following the Wagner's model[51].

1.7.3. Interconnect oxidation

Chromia forming alloys tend to produce dense and protective scales, following parabolic behaviour. The corrosion resistance of Ferritic Stainless Steels (FSS) is primarily attributed to the selective oxidation of chromium, which forms a dense and adherent Cr_2O_3 scale on the surface. FSS will form a continuous and protective chromia layer if a minimum chromium content between 16–20 wt% is present[12,56]. This threshold may vary depending on the alloying elements used, the exposure conditions, and if surface treatments were performed[11].

There has been considerable debate regarding the rate-controlling mechanism of Cr_2O_3 growth. While some studies suggest that outward diffusion of chromium through the oxide scale dominates[57], others propose a significant contribution from inward transport of oxide ions[58,59]. Despite these differing views, it is now widely accepted that lattice diffusion of both Cr and O is extremely slow[60], and that fast diffusion pathways, such as grain boundaries, pores, and microcracks, play a dominant role in scale growth[53,59]. In FSSs used under SOEC/SOFC working conditions, the chromia scale is believed to predominantly grow by outward Cr diffusion [48,61].

As previously indicated (Table I.1), multiple materials can be used for the interconnects. The parabolic rate constant (k_p) can be used as method of comparison between such materials to evaluate their oxidation performance. Some studies have considered the k_p values to estimate the evolution of the oxide scale thickness and the lifetime of the materials. These materials exhibit k_p in the range of 10^{-14} to 10^{-13} $g^2 \cdot cm^{-4} \cdot s$ at 800 °C in air[62–65]. Reddy et al. evaluated some of these compositions regarding their oxidation performance[47,48]. Crofer 22 APU showed better performance likely due to presence of reactive elements (RE). The more economical alternatives, AISI 430, 441 and 444, showed slightly higher oxidation rates. Elevated oxidation rates are particularly detrimental during long-term exposure, as they can lead to: (i) chromium depletion within the alloy, and (ii) excessive growth of Cr-rich poorly conducting phases, both of which compromise material performance. Quaddakers et al. demonstrated that the oxidation lifetime of chromia-forming steels is strongly influenced by both the chromium content and the thickness of the metallic substrate[66]. Prolonged oxidation gradually depletes chromium from the alloy matrix, leading to the loss of scale protectiveness (oxidation of iron oxide occurs too fast), which may be further accelerated by spallation of the oxide layer. This susceptibility to spallation increases as the thickness of interconnect components is reduced, a trend driven by cost-reduction efforts that have brought typical interconnect thicknesses down to approximately 200 μm[67,68]. As reported by Huczkowski et al.[67], thinner components are more prone to rapid depletion of minor alloying elements and to mechanical failure of the oxide scale, especially under thermal cycling. If spallation occurs, the protective chromia layer is compromised, promoting the formation of a fast-growing and non-protective iron oxide scale that severely degrades material integrity and performance. This fast growth is highlighted in Figure I.7 by the breakaway oxidation mechanism.

1.7.4. Cr-evaporation

Another critical issue affecting ferritic stainless steels (FSS) during SOFC and SOEC operation is the evaporation of chromium species[69,70]. While oxides such as Cr_2O_3 initially form dense and protective scales, they can react with the surrounding environment to produce Cr volatile compounds[71]. The chromia (Cr_2O_3) protective scale formed on ferritic stainless steels becomes thermodynamically unstable at high temperatures in environments containing oxygen, and particularly water vapor[72]. In dry oxidizing atmospheres, Cr_2O_3 can react to form volatile chromium trioxide (CrO_3), as described by the reaction:

$$Cr_2O_{3\,(s)} + \frac{3}{2}\,O_{2\,(g)} \rightarrow\ 2\,CrO_{3\,(g)}$$

In humid environments, chromium volatilization occurs at significantly lower temperatures through the formation of hydroxylated chromium species, such as $CrO_2(OH)_2$ and $CrO_2(OH)$, via the following reactions:

$$Cr_2O_{3\,(s)} + \frac{3}{2}\,O_{2\,(g)} + 2\,H_2O_{\,(g)} \rightarrow 2\,CrO_2\,(OH)_{2\,(g)}$$

$$Cr_2O_{3\,(s)}\ +\ O_{2\,(g)}\ + H_2O_{\,(g)} \rightarrow 2\,CrO_2\,(OH)_{\,(g)}$$

Both theoretical and experimental studies have shown that $CrO_2(OH)_2$ is the dominant volatile species below 900 °C[72–74]. Figure I.9 shows the partial pressure of two volatile Cr-species, CrO_3 and $CrO_2(OH)_2$, in function of the temperature. The graph highlights that the production of Cr-species should be much higher in humid environments since the partial pressure of hydroxides is 2-3 orders of magnitude greater than CrO_3 between 700 and 800 °C.

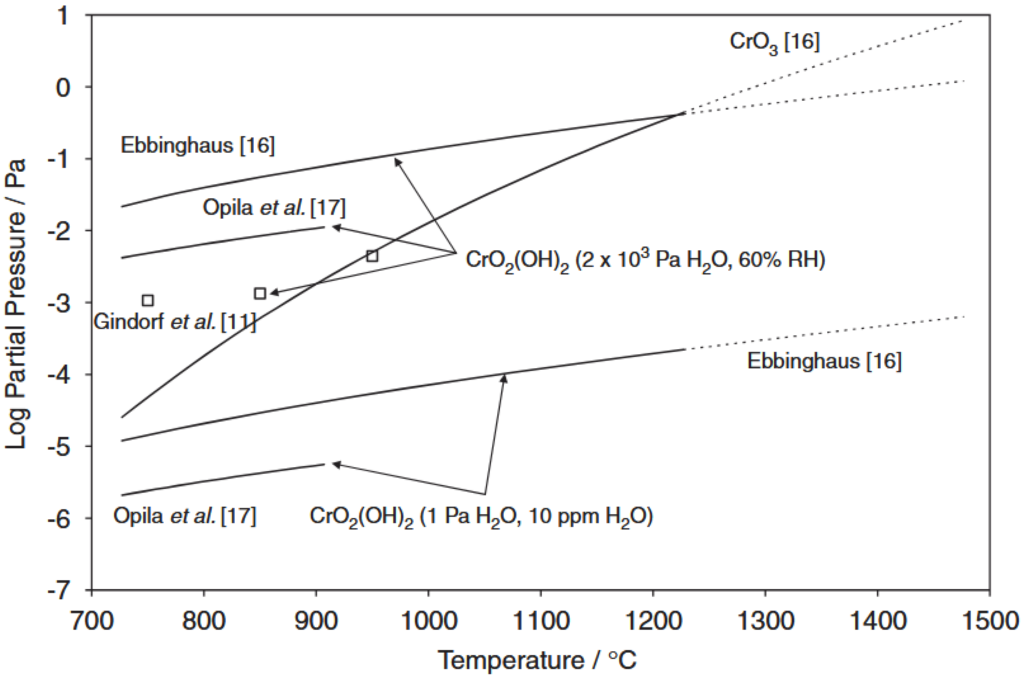

Figure I. 9 - Vapor pressure of two Cr-oxide species ($CrO_2(OH)_2$ and Cr_2O_3) as a function of temperature. [from Fergus[73]].

The rate of chromium evaporation from ferritic stainless steels (FSS) is influenced by several factors, including temperature, water vapor content[74], and gas flow rate[75]. Studies have shown that the presence of manganese in the steel composition can mitigate chromium volatilization[76–78]. Higher Mn content promotes the formation of a thicker, Mn-rich $(Cr,Mn)_3O_4$ spinel layer atop the chromia scale, which acts as a diffusion barrier. Holcomb and Alman attributed this effect to a decrease in chromium activity within the spinel layer[77]. Despite this reduction, chromium-containing volatile species are still formed. At 800 °C, typical chromium evaporation rates[48,76,78] for FSS range between 100 and 2000 × 10^{-10} $mg \cdot cm^{-2} \cdot s^{-1}$.

Oxidation kinetics are often evaluated using mass gain measurements, which can effectively track oxide scale growth. However, in the presence of chromium evaporation, these measurements tend to underestimate actual material degradation. Chromium volatilization contributes negatively to mass gain, masking the true extent of alloy consumption. Additionally, the loss of chromium through evaporation can lead to thinner oxide scales, which in turn accelerates oxidation rates and promotes further chromium depletion.

When chromium volatilization becomes significant, oxidation kinetics deviate from ideal parabolic behaviour and may transition to a paralinear regime (Figure I.7) with a net consumption of the growing scale. Therefore, to accurately evaluate the oxidation behaviour and calculate the parabolic rate constant (k_p), chromium evaporation must be considered[11].

Besides the issues observed in the steel composition and oxidation protection, these Cr-volatile species migrate and poison other parts of the cell. This poisoning was profoundly studied in SOFC conditions[79–82], where the chromium gaseous species react with other elements to form mixed spinel phases, such as $(Cr,Mn)_3O_4$. It is proposed that these compounds accumulate near the cathode/electrolyte interface, blocking electrochemically active sites and significantly reducing both electronic and ionic conductivity.

In SOECs, the effect of Cr-volatilisation on the electrical performance of interconnect combined with the contact layer (here LSM) appears to be less pronounced. Bouvier et al.[83] explained this behaviour by the opposite current direction for SOEC and SOFC modes. Cr-volatile species are in the oxidation state Cr^{VI}, which must be reduced to form a solid Cr-rich oxide. For the $Cr^{VI} \Rightarrow Cr^{3+}$ reaction to happen, electrons are required, which are limited in SOEC conditions. Although the effect is generally less severe in Solid Oxide Electrolysis Cells (SOECs), it still poses a concern. Chen et al. reported the formation of CrO_x and $SrCrO_4$ near the LSM (O_2 electrode)/electrolyte interface in SOECs[84]. Due to the anodic polarization, the Sr ions segregate preferentially, forming active sites for the incorporation of the volatile Cr-species. Figure I.10 schematically illustrates the migration (a) and deposition (b) pathways of volatile chromium species at the electrode/electrolyte interface. The excessive formation of volatile Cr compounds not only accelerates interconnect degradation but also poisons the electrocatalytic activity of the oxygen electrode, thereby impairing the oxygen evolution reaction (OER). Moreover, these reactions may contribute to electrode delamination, undermining the mechanical integrity of the cell[84].

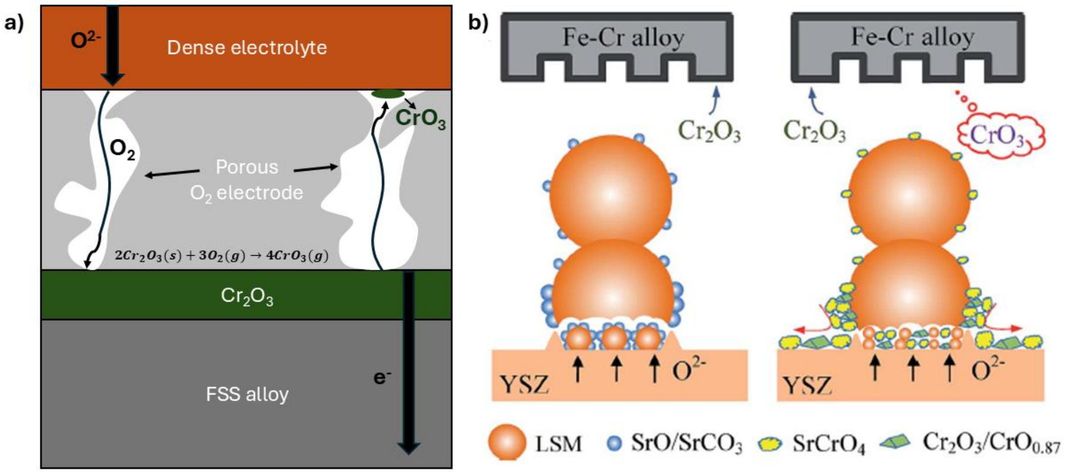

Figure I. 10 - a) Scheme illustrating the interconnect/O_2 electrode/electrolyte cross section. The scheme highlights the passage of O_2 gas through the porous electrode to react with Cr_2O_3, which forms gaseous species (CrO_3). Adapted from Dejob[16]. b) Scheme highlights the Cr-poisoning effect produced by the Cr-volatile species on SOEC mode[84].

1.8. Protective Coatings

Despite considerable advances in optimizing steel compositions for interconnect applications, uncoated Ferritic Stainless Steels (FSS) remain very likely unsuitable for long-term use due to their very high oxidation rates and chromium volatilization. For SOCs to be commercially viable, operational lifetimes of up to 40,000 hours (ca. 4,5 years) are typically required[11], with an area-specific resistance (ASR) below 50mΩ·cm^2, generally considered acceptable for interconnects[12].

As an alternative to bulk alloy modifications, protective surface coatings have emerged as a promising strategy to reach such requirements. These coatings form conductive and protective layers on the surface of metallic interconnects, significantly reducing both chromium evaporation and the growth rate of chromia scales[12,13,56].

The requirements for interconnect coatings closely resembles those of the base alloy. Coatings must possess a thermal expansion coefficient (TEC) compatible with neighbouring cell components, maintain high electrical and thermal conductivity, exhibit chemical and thermal stability, adhere strongly to the substrate, and be both cost-effective and scalable for industrial production. Critically, they must also suppress chromium volatilization and limit oxide scale growth to preserve long-term performance[12,39]. Interconnect coatings are generally categorized into two main types: spinel-type and perovskite-type coatings.

1.8.1. Perovskites

Perovskite oxides, with the general formula ABO_3, have been investigated as protective coatings for metallic interconnects in Solid Oxide Fuel Cells (SOFCs)[85–87]. In this structure, A-sites are typically occupied by low-valence cations such as La, Sr, or Ca, while B-sites have higher-valence transition metals like Mn, Co, Fe, or Cr. Lanthanum-based perovskites, such as $La_{1-x}Sr_xMnO_3$ (LSM), $La_{1-x}Sr_xCoO_3$ (LSC), and $La_{1-x}Sr_xFeO_3$ (LSF), are particularly attractive due to their high electronic conductivity, thermal expansion coefficients compatible with other SOFC components, and chemical stability under oxidizing conditions[87,88].

Nonetheless, their effectiveness strongly relies on coating density, which is an issue to achieve at sufficiently low processing temperatures. Thus, their practical application remains a challenge by processing constraints and variability in performance. Moreover, perovskites are generally less effective as barriers for oxygen diffusion and chromium evaporation compared to spinel coatings[85,87,88].

1.8.2. Spinels

Spinel oxides have attracted significant attention as protective coatings for interconnects. Research has primarily focused on $Co_{3-x}Mn_xO_4$ compositions (with x = 1 or 1.5), along with various doped versions incorporating elements such as Fe, Ti, and Cu[14,87]. Although Cu-Mn and Cu-Fe spinels have been investigated[11,89], they generally exhibit poor oxidation resistance. Recently, metallic cobalt has attracted attention due to its excellent performance with the spinel formation during operating conditions[90–92]. Furthermore, spinel coatings can typically be fabricated with higher density than perovskite-based alternatives, improving their protective capabilities[88].

The spinel structure widespread occurrence is largely due to its structural flexibility, which allows it to accommodate cations of various sizes and valencies[93,94]. This structural versatility gives rise to a broad range of functional properties in spinel oxides, including magnetism, superconductivity, and optical transparency combined with electrical conductivity[94,95].

1.8.3. Structure

Figure I.11 illustrates the spinel crystal structure, which is based on a cubic close-packed arrangement of oxygen anions. The general formula for a normal spinel is $A^{2+}B^{3+}_2O_4$, where

A cations occupy tetrahedral sites and B cations occupy octahedral sites. However, some spinels exhibit a degree of inversion, where a portion of B cations occupy tetrahedral sites and A cations shift to octahedral sites[94,96].

In the cubic spinel unit cell, there are 32 oxygen anions, 64 tetrahedral sites (with only 8 occupied), and 32 octahedral sites (half of which are occupied). Each unit cell contains 8 formula units of AB_2O_4. Most spinels crystallize in the Fd3m space group, although symmetry can be reduced due to Jahn-Teller distortions, in particular for compounds containing transition metals like Mn^{3+}. These distortions arise from uneven occupancy of degenerate orbitals, leading to geometric changes in the lattice[97].

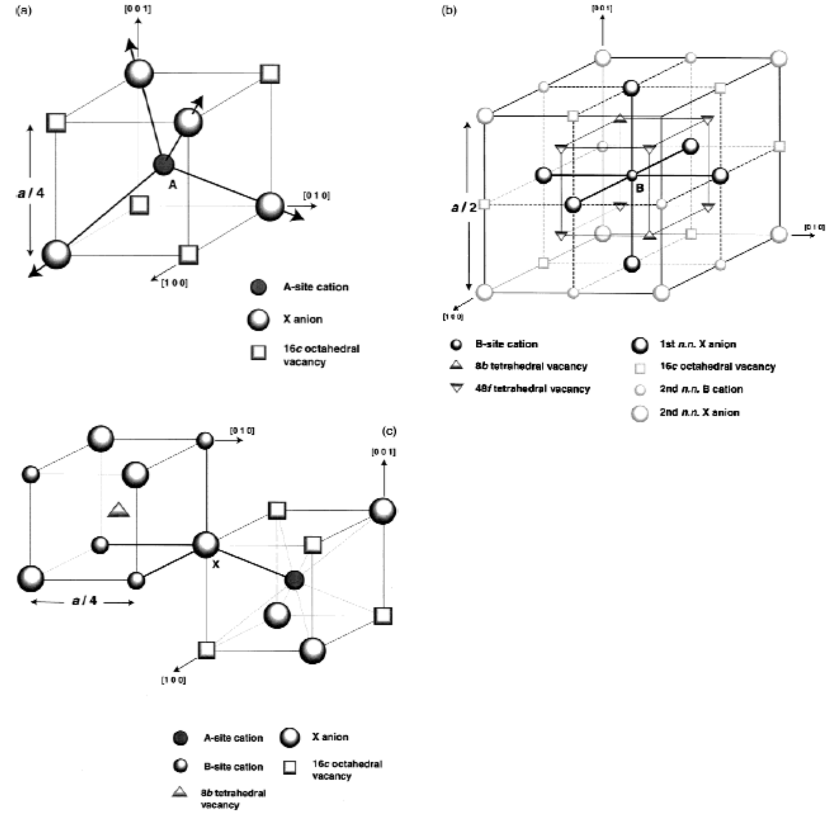

Figure I. 11 - AB_2O_4 spinel structure where the lattice surroundings and nearest neighbours are represented as (a) the tetrahedral A-site, (b) the octahedral B-site, and (c) the tetrahedral anion X-site[94].

In the $Co_{3-x}Mn_xO_4$ system, Jahn-Teller distortions become prominent for $x > 1.3$ at room temperature, resulting in the coexistence of cubic and tetragonal phases[98–100]. This phase transition is driven by the increasing concentration of Mn^{3+} ions in octahedral sites, which induces lattice distortion.

The oxygen positional parameter (*u*) is commonly used to evaluate the packing density of the spinel structure. This parameter is also used to determine the position of oxygen anions relative to the cation's sizes in tetrahedral and octahedral sites and can be calculated accordingly[94]:

$$u = \frac{\frac{R^2}{4} - \frac{2}{3} + \left(11\,\frac{R^2}{48} - \frac{1}{18}\right)^{1/2}}{2\,R^2 - 2}$$

where *u* is the anion or oxygen parameter and *R* is the ratio of the octahedral to tetrahedral cation-anion bond lengths. For an ideal cubic packing, *u* equals 0.25 and the octahedral/tetrahedral bond ratio is 1.155. Spinels, in general, deviate from these values, showing higher *u* values and lower oct/tet ratio. The lower ratio involves an expansion of the tetrahedron and a compression of the octahedron, which can be approximated by[93,94]:

$$R = \frac{r_{oct} + r_O}{r_{tet} + r_O}$$

The deviation from the ideal cubic packing leads to several crystallographic implications, such as variation in bond lengths (Figure I.12a,b,c), bond angles, polyhedron volumes (Figure I.12d) and symmetries of coordination[93,94,101]. The distances between cations and neighbouring vacancies play a crucial role in determining self-diffusion mechanisms in spinel structures[94].

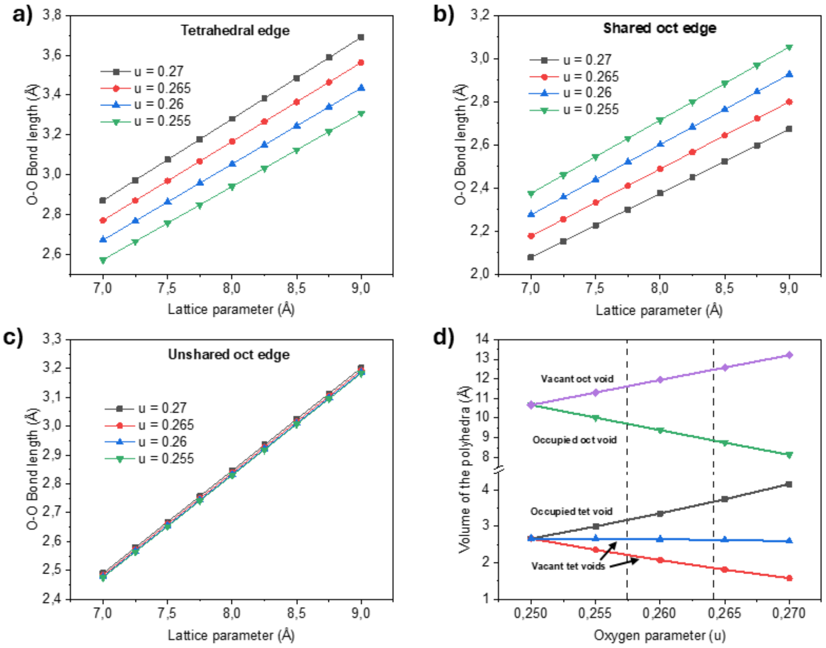

Figure I. 12 - Bond length distance between the O-O bonds in the tetrahedral edge (a) and shared (b) and unshared (c) octahedral edge in function of oxygen parameter (u) and the *lattice parameter (a). The polyhedron volume is also plotted in function of u (d). Adapted from Sickafus*[94].

For instance, B-site cations diffusion involves a jump to a nearby vacant octahedral site, either directly or indirectly via a first nearest-neighbour vacant tetrahedral site. In an ideal cubic close-packed anion framework, the indirect path via the tetrahedral site is generally favoured, as the direct jump requires displacing neighbouring anions. However, when the anion positional parameter u exceeds 0.26, both diffusion pathways may become competitive[94]. Similarly, A-site cations diffuse to a neighbouring empty tetrahedral site either directly or indirectly. Like in the B site, the direct path is preferred solely for large u values.

1.8.4. Cation distribution

Cation distribution in spinel structures plays a critical role in determining their electrical and thermal behaviour[11,102]. Spinels conduct electrons via the Verwey-de-Boer mechanism[95,103]. It comprises electron hopping primarily between octahedral sites, which requires the presence of multivalent cation pairs such as Mn^{3+}/Mn^{4+} or Co^{2+}/Co^{3+}[99,102,104,105]. Similarly, the thermal expansion coefficient (TEC) is influenced by the cation distribution, due to the amount of multivalency in the octahedral sites[102].

Numerous studies have evaluated the cations distribution in spinels by means of the Octahedral Site Preference Energy (OSPE)[96,101,106,107]. Figure I.13a shows the OSPE values for various cations from the transition metals. More negative OSPE values indicate a stronger preference for octahedral sites, as seen with Cr^{3+} and Mn^{3+}. Conversely, positive values indicate tetrahedral preference. Generally, these preferences were confirmed by experimental data from X-ray and neutron diffraction analysis[99,100,108]. For instance, in Co–Mn spinels, Co^{2+} typically occupies tetrahedral sites, while Mn^{3+} and Co^{3+} are found in octahedral coordination [99,109]. Mn^{4+} may also be present, and in some cases, Co^{2+} can partially occupy octahedral sites. Mn^{2+} ions have high tetrahedral preference. Still, they do not primarily occupy the tetrahedral sites due to their strong valence variability[110], and other ions, i.e., Mn^{3+} and Mn^{4+} having strong octahedral preference.

Moreover, cation distribution in spinels varies significantly with temperature and pressure. Chen et al. showed that Co_3O_4 is a normal spinel at room temperature but exhibits increased inversion at elevated temperatures, with Co^{2+} increasingly occupying octahedral sites and Co^{3+} shifting to tetrahedral positions to maintain charge neutrality[111]. This behaviour highlights that OSPE assessments become less significant at high temperatures.

Pelton et al. made a similar assessment for Co-Mn spinels using Gibbs free energy minimisation calculations[107]. Brylewski et al. demonstrated this dynamic nature by comparing Co–Mn spinels at room temperature and 800 °C using X-ray diffraction technique[112]. Spinels with high Mn content exhibit tetragonal structure close to room temperature, but full cubic structure at high temperature, as indicated by the red line in Figure I.13b. In the same work, a strong increase in the lattice parameter was observed at high temperature when the Co content was high. Similarly, Kale et al. observed an abnormal expansion on pure Co_3O_4 spinels[113]. They suggested that the expansion was related to spin variation of $Co^{III} \rightarrow Co^{3+}$, followed by increased presence of Co^{2+} in octahedral sites. Both mechanisms translate into an increase in the ionic radii of the cations, justifying the increase.

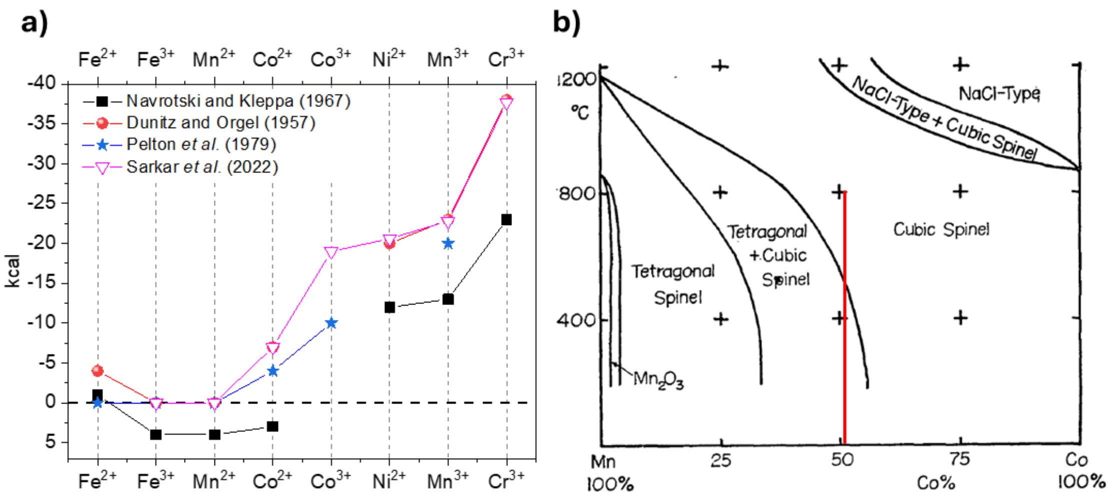

Figure I. 13 - a) Octahedral site preference energy (OSPE) for various cations from transition metals[96,107,114,115]. b) Co-Mn-O phase diagram[116].

Although end-member spinels like Mn_3O_4 have poor conductivity, intermediate Co-Mn compositions can exhibit high conductivities (> 100 $S \cdot cm^{-1}$) at SOCs operating temperatures due to enhanced hopping conduction. These intermediate compositions showed a significant amount of cation pairs. $(Co,Mn)_3O_4$ spinels exhibit significantly higher electrical conductivity than Cr-rich spinels, due to Co and Mn multivalences. On the other hand, Cr is mainly stable as Cr^{3+} and occupies the octahedral site due its high OSPE values, limiting the formation of cation pairs, and the electronic transport[11,117,118]. Regarding the TEC values, the Co-Mn spinels show a good match with the interconnect materials for $1<x<1.5$ in $Co_{3-x}Mn_xO_4$ ($11\text{-}13 \times 10^{-6}$ K^{-1}). The TEC values were shown to decrease with increasing Mn content, likely due to a decrease in multivalence cations in the octahedral sites. Further Mn addition led to low TEC values (7.4 × 10^{-6} K^{-1} for x=2)[102]. Similarly, the increased incorporation of Cr resulted in very low TEC values (6.9 × 10^{-6} K^{-1} for $Mn_{0.5}Co_{0.5}Cr_2O_4$)[118].

1.9. Performance - Oxidation

The Co-Mn spinel oxides have been extensively used as protective coatings for SOEC and especially SOFC interconnects. In this work, several types of coatings will be presented, all from the Co-Mn spectrum. The difference comes from the initial coating composition and its stoichiometries. Co-Mn spinels, called here MCO, can be directly deposited onto the substrate with the desired stoichiometry varying generally between Co_2MnO_4 to $Co_{1.5}Mn_{1.5}O_4$ or formed during the operating conditions by the diffusion of Mn from the substrate into the Co-oxide[90,119,120]. The latter is generally deposited as metallic Co and variations with the addition of reactive element (RE) are common. Other coating types involve the doping of the Co-Mn spinels with elements such as Fe, Ti, Cu[15,121–123].

1.9.1. Oxidation rate

Different coatings of the Co-Mn spectrum were identified to contribute to the reduction of the oxidation rate. For instance, Yang et al. evaluated AISI 441 substrate coated with $Mn_{1.5}Co_{1.5}O_4$ at 800 °C for 1200 h[124]. The coating thickness was not reported but, by SEM micrographs it appears to be several micrometres. The coating decreased the parabolic rate constant (k_p) from 5 to 2 × 10^{-14} $g^2 \cdot cm^{-4} \cdot s^{-1}$. Experiments from our group using AISI 441 substrates and metallic Co (~600 nm) deposited by PVD, exhibited a more modest decrease in the oxidation rate from 7.6 to 5.8 × 10^{-14} $g^2 \cdot cm^{-4} \cdot s^{-1}$ at 800 °C. Figure I.14 summarizes the k_p of several coated (black) and uncoated (red) alloys obtained from the literature. Three alloys were considered here: AISI 441, Crofer 22 APU and AISI 430 while all the coatings refer to the Co-Mn spectrum. The graph highlights the effect of the coatings on the oxidation kinetics of the alloys. Reddy et al.[15] evaluated multiple coatings from the Co-Mn spectrum with or without doping additions (Fe, Cu and/or RE) and a $CuMn_{1.8}O_4$ coating on Crofer 22 APU substrates. They were evaluated regarding their performance as protective coatings (mass gain and Cr evaporation rate) after annealing experiment for 1000 h at 800 °C. In all cases, the coatings reduced the mass gain and the Cr evaporation rate (100 times) in comparison to the uncoated samples. Curiously, only the sample outside the Co-Mn spinel spectrum ($CuMn_{1.8}O_4$), presented a higher mass gain, and considerably higher Cr-evaporation (at least 20 times higher) than the other coatings.

Zhu et al. indicated that to provide good Cr-barrier properties a dense MCO coating is required[14]. A dense coating is considered a coating with low open porosity and no through-layer cracks. The increased density affects the diffusion of the species coming from the steel outwards and from the air inwards to the steel. Kurokawa et al. evaluated two deposition processes (aerosol spraying and dip coating) for the production of $MnCo_2O_4$ coatings on AISI 430[125]. The two coating techniques rendered different coating densities. While the porous coating (dip coating) showed a reduction factor of 3 in Cr-evaporation rate, the dense coating (aerosol spraying) reduced up to 40 times compared to the uncoated sample. Similarly, Talic et al. evaluated $MnCo_{1.7}Fe_{0.3}O_4$ coatings on Crofer 22 APU sintered in different conditions (oxidation at 900 °C, or reduction at 900 or 1100 °C and oxidation at 800 °C). The reduction step at 1100 °C promoted the formation of denser coatings, which translated into better oxidation performance (lower k_p) and reduced Cr-volatilisation.

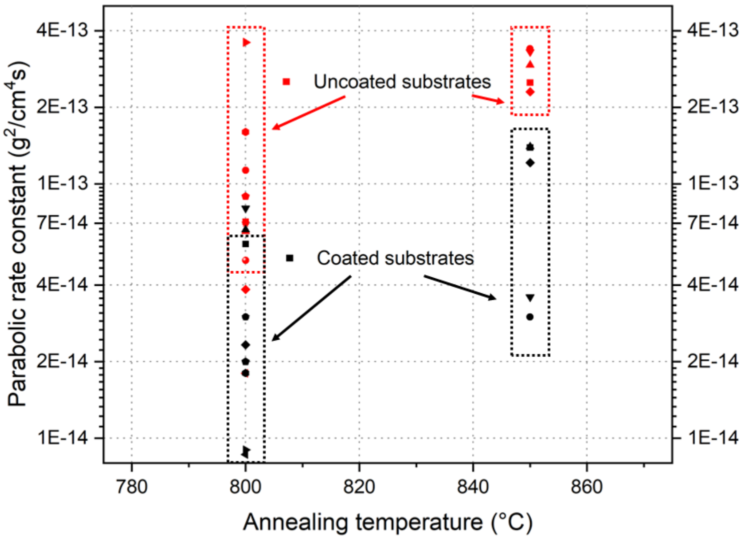

Figure I. 14 – Parabolic rate constants obtained from literature of uncoated (red) and coated (black) alloys annealed at 800 and 850 °C. Values were obtained for AISI 430, AISI 441 and Crofer 22 APU[48,62,83,119,124,126–132]. Coating type (from the Co-Mn spinel spectrum) and experimental conditions (laboratory air, dry O_2 and air + H_2O) are given in Appendix I.1.

Some studies evaluated the influence of the coating thickness on the performance of coated stainless substrates[14]. Zhang et al. studied three coating thickness (800, 1500 and 3000 nm) for varying compositions of Co-Mn metallic coatings, deposited by DC magnetron sputtering (Pure Co, $Mn_{20}Co_{80}$, $Mn_{40}Co_{60}$) on AISI 430[120]. Samples were annealed at 800 °C over time. All samples indicated an increase of the Mn content with time, which was more noticeable on the thinner coatings. For instance, the Mn/Co passed from 0 to 0.2 for pure

Co coating (800 nm) over 1000 h. This Mn increase is a result from diffusion of substrate elements, notably Mn outwards, being incorporated to the coating. Thinner coatings have a smaller reservoir of Co and are more affected by the incoming Mn from the substrate[120]. Such result is critical to consider when defining the coating composition. Chesson et al.[117] and Gao et al.[110] indicated that MCO spinels with high Mn content offer a less effective Cr-barrier. Therefore, it is fundamental to consider the Mn diffusion during oxidation to produce the intended coating composition.

A study from Molin et al.[133] using $Mn_{1.5}Co_{1.5}O_4$ spinel coatings on Crofer 22 APU evaluated the difference between thin films, produced by thermal co-evaporation and RF magnetron sputtering (1-1.5 μm) and thicker ones, produced by electrophoretic deposition (~15 μm). After 5000 h, the thin films presented high Cr content in the oxide surface (~15 %) while the thicker coatings showed less amounts (< 1 %). In both cases, Mn content increased over Co, likely diffusing from the steel substrate. For both coatings, a Cr-rich Reactive Layer was formed between the Co-Mn spinel and the chromia layer. However, in the case of thinner coatings, the spinel layer was completely consumed, and Cr reach the surface of the oxide, which was not the case on the thicker coatings[133]. The formation of a Reactive Layer will be discussed in detail in the next section.

Thin metallic Co (640 nm) coatings were designed by the Chalmers groups using Physical vapor deposition (PVD) technique[90]. Magrasó et al have shown that these coatings are not effective regarding the oxidation rate[92]. However, if a 10 nm-thick Ce layer is applied between alloy and metallic Co (Ce-Co coating), much better results were obtained with a significant reduction of the oxidation rate (~3-fold decrease at 850 °C).

Considering all these results, it is clear that many factors will influence the protective character of the coatings. They range from thickness to coating density, but it is also fundamental that the chemical composition is adequate. Thinner films are appealing for an economic standpoint, but it is important to be attentive to the film composition variation during oxidation.

1.9.2. Reactive layer

As previously indicated, during oxidation a Reactive Layer may be formed between the chromia and coatings layer. The formation of this Reactive Layer (RL) is defined in Figure I.15 has some consequences. Talic et al. considered the Reactive Layer to be beneficial since there will be a reduction in the growth rate of chromia[11]. The formation of a Cr-containing phase was proposed to slow down the oxygen inward diffusion[59], reducing the chromia growth. This RL was observed to have a higher electrical conductivity than chromia, which could represent an overall optimisation of the electrical performance of interconnects[11]. However, these advantages depend on the RL growth rate, the thickness of the coating, the Cr-concentration in the RL, and particularly if Cr has reached the outermost surface. As shown by Molin et al., the RL growth can lead to complete consumption of the coating and Cr reaching the oxide/gas interface, which translates into increase of Cr evaporation rates[133]. Another detrimental factor depends on the Cr-content in the RL. Liu et al. showed that for $Mn_{1.5-x}Co_{1.5-x}Cr_{2x}O_4$, the electrical conductivity become equal or even lower than chromia for x close to 1[118].

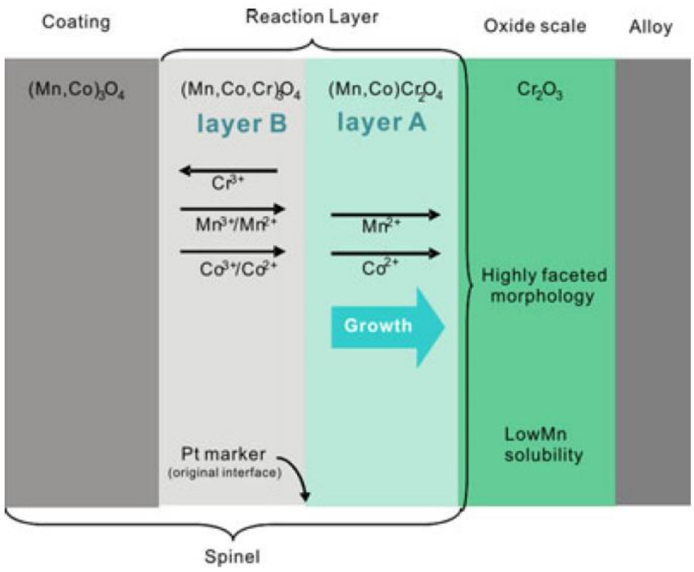

Figure I. 15 - Scheme indicating the diffusion mechanisms behind the formation of a reactive layer between Co-Mn spinels and the chromia layer at high temperatures[121].

The formation of this reactive layer was studied in various works[11,119,121,134]. Diffusion couple studies using $MnCo_2O_4$ and $Mn_{1.5}Co_{1.5}O_4$ with Cr_2O_3 indicated that the formation of the reactive layer happens through a counter diffusion process. Figure I.15 shows the model presented by Wang et al.[121] (a similar model was presented elsewhere[11,110,119,134]). The model suggests the outward diffusion of Cr and inward diffusion of Co, Mn cations. They observed two distinct Reactive Layers, one closer to the chromia phase and another closer to the Co-Mn coating. The growth of layer A was faster than layer B, suggesting that Co and Mn cations are more mobile than Cr. Such result is not surprising considering the study from Cox et al.[135] regarding diffusion properties, where it was suggested that the diffusivity of cation is inversely proportional to their crystal field preference energy (CFSE). Cr having the higher CFSE (Figure I.13a), it should present lower diffusivity. Sun[136] studied the diffusion of Co and

Cr into $CoCr_2O_4$ and suggested that Cr diffusion is only allowed if sufficient strain energy is applied to the lattice (i.e., lattice distortion), which makes it more difficult for Cr to diffuse than Co. Moreover, the Co/Mn ratio was shown to increase in the Reactive Layer. Several cation tracer studies, from Lu and Dieckmann [137–139] and Töpfer et al.[140] evaluated the diffusion of Co, Mn and Cr in $Co_{3-x}Mn_xO_4$ and $(Cr,Fe)_3O_4$ spinel oxides. Among them, Co diffuses slightly faster than Mn, and both much faster than Cr, which could explain the variation.

Talic et al. observed the formation of a Reactive Layer on $MnCo_2O_4$ coated Crofer 22 APU substrates (electrophoretic deposition [EPD]) annealed at 800 °C[123]. The measured RL thickness values were compared with the growth rate obtained on $Mn_{1.5}Co_{1.5}O_4/Cr_2O_3$ diffusion couples also annealed at 800 °C. Using the growth rate values measured by diffusion couples, a 12 µm-thick RL was expected for the coated substrate. In contrast, the Reactive Layer formed on the coated substrate was only 2 µm-thick. Similar differences were obtained by Magdefrau et al.[141] using coated samples. This reduction was explained by the variation in composition of the coatings in comparison to the diffusion couples and a variation on the oxygen supply. Gao et al.[110] evaluated the oxidation behaviour of $Mn_{1.5}Co_{1.5}O_4$ and $MnCo_2O_4$ coatings, produced by slurry deposition followed by microwave sintering step, on Crofer 22 H annealed at 800 °C for different oxidation times (from 50 to 400 h). The formation of a Reactive Layer was observed in both cases. However, for the coating richer in Co ($MnCo_2O_4$), the formation was delayed, and the final Cr-rich Reactive Layer was much thinner. The study suggested that Cr replaces the Mn cations in the octahedral sites due to its high CFSE values. Since Mn content is higher in $Mn_{1.5}Co_{1.5}O_4$, more octahedral sites are expected to be filled. In addition, Mn shows high valence variability and can easily be disproportionate to re-oxidize elsewhere. The study also suggested that a lower Mn/Co concentration ratio in the coating should be beneficial for reaching better Cr-barrier properties. This hypothesis was confirmed by Chesson et al. through the evaluation of diffusion couples using different $Co_{3-x}Mn_xO_4$ stoichiometries ($1<x<1.5$) and chromia at 900 °C. They observed a strong decrease of the RL growth rate for lower Mn/Co concentration ratios[117].

1.9.3. Electrical performance

Interconnects must ensure proper conduction of electrons, thereby electrically connecting the cells in the SOEC stack. Although interconnects are produced in FSS, which are highly conductive, poorly conducting oxide scales are formed during oxidation at high temperatures. The growth of this oxide scale increases the overall resistance of the steel, decreasing the efficiency of the fuel cell. The degradation can be experimentally evaluated using the area specific resistance (ASR). Lower ASR values represent a good current passage and ensure a more efficient operation of the SOEC cell. Generally accepted values lie between 50[12] and 100[13] mΩ·cm^2. Figure I.16 represents a scheme with the various layers that are taken into consideration for the measurement of the ASR, defined by a circuit of resistances in series[14]. The total ASR is the sum of each component, and can be considered as follows:

$$ASR = \frac{th_A}{\sigma_A} + \frac{th_{Cr_2O_3}}{\sigma_{Cr_2O_3}} + \frac{th_{RL}}{\sigma_{RL}} + \frac{th_{coating}}{\sigma_{coating}} + \frac{th_{CL}}{\sigma_{CL}} + ASR_{interfaces}$$

where *th* refers to the thickness and σ to the electrical conductivity of each layer, A being the alloy, RL the reactive layer and CL the contact layer. The equation shows that the ASR is highly dependable on the electrical conductivity of each layer, and it increases with increasing thickness.

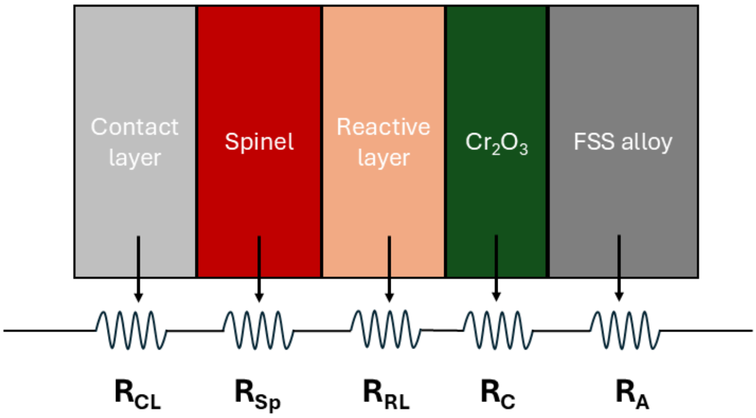

Figure I. 16 - Scheme highlighting the various layers that should be considered for the area specific resistance (ASR) measurements for interconnect materials. [Adapted from Zhu[14]].

The electrical conductivity of an oxide results from the combined contribution of electronic and ionic charge carriers. At elevated temperatures, the electronic mobility typically decreases due to enhanced phonon scattering, whereas the ionic mobility and the concentration of thermally activated charge carriers increase. As most oxides exhibit semiconducting behaviour, their conductivity generally rises with temperature, reflecting the thermally activated nature of charge transport[142,143].

Considering the metallic nature of the alloy, the electrical resistance of the substrate is negligible. Conductivity values from the contact layer are high and can also be neglected.

The electrical conductivity values for chromia, various coating types and the reactive layer are shown in Table I.3. The tendency is that the conductivity increases with the addition of Mn[105] and reduces drastically with the addition of Cr. Although much lower than the alloy, the electrical conductivity values of the coating are generally neglected. Indeed, let's consider Co_3O_4, which has one of the lowest σ in the $Co_{3-x}Mn_xO_4$ spectrum (for $x < 2$)[14]. Considering the σ as 2.2[89] S·cm^{-1} at 800 °C, and an oxide thickness of 10 µm, the resistance of the layer would be 0.45 mΩ·cm^2, far from the 50 mΩ·cm^2 indicated as target[12]. In contrast, using the same thickness for Cr_2O_3 layer, and the highest values obtained in literature (0.05 S·cm^{-1}), the resistance of the layer raises to 20 mΩ·cm^2, and this considers the most favourable scenario. Using the lowest conductivities, values soar to 1000 mΩ·cm^2.

Thus, it can be concluded that the ASR values will be driven by chromia and the formed Cr-rich Reactive Layer. Chromia values vary significantly throughout the literature by more than one order of magnitude due to measurements on bulk chromia (with varying impurity concentration) and on thermally grown chromia on different substrates (i.e., pure Cr or an alloy). In addition, the values were shown to strongly vary with the doping elements and varying oxygen partial pressure[144–147]. Using Ce-Co coatings, Goebel et al.[90] conducted ASR experiments on AISI 441 coated samples for 37000 h at 800 °C. They calculated the electrical conductivity of chromia from the ASR value at the end of the test and the measured chromia thickness and compared the obtained electrical conductivity value with lower (0.001 S·cm^{-1}) and upper (0.05 S·cm^{-1}) values found for chromia at 800 °C in literature. They reported a chromia layer of approximately 15 µm and an ASR of 34 mΩ·cm^2, which represented an electrical conductivity of 0.04 S·cm^{-1}. Reddy et al. reported an ASR of 23 mΩ·cm^2 for a chromia layer of 4 µm (0.017 S·cm^{-1}) after 3000 h. Both values were thus in the higher values domain. Talic et al[123] reported lower conductivity values (0.006 S·cm^{-1}) based on a chromia scale of approximately 3 µm and an ASR of 50 mΩ·cm^2. These calculated values highlight the significant variation from one case to another. This could be due to a variation of the exact composition of chromia and/or the experimental procedure, particularly the facility and the electrical contact layer, that is used to measure ASR.

The Reactive Layer conductivity strongly depends on the Cr quantity on the spinel oxide. The small polaron hopping mechanism is more pronounced in the octahedral sites. Therefore, if Co and Mn cation pairs are available in the octahedral sites, the conductivity should remain acceptable. Liu et al. studied the properties of the $Co_{1.5-(x/2)}Mn_{1.5-(x/2)}Cr_xO_4$ spinel ($0 \leq x \leq 2$). This study showed that the Cr-rich layer does not show extremely low conductivity values except for x close to 2. At $x = 2$, Cr has occupied all the octahedral sites, restraining the polaron hopping mechanism and reaching an electrical conductivity equal or inferior to the chromia layer[118]. Many studies have shown the formation of a Reactive Layer without any significant impact on the ASR values. In these studies, the Reactive Layer shows a Cr concentration gradient, suggesting that in most of the RL, Cr is far from fully occupying the octahedral sites[123,148]. However, more studies are needed to understand the long-term behaviour of this RL, more specifically if the continuous Cr-enrichment, in concentration and thickness, can become detrimental to interconnect electrical properties.

Table I. 3 - Electrical conductivity and thermal expansion coefficient (TEC) for several compounds that may be present after the oxidation of an interconnect.

Compound	**Electrical conductivity at 800 °C (S·cm^{-1})**	**TEC (10^{-6} K^{-1})**	**References**
Co_3O_4	2.2-33.8	9.3	14,89,149
$MnCo_2O_4$	21-157	13.3-14.1	14
$Mn_{1.5}Co_{1.5}O_4$	61-87	10.4-10.8	14
$Mn_{2.5}Co_{0.5}O_4$	1.9	-	102
$Mn_2Co_1O_4$	6.4-21	6.9-7.4	14,102
$Mn_{0.5}Co_{0.5}Cr_2O_4$	0.007-0.09	6.7	118,121
Cr_2O_3	0.001-0.05	9.6	118,144–146,150,151
$MnCr_2O_4$	0.002-0.03	7.47	142,152,153
$Mn_{1+x}Cr_{2-x}O_4$	0.002-1	-	89,142,152,153
$Co_{2-x}Mn_{1+x}O_4$	20-160	6-14.7	102
$MnCoCrO_4$	2.5	8.7	118
$Mn_{0.75}Co_{0.75}Cr_{1.5}O_4$	0.45	7.5	118

Overall, coatings are fundamental to decrease ASR values, both for reducing the formation rate of chromia and for reducing the Cr evaporation rate. Figure I.17 shows five different alloys coated with Ce-Co coatings oxidized for 3000 h at 800 °C and tested regarding their ASR performance. The objective of the experiment was to show that despite having varied elemental compositions, tailor-made alloys and low-cost alternatives could be effective as interconnect material as long as a coating was applied. In all cases, the coatings drastically reduced Cr evaporation, and rendered very similar ASR values, except for AISI 430 likely due to its higher Si content. Bouvier et al. [unpublished CEA study] conducted *in-situ* ASR measurements on uncoated and Ce-Co coated AISI 441 at 800°C. In SOFC mode, they have observed a strong ASR increase at approximately 5000 h, which was attributed to a Cr evaporation/redeposition event. Such behaviour was completely avoided by coated samples, which exhibited a stable steady ASR increase.

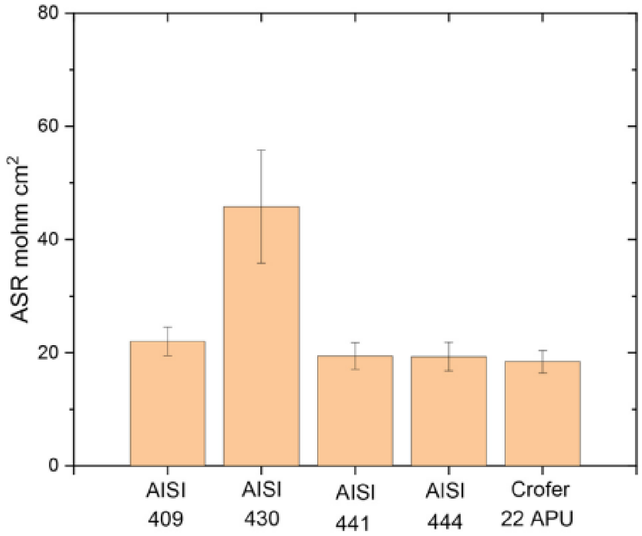

Figure I. 17 - ASR values obtained for five different alloys after 3000 h annealing at 800 °C for Ce-CO coated substrates[48].

1.9.4.Thermal expansion coefficient

The thermal expansion coefficient (TEC) is a critical parameter in solid oxide electrolysis cells (SOECs). Minimizing the difference in TEC between the various layers of the cell is essential to prevent excessive thermal stresses that can lead to oxide spallation. The TEC values of the main SOC components typically range[5,12] from 10.5 x 10^{-6} to 12.5 x 10^{-6} K^{-1}.
Table I.3 summarizes the TEC values of $Co_{3-x}Mn_xO_4$ coatings, Cr-rich phases formed during oxidation. SiO_2 oxides may also be formed and are detrimental due to their low TEC values. A significant mismatch in TEC between layers can promote the spallation of oxide scales.
The TEC of Co–Mn spinels are generally comparable to that of other SOEC components, except when the Mn content becomes too high. Increasing the Mn concentration leads to a continuous decrease in TEC, reaching 7.4 x 10^{-6} K^{-1} for x = 2. Reported values for chromia (Cr_2O_3) vary in the literature, with 9.6 x 10^{-6} K^{-1} being the most used for SOEC applications[102].

Finally, Cr-rich spinel phases exhibit relatively low TECs (<8 x 10^{-6} K^{-1}) at high chromium contents.

1.10. Coating processes and impact on properties

A variety of techniques have been employed to fabricate Co-Mn spinel coatings, with the most commonly used methods summarized in Table I.4. Zhu et al.[14] classified these approaches into three categories based on precursor type: (i) direct spinel methods, (ii) ceramic precursor methods, and (iii) metallic precursor methods. Each technique presents distinct advantages and limitations in terms of coating quality, processing complexity, and cost.

Economical methods such as slurry coating, thermal spraying, and electrodeposition tend to produce thicker (10–100 µm) but more porous coatings. They often require multistep treatment, such as reduction and pre-oxidation of the coated samples, to improve coating densification. These treatments are time-consuming, typically involve high temperatures (up to 1100 °C), and residual porosity often remains. In contrast, Physical Vapor Deposition (PVD) offers the advantage of producing dense coatings without the need for high-temperature annealing, although substrate pre-oxidation is sometimes applied before the deposition to limit Fe incorporation into it[154,155]. PVD coatings are generally thinner due to the slow deposition rate and are limited by the high cost and low-pressure requirements of the equipment, which could pose challenges for industrial scalability.

Table I. 4 – Main deposition techniques reported in literature for the synthesis of Co-Mn spinel oxides. Reprinted from Zhu et al.[14]

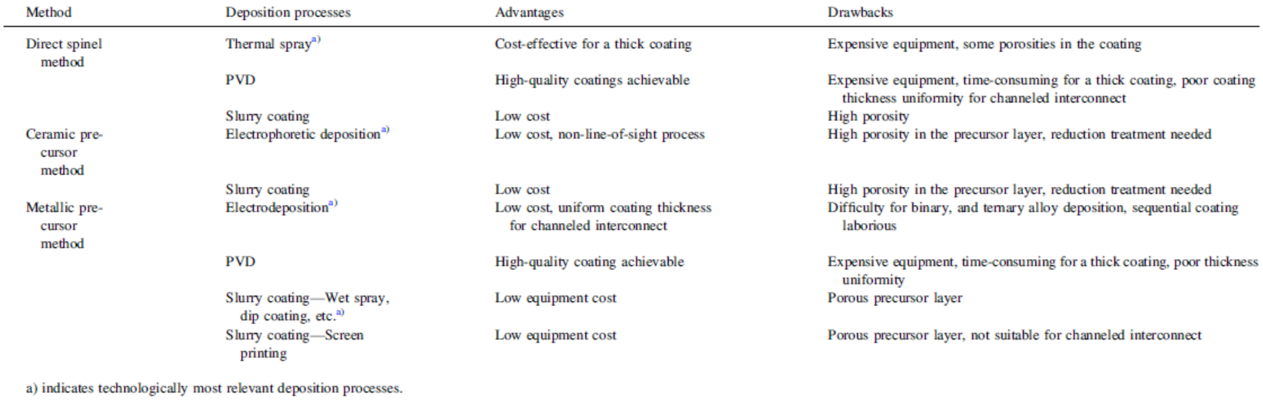

Method	Deposition processes	Advantages	Drawbacks
Direct spinel method	Thermal spray[a)]	Cost-effective for a thick coating	Expensive equipment, some porosities in the coating
	PVD	High-quality coatings achievable	Expensive equipment, time-consuming for a thick coating, poor coating thickness uniformity for channeled interconnect
	Slurry coating	Low cost	High porosity
Ceramic pre-cursor method	Electrophoretic deposition[a)]	Low cost, non-line-of-sight process	High porosity in the precursor layer, reduction treatment needed
	Slurry coating	Low cost	High porosity in the precursor layer, reduction treatment needed
Metallic pre-cursor method	Electrodeposition[a)]	Low cost, uniform coating thickness for channeled interconnect	Difficulty for binary, and ternary alloy deposition, sequential coating laborious
	PVD	High-quality coating achievable	Expensive equipment, time-consuming for a thick coating, poor thickness uniformity
	Slurry coating—Wet spray, dip coating, etc.[a)]	Low equipment cost	Porous precursor layer
	Slurry coating—Screen printing	Low equipment cost	Porous precursor layer, not suitable for channeled interconnect

a) indicates technologically most relevant deposition processes.

To address these limitations, alternative deposition techniques offering better scalability and more economically processes should be explored. One such method is Atmospheric

Pressure Plasma-Enhanced Chemical Vapor Deposition (AP-PECVD), which is gaining attention for its ability to deposit thin films using plasma energy to drive chemical reactions[18,19]. The key advantage of AP-PECVD lies in its operation at atmospheric pressure, eliminating the need for energy-intensive vacuum systems and enabling compatibility with complex substrate geometries. In addition, this technology offers easily scalable process for industrial application[19,20].

However, AP-PECVD technique has not yet been applied to the deposition of Co or Co-Mn oxides. To date, it has been primarily used for depositing common inorganic films such as SiO_2[156,157], TiO_2[158,159], and ZnO[160], as well as polymeric coatings[161,162]. Recent developments on the use of plasma technologies for the deposition of inorganic, organic and composite coatings suggest its broader potential[18,20,163]. For example, Huerta-Flores et al. produced $SrTiO_3$ films using a blown arc discharge equipment[164], and Patel et al. developed ZrO_2 and Ce-doped ZrO_2 coatings using a plasma jet[165]. While these studies reported challenges such as lower growth rates, residual contamination, and film cracking, they demonstrate the feasibility of depositing a wide range of inorganic materials using AP-PECVD technology.

2. Atmospheric Pressure Plasma Enhanced Chemical Vapor Deposition (AP-PECVD)

Plasma has high energy available and presents several advantages to thin film deposition[166]. Differently, from traditional CVD processes, plasma CVD is not solely dependent on thermal energy for the activation of the reactions, since it offers a high concentration of chemically active and reactive species[166,167]. Their presence enables shifting chemical processes to lower activation energies, as shown in Figure I.18a. The A, B and C passing through AB* and with an activation energy X represents the typical CVD process, while A*, B* and C* with activation energy Y represents the plasma deposition CVD. The decreased activation energy happens since plasma species offer different pathways for the chemical reactions, participating in the precursor activation[21], radical production[168,169], and will provide additional reactive species to ease chemical reactions with the precursor[166,167,170]. The result is that lower thermal input is necessary, i.e., lower substrate temperatures, for producing high quality thin films, and higher deposition rates can be obtained.

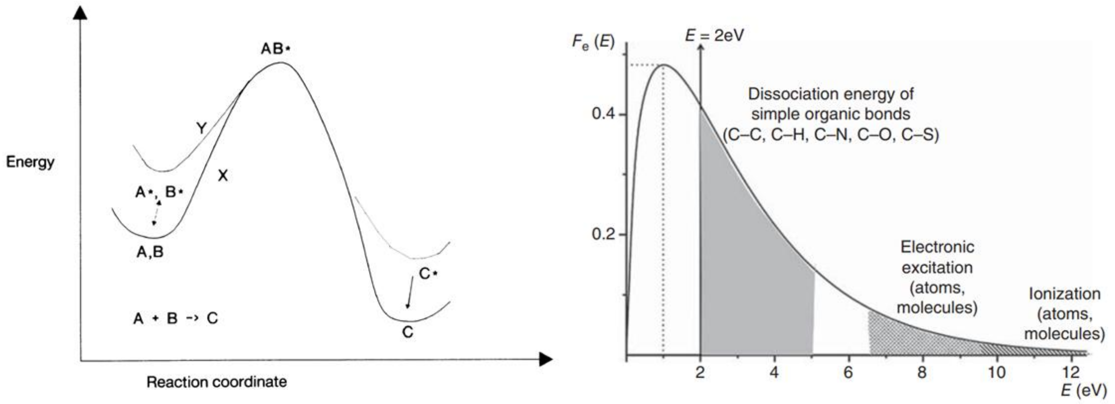

Figure I. 18 - Representation of the chemical reaction happening in CVD and plasma-driven CVD. A, B and C represent the typical CVD reaction while A, B* and C* the plasma process. The activation energy Y is smaller than the activation energy X from CVD process[167]. (a) Electron energy distribution function (EEDF) represents the typical distribution of electron energy in plasma. Here, it follows Maxwellian-Boltzmann shape while it may vary at atmospheric pressure. Average energy is below 2 eV and above that, inelastic process may happen (b)[21].*

2.1. Plasma generation

Plasma consists of a mixture of free electrons, ions, and neutral species, collectively referred to as *plasma species*. These species maintain a state of *quasi-neutrality*, meaning that, on average, the number of positive and negative charges is balanced. However, local fluctuations may create regions with a higher density of either electrons or ions. The mixture of these species is formed through the ionisation of a gas, requiring an input of energy, in the form of heat or electricity. This leads to altering the electronic structure of atoms and molecules by causing a loss or gain of electrons while generating ions and other excited species[166,167]. Since electrons are much lighter than other species, they will be easily accelerated and will gain kinetic energy. Thus, electrons act as carriers of energy and determine the plasma chemistry[166,167] by transferring this energy through collisions, which can be elastic or inelastic.

- Elastic collisions transfer energy without altering the internal structure of the neutral species. Instead, they increase their kinetic energy, leading to heating[19,166].
- Inelastic collisions occur when electrons possess enough energy to modify the electronic structure of neutral species. These interactions produce excited species or even ionized particles, making inelastic collisions essential for driving chemical reactions[19,171].

The electron energy profile is often approximated by a Maxwellian distribution for simplicity. However, in atmospheric pressure plasmas, the actual electron energy distribution function (EEDF) is typically non-Maxwellian due to the high frequency of collisions and the nonequilibrium nature of the discharge. Figure I.18b shows that low-energy electrons (typically < 2 eV) dominate, and they will primarily contribute to elastic collisions. Meanwhile, the high-energy tail of the EEDF, despite having lower electron population, is critical for driving inelastic processes such as excitation, ionization, and dissociation. These energetic electrons play a central role in determining the overall plasma chemistry and the generation of excited species[21]. In atmospheric plasmas, the species created initially by these electrons will actively participate in the deposition reactions[172].

Figure I.19 shows the influence of pressure on the plasma temperature. The plasma temperature is generally divided into rotational temperature (T_g) and electron temperature (T_e). As the pressure rises, the two temperatures approach each other. This happens since the temperature is directly affected by the number of elastic collisions, which drastically rises close to atmospheric pressure. Figure I.19 is divided into two regions: non-local thermodynamic equilibrium (non-LTE) and local thermodynamic equilibrium (LTE)[19,173], which can be defined as follows:

1. Non-Local Thermodynamic Equilibrium (Non-LTE) occur when the electron temperature (T_e) differs significantly from the gas temperature (T_g). As illustrated in Figure I.19, this condition is more easily achieved at low pressure, where the mean free path (λ) is large, reducing the frequency of collisions. With fewer interactions, electrons gain kinetic energy between collisions, often exceeding the threshold for inelastic processes. This makes low-pressure plasmas ideal for starting chemical reactions, such as those in Plasma-Enhanced Chemical Vapor Deposition (PECVD), a widely used technique for producing thin films.
2. Local Thermodynamic Equilibrium (LTE) Plasmas occur when plasma species reach thermal equilibrium ($T_e \approx T_g$), typically at high pressure, as shown in Figure I.19. Under these conditions, frequent collisions efficiently transfer energy from electrons to heavier particles, leading to uniform heating. LTE plasmas are commonly found in high-temperature applications such as arc plasmas used for cutting or welding. However, in thin film deposition, LTE plasmas are avoided, as they can cause overheating, substrate degradation, precursor decomposition, and even powder formation.

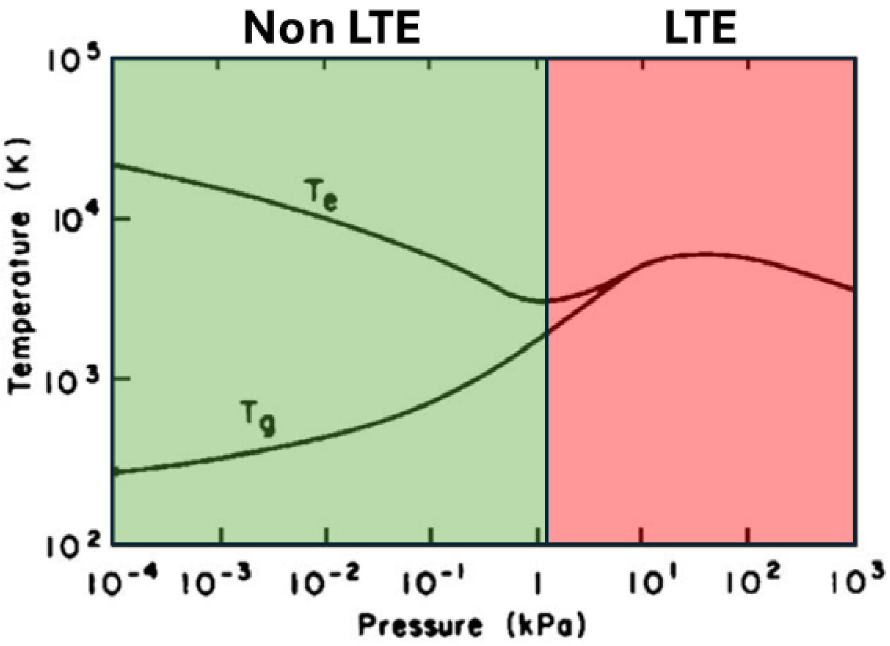

Figure I. 19 - Gas (T_g) and electron (T_e) temperature in function of the pressure. Adapted from Merche et al.[19]

LTE conditions drive the process to extremely high temperatures, which should be avoided in thin film deposition processes. Although easier to keep non-LTE conditions under operating at low-pressure, the process has a few drawbacks, such as low deposition rates, requirement of energy-consuming pumps, and are not adaptable to continuous processing[18,19]. Non-LTE may also be reached at atmospheric pressure by reducing collision processes. Some tricks should be implemented, which are summarized below:

- High frequencies: when using low frequencies, electrons and other species tend to follow the oscillation of the electric field. However, by increasing the frequency, only electrons managed to keep following it, which leads to a reduction in their interactions.
- Dielectrics: the addition of the dielectric to one of the electrodes provoke an accumulation of electrons on this side. Thus, decreasing the apparent voltage difference between the electrodes. Consequently, the electric field, responsible for the acceleration of the electrons, is decrease, and so do the subsequent collisions.
- Pulsed plasma: nano or microseconds pulse are applied to the plasma. Since electrons are much lighter, they respond fast to the electric field, while heavier particles require longer times.
- Blown arcs: in this case, the arc is produced between a high voltage and ground electrode. However, a high gas flow passes through the arc, which only partially ionizes the gas, keeping the temperatures lower.

Atmospheric pressure plasmas, particularly non-thermal (cold) plasmas, are effective tools for surface treatment and thin-film deposition due to their ability to generate a diverse range of energetic species without causing substrate damage. These plasmas operate with electron temperatures significantly higher than gas temperatures, enabling controlled and energy-efficient interactions.

2.2. Plasma jets

Among plasma technologies, plasma jets appear as an attractive solution since the plasma production and substrate are not in the same chamber. Winter et al.[174] have grouped plasma jets based on their configurations, comparing the specific input energy (SIE), defined by the power dissipated by the dilution gas volume, in function of frequency (Figure I.20). Higher energy densities will lead to more energetic species due to increase in the provided energy. Inversely, low energy densities (below 10^2 $J \cdot L^{-1}$) present only moderate increase in gas temperatures. Consequently, to avoid gas thermalization, it is critical to keep a good compromise between energy and dilution gas flow. The use of higher frequencies reduces the mean free path, and thus the collision frequency between electrons and other species. Concomitantly, it allows the electrons to gain more kinetic energy, and more energetic species will be present. To avoid thermalization, low energy densities must be kept or operate at intermediate frequencies. For the sake of comparison, the configuration used in the present work is indicated in the graph (red triangle). It can be defined as an AC plasma jet with intermediate energy density (1.2×10^3 $J \cdot L^{-1}$) and frequency (100 kHz).

Although useful for a general classification, the graph is shown solely to highlight the wide variety of plasma jet configurations. Plasma properties may strongly vary between one condition and another since other parameters (e.g. geometry and gas composition) will also influence. Besides, the same SIE may lead to much higher temperatures at DC configuration than at higher frequencies.

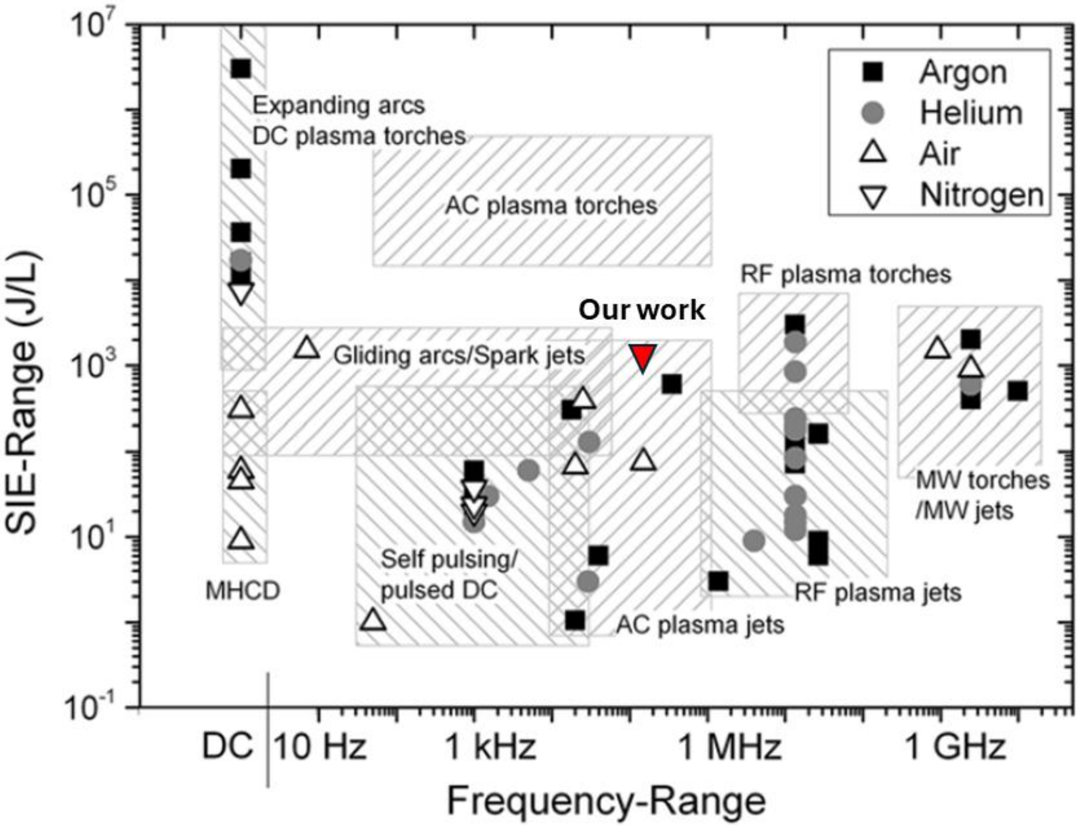

Figure I. 20 - Classification of plasma jets using the specific input energy (SIE), defined by the plasma power dissipated by the dilution gas volume, in $J \cdot L^{-1}$. Each box defines a plasma jet configuration. Red triangle represents the configuration used in the present work. Adapted from Winter et al.[174]

Considering AP-PECVD systems, only non-LTE plasma jets are used, avoiding then the very high energy density configurations. Despite the wide variety of plasma jet geometries, most of them integrate the high-voltage electrode and the ground electrode in the same chamber. A schematic representation of a plasma jet is shown in Figure I.21. Other typical plasma configurations use the substrate as the ground electrode or right above it. Thus, plasma jets generate the electrical discharge in a separate chamber, avoiding its direct contact with the substrate[20]. The plasma is forced out from the chamber by a dilution gas flow at high speed, enabling remote operation outside the discharge region. This configuration avoids the substrate exposure to harsher conditions from the discharge region.

Once the plasma exits the chamber, it transitions from the active discharge zone to a downstream region commonly referred to as the afterglow or plasma plume. The afterglow is characterized by the presence of reactive species (e.g., radicals, metastables, and ions) after the termination of the active plasma excitation[20]. Although the densities of the excited species, particularly electrons and ions, decrease rapidly due to their limited lifetimes, the remaining reactive species can still participate in surface interactions and chemical reactions.

The temperature within the plasma plume typically ranges from room temperature to approximately 1000 K, depending on the operational parameters (SIE and frequency) and the distance from the plasma source. This gradient in temperature and reactivity further emphasizes the versatility and tunability of plasma jets for surface processing applications[18,20,175].

2.3. Precursor Injection

Besides the substrate position, another fundamental parameter in AP-PECVD deposition system relies on the precursor injection. The interaction region of the precursor and the plasma reactivity species will influence on its activation, and consequently on the production of film-forming species[21,172]. Too high reactivity from precursor or plasma species may lead to powder formation while low reactivity could lead to low deposition rates or unsuccessful elimination of impurities. The precursor injection position is an important parameter to consider in this case since it will define the reactivity of the plasma. Figure I.21 presents three distinct regions: A, B and C. It is possible to observe that reactivity and temperature decrease by moving away from the plasma formation zone. Inversely, neutral species tend to increase[20,176].

Region A corresponds to the discharge zone, where the plasma is actively sustained. This region exhibits the highest density of energetic species and elevated gas temperatures. Although favourable for precursor activation, it triggers gas-phase reactions leading to internal reactor coating and powder formation.

Region B represents the injection in the downstream region, avoiding excessive gas-phase reactions, and it is widely used for thin film deposition[177,178]. While energetic species reduce compared to Region A, reactivity is still high. Very energetic species will lead to excessive fragmentation and recombination reactions will depend on the residence time of the precursor. This region is ideal for precursor with low reactivity or to induce the formation of nanoparticles[163].

Region C is a less energetic alternative, and this region is defined as the afterglow[20,176]. By injecting the precursor below the source outlet, many of the plasma species were already quenched by environment species (surrounding atmosphere) before interacting with the precursor. Despite the quenching and the reduction of energetic species, the afterglow retains chemically active species, including radicals, metastables, and UV photons, which are still capable of driving surface reactions[179,180].

Determining the optimal precursor injection point requires balancing the available energy and residence time to promote film growth while minimizing unwanted side reactions. Plasma species must retain sufficient energy to activate the precursor, but excessive energy promotes gas-phase reactions and powder formation, which degrade film quality.

Olivier et al. demonstrated that shifting the injection point further downstream reduces the energy density, thereby decreasing powder formation while still enabling thin film deposition with low residual contamination[181]. According to Massines et al., powder formation arises from either the accumulation of negative ions or the recombination of reactive precursor radicals in the gas phase[18]. To mitigate this, several strategies have been proposed, including lowering precursor concentration or reactivity, reducing power input, and increasing dilution with inert gases[18,19].

Additionally, Belmonte et al. discussed the effect of the plasma-substrate distance, pointing out that increased distance will increase the residence time and thus gas-phase reactions[182]. Chemin et al. showed that by varying the injection position of the precursor it is possible to control the film nature. Longer residence time at high energy densities resulted in nanoparticle formation while injecting the precursor closer to the substrate favours surface-based reactions[159]. Among the three regions, Region C offers a more stable and controllable environment for deposition, with shorter residence times and lower plasma reactivity.

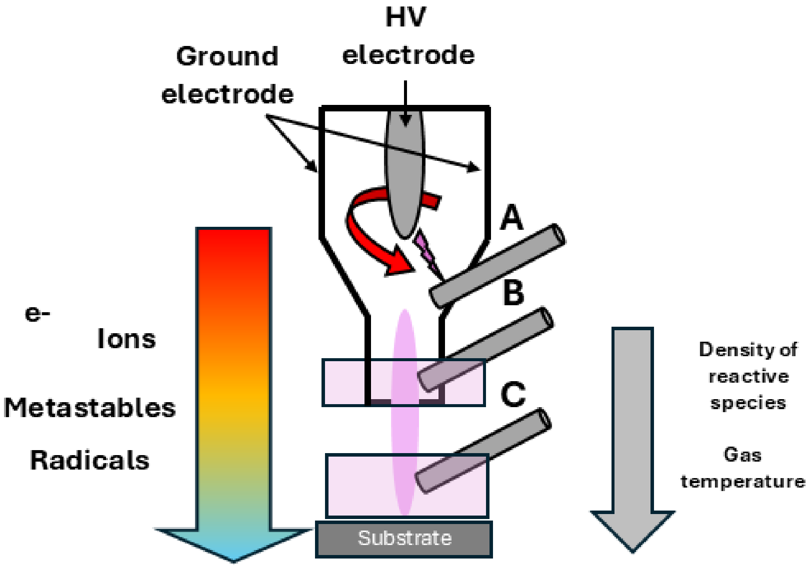

Figure I. 21 - Scheme of a plasma jet configuration. Definition of three regions: A refers to the plasma discharge, B to the downstream region in a separate chamber to the discharge and C to the afterglow after the outlet exit. The right arrow indicates that the reactive species and gas temperature decreases downstream. Adapted from Fanelli et al. (2017) and Bardos et al. (1988).

2.4. Precursor injection Systems for Plasma Processing

In addition to the injection position, proper precursor delivery is essential to optimize interaction with the plasma. Delivery methods depend largely on the precursor's physical state. For volatile precursors, direct vaporization into the plasma zone is possible. A common approach uses bubblers, where an inert carrier gas passes through the liquid precursor. When dealing with low-volatility or solid precursors, heating systems are required to ensure sufficient vapor pressure, demanding precise thermal control to avoid undesired condensation or precursor decomposition.

Alternatively, aerosol-assisted delivery is well-suited for low-volatility or thermally unstable precursors[18,163]. In this method, a precursor solution is converted into a fine spray via ultrasound atomization or through the Venturi effect, which employs a high-speed gas stream to generate a pressure drop that fragments the liquid. Aerosol methods enable consistent precursor introduction and, as suggested by Massines et al.[18], may also reduce gas-phase fragmentation during deposition. Solid precursors can be dissolved in appropriate solvents to allow aerosolization, provided they exhibit good solubility, and the solvent is sufficiently volatile and chemically inert[164,183]. Additional considerations on precursor selection are discussed in Section 3.3.2.

2.5. AP-PECVD drawbacks

Despite the numerous advantages of atmospheric pressure plasma-enhanced chemical vapor deposition (AP-PECVD) as previously discussed, the process remains inherently complex. While significant progress has been made, several challenges persist, particularly in understanding and controlling the mechanisms governing thin film growth[19,184].

Among the most critical issues are the fluid dynamics of the plasma jet, process optimization, and reproducibility[20]. Although various plasma configurations have been explored in the literature, comparison across studies is often difficult due to the diversity of reactor designs, many of which are developed in-house with limited standardization[18,20].

A major challenge lies in the complex interplay between plasma species, surrounding air, precursor chemistry, and substrate reactions phenomena. As noted by Merche et al., a deeper understanding of these interactions is still needed to fully control the deposition process and improve film properties[19]. A good understanding of these processes could help in controlling AP-PECVD drawbacks, such as achieving dense, uniform coatings with low impurity levels and minimal particle formation. In the following section, we will first outline the fundamentals of CVD and plasma processes. Then, we will review recent studies aimed at improving our understanding of plasma–precursor–substrate interactions under atmospheric conditions.

2.6. Thin film growth – Mechanisms involved

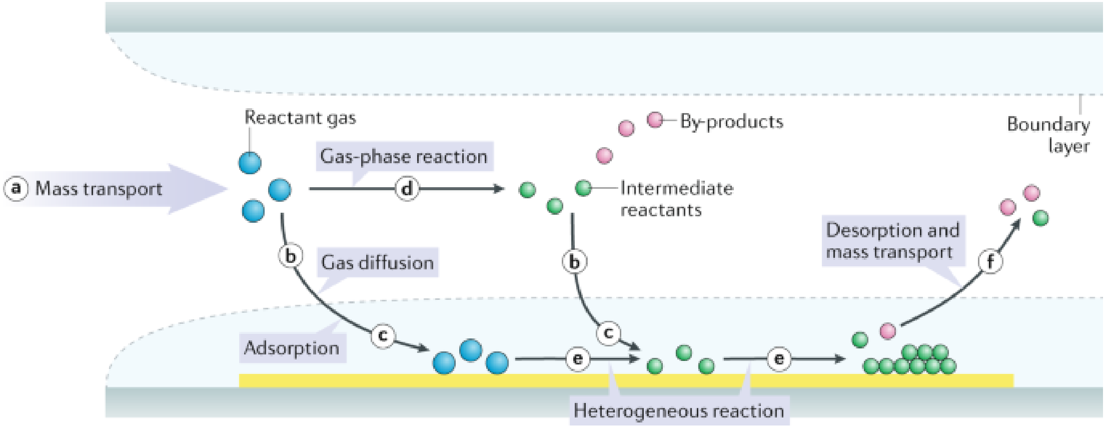

Figure I. 22 – Schematic representing a typical vapour deposition reactor with the specific conditions. Reprinted from Sun et al.[185].

Before examining the mechanisms specific to the AP-PECVD process, it is useful to recall the fundamental reactions governing conventional chemical vapor deposition (CVD). In CVD, thin films form on a substrate through chemical reactions occurring in the gas phase, as illustrated in Figure I.22. The process begins with the introduction of precursor gases, often accompanied by co-reactants, which are transported to the reaction zone by diffusion and convection. Gas-phase reactions between these species produce reactive intermediates and by-products; their concentration must be carefully controlled to prevent unwanted powder formation.

Near the substrate surface, these reactive species diffuse through a boundary layer where heterogeneous reactions dominate. Adsorption of precursor molecules is followed by surface diffusion toward energetically favorable sites, nucleation, and film growth, accompanied by the desorption of gaseous by-products. The efficiency of each step depends on parameters such as temperature, pressure, and gas composition.

The chemical reactions require a certain amount of energy to happen, generally provided by heating the substrate in CVD processes. As indicated in Figure I.18a, using plasma allows to lower this energy by the presence of reactive species which promote alternative reaction pathways and enable precursor activation through collisions, enhancing the overall deposition efficiency. The precursor activation is defined by producing film-forming species through the fragmentation of the precursor. Plasma additionally provides energy in the form of heat, and energetic species[167].

Although AP-PECVD shares the foundational steps of CVD, its non-thermal nature and interaction with charged and neutral species introduce complexities in precursor activation, transport, and surface interactions. The presence of a high-velocity gas flow, the interaction with the surrounding air and the variety of species (in neutral or excited state) in AP-PECVD further complicate the control over these mechanisms.

2.6.1. Plasma role (species)

Upon plasma ignition, a wide range of reactive species are generated. Among these, electrons are the most mobile and carry the highest kinetic energy, typically ranging from 1 to 10 eV although even more energetic species may be present[18,166] (see Figure I.18b). Their interaction via inelastic collisions with neutral gas molecules governs the initial stages of plasma chemistry[167]. In nitrogen-containing plasmas, for instance, electron collisions with N_2 molecules can lead to excitation, dissociation, or ionization, depending on the electron energy[166,186,187]. Excitation of N_2 begins around 6.2 eV, while dissociation requires approximately 9.8 eV, and ionization occurs at energies above 15.6 eV[186]. Figure I.23 illustrates the energy level diagram for N_2, which shows the required energy for producing excited states of the N_2 molecule. Among these excited states are ionized N_2^+ states (X, A and B), N_2 vibrationally excited molecules (A, B and C) defined as N_2^*. The metastable state $N_2(A^3\Sigma^+_u)$ or N_2^m plays a critical role due to its relatively long lifetime[18,187,188], typically in the millisecond to second range, enabling it to participate in reactions far from the discharge region. In contrast, electrons, ions, and most excited states possess much shorter lifetimes, often in the microsecond regime or below[169,189]. These short lifetimes are related to relaxation mechanisms. Electrons, ions and other excited species will tend to lower their energy states by radiative decay (photon emission) or through collisions[167].

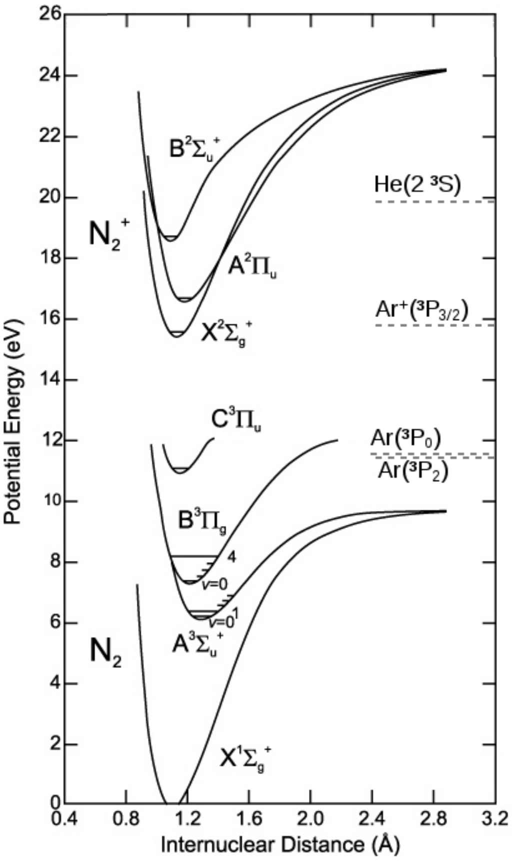

Figure I. 23 - Energy level diagram of N_2 molecules. On the right side, a comparison with Ar and He metastable states. Reprinted from do Nascimento[190].

The maintenance of metastable species is attributed to quantum selection rules, which limit their ability to undergo radiative decay[167]. As a result, spontaneous photon emission is highly suppressed, and energy transfer must occur primarily via collisional processes. These metastables can efficiently transfer energy to other gas molecules or precursor species, either promoting dissociation or facilitating surface reactions.

It is also important to account for interactions with the environment. Using the remote plasma case, there will be direct contact with the open-air atmosphere. It is common that the plasma gas mixes with the surrounding gas[20,191]. This mixing leads to the production of additional species. O_2, humidity and other contaminants are largely present in the atmosphere. Van Gessel et al. investigated the quenching of these species by the plasma[192]. These species will quench the highly energetic plasma species and form new reactive species[177,181,189,193]. The interaction of the excited plasma species with air will lead to dissociation (production of atoms, i.e. N, O and H), and formation of NO and OH radicals. The OH radicals are formed from the fragmentation of H_2O molecules[194], while the NO formation pathway possibly comes from excited N_2^* species encountering O_2 molecules (other pathways are discussed in literature)[192,194].

$$N_2\,(A^3\Sigma_u^+) + O_2\,(X^3\Sigma_g^-) \rightarrow NO\,(X^2\Pi_r) + NO\,(X^2\Pi_r)$$

Further collisions will lead to the excitation of these radicals, which will happen through:

$$N_2\,(A^3\Sigma_u^+) + NO\,(X^2\Pi_r) \rightarrow NO\,(A^3\Sigma_u^+) + N_2\,(X^1\Sigma_g^+)$$

Or

$$e + NO\,(X^2\Pi_r) \rightarrow NO\,(A^3\Sigma_u^+) + e$$

These species are known as reactive oxygen and nitrogen species (RONS)[187], which have great importance in chemical reactions[166,169,180,192]. RONS were widely studied for the treatment of pollutants due to their high oxidative character[170,187,195]. Besides, RONS have longer lifetimes than the other species and may be effective even further away in the plasma zone[166,196]. Takeda et al. studied the evolution of RONS, N and O atoms and high-energy photons using a plasma jet system. He observed a decreased intensity for photons and O and OH species while NO and N atoms slowly increased moving away from the plasma outlet[169]. Similar results were observed elsewhere[193,197,198]. However, the concentration of these species in the afterglow will strongly depend on the plasma power, in the gas composition and the environment since the generation of these species varies with these conditions[169,189,197].

Moreover, the observed decrease in atomic species intensity can be attributed to recombination processes. Due to their high reactivity, these atomic species readily undergo secondary gas-phase reactions, leading to the formation of a variety of reactive oxygen and nitrogen species (RONS). For instance, excited nitrogen and oxygen atoms can recombine with other atmospheric molecules, triggering collision-induced reactions that generate nitrogen oxides (NO_x), ozone (O_3), and additional atomic radicals.

While atomic species tend to have short lifetimes and react rapidly near the discharge zone, more stable species such as NO and NO_2 are less reactive and can be effectively transported downstream by the gas flow. In parallel, vacuum ultraviolet (VUV) photons are emitted in the plasma jet through the radiative decay of excited species, i.e., N_2^*. However, these high-energy photons are quickly absorbed by atmospheric gases that diffuse into the plasma, thereby limiting their propagation and reducing their influence in the far-field plasma region[179,180].

Table I.5 sums up the internal energy present in the main excited molecules previously discussed. N_2 molecules have a high available energy, which can be partly lost through interaction with open-air molecules. The energy from these species is critical for the CVD process since it may be used for the dissociation of the precursor and production of radicals. These reactive species will also participate in chemical reactions, such as cleaning and activation of the surface. Oxygen-rich molecules, i.e., NO and OH have a strong oxidizing character, and may be fundamental for the latter, as well as in chemical reactions with the precursor.

Table I. 5 - Internal energy of several molecular species available in AP-PECVD using a N_2 plasma gas under open-air conditions. Values were obtained from Huber et al.[199] and Liu et al.[179].

Molecular species	**Internal energy (eV)**
$N_2\ (A^3\Sigma_u^+)$	**6.22**
$N_2\ (C^3\Pi_u)$	**11.03**
$N_2^+\ (B^2\Sigma_u^+)$	**18.7**
$NO\ (A^2\Sigma_u^+)$	**4.76**
$NO\ (B^2\Pi_u)$	**5.69**
$OH\ (A^2\Sigma_u^+)$	**4.04**
$VUV\ (photons)$	**6-20 eV**

Another factor important when considering the influence of plasma to thin film growth is the thermal energy input. When considering a plasma jet, thermal energy is provided by the plasma gas in a convective manner. This energy translates into easing chemical reactions, vaporisation processes, and, depending on the temperature and thin film, on crystallization. Although non-thermal, cold plasma do not necessarily operate at room temperature. Fanelli et al. indicated that plasma gas temperature ranges from room temperature to 1000 K[20]. While the lower end should not provide any variations, getting closer to the upper limit will strongly influence thin film formation.

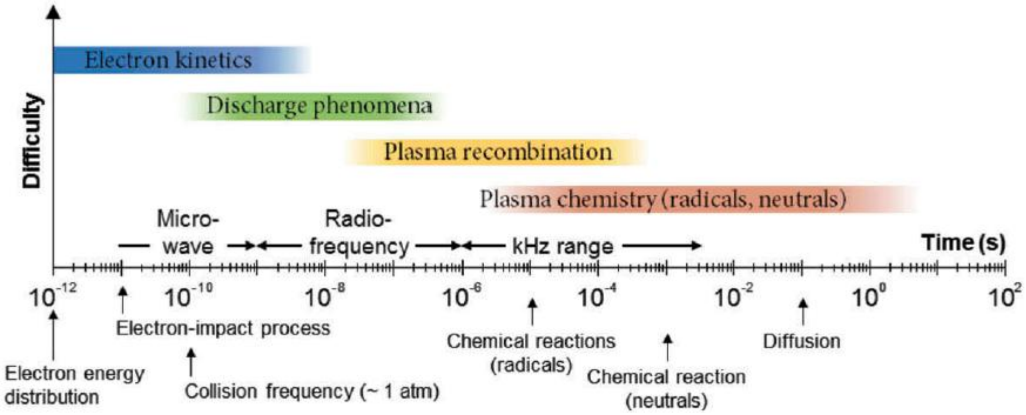

Figure I. 24 - Timescale of the typical processes happening in plasma deposition. Reprinted from Park et al. [200].

Figure I.24 illustrates the processes happening in a plasma in their timescale. Electron production and collisions happen in nanoseconds. On the other hand, plasma chemistry is mostly changed in the order of milliseconds. Considering that plasma gas velocities are in the order of hundreds of metres per second[182], a substrate located at >1 cm from the plasma would be mostly affected by the plasma chemistry since it would take several *ms* for them to reach the substrate. The predominance of one specific process is defined by the concentration of the species responsible for such a process. Thence, processes happening far from the plasma discharge will less likely involve electrons since their destruction rate happens in the order of 10^{-9} seconds[176].

Overall, thin film production in plasma-assisted processes is influenced by a combination of energetic and reactive species. Electrons and ions initiate most inelastic collisions, driving the formation of excited species, radicals, and atoms that enhance chemical reactivity. Radicals and excited neutrals are particularly effective in activating precursors due to their moderate energy and longer lifetimes, especially in the afterglow region. VUV photons contribute by breaking molecular bonds and enabling photochemical pathways, though their range is limited by air absorption. Lastly, thermal energy, while generally lower than in conventional CVD, still plays a role by supporting surface diffusion and adsorption. The synergy between these factors allows for efficient thin film deposition at lower temperatures and atmospheric pressure.

2.6.2. Plasma – precursor interactions

Maintaining a balance between plasma energy, carrier gas flow, and precursor concentration is critical to achieving uniform and well-defined coatings. Otherwise, suboptimal conditions can result in undesired outcomes, including incomplete curing, powder formation, or non-uniform films. While various plasma configurations exist, the following discussion will focus specifically on the interactions between plasma-generated species and the precursor.

The species present in the plasma phase, such as reactive radicals, VUV photons, and thermal energy, play a central role in thin film formation. Primarily, these species activate the precursor through collisions, leading to the generation of film-forming fragments[19,21,201]. In parallel, they may also contribute to surface activation, enhancing reactivity at the substrate[18,19]. The formation and effectiveness of these species depend strongly on the precursor's residence time in the active plasma zone, its chemical stability, and the energy and density of plasma-generated species. These aspects can be broadly categorized into precursor and plasma reactivity. Once activated, the reactive fragments migrate to the substrate, where they undergo surface reactions.

2.6.3. Precursor Activation

Regarding precursor activation, it was suggested to happen through partial fragmentation of the precursor and formation of radicals[19,21,201,202]. Due to their longer lifetimes and relatively high energies, metastables could be the main driver of precursor activation and radical formation. Bardos studied the use of the afterglow to promote thin film deposition[176]. In the afterglow region, the density of ions and electrons is very low while the concentration of metastables and long-lived radicals is high. He states that, in this region, chemical reactions are enhanced by plasma metastables. Using SiH_4 as precursor, he indicated that the interaction with plasma metastables leads to the formation of SiH_x and H[176,203]. The same pathway was observed by Kono et al.[168] using an Ar or Xe as the working gas through the following reaction:

$$SiH_4 + Ar/Xe^* \rightarrow SiH_2 + (H_2 \text{ or } 2H) + Ar/Xe$$

Another possible mechanism was introduced by Schaefer et al.[204], who considered the formation of precursor ions fundamental for film formation. Precursor ions, like precursor radicals, can be formed by electron impact, or most likely through Penning ionization. The latter comprises the impact of two or more neutral species, one of them being a metastable in the following manner[18]

$$N_2^m + X \rightarrow N_2 + X^+ + e$$

With N_2^m being N_2 metastables, X the precursor, and e the electron. However, Penning ionization process happens when the energy of the metastable is higher than the ionization potential of the target molecule. In general, this process is more common when using more energetic gases, such as He or Ar. Yet, it can also work for N_2 gas for molecules presenting lower ionization potentials. For these reactions to occur, metastable species must possess sufficient internal energy to dissociate chemical bonds and be present in high concentrations. The higher their density, the greater the likelihood of collisions with precursor molecules. Metastables concentration in the plasma is tightly regulated by their destruction rate, particularly through quenching by ambient air contaminants such as O_2 and H_2O. Electrons, ions or other excited species, if present in high concentrations, should provide a similar pathway for radical formation.

Guruvenket et al.[205] investigated various Si-rich monomers for the deposition of SiCN thin films using a dielectric barrier discharge (DBD) system, focusing on the interactions occurring in the afterglow region. Their findings highlighted that thin film formation primarily occurred through radical-induced reactions, with nitrogen (N) radicals playing a key role in initiating the precursor fragmentation. In particular, the N radicals were believed to dissociate the weakest bonds within the precursor molecules. Notably, only precursors containing the Si–H bond (bond dissociation energy ~3.2 eV) resulted in successful film formation, while those featuring stronger Si–C (~4.5 eV) or Si–O (~8.3 eV)[206] bonds failed to produce Si radicals. Cui et al.[207] compared multiple Si-based precursors for silica film deposition on PMMA substrates using a He/O_2 plasma. He correlated deposition efficiency with the bond dissociation energies of functional groups bonded to Si. Precursors with weaker bonds enabled faster deposition due to easier fragmentation and radical formation. Moreover, the increase of precursor delivery temperature led to higher deposition rates, likely due to reduced energy losses during vaporization. This emphasized the importance of precursor chemical structure and bond strength in plasma-assisted deposition processes. Complementary findings have been reported in several other studies. Fakhouri et al.[178] used a plasma jet system to deposit TiO_2 thin films from *titanium tetra iso-propoxide* (TTIP) precursors. Using optical emission spectroscopy (OES) technique, they observed that plasma species, specifically the NO and NO_2 continuum, were quenched in the presence of the precursor. This suggested active consumption of these excited species for precursor dissociation. Johnson et al.[208] proposed a similar mechanism for the synthesis of *aluminum zinc oxides* (AZO), in which OH and H radicals triggered the cleavage of metal–oxygen bonds, leading to an intermediate hydroxide phase prior to its thermal conversion into an oxide. Finally, Hodgkinson et al.[184] observed that raising the plasma power improved the stoichiometry of TiO_x films. The increased power, as discussed by Alexandrov[209], elevated both the concentration and energy of excited species, promoting stronger precursor fragmentation and enhancing the availability of reactive Ti sites for oxygen incorporation. Overall, the most likely pathway for initiating chemical reactions in plasma-assisted processes involves at least the partial dissociation of the precursor in the gas phase. For this to occur efficiently, the plasma species must possess internal energies that exceed the bond dissociation energy of the precursor, ensuring sufficient energy transfer to break the targeted bonds.

2.6.4. Powder formation

Under certain conditions, however, excessive radical formation and high precursor concentrations can lead to powder formation instead of thin films. As discussed by Massines et al.[18], powder nucleation in atmospheric pressure PECVD likely follows mechanisms similar to those observed at low pressure, involving either negative ion accumulation or radical–radical recombination. These scenarios typically occur when large amounts of highly reactive species interact with high precursor flow rates, resulting in uncontrolled nucleation in the gas phase.

Importantly, powder formation is not directly linked to the presence of highly energetic plasma species. This is primarily due to energy conservation constraints: excited species generally possess very few internal degrees of freedom, making energy-balanced recombination reactions with other species highly improbable[167]. As a result, gas-phase reactions often require three-body collisions to conserve energy—conditions rarely met through binary interactions alone. In contrast, radicals possess more degrees of freedom and are thus more reactive. This distinction also helps explain why most effective reactions occur at the gas–surface interface. In this context, the substrate acts as a third body, enabling energy dissipation and supporting reaction equilibrium, thereby playing a crucial role in film growth.

Avoiding powder formation therefore requires careful tuning of both plasma and precursor parameters, with particular attention to limit radical production. Strategies include lowering the precursor's reactivity, reducing its flow rate, diluting it with carrier gas, or pulsing the plasma to decrease residence time and radical density. For instance, Chemin et al. deposited TiO_2 nanoparticles in a SiO_2 matrix by varying the injection of the TTIP and HMDSO precursors, respectively. The TTIP precursor was injected closer to the arc formation, thereby exposing the precursor to more energetic species and increasing the formation of radicals. The residence time of the molecules increases their probability of nucleating the particles. On the other hand, HMDSO was injected further downstream, reducing the formation of radicals and their residence time. Another effective approach involves using aerosols to moderate precursor exposure and reduce excessive fragmentation[210]. Controlling the injection point, as shown by Merche et al.[19], is also key to limiting powder formation by avoiding early precursor decomposition in the discharge region.

2.6.5. Oxidation (Thin film and contaminants)

Finally, the thin film formation in the gas-surface interface involves chemical reactions for the growth of the film and elimination of residual compounds. Since the goal is to produce an oxide, we will focus on oxidation processes. Merche et al.[19] stated that O_2 presence in the plasma gas phase is fundamental for producing high quality films. This is true even for precursors that possess oxygen already bonded to the metal centre. The O_2 addition to the plasma gas phase leads to the formation of excited oxygen species, i.e., O_2^*, O^*. He suggests that excited oxygen species facilitate reaching stoichiometric oxides and removing carbonaceous contaminants.

Cui et al.[207] results suggest the same behaviour. By varying the precursor injection rate, he increased the formation of precursor radicals, without varying the density of excited species. He noticed an increase in carbon contamination suggesting that insufficient oxygen reactive species were present in the gas phase. Consequently, not enough reactive oxygen species were available to oxidize the carbon groups. Reuter et al.[211] suggested that carbon removal happens mainly in the substrate surface[18]. He showed, by increasing the O_2 content in the discharge gas, that oxygen reactive species reduce the concentration of carbon impurities. No benefit was observed after an O_2/HMDSO ratio threshold was reached.

Starostine et al.[212] stated that atomic oxygen radicals or excited oxygen molecules are necessary to produce pure SiO_2 films. He evaluated the evolution of the chemical composition by increasing the oxygen content in the discharge. With 0% O_2 in the discharge, the thin film kept the organic character of HMDSO precursor. As the O_2 content increases (> 2%), the thin film progressively gains the inorganic SiO_2 character with concomitantly decreasing carbon moieties. Similarly, Morent et al.[213] conducted experiments using pure Ar and Ar/air as plasma gas. Using pure Ar, high retention of the organic groups was observed while the very low carbon content remains by using the Ar/air mixture. These results highlight the importance of reactive oxygen to elimination of undesired compounds. Ghobeira et al.[194] observed the incorporation of N to the thin films for a pure N_2 plasma. Upon O_2 addition, a steep decrease of N was observed. He related the O_2 addition to the quenching of very energetic N_2 species, decreasing thus their chance being incorporated to the surface.

Although overlooked in thin film deposition studies, oxygen-rich species, particularly reactive oxygen and nitrogen species (RONS) like NO and OH, play a critical role in contaminant degradation. According to Brisset et al.[170], these species possess high oxidizing power and are key in converting hydrocarbons into CO_x compounds, which could be also envisaged for carbon content reduction in thin films.

Overall, the nature of the resulting film (organic or inorganic) relies heavily on the plasma parameters, such as energy input, precursor chemistry, and oxygen availability. The presence of oxygen reactive species is important to reach an inorganic character. However, in case of low precursor reactivity or low energy plasmas the organic precursor will not be fully converted[204,214]. This retention of organic character is directly related to the decrease in radical formation. Sawada et al.[215] investigated the influence of plasma gas temperature on the production of thin films. Higher gas temperatures led to purer inorganic coatings due to enhancing chemical reactions and favouring the elimination of carbonaceous products via volatilisation of these compounds. Increasing the substrate heating temperature showed the same behaviour elsewhere[208].

Moreover, the plasma temperature may induce the crystallization of the thin films, observed in TiO2 nanotubes[216] and SiO2 nanoparticles[217]. Using a different approach, Huerta et al.[164] produce crystalline $SrTiO_3$ perovskites. The crystallization was induced by a heating plate placed below the substrate.

2.6.6. Growth rate increase

Deposition rate and powder formation often exhibit an inverse correlation, as shown by Massines et al.[18], particularly in atmospheric pressure PECVD processes. The main parameters are related to i) precursor, ii) transport and iii) power. Generally, increasing the precursor reactivity, concentration or injection rates leads to increased growth rates. For instance, Cui et al.[207] demonstrated that increasing the precursor injection rate leads to a higher deposition rate. However, this increase translated in a proportional rise in carbon content and film porosity. This trade-off is largely attributed to the imbalance between the number of reactive species and the number of precursor molecules in the plasma phase. When the precursor density approaches the availability of reactive oxygen species, not all precursor molecules can be fully oxidized or incorporated effectively into the film[207].

This scenario is analogous to the Yazuda mechanism[218], originally proposed for low-pressure PECVD, which relates the energy input to the precursor concentration. At moderate energy-to-precursor ratios, the increased energy facilitates fragmentation and radical formation, thereby boosting the deposition rate through efficient gas-phase activation and surface reactions. However, beyond a critical ratio, excessive radical production or precursor density may lead to increased recombination in the gas phase. Otherwise, insufficient power will retain organic features.

2.7. Choice of precursor

Generally, precursor choice is fundamental for reaching high deposition rates and high-quality thin films. For instance, vaporisation temperature will define the amount of energy that should be provided to the precursor to vaporise it. The vapor pressure relates to the reactivity of the compound. Another important aspect is the toxicity of the compounds. As the process happens at atmospheric pressure, it is preferred to work with safer alternatives. Widely used in AP-PECVD are organometallic and metalorganic precursors designed for SiO_2 and TiO_2 deposition. They are generally in liquid form, relatively safe to manipulate, have high vapor pressure and low boiling points making them ideal for being sprayed or vaporized into the reactor. On the other hand, Cobalt precursors are less widespread. Most of the alternatives are very toxic or in solid form, or both.

Table I.6 lists a few options that were used for Co-oxide deposition using generally low-pressure systems. Cobalt carbonyl and cobaltous nitrate have lower vaporisation temperatures but are toxic and require careful manipulation. $Co(acac)_2$ is a variation of $Co(acac)_3$ compound. Although possessing lower vaporisation temperature, it is still solid at room temperature. Kouotou et al. use liquid solutions of $Co(acac)_2$ and $Co(acac)_3$ compounds[183]. Using ethanol as the solvent, low chemical stability was observed for the former, with the Co^{2+} cation converting to Co^{3+} in the matter of days.

As discussed previously, one of the mechanisms leading to thin film deposition happens through the precursor fragmentation. $Co(acac)_3$ and $Co(thmd)_3$ have similar structures with the Cobalt metallic centre surrounded by 6 O atoms. Thus, similar fragmentation energies would be required to activate the precursor. However, the $Co(acac)_3$ structure is considerably smaller than $Co(tmhd)_3$ and possesses less carbon. In order to avoid unwanted carbon impurities, the $Co(acac)_3$ precursor was chosen for the thin film depositions.

Table I. 6 – Main Co-based precursors observed in the literature.

Precursor	Vaporisation temperature	Decomposition temperature	Toxicity	Physical state	Chemical stability
$Co(acac)_3$[219,220]	~180°C	220-300°C	Medium	Solid	High
$Co(acac)_2$[219,220]	~170°C	200-280°C	High	Solid	Moderate
$Co(tmhd)_3$[221]	~200°C	250-350°C	Low	Solid	High
$Co_2(CO)_8$[222]	~60°C	100-150°C	High	Solid	Poor (pyrophoric)
$Co(NO_3)_3$[223]	~120°C	250-300°C	High	Solid	Poor

3. Summary and Strategy

From a literature review (Chapter I), it is shown that ferritic stainless steel interconnects of Solid Oxide Cell oxidize at high operating temperatures, forming Cr_2O_3 and Cr–Mn spinel oxides. These compounds exhibit poor electrical conductivity and may further react with the oxidizing atmosphere, producing volatile chromium species. To mitigate this degradation, tailor-made ferritic stainless steel alloys have been developed to enhance oxidation resistance. However, even these advanced alloys show limited long-term stability due to continuous chromium evaporation and oxide spallation.

To overcome these limitations and ensure a lifetime of at least 40,000 h (*ca.* 4.5 years), protective coatings have been extensively studied. Such coatings not only hinder chromium volatilization but also enable the use of more economical ferritic stainless steel alloys, such as AISI 441, which was selected for this work. Among the most effective are Co–Mn-based spinels, typically synthesized by various deposition techniques (*e.g.*, PVD, slurry deposition and electrophoretic deposition (EPD)). The literature highlights that coating density is crucial to enhance oxidation protection. However, conventional cost-effective methods (*e.g.*, slurry deposition, EPD) generally require additional high-temperature reduction (H_2) and oxidation steps to achieve dense coatings.

In this context, the present PhD work explores an alternative process, namely Atmospheric Pressure Plasma Enhanced Chemical Vapour Deposition (AP-PECVD), for producing thin Co_3O_4 protective coatings. From literature review, the fundamentals of AP-PECVD and the influence of plasma parameters on film properties were also discussed in a second part of Chapter I.

In this PhD work, the objective was to understand the AP-PECVD conditions enabling the formation of stoichiometric, dense Co_3O_4 coatings with minimal residual impurities. To reach such properties, it is crucial to study the plasma-precursor interactions, which are mainly dependent on the energy of plasma species, on the plasma chemistry and surface temperature. Therefore, the AP-PECVD device and precursor injection configuration are studied, and the influence of O_2 concentration, deposition atmosphere, and substrate temperature were systematically investigated (Chapter III). Two deposition strategies are explored: one with low displacement speed and few scans, and another with tenfold higher speed and multiple scans, and their impact on coating homogeneity assessed. The performance of the coatings is then evaluated under SOEC operating conditions (700 – 850 °C). Previous studies reported that Mn diffuses from the AISI 441 alloy substrate, inducing the formation of a protective Co–Mn spinel during oxidation. A similar mechanism is anticipated here for the synthesized Co_3O_4 coatings, with coating thickness expected to influence the resulting spinel stoichiometry. As high Mn/Co concentration ratios have been linked to inferior Cr-barrier properties in literature, the oxidation performance of various Co_3O_4 coating thicknesses (400–2000 nm) is investigated.

The Co_3O_4 coating microstructure, chemistry, and crystallinity are characterized by complementary techniques (detailed in Chapter II). The protective efficiency of Co_3O_4 coated AISI 441 substrates is assessed in terms of oxidation kinetics and chromium evaporation (Chapter IV) and in terms of electrical performance (Chapter V), then compared to uncoated AISI 441 substrate. The experiments, designed to replicate SOEC operating conditions, enable *in-situ* monitoring of oxidation and ASR evolution with temperature and time.

Chapter II - Experimental section

1. Substrates

In this work, the AISI 441, a ferritic chromium stainless steel, was chosen as the interconnect material. Table II.1 shows the composition of the as-received AISI 441 substrates, characterised by glow discharge mass spectrometry by the manufacturer (APERAM). The stainless steel samples were received as 200 µm thin plates and cut using a guillotine to the desired measurements. The AISI 441 substrates dimensions varied with the targeted functional experiment are shown in Figure II.1, and are described as follows:

1. 10 mm x 20 mm coupons with a 1.8 mm-diameter hole to hang the sample for thermogravimetric experiments.
2. 10 mm x 20 mm or 20 mm x 20 mm coupons for short and long-term oxidation experiments.
3. 15 mm x 20 mm coupons for Cr vaporization experiments.
4. 13 mm diameter disk-shaped samples with a rectangular strip (8 mm x 2 mm) on which was welded a AISI 440 wire for Area Specific Resistance (ASR) measurements.
5. 8 mm x 20 mm coupons for experiment in isotopic O_2.

The substrates were used as-received in all cases, without any thermal treatment, additional polishing nor cleaning. The plasma species available during the deposition process can eliminate impurities, e.g. atmospheric contamination, that may have adhered to the surface prior to the deposition experiment.

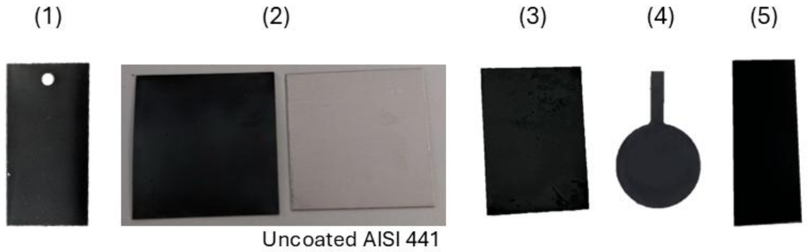

Figure II. 1 – Photos of the coated samples with different dimensions (described above) for each experiment. An uncoated sample is given for comparison.

Additionally, Si (100) wafers (Siegert wafer GmbH) were used as substrates to enable a comprehensive physico-chemical characterisation of the thin films. Indeed, Si wafers possess attractive characteristics for the study of coatings, such as low surface roughness, analytical compatibility and a good and stable reference for other studies.

*Table II. 1 - AISI 441 chemical composition from GDMS analysis in %wt. * :the carbon concentration was measured by combustion analysis coupled with infrared detection.*

Cr	Mn	Si	Nb	Ti	Ni + Mo	C*	Fe
17.61	0.25	0.45	0.44	0.12	0.17	0.014	Bal.

2. AP-PECVD setup

Figure II.2 presents a schematic of the AP-PECVD setup, which operates using a blown arc discharge system, commonly referred to as a plasma jet (ULS Omega) and supplied by AcXys Technologies. In this configuration, the N_2 plasma is generated by igniting an electric arc between an internal high-voltage electrode (*b*) and an external grounded electrode (*c*) which are driven by a sinusoidal (100 kHz) high-voltage power supply (1000 W). To maintain a stable arc, a 50 L·min^{-1} N_2 flow (*a*) is introduced to create a vortex between the electrodes. This vortex motion makes the arc rotate around the internal electrode and be expelled through the outlet nozzle.

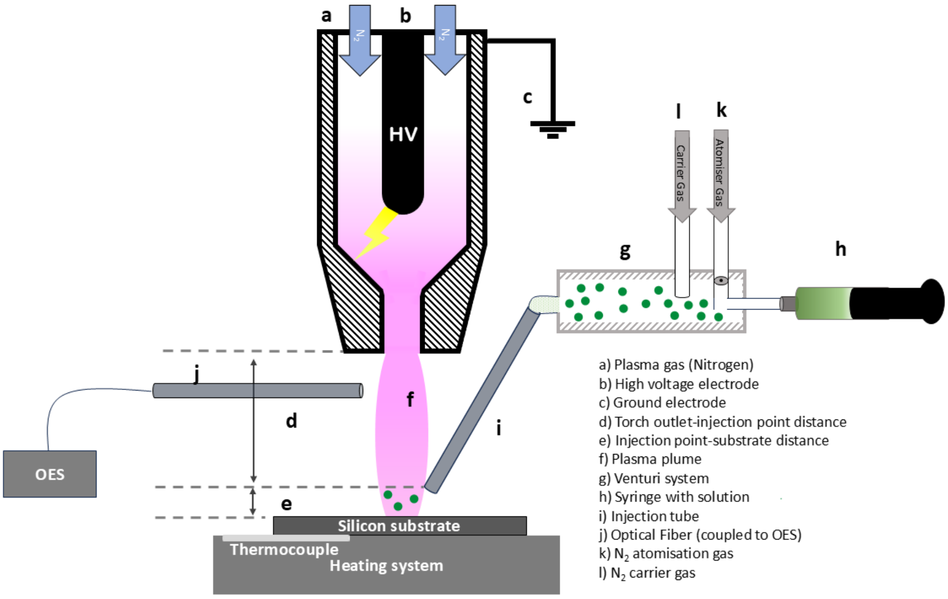

Figure II. 2 - AP-PECVD schematic illustration describing the configuration system.

The solution within the syringe (h), which contains a cobalt precursor and a solvent, is injected with a rate of 400 μL·min^{-1} in the plasma region (f) as an aerosol. This aerosol was produced by a Venturi atomizing system (g). The atomization consists of a N_2 flow (l) (2 L·min^{-1}) that is forced through a 300 μm constriction generating a high-speed gas flow. This gas flow breaks the precursor solution into micrometre sized droplets, which range from 1 to 5 μm). These droplets are then conducted to the plasma afterglow region via a 1/8 in. tube (*i*), using a carrier gas (k) flow of 2 L·min^{-1} (N_2 and/or O_2), which sum up for a 4 L·min^{-1} total gas flow injected in the tube (i) and fed to the post-discharge region (f). The tube's outlet remains at distance (*e)* to the substrate, whereas the plasma nozzle outlet is located at a distance (*d)* above the injection tube outlet. The plasma jet is coupled to a 6-axes robotic arm from FANUC (Figure II.3) that displaces at a constant linear speed over the substrate. Various plasma nozzle outlet and injection tube outlet distances (*d)* (15-40 mm), the displacement speeds (0.05–5 mm·s^{-1}) and number of scans (1-200) were studied as deposition parameters.

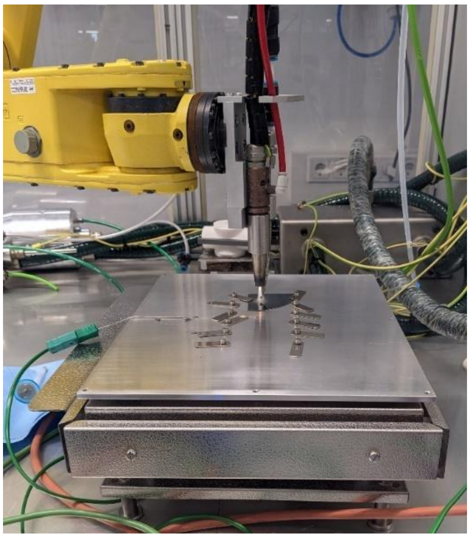

Figure II. 3 - Plasma jet connected to the 6-axes robotic arm.

For all the experiments performed in chapter III, Si wafers (100) were used as substrates. The wafers were positioned onto a heating plate and a thermocouple fixed on their backside to determine their temperature. However, the accuracy of the temperature measurement made from these thermocouples may be affected by a poor contact between the substrate and thermocouple. Therefore, to measure precisely the temperature, trials in which plasma was directly applied onto the thermocouple were performed, reducing possible heat losses that might occur from air gaps between substrate and thermocouple. In addition, to improve thermal conductivity and ensure accurate readings, the thermocouple was wrapped by Cu foil.

For the experiments from chapter IV and V, Ferritic Stainless Steel (FSS) substrates (AISI 441) were used. To hold the substrates under the plasma flow (50 L·min^{-1}) and ensure a complete coverage of the substrate surface, Sm-Co magnets (from Magsy), which have high thermal resistance (~300 °C), were used. A stainless steel plate was placed below the substrate support in which 5 holes were made to accommodate the magnets, and a Si wafer was place between the substrate and the support to avoid direct contact between sample and the magnets (Figure II.4).

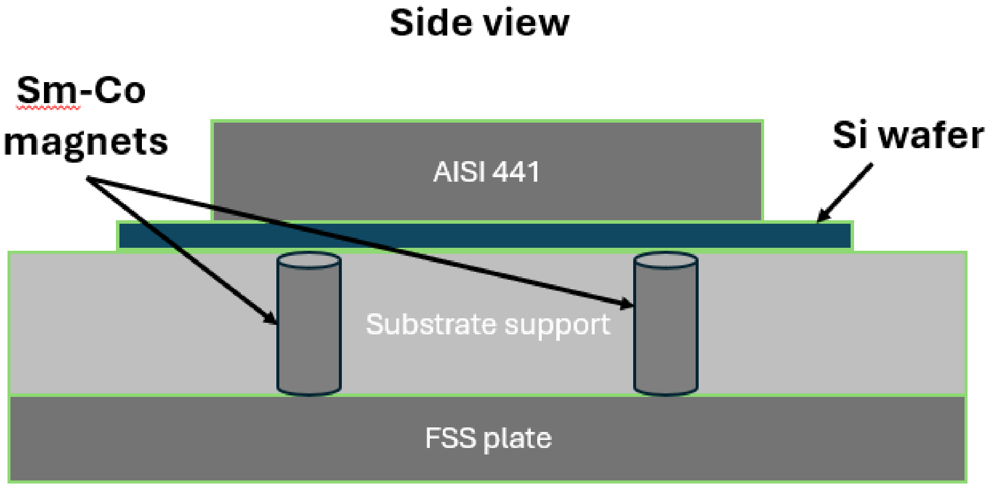

Figure II. 4 - Schematic of the AISI 441 substrates support to hold the samples during deposition.

2.1. Precursor solution preparation

Precursor solutions were prepared from solid cobalt-based compounds, Co(acac)$_2$ and Co(acac)$_3$, which were dissolved in various solvents: water, ethanol, acetone, and isopropanol. To assess solubility, a fixed solvent volume (100 mL) was used while gradually adding the solid precursor until the solubility limit was reached. Each solution was then placed in an ultrasonic bath for 15 minutes to ensure homogeneity.

Solution stability was evaluated after 48 hours settling. All Co(acac)$_2$ solutions showed poor stability, varying the colour from pink to green. Such behaviour was previously reported by Kouotou et al.[183], which attributed this colour change to the oxidation state variation of Co (from 2+ to 3+). In contrast, Co(acac)$_3$ demonstrated better overall solubility and stability, although it remained poorly soluble in water. Isopropanol solutions of Co(acac)$_3$ also exhibited precipitation upon aging. To minimize the risk of precipitation during deposition experiments, all working solutions were prepared at concentrations at least three times lower than their respective solubility limits, ensuring adequate long-term stability.

2.2. Influence of the surrounding gas environment

We have investigated the influence of the surrounding gas environment on the AP-PECVD reaction through an experiment in controlled conditions, N_2 atmosphere. The plasma jet was placed inside an acrylic box of 50×50×50 cm^3. The experiment was performed in static conditions since the robot could not be placed inside the box. Figure II.5 shows the experimental setup for the experiment performed under controlled atmosphere. An O_2 detector was placed inside the box to measure the O_2 concentration. Prior to performing the deposition, a 50 $L\cdot min^{-1}$ flow of N_2 was purged onto the acrylic box until reaching an O_2 concentration below 0.1%. Importantly, during the experiment, no O_2 was added to the carrier, atomizing or dilution gas. Furthermore, no supplementary substrate heating was used. A thermocouple was added to follow the temperature on the substrate during the experiment.

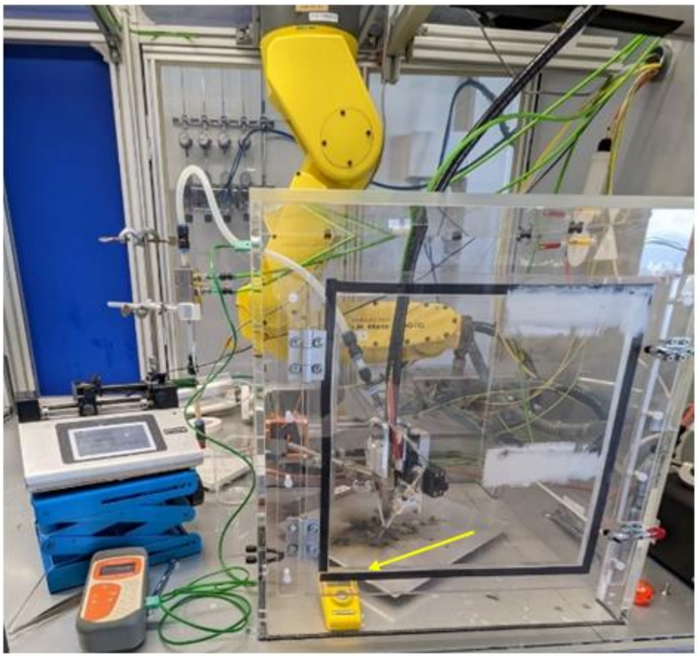

Figure II. 5 - Experimental setup for the test under inert N_2 atmosphere. The plasma jet was placed in an acrylic box. The O_2 detector was placed inside the box to measure the O_2 concentration (yellow arrow). Prior to performing the deposition, N_2 was purged to ensure low O_2 concentration.

2.3. Plasma characterisation

Optical Emission Spectroscopy (OES) measurements were performed in the absence of substrate to i) obtain an estimation of the plasma gas temperature at multiple points and ii) to describe the evolution of radiative species in the plasma afterglow region.

OES measurements were carried out using a spectrometer SpectraPro-2500i from Princeton Instruments, using an optical fibre fitted with a collimator and connected to the spectrometer with a 50 mm focus (a stainless-steel tube was used to guide and focus the measurement) and using a grating of 300 lines mm^{-1} blazed at 500 nm were used for its measurements. The spectra at different distances were used to simulate the plasma gas temperature. The software LIFBASE enables the simulation of the rotational temperature (plasma gas temperature) using a Boltzmann plot[224]. The software calculates a spectrum based on the conditions set on the experiment (pressure, resolution of the spectra) for different radiative species. NO (B-X) was chosen here since it was the solely compound present in all spectra. The simulated spectrum was superposed by the experimental spectrum, and the temperature varied (Figure II.6). It is important to note that these values are approximations, and no fitting was performed.

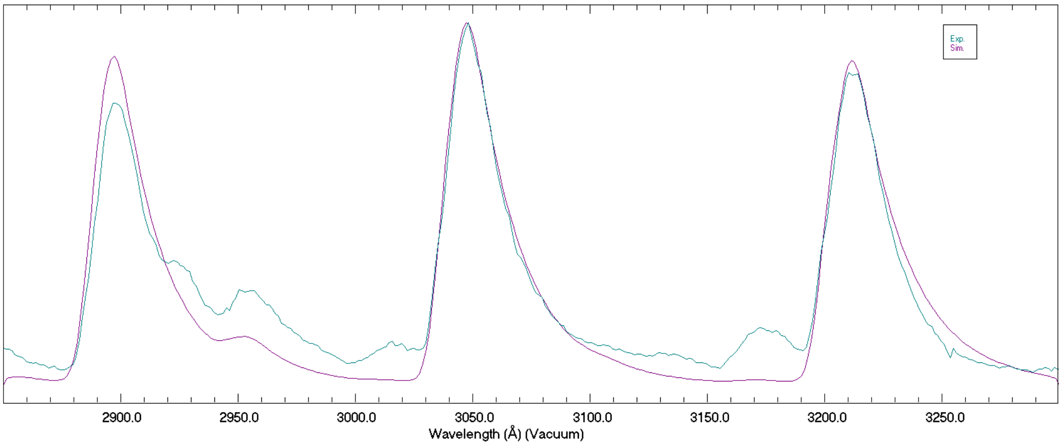

Figure II. 6 - OES spectra of (Exp.) the real experiment in light green and (Sim.) the simulated spectrum from the LIFBASE software. The simulated spectrum considers only the NO species, thus the slight difference between spectra.

The temperature and radiative species were evaluated at the plasma nozzle exit, +10 mm, +15 mm, and +20 mm. The temperature profile from the LIFBASE simulations was compared with thermocouple measurements, obtained from a wider range (7.5 to 60 mm). To enhance thermal conductivity, and increase the measurement area, a copper foil was wrapped around the end of the thermocouple. After the plasma ignition, there was a rapid temperature increase until its stabilization after a few seconds.

The plasma interaction with precursor, carrier gas and solvent were investigated by placing the optical fibre right below the precursor injection point (~17 mm). The emission spectrum of plasma alone was first recorded, followed by measurements after introducing the carrier gas, solvent and precursor. This sequential approach, plasma alone ➔ plasma-precursor interaction, avoid variations from the environment conditions.

3. Oxidation experiments

The Co_3O_4 coated stainless steel (AISI 441) substrates were exposed to an oxidizing environment to evaluate their oxidation and electric performance. The samples were compared to bare AISI 441 substrate in all cases. The oxidation experiments were performed to evaluate:

- The oxidation kinetics of the samples (thermogravimetric experiments).
- The evolution of the chemical composition of the surface with time (short and long-term annealing experiments).
- The Cr-evaporation rate.
- The electrical performance determined from the area-specific resistance (ASR).
- The isotopic $^{16}O_2/^{18}O_2$ experiment.

These experiments are described in detail in the next sections.

3.1. Thermogravimetric experiments

The oxidation kinetics was evaluated using a SETARAM TGA24 16 thermobalance. During the experiments, a constant synthetic dry air flow of 2 $L \cdot h^{-1}$ at 1 $mm \cdot s^{-1}$ was used to mimic the operating conditions of the O_2 electrode. The experiment consists of a constant measurement of the weight variation of the sample with a resolution of 5 µg (corresponding to ~ 0.00125 $mg \cdot cm^{-2}$ with samples measuring 10 x 20 x 0.2 mm^3). The samples had a small hole by which they were hanged on a Pt support. The measurement follows solely the mass gain profile in the isotherm. The mass gain prior to reaching the isotherm is not considered due to the evolution of the buoyancy effect during heating and cooling which induces mass evolution[11,83].

The mass variation corresponds to the incorporation of oxygen by the formation of the oxide (weight gain) scale, described in R1 and R2, and by the volatilisation of chromium species (weight loss), highlighted in R3. If the Cr_2O_3 formation is predominant, a parabolic behaviour is expected while paralinear behaviour is expected if R3 is more pronounced. By integrating the mass gain over time, using Wagner's law (R4)[54,55], it is possible to determine the oxidation kinetics. Figure I.7 describes the different kinetic behaviours during oxidation. This experiment enables the evaluation of the influence of the Co_3O_4 coating on the oxidation growth.

$$Mn_{(s)} + {}^{1}\!/_{2}\, O_{2\ (g)} \rightarrow MnO_{\ (s)} \qquad \text{(R1)}$$

$$2\ Cr_{(s)} + {}^{3}\!/_{2}\, O_{2\ (g)} \rightarrow Cr_2O_{3\ (s)} \qquad \text{(R2)}$$

$$2\ Cr_2O_{3\ (s)} + {}^{3}\!/_{2}\, O_{2\ (g)} \rightarrow 2\ CrO_{3\ (g)} \qquad \text{(R3)}$$

$$\Delta m/_{A}{}^{2} = K_p \times t + C \qquad \text{(R4)}$$

Where $\Delta m/_{A}$ represents the variation of mass per unit area ($mg{\cdot}cm^{-2}$), K_p is the parabolic rate constant, and t is the time in seconds, and C is an integration constant. K_p is generally calculated from the plot $\Delta m/_{A}{}^{2}$ vs time. In the present work, the experiments were performed between 200 and 500 hours at 800 °C for the coated and uncoated samples. Additional experiments using an extra 50 µm thick coating layer of Lanthanum Strontium Manganate (LSM), used typically as contact layer material, were performed at 700, 800, and 850 °C. LSM was applied on the surface by thermopressing at CEA/LITEN (Grenoble).

3.2. Isothermal oxidation experiments

The samples were evaluated in function of time to observe the chemical evolution of the coated and uncoated sample during oxidation. Only one side of the substrates was coated for the coated samples. 10 x 20 x 0.2 mm^3 coupons were placed in a muffle furnace (Nabertherm LHT 08/17 BO) and heated up to 850 °C at 1 $°C{\cdot}min^{-1}$ using static laboratory air. The annealing time varied between 1 and 120 hours followed by a cooling down at a rate of 1 $°C{\cdot}min^{-1}$. Samples were weighed before and after the experiment using a Sartorius ME36S microbalance (resolution: 1 µg) to determine the mass gain/oxidation rate of the samples. Additionally, fully Co_3O_4 coated AISI 441 substrates of 20 x 20 x 0.2 mm^3 were placed in a vertical muffle furnace at 800 °C for 2500 and 5000 hours using laboratory air. In both experiments, the relative humidity was not controlled nor measured.

3.3. Cr-evaporation measurements

Coated and uncoated AISI 441 stainless steel samples (15 × 20 × 0.2 mm^3) were examined in this experiment. The samples were exposed to static laboratory air at 800 °C for 2000 hours in a vertical furnace (Figure II.7a). They were placed in a quartz crucible and supported at four points by the crucible itself to prevent direct contact with the retention powder.

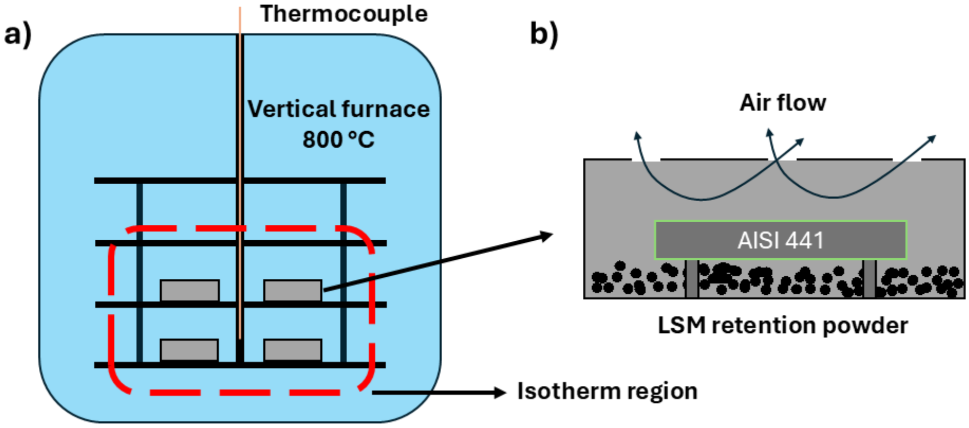

Figure II. 7 - Schematic illustration of the Cr-evaporation experiments. The furnace is shown in a) in which the isotherm region is highlighted by the red dotted square. The quartz crucibles (b) containing the substrates are positioned in the isotherm. The samples are placed inside the quartz crucible above four support points to avoid direct contact with the LSM powder. Holes were performed on top of the box to maintain a constant air flow [Adapted from Dejob[16]].

To capture volatile species emitted during annealing, 0.3 g of lanthanum strontium manganite (LSM) powder (from NEYCO) was selected as retention powder. The crucible lid was perforated at four points to allow a steady flow of ambient air inside the box (Figure II.7b). Figure II.8 shows the quartz crucible alone (a), with LSM powder (b), and with the substrate above (c). This experiment focused on the volatilization of chromium species (CrO_3 or $CrO_2(OH)_2$), which were subsequently trapped in the LSM powder. While this setup does not capture all volatilized species, as reported in previous studies[16,83], it enables a comparative assessment between several samples. Moreover, the masses of both the samples and the LSM powder were recorded before and after the annealing process.

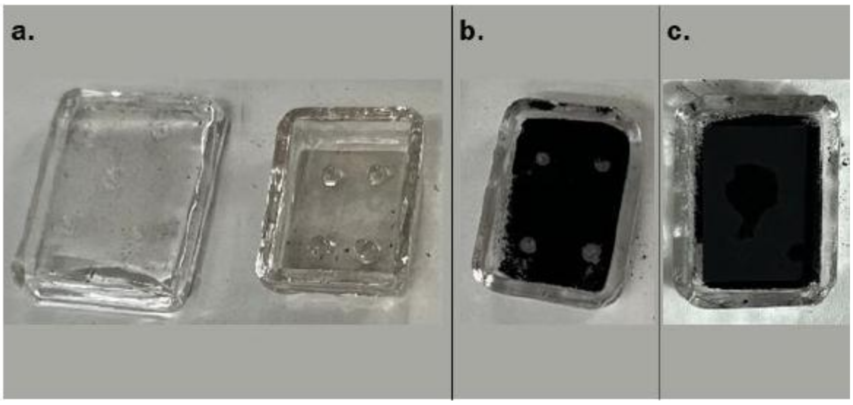

Figure II. 8 - a) Quartz crucible for the Cr-evaporation experiment. b) Crucible filled with LSM powder. c) Crucible filled with LSM powder and coated AISI 441 substrate.

After the annealing process, the samples were removed from the furnace, and the retention powder was carefully collected for analysis. The concentrations of chromium (Cr) and cobalt (Co) retained in the lanthanum strontium manganite (LSM) powder were quantified using Inductively Coupled Plasma–Optical Emission Spectrometry (ICP-OES).

The analytical procedure involved:

1. The complete dissolution of the LSM powder. The powder was dissolved using a mixture of 15 mL of concentrated nitric acid (HNO_3, 68%) and 5 mL of concentrated hydrochloric acid (HCl, 37%). In case of incomplete dissolution, additional 5 mL of the concentrated solution were added to the mixture. To ensure complete dissolution, the mixture was heated on a hot plate at 90 °C for 24 hours. Once the total dissolution was confirmed, the first dilution masses were recorded, and the mixture defined as solution 1.
2. Following this step, approximately 1.5 g was taken from solution 1, and diluted using distilled water. This dilution step was performed to lower HNO_3 concentration. Keeping a value close to 2 vol.% HNO_3 is critical to avoid matrix effects during the ICP-OES measurements. The obtained second dilution is called solution 2. The total mass of the solutions was recorded to enable precise dilution calculations.
3. Chromium and Cobalt solution (1000 ppm in a 2% HNO_3 solution) from Merck (99% purity) were used as standards. The reference solutions were prepared by diluting the standards in 2% HNO_3. Solutions with concentrations from 0.5 to 10 ppm of each element were produced for the calibration of the equipment. All samples and standards were analysed within the same analytical session to ensure consistency.
4. The wavelengths selected for the ICP-OES analysis were 283.563 nm and 230.786 nm for Cr and Co, respectively. They were chosen for having the strongest

intensity peaks. The calibration standards were used to establish a calibration curve through a linear regression based on the intensity (y) vs known concentration (x), shown in Figure II.9. The elemental concentrations were obtained from these linear regression equations. By using the recorded masses from solutions 1 and 2, it was possible to obtain the dilution factors (DF). The DFs were used to obtain the final concentrations of Cr and Co in the retention powder alone. Results are expressed in function of the samples surface are (µg·cm^{-2}) of LSM powder, based on the initial powder mass determined during sample preparation. The total mass retained can be calculated by

$$Mass\ retained = C_{ICP-OES} \times DF \times m_{LSM} \qquad eq. II.1$$

Where $C_{ICP\text{-}OES}$ is the concentration of Cr or Co obtained from the ICP-OES measurements, DF is the dilution factor, and m_{LSM} is the LSM powder mass on the experiment. The concentration of chromium in the retention powder provides insight into the effectiveness of the coating in limiting Cr volatilization during high-temperature exposure. Co volatilization phenomenon was also checked. Finally, these values obtained can be converted to actual mass loss per area and compared to the mass gain by considering :

$$\Delta m/_{A} = \frac{mass\ retained}{A_{substrate}} \qquad eq. II.2$$

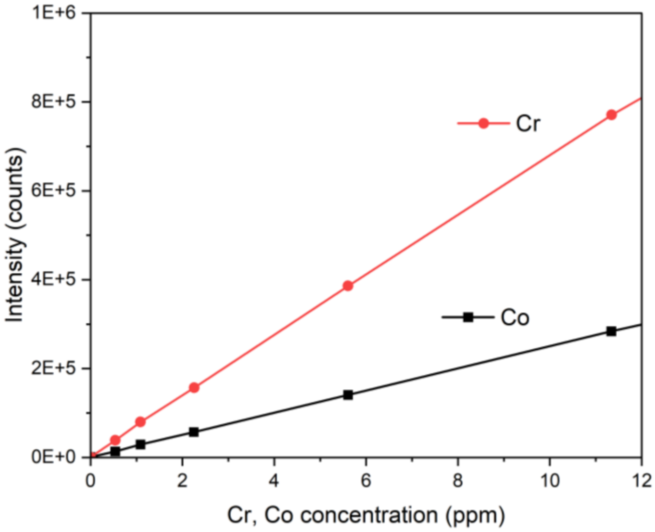

Figure II. 9 - Calibration curve of Co and Cr elements for the ICP-OES measurements.

3.4. Electrical measurements

Figure II.10a-c shows the geometry of the samples used for area-specific resistance (ASR) measurements. Each sample includes a 13 mm diameter region of interest (highlighted by a yellow dashed circle) and a narrow tab (8 mm × 2 mm) for electrical connections. This geometry matches the Pt electrodes used in the assembly. Coated and uncoated AISI 441 samples were prepared, with the coated ones featuring Co_3O_4 layers on both sides. All samples received a ~ 50 µm thick LSM contact layer on both sides, which was deposited by tape casting at CEA/LITEN, to improve electrical contact.

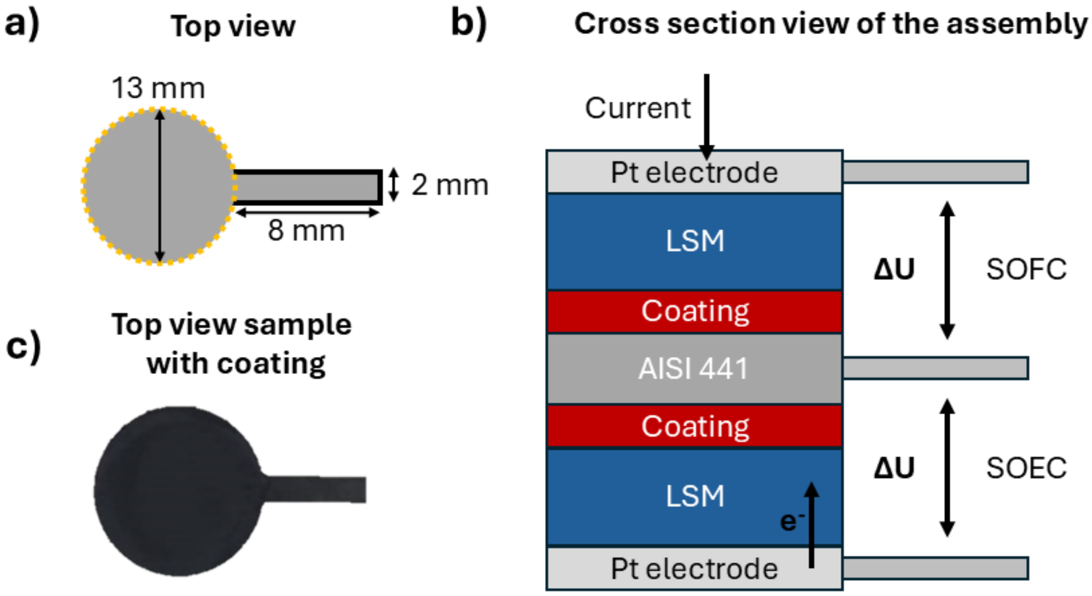

Figure II. 10 - Illustration of the ASR system showing a schematic of the ASR sample (a) with its dimensions where the region of interest is highlighted in yellow, and the coated ASR sample (c). b) indicates the cross-section of the ASR stack. The samples are placed in-between two Pt electrode, which have the same shape as the samples. The Co_3O_4 coating is present on both sides of the samples as the LSM (50 µm) coating. The voltage is measured in each one of the strips. The current flow determines the SOC mode.

Samples were assembled between two Pt plates in a sandwich configuration (Figure 9b). The voltages were measured in the Pt electrodes and AISI 441 samples through the tabs. Electrical connections were made using spot-welded ferritic stainless steel (AISI 430, NEYCO) wires attached to the Pt electrodes and AISI 441 tabs. These wires were insulated with flexible alumina fibre sleeves and alumina beads (72% Al_2O_3 / 28% silicate, Final Advanced Materials), then routed through rigid alumina tubes inserted into a Pyrex cover (Figure II.11b). The wires were connected to a DAQM901A multiplexer interfaced with a

Keysight DAQ970A data acquisition system. The first and last Pt electrodes were connected to a DC current source (MX100Q, Aim-TTI). Current direction was defined to distinguish SOEC (electrons from Pt to sample) and SOFC (electrons from sample to Pt) modes, enabling both configurations to be assessed within a single experiment. Prior to each run, I–V curves (0.1–1 A) were recorded to verify Ohmic behaviour and confirm the accuracy of resistance measurements. During experiments, a DC current of 0.5 A was applied, corresponding to a current density of ~ 0.4 A·cm^{-2}.

Proper densification and interfacial contact were achieved in situ: an initial thermal treatment at 850 °C for 1 hour was applied while maintaining a constant compressive force of 50 N using a 5 kg static load placed atop alumina rods (Figure II.11a,c). The sample stack was housed in a slotted quartz tube holder (Quartz Alliance) under a continuous 5 L·h^{-1} flow of synthetic air (Figure II.11c).

To simulate long-term operation under accelerated conditions, the ASR measurements were conducted at elevated temperatures. After the initial densification step at 850 °C, samples were exposed to successive isothermal holds: at 700 °C, 800 °C and 850 °C. Additional short-duration isothermal steps were performed during cooling to assess temperature-dependent ASR behaviour. The ASR dependence to the temperature is used to calculate the activation energy of the process, allowing the identification of the compounds driving the ASR values. The use of higher temperatures accelerates oxidation kinetics, effectively simulating longer exposure times within a shorter duration. This simulation is favourable if no new oxide scale composition is formed due to temperature higher than expected in SOEC) .

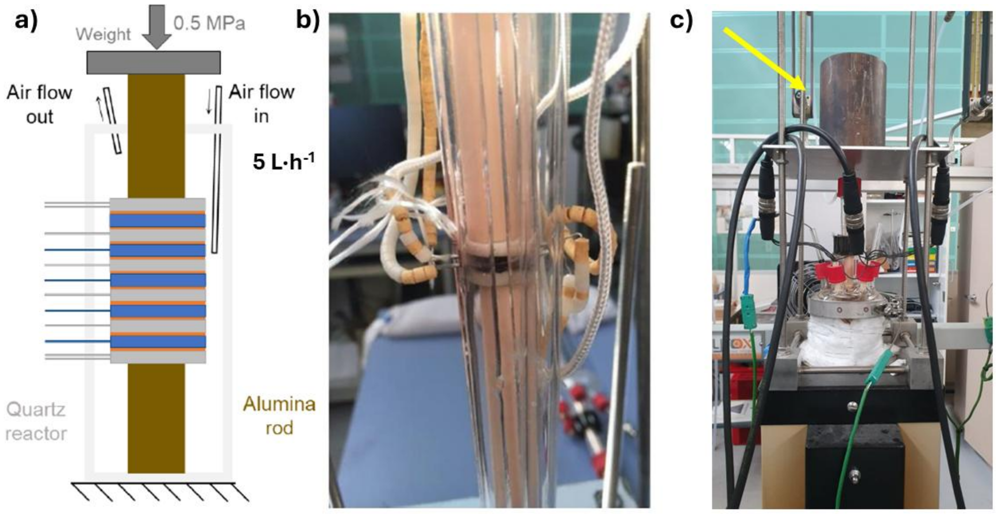

Figure II. 11 - Scheme of the ASR experiment (a) showing a stack with various samples and electrodes placed inside a reactor with a constant air flow. A 5 kg (0.5 MPa) weight was *placed above the reactor. b) Assembly of samples/Pt electrodes compressed between alumina rods in the tubular quartz sample holder. c) Setup before insertion into the quartz reactor. Yellow arrow indicates the 5 kg weight.*

3.5. $^{16}O/^{18}O$ experiments

AISI 441 samples measuring 8*20*0.2 mm^3 were used as substrate. Co_3O_4 coatings with a thickness of approximately 1000 nm were performed in one side of the sample with the other side being the bare AISI 441 steel. This configuration enabled the evaluation of coated and uncoated samples in one experiment. Samples were weighted before and after the experiments.

The experiment consisted of a two-step oxidation comprising a first oxidation step using $^{16}O_2$ for 72 hours, and a second oxidation step using $^{18}O_2$ for 168 hours at 800 °C. The oxidation time was defined considering the parabolic oxidation kinetics of the samples, obtained from thermogravimetric experiments. Based on the calculations, 500 nm of Cr_2O_3 were expected after the first oxidation step and additional 500 nm of Cr_2O_3 after the second oxidation step.

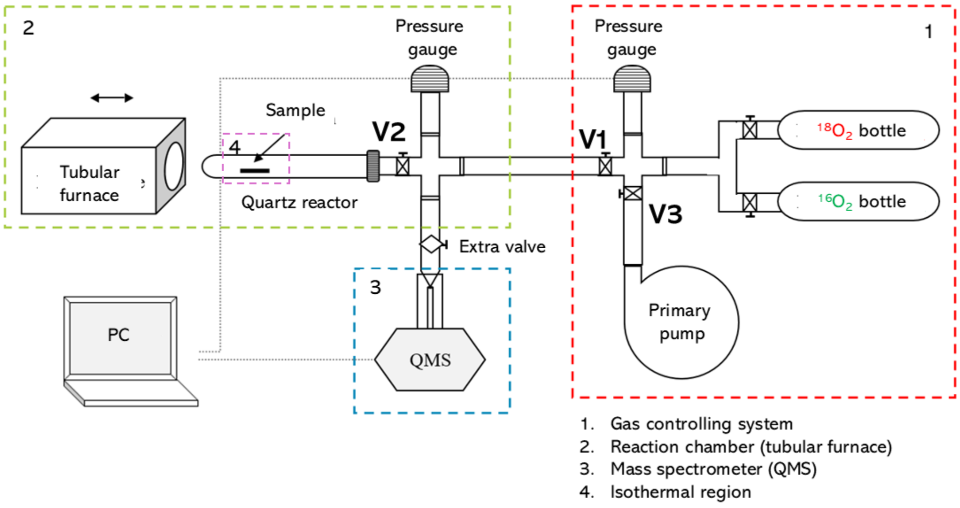

Figure II. 12 – Schematic representation of the experimental setup used for the sequential $^{16}O_2/^{18}O_2$ isotopic tracer experiment. Adapted from Diez-Mayo et al. [unpublished work].

Figure II.12 presents a schematic of the experimental setup. The reactor system is divided into multiple zones, each separated by gas valves (Figure II.13a), allowing precise control of the gas composition in each zone. System pressure and gas composition were continuously monitored using capacitive pressure gauge (INFICON®, full scale = 1000 mbar) and a quadrupole mass spectrometer (INFICON® Transpector 2 H100M), respectively. A thermocouple was also placed near the cross region to follow the gas temperature near the reactor exit. Temperature and pressure readings were recorded every 5 minutes.

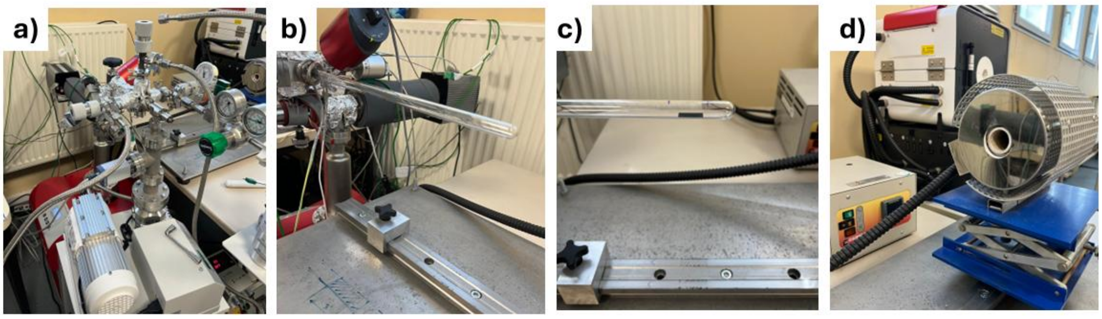

Figure II. 13 - Experimental setup showing gas valves and pumping system (a), quartz reactor (b), substrate in the isothermal region (c), and portable oven (d).

The reactor consists of a 400 mm long and 10 mm in diameter quartz tube (Figure II.13b). A moving furnace on a rail (Figure II.13d) was used to heat the sample, which was positioned in the isothermal region (Figure II.13c), highlighted by the light violet dotted square in Figure II.12, spanning approximately 30 mm.

Experimental Procedure

1. Sample Loading: The sample was initially placed at the entrance of the quartz reactor, and not in the isothermal zone yet (Figure II.13b).
2. Initial Pumping and Gas Introduction: The reactor was evacuated to a ~ 10^{-4} mbar pressure using a secondary vacuum pump to remove air. Once high vacuum was reached, valve V3 was closed, and the pump was turned off.
3. Valve V1 was opened, and the chamber was filled with 200 mbar of $^{16}O_2$ gas by controlling the pressure increase on the capacitive pressure gauge. Once reached, valve V1 was closed, valve V2 was opened, and the test is ready to start with static 200 mbar of $^{16}O_2$.
4. First Oxidation Step:
   - After pressure stabilization, the furnace at 800 °C was slid into position around the reactor.
   - As the temperature increased in the reactor, pressure variations followed the ideal gas law ($PV = nRT$).
   - Once thermal and pressure equilibrium were reached, the furnace was temporarily removed, the sample was placed into the isothermal zone using

a magnet, and the furnace was repositioned fast to begin the first oxidation step. This procedure last less than 10 s.

5. Gas Exchange: After the first oxidation step, the reactor was pumped again to remove the $^{16}O_2$ gas by opening valves V2 and V3.
6. Second Oxidation Step: The chamber was then refilled with 200 mbar of the isotopic $^{18}O_2$ gas while maintaining the sample at 800 °C. The microvalve allowing a very low flux of the gas phase to go towards the MS analysis chamber is opened. This procedure allows to measure any isotopic exchange between the $^{18}O_2$ gas phase and the ^{16}O rich oxide scale. Figure II.14 shows the MS analysis of the gas. First, the spectrum confirms that the gas is mainly composed of $^{18}O_2$ with minor residual concentration of $^{16}O_2$, as expected (4.35 vol.% of $^{16}O_2$). Additionally, no formation of $^{16,18}O_2$ molecules could be detected demonstrating that there was no isotopic exchange on the oxide surface. This result confirms that the ^{18}O enrichment zone that will be detected in the oxide scale after test will allow to determine the oxide growth mechanism.

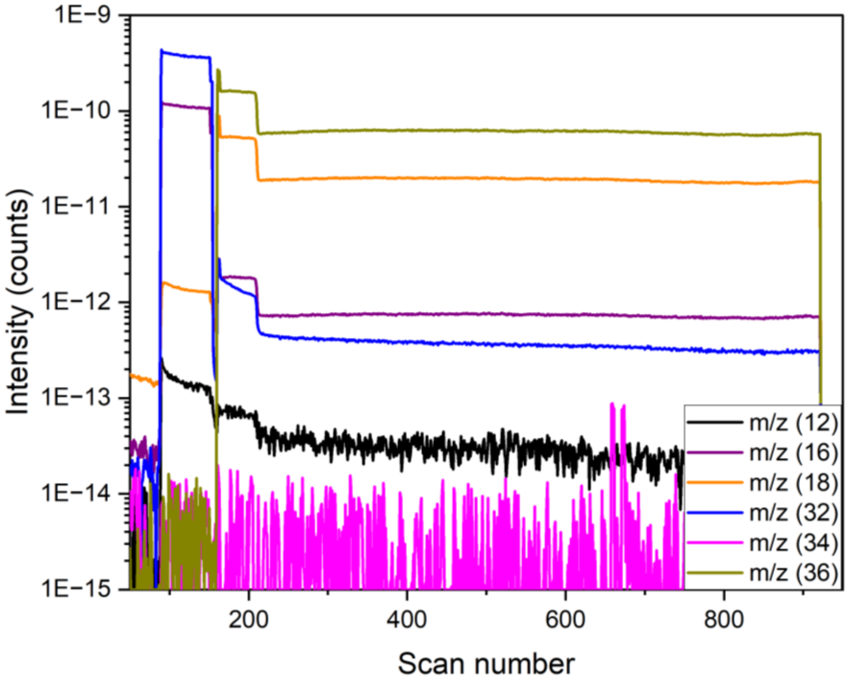

Figure II. 14 - MS spectrum of the output gas composition during second oxidation step (isotopic $^{18}O_2$).

4. Thin film characterisation

4.1. Morphology

The cross-sections were prepared by means of an automatic precision cut-off machine Accutom-5 or a wire diamond saw. Subsequently, the samples were mounted using a conductive resin (POLYFAST) and polished up to 1 µm using a SiC paper foil and diamond paste for finer polishing. Some of the samples were coated with a 50 nm thick gold layer and electroplated with Ni to avoid oxide spallation during preparation.

4.1.1. Scanning electron microscopy (SEM)

Multiple SEM/EDS equipment were employed to characterize the microstructure/chemical composition of the coatings. The equipment characteristics are described below:

- Hitachi SU-70 FE-SEM
- JEOL IT500HR (type FEG) Low Vacuum equipped with a Bruker *XFlash®* Generation IV 4030, detector RX ø=30 mm^2 for EDS.
- SEM-FEG Ultra55 ZEISS, and a BRUKER Quantax EDS-X.

4.1.2. Focused Ion Beam (FIB)

Cross-sectional analysis of the oxide layers on selected oxidized samples was performed using Focused Ion Beam (FIB) milling, followed by characterization with a ZEISS Crossbeam 550 system.

4.1.3. Confocal microscope

Surface topography analyses were performed using a confocal microscope (Lambda, Rtec instruments). Measurements were acquired at 20x and 100x magnifications, corresponding to scanned areas of 750 x 630 µm and 150 x 125 µm, respectively. Data treatment was carried out with MountainsMap®10.1 software. First, the surfaces were levelled using a first-order polynomial as the remove form operator. Subsequently, a Gaussian filter, in accordance with ISO 16610-61, was applied to decouple waviness from roughness. A cut-off value of 80 x 80 µm was used for the 20x magnification images, while a 50 x 50 µm for the 100x. Finally, the treated images were cropped for detailed evaluation, and the resulting 3D surface topographies were plotted.

4.2. Chemical composition

4.2.1. Raman spectroscopy

The Raman spectra were recorded with a Renishaw inVia micro-Raman spectrometer using the excitation wavelength 532 nm and 785 nm with a laser power of approximately 2.5 mW and 0.8 mW, respectively focused on a 5 μm^2 spot. The gratings were 2400 gr and 1200 $gr \cdot nm^{-1}$ for the 532 nm and 785 nm lasers, respectively, and the acquisition time remained at 20 s.

The full width at a half maximum (FWHM) and peak positions were obtained using a Lorentzian deconvolution from the Origin software. The data was compared to a reference from literature (Hadjiev et al.[225]) and to a Co_3O_4 standard produced in the laboratory (metallic cobalt oxidized for 24 hours at 600 °C.

4.2.2. Fourier Transform Infrared Spectroscopy (FTIR)

FTIR analyses were performed in transmission mode on Si wafers using a Bruker Vertex 70 spectrometer with a MCT detector. The spectra were obtained over a range of 4000–400 cm^{-1} with a resolution of 4 cm^{-1}. The acquisition of the FTIR spectrum of the $Co(acac)_3$ precursor was obtained from the spin-coated precursor on a Si wafer and acquired with the same FTIR spectrometer using an attenuated total reflection (ATR).

4.2.3. X-ray Photoelectron spectroscopy (XPS)

X-ray photoelectron spectroscopy (XPS) analyses of the thin films were performed both at the surface and in-depth using a Kratos Axis-Ultra ThermoFisher Nexsa G2 system equipped with a monochromatic Al Kα X-ray source (hv = 1486.6 eV). Surface characterization was complemented by near-surface analysis, conducted after removing surface contamination with Argon cluster sputtering (Ar_{1000}^+, 4 keV, 900 s). To probe the bulk composition, monatomic Argon sputtering (Ar^+, 4 keV, 900 s) was employed. For reference, the cobalt precursor, $Co(acac)_3$, was compressed onto an indium foil and analyzed at the surface and following sputtering with Ar_{150}^+ clusters for 300 s. High-resolution spectra were deconvoluted using the CasaXPS software, and energy calibration was based on the C 1s peak of adventitious carbon set at 284.8 eV.

Additional analyses were conducted using a ThermoFisher Escalab 250 Xi X-ray Photoelectron Spectrometer (XPS), equipped with a monochromatic Al Kα source (1486.6

eV). Depth profiling was performed over a 2 x 2 mm^2 area using an Ar^+ ion gun at 3 keV for 9500 seconds. The analysis focused on the elemental distribution of Co, Cr, and Mn, with quantification based on the survey spectra.

4.2.4. Time of Flight Secondary Ion Mass Spectroscopy (ToF-SIMS)

Molecular structures present in the thin films were identified using Time of Flight Secondary Ion Mass Spectrometry (ToF-SIMS 5, IONTOF), equipped with a Bismuth liquid metal ion source for surface spectral acquisition. To maintain static conditions and avoid surface damage, the Bi_3^+ primary ion dose density was kept below 10^{12} ions·cm^{-2} during analysis.

4.2.5. SIMS/NanoSIMS

Secondary Ion Mass Spectrometry (SIMS) was used in depth profiling mode in the coated and uncoated AISI 441 substrates after oxidation, and for nano imaging using samples cross-sections. Samples used for depth profiling received a thin gold layer (10 nm) prior to the measurements to limit charging effect during sputtering. The cross-sections were cut and mounted in conductive resin. They were grounded and polished up to 1 µm prior to the analysis.

A CAMECA SC-Ultra instrument (CAMECA, France) with a 1 keV Cs^+ sputter beam was used for depth profiling. Secondary positive ions—defined as MCs_x^+ (M being H, C, O, Si, Ti, Cr, Mn, Fe, and Co)—were collected from a 60 µm-diameter analysis spot centred within a 200 x 200 μm^2 sputtered area. Further analysis was performed on the samples oxidized in isotopic $^{18}O_2$ atmosphere. For these samples, both $^{16}OCs^+$ and $^{18}OCs^+$ were followed.

Nano imaging was performed in a CAMECA NanoSIMS 50, operated in multi-collection mode to acquire both 2D and 3D maps. A 16 keV Cs^+ beam at 1.5 pA was used to sputter and simultaneously detect MCs^+_x ions, with M being Si, Ti, Cr, Mn, Fe and Co. Images were recorded over a 20 x 20 μm^2 field at 256 × 256 pixels with 10 ms per pixel dwell time. The primary beam was focused to ~150 nm to balance sputter rate (for full-layer imaging) and lateral resolution, and the analysis chamber pressure was held at ~1 x 10^{-9} mbar.

4.2.6. Glow Discharge–Optical Emission Spectroscopy (GD-OES)

Glow Discharge–Optical Emission Spectroscopy (GD-OES) provides rapid, quantitative elemental depth profiling with excellent sensitivity across the periodic table and minimal sample preparation. Using a Horiba Scientific Profiler 2 in non-pulsed mode (25 W, 8.5 mbar

Ar), elemental concentration vs. depth profiles were obtained for coated and uncoated samples by sputtering a 12.5 mm^2 area. Quantification was done from standards.

4.3. Structural characterisation

4.3.1. X-ray diffractograms (XRD)

Structural characterization of the thin films was carried out using a Bruker D8 X-ray diffractometer equipped with a Cu Kα radiation source (λ = 0.154 nm). Measurements on Si wafer were performed in the 2θ range of 30° to 70°, using a step size of 0.02° and a grazing incidence angle of 0.2° while the measurements on the AISI 441 coated and oxidized samples were performed in locked couple using a 0.05° step size. The crystallite size and lattice strain were determined using the Williamson–Hall method. Peak broadening was analyzed by deconvoluting the FWHM of each diffraction peak using a pseudo-Voigt function. Instrumental broadening was accounted by subtracting the contribution obtained from a reference Al_2O_3 (corundum) sample. The results were plotted as FWHM·cos(θ) versus sin(θ), from which the strain and crystallite size were extracted. The strain is obtained from the slope of the linear fit and the crystallite size is calculated from the y-intercept using the Williamson–Hall equation

$$D_{W-H} = \frac{K\lambda}{y_{intercept}}$$

where K = 0.94 represents the shape factor and λ is the Cu K_α wavelength.

4.3.2. Transmission electron microscopy (TEM)

TEM lamellae were prepared by the lift-out method using an FEI Helios Nanolab 650 FIB-SEM. Analysis was conducted on a JEOL JEM-F200 cold FEG TEM operating at 200 kV. Crystallinity was assessed via high-resolution TEM (HRTEM) imaging combined with fast Fourier transform (FFT) analysis and selected-area electron diffraction (SAED) was used to confirm phase identification. Electron energy loss spectroscopy (EELS) spectra were obtained in STEM mode with a GATAN GIF Continuum ER post-column spectrometer. The convergence and collection angles were set to 10.7 mrad and 22.3 mrad, respectively, with an energy dispersion of 0.3 eV/channel.

Chapter III - Synthesis of Co_3O_4 by AP-PECVD technique: Growth Mechanisms

1. Introduction

As described in Chapter I, cobalt oxide (Co_3O_4) is a promising candidate to be used as a protective coating in Solid Oxide Electrolysis Cell (SOEC) interconnects, due to its chemical stability and favourable electrical conductivity properties[15,119,154,226]. For such applications, Co_3O_4 should preferentially be deposited as a thin film with well-controlled density, stoichiometry, and minimal impurity levels[11,14,117].

To date, various deposition techniques have been explored to produce Co_3O_4 thin films, including sol-gel[227], electrodeposition[228], chemical vapor deposition (CVD)[183], atomic layer deposition (ALD)[229,230], physical vapor deposition (PVD)[154,231,232], plasma spraying[233], and metal-organic CVD (MOCVD)[234]. For SOC applications, slurry deposition[119] and plasma spraying[226] were already used to deposit Co_3O_4 films. However, these processes often require post-deposition annealing or result in porous, carbon-rich coatings due to incomplete precursor decomposition[14].

Atmospheric pressure PECVD (AP-PECVD) is an attractive technology for the direct synthesis of crystalline oxide films such as TiO_2[158,159], ZnO[235], and $SrTiO_3$[236], combining the presence of reactive species and relatively high temperatures. Operating at atmospheric pressure, AP-PECVD is particularly attractive for large-area and industrial applications[19,163,171]. Despite its promise, the application of AP-PECVD for Co_3O_4 deposition remains underexplored.

Nonetheless, achieving dense, uniform, and stoichiometric oxide thin films with low impurity content is challenging due complex relationship of plasma chemistry, surface reactions and process parameters[19,163,184]. In CVD systems, the film growth relies primarily on the energy provided and the reactivity of the species[167,237,238]. The discussion in Section I.2.6 highlighted a similar relationship between the energetic input[174], provided by plasma-excited species, gas, or substrate temperature, and the overall reactivity, which depends on the plasma chemistry, the surrounding environment, and the precursor itself[21,167,237]. Two factors are considered as especially important for achieving dense, low-impurity and stoichiometric Co_3O_4 thin films:

- Reactive Oxygen Species (ROS), which drive oxide formation and facilitate the removal of residual carbon from the film.
- Temperature, both from the plasma itself (plasma gas temperature) and from external sources (substrate heating), which aids in film densification, crystallization, and decomposition of organic residues.

In this work, we systematically investigate how the process parameters affect the AP-PECVD of Co_3O_4 thin film. Oxygen was introduced through three pathways: direct O_2 addition to the carrier gas, environmental air exposure, and the oxygen content of the precursor. The effect of oxygen was studied by varying its addition and by controlling the deposition atmosphere. Temperature effects were investigated using external substrate heating and by modifying the distance between the substrate and the plasma torch outlet, which indirectly influences both the local gas temperature and the flux of plasma reactive species. This parametric study, complemented by plasma diagnostics and comprehensive thin film characterization, provides new insights into the underlying growth mechanisms of Co_3O_4 thin films deposited by AP-PECVD.

2. Methodology

The deposition of Co_3O_4 thin films was carried out using an Atmospheric Pressure Plasma-Enhanced Chemical Vapour Deposition (AP-PECVD) process based on a blown arc discharge (plasma jet). This plasma source has previously demonstrated effectiveness for the low-temperature deposition of crystalline metal oxide thin films such as TiO_2 and $SrTiO_3$[159,236].

Cobalt acetylacetonate [$Co(acac)_3$] was selected as the cobalt precursor due to its high chemical stability at room temperature compared to $Co(acac)_2$[183], and its suitable thermal properties for AP-PECVD: a low onset volatilization temperature (~180 °C) and a decomposition temperature near 250 °C[219,220,239]. The $Co(acac)_3$ solutions (acetone, ethanol and 1:1 acetone/ethanol mix) were evaluated for atomization into fine aerosols, which were then transported to the plasma afterglow region (see Figure II.2).

The aerosolized precursor solution was injected 1 mm above the substrate surface (distance *e*), directly into the plasma afterglow. This geometry was maintained throughout all experiments to minimize unwanted gas-phase reactions and powder formation[158]. The distance between the precursor injection outlet and the plasma torch outlet (distance *d*) was varied in selected experiments to evaluate its influence on plasma–precursor interactions.

The experimental workflow consisted of two main phases:

1. Optimization Stage: Solvent selection, precursor concentration, and injection flow rate were optimized to ensure stable deposition and good film quality.
2. Parametric Study: After optimization, four key parameters were independently varied to assess their impact on thin film formation:
    - O_2 content in the precursor carrier gas
    - Substrate heating temperature
    - Plasma jet outlet–precursor injection outlet distance (distance *d*)
    - Composition of the surrounding atmosphere (open-air and non-oxidizing environments).

An overview of the investigated deposition parameters is presented in Table I.1. The experiments were designed to systematically evaluate the role of plasma-precursor interactions, oxygen availability, and substrate temperature on the growth mechanisms and properties of Co_3O_4 thin films grown by AP-PECVD.

Table III. 1 - Experimental parameters evaluated for the AP-PECVD experiments.

Varied parameters	**O_2 variation**	**Substrate heating temperature**	**Plasma torch outlet-substrate distance**	**Surrounding environment**
Plasma Gas	N_2 – 50 L·min^{-1}			
Plasma power	1000 W			
Atomising gas	N_2 – 2 L·min^{-1}			
Carrier gas	N_2 (0.8-2 L·min^{-1}) + O_2 (0-1.2 L·min^{-1})	N_2 (1.2 L·min^{-1}) + O_2 (0.8 L·min^{-1})		N_2 – 2 L·min^{-1}
Precursor concentration	10 mM (0.356g/100 mL) – 40 mM (1.42 g/100 ml)			
Precursor Injection rate	400 µL·min^{-1}			
Displacement speed	1 scan - 0.05 mm·s^{-1}			Static
Substrate heating temperature	250 °C	No heating – 300 °C	No heating	
Plasma torch outlet-Precursor injection outlet distance	15 mm		15 – 40 mm	15 mm
Precursor injection outlet-Substrate distance	1 mm			

3. Results

3.1. Precursor solution selection and injection (Optimization)

3.1.1. Precursor solution selection

Water, ethanol, isopropanol, acetone and a 1:1 mixture of ethanol and acetone were investigated as solvents for the solubilization of Co(acac)$_3$. Among them, three solvent systems were investigated in the solution with Co(acac)$_3$: acetone, ethanol, and a 1:1 mixture of both. Other solvents (*e.g.*, water and isopropanol) were tested but were not suitable due to limited precursor solubility. Solubility increased in the following order: ethanol, 1:1 mixture of acetone and ethanol, acetone.

During the injection through the Venturi atomization system, part of the precursor solution was observed to not be effectively atomized. This poor atomization can be observed since the non-atomized solution is recovered through a Venturi reservoir. For the Co(acac)$_3$-acetone system, no solution was recovered in the reservoir whereas it increases with increase in ethanol concentration in the solvent. In addition, the Co(acac)$_3$ precursor-solvent systems were evaluated using Raman spectroscopy and SEM. Figure III.1 shows the Raman spectra obtained for the three Co(acac)$_3$ precursor-solvent systems. The spectra exhibited five Raman peaks matching well the Co$_3$O$_4$ standard. In addition, typical peaks from the Co(acac)$_3$ precursor disappear indicating effective plasma-precursor interaction. Moreover, no significant shifts were observed between the three films produced (these peaks will be described in detail in section 3.1.2). Subtle differences involve the peak intensity and broadening, with more intense and sharp peaks following again the order ethanol > acetone/ethanol mixture > acetone.

The choice of solvent seems to also have affected the growth rate of the thin films. The cross-sections of the thin films produced from the precursor solution with acetone and with ethanol are shown in Figure III.4d,e, respectively. Despite using the same conditions, the thin film produced using acetone as a solvent rendered a 4-fold thicker film. In addition to the higher solubility from acetone, it also presents higher vapor pressure and lower boiling point than ethanol. These characteristics provide a faster solvent evaporation for acetone upon entering the high-temperature plasma zone (150–800 °C). The fast solvent depletion should facilitate direct precursor-plasma interaction. In contrast, ethanol likely forms a more persistent barrier around the precursor molecules, requiring higher energy to remove the solvent molecules and enable the growth of crystalline Co_3O_4 thin films with reduced amount of carbon and other impurities.

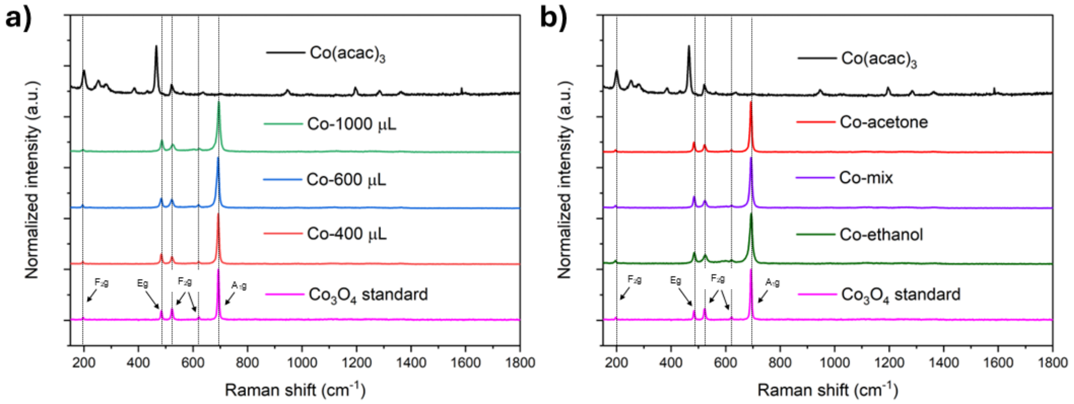

Figure III. 1 - *Raman spectra of the thin films comparing the injection rate (a) and Co(acac)$_3$ precursor-solvent system (b) variation. The Co_3O_4 standard is shown in magenta and the Co(acac)$_3$ precursor in black for reference.*

3.1.2. Precursor solution injection

Therefore, acetone provided the best solubility and was selected for further experiments. Solutions with varying Co(acac)$_3$ concentrations (10 to 40 mM) in acetone were prepared. Thin films were deposited using different precursor flow rates: 400 µL·min^{-1} for the 10 mM solution and 100 µL·min^{-1} for the 40 mM solution, to retain the same amount of precursor flow to the afterglow.

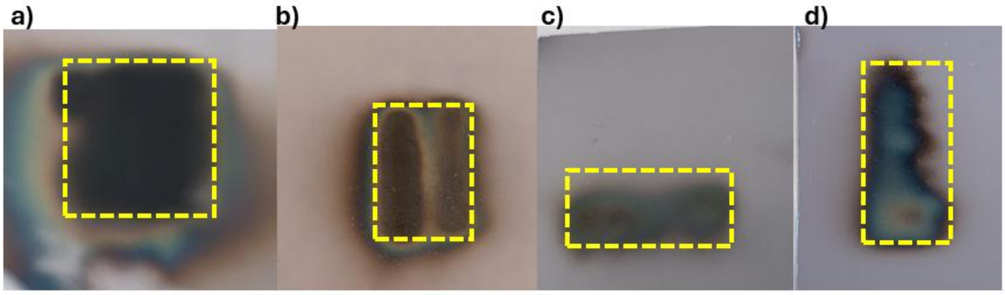

Figure III. 2 – Top-view images of the Co-based coatings deposited by AP-PECVD using (a) 10 mM, (b) 15 mM, (c) 20 mM and (d) 40 mM Co(acac)$_3$ concentration in the solution. The yellow dotted squares indicate the region covered by the plasma jet.

As shown in Figure III.2, higher-concentration solutions (> 15 mM) resulted in discontinuous thin films while the 10 mM produce a homogeneous thin film. The reduced uniformity of more concentrated Co(acac)$_3$ solutions is likely due to poor aerosol formation and clogging of the atomising system. During the experiments using more concentrated $Co(acac)_3$ solutions, there was reduction of the atomizer gas flow and precursor leakage through the syringe.

The injection rate of the $Co(acac)_3$-acetone solution was optimized based on the capacity of the Venturi atomizing system. Using a 10 mM solution, three injection rates were tested: 400, 600, and 1000 $\mu L\cdot min^{-1}$, using a 10 mL syringe. When the solution passes through the Venturi atomizer, it creates fine droplets which are transported to the deposition region. It is observed that part of the solution was not effectively atomized and was retained in the Venturi reservoir. After each run, the retained solution was measured. The solution retention increased proportionally with the injection rate, as follows:

- At 400 $\mu L\cdot min^{-1}$, less than 1 mL of residual solution was observed.
- At 600 $\mu L\cdot min^{-1}$, around 2.5 mL was retained.
- At 1000 $\mu L\cdot min^{-1}$, approximately 5 mL remained.

This indicates that the atomizer has a limited aerosolization capacity, and that higher injection rates lead to poor delivery efficiency. Raman spectroscopy analyses were carried out to evaluate the thin films deposited. The results evidence five well-defined peaks matching well the Co_3O_4 standard spectrum. The peaks correspond to A_1g, Eg, and three F_2g modes[225,240,241]. The high intensity peak, located at 693 cm^{-1}, represents the A_1g mode, which relates to the vibration of both CoO_6 octahedron (Co^{3+}) and CoO_4 tetrahedron (Co^{2+})[240]. In Co_3O_4, the main contribution arises from the Co^{3+}–O symmetric stretching of CoO_6[240,242,243]. The F_2g mode at low wavenumber (195 cm^{-1}) corresponds to the complete translation of CoO_4. Other modes, located at 483 cm^{-1}, 522 cm^{-1}, and 621 cm^{-1}, refer to the vibrations of tetrahedral and octahedral sites of Co_3O_4[240]. The Raman spectra was compared to a Co_3O_4 standard, prepared from the annealing of metallic Co substrate under air at 600°C for 24 hours, and to the $Co(acac)_3$ precursor (Figure 2). All thin films showed good agreement with the Co_3O_4 standard, and no precursor-related peaks. Considering the peak positions, there is consistently a minor red shift of less than 2 cm^{-1} for the 1000 $\mu L\cdot min^{-1}$ injection rate, and no shift for the other two. The Raman peak shift could relate to variation in stoichiometry or the presence of stress on the films[244,245]. The full width at a half maximum (FWHM) of the A_1g was deconvoluted using a Lorentzian function. The FWHM increases proportionally (from 7 to 10.5 cm^{-1}) with the injection rate increase. Conversely, peak intensity decreased proportionally with increase of the injection rate. Peak broadening[246,247] and intensity reduction[248] were attributed to increased disorder of the oxide phase. These results show that the Co_3O_4 phase was obtained irrespective of the injection rate. However, increased injection rate led to higher precursor solution retention and slight deviation from the Co_3O_4

Raman spectrum from the standard. Therefore, the 400 μL·min^{-1} injection rate was used for the following experiments.

3.2. Plasma deposition parameters

Combined with its superior solubility and low viscosity, acetone enabled efficient atomization and transport to the plasma deposition region. Considering the outcomes of these preliminary investigations, a concentration of 10 mM of Co(acac)$_3$-acetone was used for the following experiments using a 400 μL·min^{-1} injection rate.

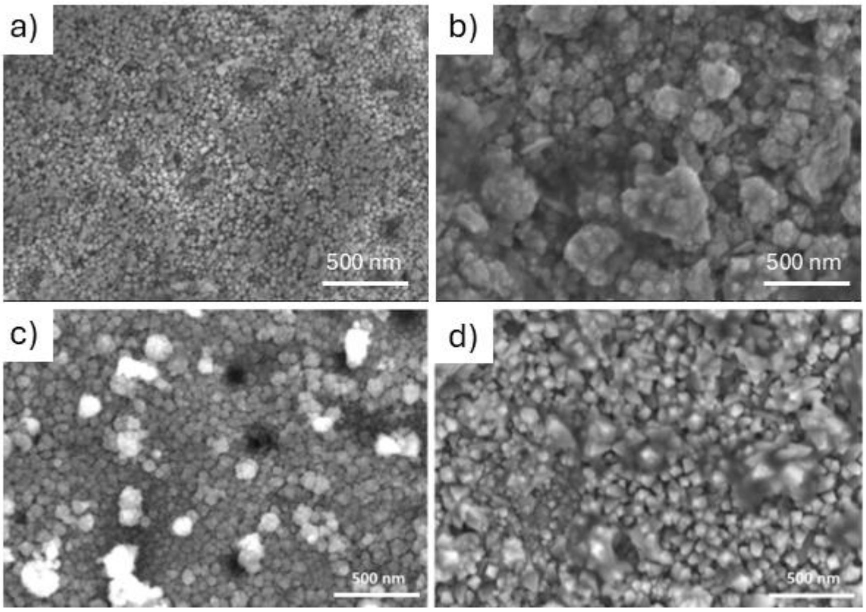

Figure III. 3 - SEM top-view images of Co_3O_4 thin films produced by AP-PECVD under open-air conditions at 250 °C and 40% O_2 addition to the carrier gas. The micrographs indicate four distinct regions of the same Co_3O_4 thin film, two at 50 k magnification (a, b) and two at 100 k magnification (c, d).

Figure III.3 shows the SEM top-view images of a sample produced by AP-PECVD using a substrate heating system (250 °C and 40 % O_2 addition in the carrier gas). The precursor injection was set at 15 mm from the plasma jet outlet. The surface morphology of the Co_3O_4 thin films exhibits very fine grain sizes (ranging from 50 to 100 nm) with angular facets (Figure III.3a,d). However, some regions exhibit spheroidal grains and even cluster of larger aggregates (Figure III.3b,c). Previous works suggest that these aggregates likely derive from homogeneous reactions in the gas phase[158]. Additionally, the contrast in top-view images indicates spatial variation in local film thickness. Indeed, controlling the uniformity of the thin film is challenging using the studied AP-PECVD process[19].

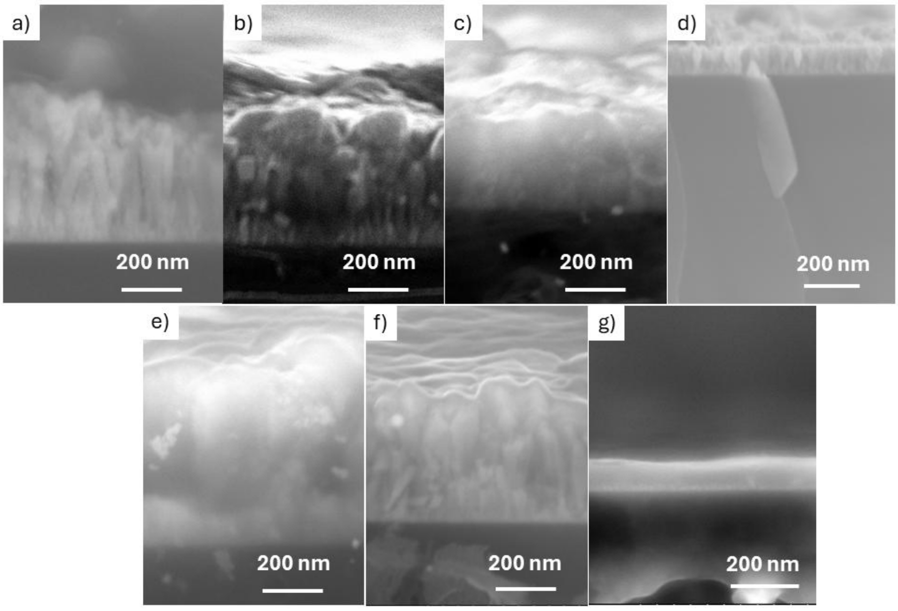

Figure III. 4 - SEM cross-section images showing the thin films produced at 250 °C and 0% O_2 (a), 40% O_2 (b) and 60% O_2 (c), the films produced using 40% O_2 without heating using ethanol as the solvent (d) and acetone (e). (f) 300 °C substrate heating and 40% O_2 and (g) shows the thin film produced in non-oxidizing atmosphere.

Figure III.4 shows several cross-section micrographs from the varied parameters. From a-f, thin films presented a columnar growth type, and a thickness in the range of 500 nm for the thin films produced with acetone-based precursor solution, and ~120 nm for the thin film produced using ethanol-based precursor solution. The growth type of the thin film produced in non-oxidizing atmosphere (g) is not clear, but the film presents a smoother surface than the rest. The film thickness is ~120 nm. The films presented here represent the conditions that will be discussed in the following sections.

TEM analyses were conducted on a FIB-prepared lamella extracted from the Co_3O_4 thin film. The film was deposited on a Si wafer under ambient conditions at 300 °C, using a carrier gas containing 40% O_2. As shown in Figure III.5a, the coating exhibits a dense microstructure with a columnar growth morphology. The column widths range from approximately 30 to 100 nm (indicated by yellow arrows in Figure III.5a), consistent with the grain size observed in SEM top-view images (Figure III.3a,c,d). The interface between the Co_3O_4 layer and the substrate appears compact and continuous, without evidence of delamination or interfacial porosity, indicating strong adhesion. Such adhesion is commonly attributed to the presence of energetic plasma species during deposition, which promote both surface activation and efficient removal of organic residues[18,21].

The crystalline nature of the film was examined by selected area electron diffraction (SAED, Appendix III.1) and high-resolution TEM (HRTEM) combined with fast Fourier transform (FFT) analysis. Figures III.5c,d display a representative crystalline region and its corresponding FFT pattern, respectively, revealing a Co_3O_4 spinel phase oriented along the [110] zone axis. Overall, the thin films were composed of a few particles close to the surface but displayed mainly a dense film.

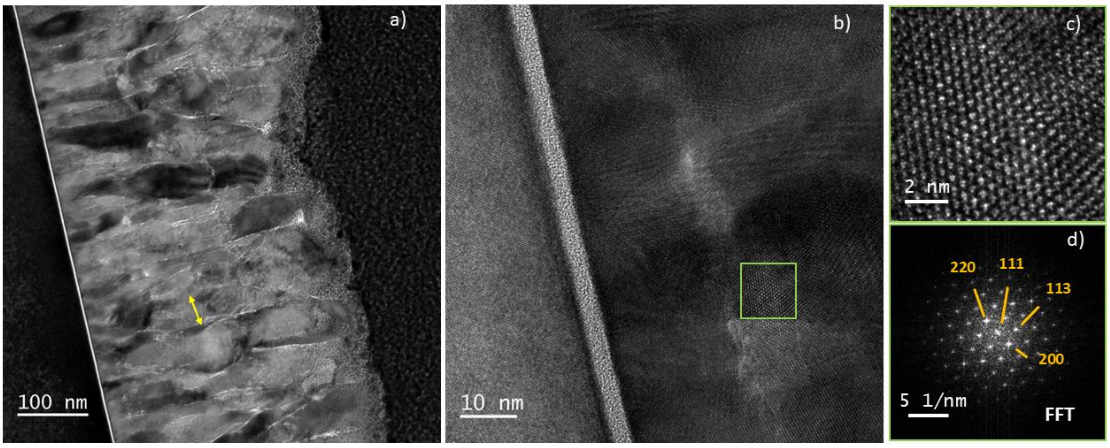

Figure III. 5 - TEM observations of the Co_3O_4 thin film prepared by AP-PECVD of $Co(acac)_3$ under open-air conditions, and a substrate heating temperature of 300 °C. The gas flow comprised a N_2 gas mixed with 40% O_2 for cobalt precursor injection: (a) Cross-section image of the Co_3O_4 thin film using bright-field TEM. (b) High resolution TEM micrograph at the substrate/coating interface. (c) Enlarged region obtained from image b (within green solid squares). (d) Identification of the lattice planes by Fast Fourier transform (FFT) performed from image (c).

3.3. Influence of O_2 addition in the carrier gas

Experiments investigating the effect of oxygen concentration were conducted using O_2 contents ranging from 0% to 60% in the carrier gas used to transport the atomized precursor solution. This range corresponds to approximately 0% to 2.2% O_2 in the total gas flow (plasma gas, atomising gas and carrier gas). The addition of O_2 was at first thought essential for the removal of carbon and nitrogen containing moieties in the films and enabling a stoichiometry close to Co_3O_4, as reported for other oxide coatings[19,211,212]. During these experiments, the substrate temperature was maintained at 250 °C (see Table III.1). The resulting films were characterized using Raman spectroscopy (for phase identification), SEM (for morphology), and ToF-SIMS and XPS (for chemical composition).

Figure III.6a shows the Raman spectra of the four thin films produced from varying O_2 concentration in the carrier gas. For comparison, the reference Co_3O_4 is also shown.

Irrespective of the O_2 concentration, five Raman peaks were observed to match well Co_3O_4 reference peaks. Besides the Raman shift positions, a high degree of similarity of the peak broadening was observed between the different films (Figure III.6a). The smaller FWHM for the Raman peaks recorded for the reference Co_3O_4 sample is attributed to higher crystallinity, and increased crystallite sizes[249] originating from the synthesis conditions, i.e. 600 °C in 24 hours annealing.

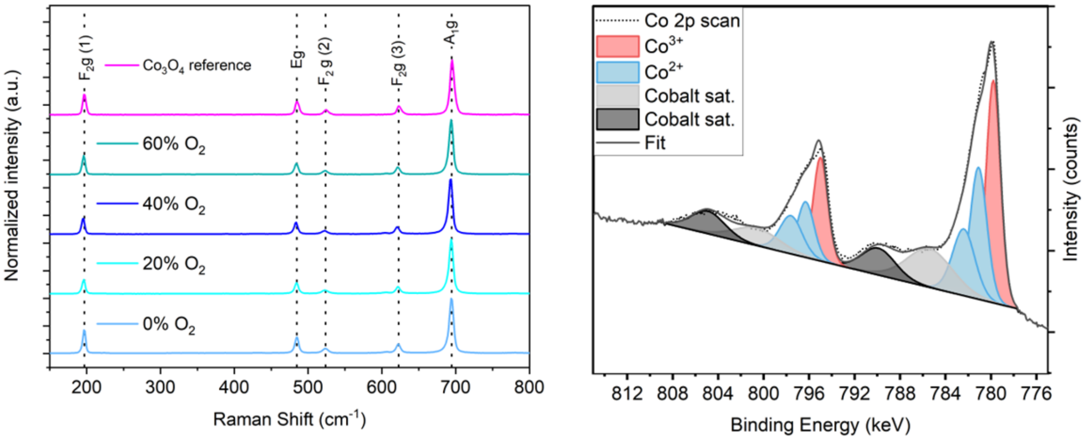

Figure III. 6 - Raman spectra (left) of thin films produced at 250 °C (substrate heating) and varied O_2 concentrations in the carrier gas. Standard Co_3O_4 is shown for reference (magenta). High-resolution X-ray photoelectron spectroscopy (HR-XPS) of Co 2p for the film produced with 40% O_2.

X-ray photoelectron spectroscopy (XPS) was used to evaluate both the surface and near-surface regions of the deposited thin films. High-resolution XPS (HR-XPS) analysis of the Co 2p region (Figure III.6b) showed a spectral signature consistent with Co_3O_4. The deconvolution was carried out using the model proposed by Biesinger et al.[250] To evaluate the chemical composition, an Ar_{1000}^{+} gas cluster ion source was employed to reduce surface contamination, particularly adventitious carbon. All conditions matched well the Co_3O_4 with similar area for each peak.

Table III.2 presents the chemical composition obtained from the near-surface region. Regardless of the O_2 content in the carrier gas, the films consistently exhibited approximately 24 at.% carbon, which is relatively high. Additionally, nitrogen content remained negligible across all samples (below 1 at.%), indicating minimal contamination from the plasma species to the film.

Table III. 2 - Chemical composition of the thin films obtained using various O_2 concentrations in the carrier gas. Results shown here were obtained by HR-XPS after a cluster Ar sputtering (Ar_{1000}^+) for 900 s.

	0 % O_2	**20 % O_2**	**40 % O_2**	**60 % O_2**
Co (%)	28.8	30.6	29.5	30.6
O (%)	47.3	46.2	45.6	45.8
C (%)	24.2	23.5	24.9	24.1
N (%)	0.6	0.6	0.5	0.7

Relatively high carbon concentration was obtained near the thin film surface. To gain deeper insight into the chemical composition distribution across the thin film depth, Time-of-Flight Secondary Ion Mass Spectrometry (ToF-SIMS) was performed on the sample deposited without O_2 in the carrier gas (0% O_2). This sample was chosen since it was considered as the least reactive conditions due to reduced oxygen availability from the carrier gas. As shown in Figure III.7a, the depth profile revealed constant cobalt (Co^+) and oxygen (O^{2-}) ion signals throughout the film, while carbon-containing ions (*e.g.*, CN^+, CO^+, CO_3^-) were concentrated near the surface. Notably, the intensity of CO_3^- dropped sharply after sputtering the top few nanometres and stabilized at low levels in the film's bulk. These results are consistent with XPS data from the bulk region of the sample deposited with 40% O_2 (discussed in Section 3.4.1).

The near the surface carbon is likely due to residual organic fragments from the precursor and environmental contamination after deposition. ToF-SIMS (Figure III.7a) and XPS (Table III.3) results confirmed that this contamination is limited to the near-surface and does not significantly affect the film bulk even in the absence of O_2 in the carrier, atomising and plasma gases.

Overall, these findings indicate that the addition of O_2 to the carrier gas has limited influence on the removal of organic ligands and residual contaminants during deposition. Co_3O_4 thin films were formed successfully in all cases without noticeable effect on stoichiometry. This lack of variation irrespective of O_2 concentration will be discussed in detail in Section 3.5.

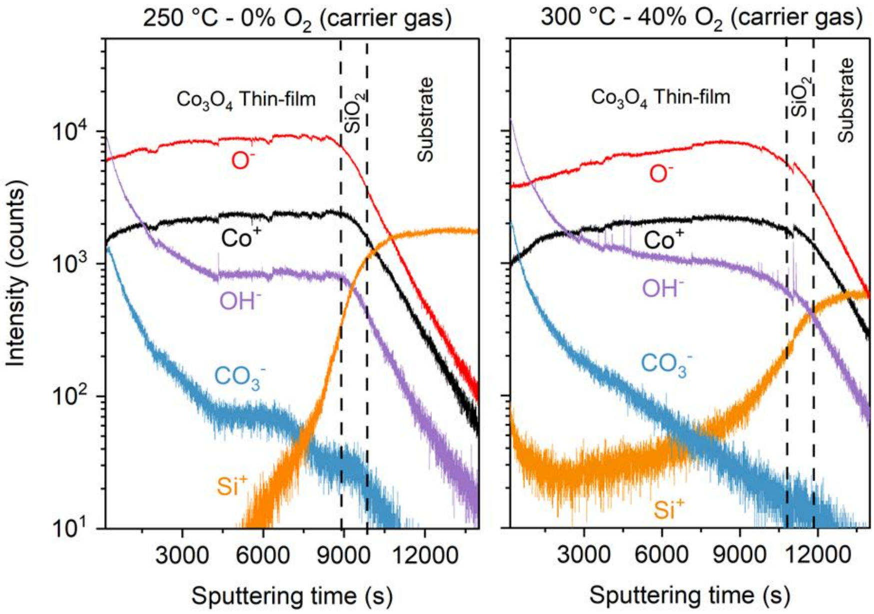

Figure III. 7 - ToF-SIMS profile of the thin films prepared by AP-PECVD under open-air conditions at 250 °C and 0% O_2 in the carrier gas (left), and at 300 °C with 40% O_2 in the carrier gas. The thin film/SiO_2 native layer interface was identified by the variation of the inflection point from the different elements observed in the profile.

3.4. Substrate heating temperature

The effect of the substrate heating temperature (no external heating, 200°C, 250°C, and 300°C) was investigated regarding the Co_3O_4 phase formation and carbon contamination. For these experiments, the O_2 concentration in the carrier gas remained at 40%. The films were investigated using Raman and XRD for structural analyses and ToF-SIMS and XPS for chemical composition.

Table III.3 indicates the chemical composition of the films produced using different substrate heating temperatures at the near-surface, and for two conditions in the bulk as well. The near-surface analysis showed a pronounced benefit from increased substrate heating temperature, as it is shown by the higher carbon content in intermediary conditions (200 and 250 °C). Although relatively high close to the surface, the carbon contamination reduces to below 3 at.% in the bulk (Ar^+ 900 s).

ToF-SIMS analysis was performed for samples deposited without heating, and at 300 °C. The Co_3O_4 thin film deposited with substrate heating of 300 °C exhibited a rapid decrease of carbon-related compounds, as it can be seen in Figure III.7b. Even the film produced without any external heating showed a rapid decrease in carbon-containing species (Figure III.8a). The ToF-SIMS results were investigated using the O^{2-}/CO_3^- and O^{2-}/Co^+ intensity ratios to compare the elimination of residual contamination and stoichiometry, respectively (Figure III.8). The O^{2-}/Co^+ shows a very close relationship in all cases with minor variation across the film indicating similar stoichiometry in all cases (samples are represented by different tones of blue in Figure III.8b). The films named "non-oxidizing atmosphere" will be discussed in detail in section 3.7.2. A more pronounced variation through the film was observed regarding the residual impurities with the temperature increase. The increase in the O^{2-}/CO_3^- ratio with sputtering time confirms the strong reduction in carbon contamination after the first nanometres. Interestingly, this increase of the O^{2-}/CO_3^- ratio is more significant with higher temperatures highlighting a slight benefit if higher substrate temperature. This reduction is not surprising since higher temperatures should promote the volatilization of carbon moieties[215,237].

Table III. 3 - Chemical composition of thin films obtained using various substrate heating temperatures and 40% O_2 concentration in the carrier gas. Results shown here were obtained by HRXPS after a cluster Ar sputtering (Ar_{1000}^+) for 900 s, and from the survey spectra in the bulk after Ar+ sputtering for 900 s.

	No heating (NH)	**200 °C**	**250 °C**	**300 °C**	**NH (Bulk)**	**250 °C (Bulk)**
Co (%)	31.8	28.2	29.5	38.9	44.5	47.9
O (%)	48.6	46.3	45.6	50.0	52.2	49.4
C (%)	18.9	25	24.4	10.5	3.0	2.5
N (%)	0.7	0.5	0.4	0.4	0.4	0.2

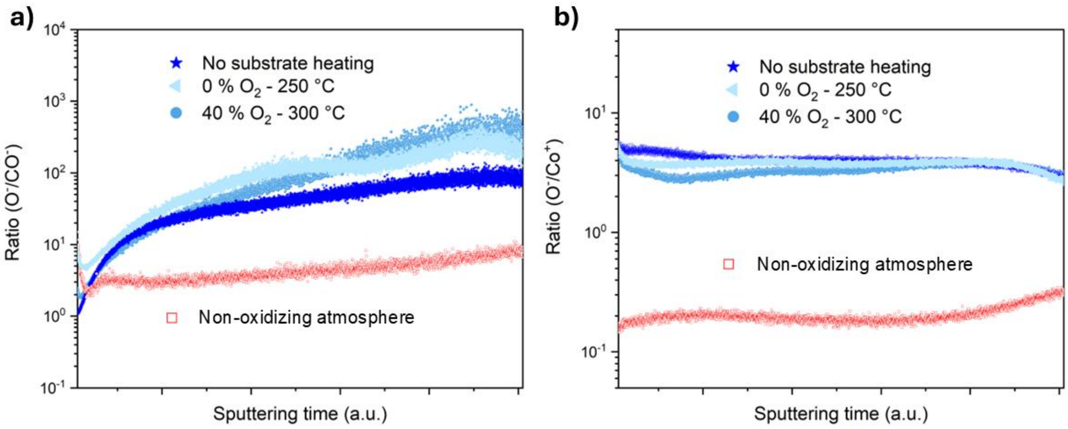

Figure III. 8 - Comparison of ToF-SIMS intensity ratios of O^-/CO^- (a) and O^-/Co^+ (b) for four films produced under open-air (different tones of blue) and non-oxidizing atmosphere (red).

The influence of the different substrate heating temperatures was further analyzed by Raman spectroscopy and X-Ray diffraction analysis. Irrespective of the substrate heating temperature, the Raman spectra of the thin films exhibit the five characteristic peaks of Co_3O_4 with a minimal shift between each other (less than 1 cm^{-1}) showing a good agreement to the reference Co_3O_4 sample prepared at 600°C (Figure III.9). Wu et al. used the $\frac{F_2g(1)}{A_1g}$ intensity ratio to infer on the relative concentration of Co^{2+} to Co^{3+}[251]. The $F_2(g)$ refers mainly to tetrahedral sites, mainly occupied by Co^{2+} ions and A_1g refers mainly to the octahedral sites, mainly occupied by Co^{3+} ions. Peak position, FWHM and the $\frac{F_2g(1)}{A_1g}$ ratio of the $F_2(g)$ and A_1g peak are presented in Appendix III.2. Very similar FWHM were observed irrespective of substrate heating condition. Additionally, the $\frac{F_2g(1)}{A_1g}$ ratio is observed to decrease as the substrate heating temperature increases, which suggests a higher presence of cobalt in octahedral sites (Co^{3+}) for the thin films produced at higher substrate heating temperatures.

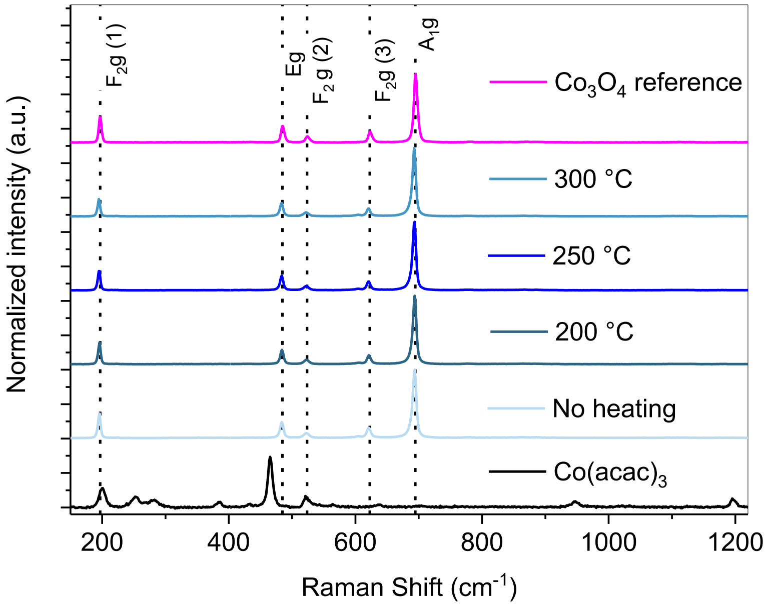

Figure III. 9 - Raman spectra of thin films produced at different substrate heating temperatures and 40 % O_2 concentrations in the carrier gas (different tones of blue). $Co(acac)_3$ precursor (black) and standard Co_3O_4 is shown for reference (magenta).

X-ray diffractograms performed for the thin film synthesized with no external heating or at 250°C and 300°C, suggested no preferential orientation with peak intensities matching the JCPDS card No. 00-042-1467 for Co_3O_4 having a cubic spinel structure (Figure III.10a). Also, no peaks from other crystalline phases are noticeable. The crystallite size was calculated using the Williamson-Hall method, explained in section II.4.3.1. The Williamson-Hall plot is shown in Figure III.10c. The crystallite size was estimated to be ca. 19, 41 and 37 nm for no heating, 250 °C and 300 °C conditions, respectively. These results suggest an increase in crystalline size with increasing substrate heating temperature. Indeed, the increase in temperature could provide extra thermal energy for the growth of crystallites. Moreover, the Co_3O_4 lattice parameter "*a*" was calculated using the same approach as [252]

$$sin^2(\theta) = \frac{\lambda^2}{4a^2}(h^2 + k^2 + l^2)$$

where θ is the Bragg angle, and (*hkl)* are the Miller indices.

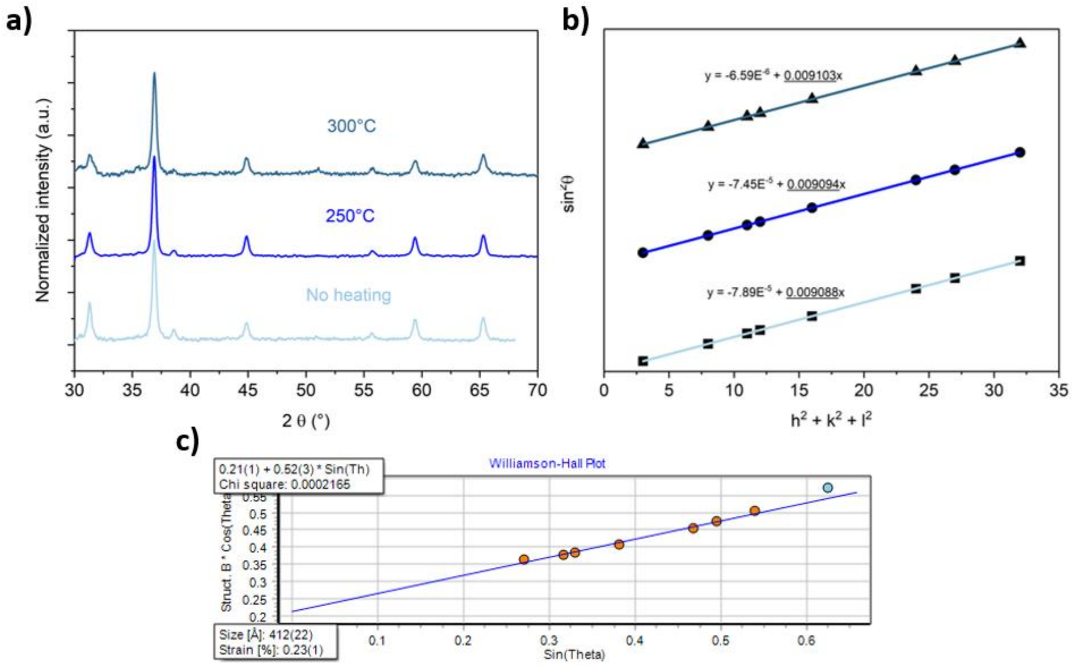

Figure III. 10 - X-ray Diffractograms of the samples produced with no additional heating, at 250°C and 300°C with 40% O_2 concentration in the carrier gas (a). Variation of $sin^2\theta$ versus (h^2+k^2+l^2) for the Co_3O_4 thin films prepared without additional heating system (light blue), at 250°C (blue) and at 300°C (dark blue). The slope of the linear fit (A) was applied in equation (A = $\lambda/4a^2$) to determine the lattice parameter 8.080 Å, 8.078 Å, and 8.074 Å, for the sample prepared without external heating, 250°C and 300°C,respectively (b). Williamson-Hall plot of the sample produced at 250°C with 40% O_2 concentration in the carrier gas (c).

The lattice parameter of the Co_3O_4 thin films was determined by plotting $sin^2(\theta)$ vs $h^2 + k^2 + l^2$. From the linear fit, slope A (highlighted in Figure III.10b) was obtained. The lattice parameter *a* was then calculated using the relation:

$$A = (\frac{\lambda^2}{4a^2})$$

The resulting values of a were 8.080 Å (no heating), 8.078 Å (250 °C), and 8.074 Å (300 °C), all of which are very close to the theoretical value of 8.084 Å for Co_3O_4 (JCPDS card No. 00-042-1467). This close agreement confirms the successful synthesis and deposition of crystalline Co_3O_4 thin films via AP-PECVD from $Co(acac)_3$ under open-air conditions, with only minor lattice distortion. Interestingly, a slight decrease in the lattice parameter was observed with increasing substrate temperature. This trend aligns with previous Raman analysis suggesting an increased incorporation of Co^{3+} at higher temperatures. Given that Co^{3+} has a smaller ionic radius than Co^{2+},[253] the observed lattice contraction is consistent with a shift in the Co ion valence state within the spinel structure.

Overall, higher substrate temperatures contributed to the improved removal of residual contamination, particularly near the surface, and a slight change in the oxide's ionic composition. Regarding the residual elimination, this result can be explained by the localized effect of plasma and the thermal decomposition of $Co(acac)_3$ which becomes more pronounced at temperatures above 250 °C. The plasma species, *e.g.*, radicals, metastables, and thermal energy from plasma are beneficial only when the plasma jet is above the area of interest. Once the plasma jet moves away, these benefits are reduced[20,158]. When heating the substrate, thermal energy will continuously assist in eliminating unreacted precursor fragments.

Despite these benefits, even the films deposited without substrate heating exhibited relatively low carbon content. Moreover, the crystalline phase and structure remained consistent across the tested substrate heating temperature range. To separate the benefit from plasma and substrate heating temperature, an additional experiment was conducted by heating the substrate to 350 °C without the ignition of plasma. The experiment was conducted for longer time than the previous set of experiments (3 scans instead of 1). No film was observed on the surface of the substrate, suggesting that temperature alone does not provide an efficient way of promoting significant thin film formation. These observations suggest that the plasma itself, *i.e.*, high-energy species and reactive environment, is primarily responsible for fragmenting the precursor and removing organic ligands. Substrate heating offers additional cleaning and slight compositional tuning but is not strictly necessary to achieve phase-pure Co_3O_4.

3.5. Plasma temperature

Considering the lack of major changes observed by varying substrate heating temperature, plasma is expected to be the main contributor for thin film formation. Thus, the plasma was evaluated regarding its gas temperature and plasma chemical composition. OES analysis was performed in the absence of the Si wafer at different points of the plasma afterglow. Carrier gas composition remained at 40 % O_2. Figure III.11a shows the evolution of the radiative species when moving away from the plasma jet outlet (0, 10 and 15 mm from the exit of the plasma torch). Three main contributions are observed: the transitions of the N_2 Second Positive System (SPS), the NO β system, and the N_2^+ First Negative System (FNS)[254], which will be discussed in detail in section 3.7. The plasma rotational temperature is known to correspond to the plasma gas temperature at atmospheric pressure, although the plasma afterglow may contain species with higher energies[192,255–257]. In this work, the LIFBASE software[224] was used to evaluate this temperature at different positions. The NO β and N_2^+ FNS radiative species from the recorded emission spectra were superposed to simulated spectra from the software (Figure II.6). The N_2^+ FNS system appeared only closer to the plasma jet outlet while NO β system was present in all positions. The simulated spectra were compared over a wide range (280 to 400 nm) to increase accuracy.

The plasma gas temperature decreases exponentially with distance from the plasma torch exit. Starting at approximately 1150 °C at 0 mm, it drops to 750 °C at 10 mm, 480 °C at 15 mm, and reaches around 430 °C at the substrate position (17 mm). This rapid decline reflects the weakening of the plasma afterglow as it moves away from the plasma jet outlet. Beyond 20 mm, the Optical Emission Spectroscopy (OES) signal becomes too weak to reliably determine temperature. To complement and validate the OES data, thermocouple measurements were employed, providing a more robust temperature profile. Both techniques confirm that the substrate is exposed to high temperatures (>400 °C) when directly beneath the plasma (Figure III.11b). The temperature reduces drastically when the plasma jet is moved away. The results from OES and thermocouples show good agreement following a similar temperature profile, except at the plasma jet exit (not measured by thermocouple).

The overall consistency between the rotational temperature (from OES) and the gas temperature (from thermocouples) supports the reliability of the measurements and indicates effective mixing with the surrounding atmosphere. Given that the cobalt precursor is injected at 15 mm from the torch exit and the substrate right below (17 mm), the thermal gradient between the injection and deposition zones is minimal.

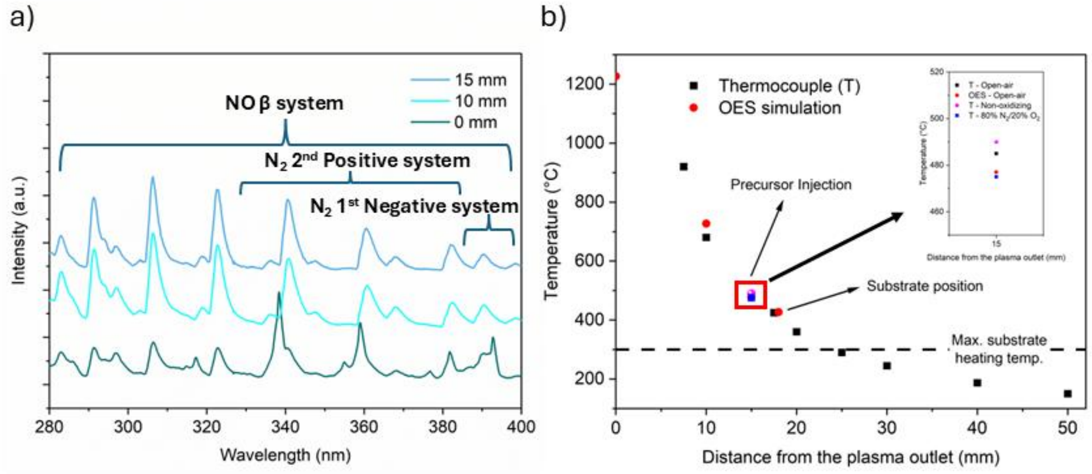

Figure III. 11 - OES measurements were performed without a heating plate and with 40% O_2 gas mixture in the carrier gas. (a) OES spectra were measured at different distances from the plasma torch outlet. (b) Temperature profile obtained from the OES (red circles) and thermocouple (black squares) measurements at different distances from the outlet nozzle. Thermocouple (T) measurements were also performed in a controlled atmosphere, either a nonoxidizing environment (magenta spheres) or an environment simulating the open-air (80% N_2/20% O_2, defined by blue squares).

The plasma gas temperature in this region, between precursor injection (480 °C) and substrate (430 °C) position, is much higher than the peak decomposition temperature of Co(acac)$_3$ (250°C)[220,258] and the highest substrate heating temperature. Although this temperature varies rapidly when moving the plasma jet, the high gas temperature combined with the reactive species likely explain the lack of differences observed by varying substrate heating temperature.

Indeed, Schubert et al. demonstrated that Co(acac)$_3$ conversion to Co_3O_4 increases with temperature, alongside with by-products formation, starting from 230°C[220]. This conversion was only possible in the presence of an oxidizing environment[219]. Moreover, they stated that the decomposition process until the formation of an oxide happens through the formation of radicals, which are produced by subsequent reaction with O_2[220,259,260]. This radical formation is likely accelerated by the interaction of the precursor molecules with the energetic plasma species, prompting the Co_3O_4 thin film formation[18,19,21].

It is important to highlight that thin film formation is expected to occur at the substrate surface. Due to the high gas velocity (>200 $m \cdot s^{-1}$) and the proximity between the precursor injection point and the substrate, the cobalt precursor has a very short residence time in the plasma afterglow[261]. Consequently, the deposition is expected to be dominated by heterogeneous surface reactions, leading to the formation of dense thin films. The surface reactions predominance is supported by cross-section images (Figure III.4 and III.5a) and SEM top-view images (Figure III.3), which show only a few isolated regions with large particle formation.

3.6. Plasma-substrate distance

To gain further insight into the role of plasma in Co_3O_4 thin film formation, the distance between the plasma jet outlet and the precursor injection point was varied (15, 25, 30, and 40 mm). Increasing this distance significantly reduces the energy and concentration of reactive plasma species[169,176,192] and lowers the plasma gas temperature, which drops from 480 °C to 190 °C (Figure III.11b).

Figure III.12 presents the FTIR (a), and Raman (b) spectra of the films deposited for different plasma torch outlet-precursor injection distances. This variation in injection distance has a strong impact on the resulting film properties. At 25 mm (290 °C), the Raman spectrum remains highly consistent with the Co_3O_4 signature peaks, as obtained at 15 mm. Peak positions are maintained, though the bands at 197 and 618 cm^{-1} are not evident. The broadening of the main A_1g peak (FWHM increases from 7 to 12 cm^{-1}) suggests a reduction in crystallite size with increase of the plasma jet outlet-precursor injection distance[241]. FTIR analysis reveals no evidence of carbonaceous contamination, indicating that the organic moieties of the precursor are efficiently decomposed and the film exhibits high chemical purity.

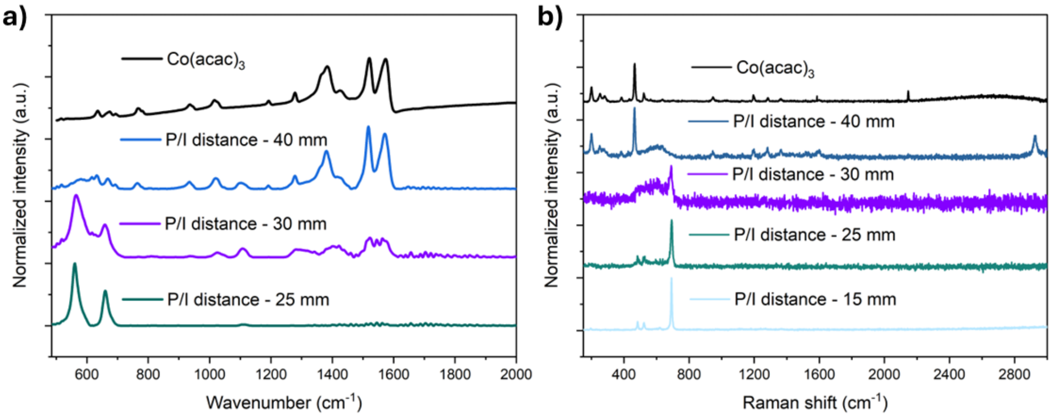

Figure III. 12 - FTIR (a) and Raman (b) spectra of the thin films produced by increasing the plasma torch outlet-precursor injection distance from 15 to 40 mm. The Co(acac)₃ precursor is provided for comparison.

At larger distances, these features degrade. At 30 mm (245 °C), FTIR analysis reveals the presence of organic signatures (listed in Table III.4), indicating incomplete precursor decomposition. Notably, the peak at 1384 cm^{-1}, associated with C–H wagging vibration[262], shows a marked shift and intensity variation compared to the pure precursor, suggesting partial plasma-induced transformation while retaining other carbon-containing fragments. At 40 mm (190 °C), the FTIR spectrum closely resembles that of the unfragmented Co(acac)$_3$ precursor, confirming low decomposition efficiency. However, the presence of a peak at 1100 cm^{-1}, absent in the precursor and attributed to C–O–C bonds[263], indicates that some degree of plasma-precursor-interaction still occurs. This bond likely arises from the fragmentation of the C=O-C precursor bonds, suggesting one fragmentation pathway that only occurs for the films produced closer to the plasma nozzle. At 25 mm, this C-O-C vibrational mode again reduces from the faster oxidation reactions limiting the concentration of organic signatures in the film.

Table III. 4 - FTIR organic signatures obtained from[262–264] *for the films produced at different plasma nozzle-precursor injections distances. The films were compared to the precursor signatures. The* Y_w *shows a strong decrease in signal compared to the precursor peak.*

Peak position (cm^{-1})	**Assignment**	**25 mm**	**30 mm**	**40 mm**	**Precursor**
1570	C=O	N	Y_w	Y	Y
1518	C=O	N	Y_w	Y	Y
1424	C-H	N	Y_w	Y	Y
1382	CH$_3$	N	Y_w	Y	Y
1361	C-H	N	Y_w	Y	Y
1280	C-O	N	Y_w	Y	Y
1191	C-CH$_3$	N	N	Y	Y
1100	C-O-C	Y	Y	Y	N
1016	=C-H	N	Y_w	Y	Y
933	C-O	N	Y_w	Y	Y

Similarly, oxide phase formation decreases as the injection distance increases. At 30 mm, a few Co–O features remain in FTIR, such as the transverse optical bands at 562 and 658 cm^{-1}[265] The A$_1$g peak is still visible in Raman but shifts to 690 cm^{-1} and broadens significantly (FWHM = 17 cm^{-1}). The remaining Co$_3$O$_4$ modes are largely obscured by a broad band centred around 600 cm^{-1}, which has been associated with amorphous CoO$_x$ by Tyczkowski *et al.*[241], suggesting a loss of crystallinity. At 40 mm (190 °C), the spectra further deviate from the Co_3O_4 reference. While well-defined oxide peaks are no longer observed, the broad Raman band near 600 cm^{-1} indicates that some oxide formation still occurs, though with a low degree of structural order.

These results confirm a clear dependence of film quality on the plasma-precursor injection distance. Increasing the plasma-precursor injection distance strongly affected the composition and phase of the thin films. Both the thermal energy and plasma reactivity are crucial for effective Co_3O_4 synthesis. The plasma provides not only thermal energy but also energetic species that fragment the precursor into reactive intermediates, which contribute to film growth and carbon elimination. Maintaining a short injection distance (≤25 mm) ensures sufficient interaction with these species, leading to the formation of dense, contaminant-free, and well-crystallized Co_3O_4 thin films.

3.7. Plasma chemistry

The influence of the plasma chemistry was evaluated by OES analysis. Figure III.11a depicted the rapid variation of plasma chemistry when moving away for the plasma jet outlet. At the plasma jet outlet, N_2 SPS and N_2^+ FNS are the major species with minor NO β concentrations. The NO radiative species become predominant at 10 mm from the exit onwards. The formation of NO molecules likely arises from the interaction with the very energetic N_2 SPS, and especially N_2^+ species. Several reaction pathways for NO formation were discussed[169,170,194,266,267], which is very common in N_2 plasma when interacting with the surrounding atmosphere[192,254]. The strong presence of NO evidence the effective mixing between plasma species and surrounding environment. The loss of N_2^+ species after the first few mm after the exit highlights its high reactivity and low short lifetime[268]. For these reasons, the N_2^+ species and electrons are not expected to participate in the AP-PECVD reaction far from the plasma jet exit. The main consequence for the lack of such species is on the fragmentation pathway, since they are extremely energetic. Electrons, ions, and other excited species have lower lifetimes tending to decay by deexcitation or through collisions with other molecules[176].

3.7.1. Plasma-precursor and plasma-air interactions

Figure III.13a displays optical emission spectroscopy (OES) spectra recorded 17 mm away from the plasma jet outlet, which corresponds to the substrate position, and directly beneath the injection system. Three conditions were analyzed: plasma alone (black), plasma with acetone (magenta), and plasma with the precursor solution (blue). The spectra reveal two dominant species: nitric oxide ($NO^•$) and hydroxyl radicals ($OH^•$). OH is commonly observed in atmospheric pressure plasmas and typically originates from the dissociation of water vapor in ambient air[194]. The reason behind OH was not observed in previous measurements (Figure III.11) is not understood.

The addition of the solvent (acetone) and precursor solution alters the plasma composition. Specifically, the intensity of NO emission decreases, while OH emission increases. The reduction in NO signal suggests a quenching effect, likely due to energy transfer from NO to the injected solvent and precursor molecules. The rise in OH intensity may result from hydrogen abstraction from organic groups in the solution.

RONS, known for their relatively long lifetimes[169], are expected to remain active during the plasma–precursor interactions throughout the deposition process. Similarly, long-lived metastable species such as N_2 metastables (N_2^m), although not directly detected by OES, are likely present[18,269] and may contribute to film formation by transferring energy to the precursor molecules.

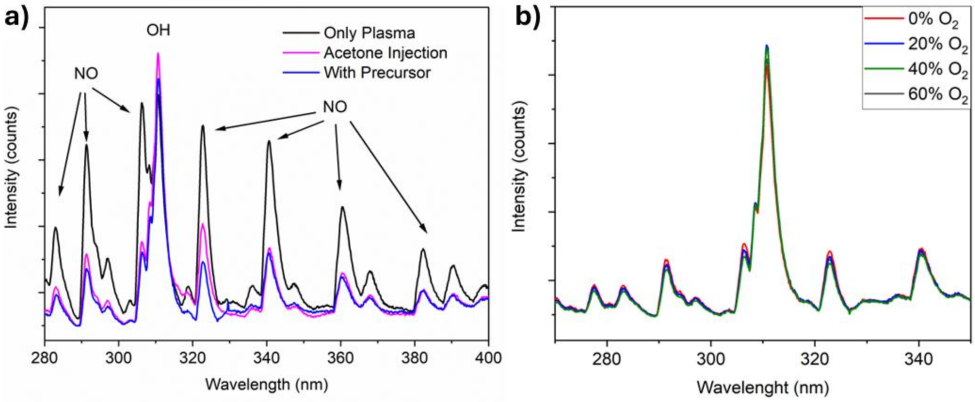

Figure III. 13 - (a) OES measurements with only plasma (black), plasma and acetone (magenta), and plasma and the precursor solution (blue). (b) OES measurements comparing various O_2 concentrations in the carrier gas.

The presence of oxygen-rich radicals after plasma-surrounding air interaction may also explain the minimal impact observed when varying the O_2 concentration in the carrier gas. These radicals likely dominate the oxidation chemistry[170], making the system less sensitive to additional O_2 input. While the O_2 in the carrier gas is injected in the same conditions as the precursor solution, at room temperature, the oxygen-rich radicals already possess higher energies when encountering the precursor. To confirm such differences, the four O_2 concentrations in the carrier gas were evaluated by OES (Figure III.13b). Indeed, no significant intensity variation was observed from the variation on O_2 concentration. Additional oxygen-rich radicals do not seem to be produced in the precursor injection position. The difference between the two oxygen sources likely arises from the energy and concentration of the species they encounter. While the surrounding air is exposed to very energetic N_2 SPS and N_2^+ FNS, the O_2 injected in the carrier gas is much less energetic, not producing additional excited radicals.

Plasma chemistry is very complex, and only part of the molecules, *e.g.*, excited species, can be identified by OES analysis. The thin film formation most likely relies on the synergistic effect of plasma reactive species and heat from the plasma gas[196]. In the present work, the plasma gas temperature is relatively high, and seems to contribute to thin film formation. However, temperature alone did not render the production of a thin film (experiment without plasma). The excited species and radicals produced after the interactions between plasma gas and the surrounding environment (*e.g.*, NO and OH) are also expected to contribute to film formation (Figure III.13a). Hence, despite the possible existence of other reactions, we used reactions R1-R3 to illustrate a possible mechanism for thin film growth. This hypothesis considers that N_2 excited species, *e.g.*, N_2 SPS and metastables, and RONS assist the thin film formation via three main reactions, that comprise the production of precursor radicals, *i.e.*, precursor activation,[21,168] by fragmenting weak precursor bonds[18] (R1) or through the reaction with NO radicals by a multi-step oxidation[220,260] (R2). R2 is possibly enhanced with the increase in temperature (Figure III.11b and Figure III.12). Precursor activation is expected to be initiated in the gas-phase through the production of film-forming species[21]. R1 is represented by the precursor collision with N_2 metastables, but comprises any possible fragmentation pathway, such as by NO or electron impact. However, electron impact should be minor since the electron density in the afterglow is expected to be minimal[176,270]. In contrast, NO β species are likely to participate in the activation process as suggested in Figure III.13a. NO β species have high internal energies (5.7 eV)[199], enabling them to fragment a wide variety of organic bonds.

$$Co - acac_3 + N_2^m \rightarrow Co - acac_2^{\bullet} + acac^{\bullet} + N_2, NO \ldots \qquad \text{(R1)}$$

$$Co - acac_3 + NO^{\bullet} \rightarrow Co - acac_2^{\bullet} + acac^{\bullet} + N_2, OH, NH \ldots \qquad \text{(R2)}$$

These precursor radicals could either react with each other[21] or through potential chemical reactions[205] with available oxygen species (excited or at the ground state). These oxygen species include RONS (*e.g.*, $NO^{\bullet}$ and $OH^{\bullet}$) and environmental O_2. The reactions with the precursor radicals (R3) will deplete the remaining acetylacetonate organic ligands ($O_2C_5H_7$) and provide the necessary oxygen to oxidize carbon and cobalt species. R3 likely occurs at the surface, as suggested by Reuters et al.[211] when exploring SiO_x formation, and confirmed by SEM and TEM images due to the minimal particle formation which suggest that homogeneous reactions are not the main contributor for thin film growth.

$$Co - acac^{\bullet}_{(ligand)} + NO^{\bullet},\ OH^{\bullet} \xrightarrow{thermal\ energy} Co_3O_4\ +\ CO_x, CH_x, NH_x, HCN \quad \text{(R3)}$$

3.7.2. Influence of the surrounding environment (non-oxidizing atmosphere)

The proposed mechanism for Co_3O_4 thin film synthesis relies on the formation of reactive oxygen and nitrogen species (RONS), which is produced through the interaction of plasma species with the environment. To evaluate the necessity of RONS and the plasma fragmentation processes, an AP-PECVD experiment was conducted in a closed chamber held at atmospheric pressure and filled with a non-oxidizing atmosphere using pure N_2 gas. Oxygen concentration inside the chamber was confirmed to be below 0.1%, with no additional O_2 (other than the oxygen available from the solvent and precursor molecules) or external substrate heating applied. The plasma colour also changed noticeably: from yellow-blue in open air to violet in the non-oxidizing environment, which indicates a shift to mainly N_2 plasma emission (Figure III.14). In this setup, the only oxygen sources were the cobalt precursor ($Co(acac)_3$), which contains six oxygen atoms, and acetone (C_3H_6O) as the solvent. Compared to open-air conditions, oxygen availability was significantly reduced, rendering oxide formation challenging. Temperature measurements (Figure III.11b) showed minimal differences between the non-oxidizing (490 °C) and open-air conditions (484 °C). In addition, a slight temperature drop (475 °C) was even observed when O_2 was introduced in the chamber to simulate the atmospheric environment (80% N_2/20% O_2).

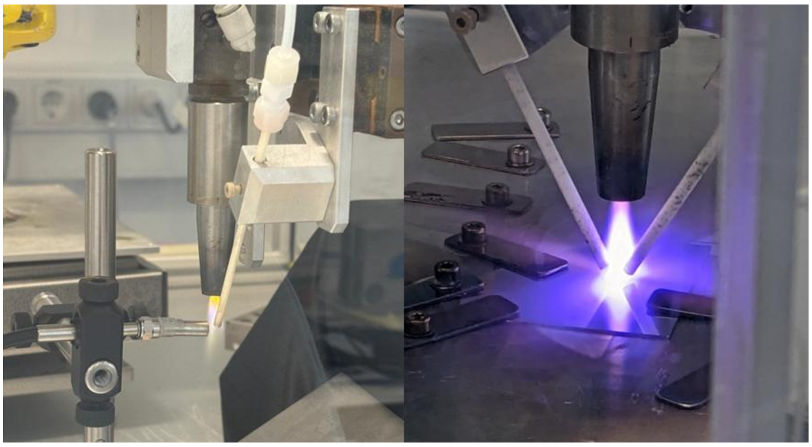

Figure III. 14 - Plasma colour variation on the open-air (left) and inert atmosphere (right). The colour change highlights the lack of O_2 in the non-oxidizing atmosphere

After 10 minutes of static AP-PECVD processing in a non-oxidizing atmosphere, the reaction of Co(acac)$_3$ produced a uniform, adherent black coating on the Si substrate. Cross-sectional SEM analysis (Figure III.4g) revealed a film thickness of approximately 120 nm, indicating a significant reduction (about -85%) in growth rate compared to deposition under open-air conditions.

Furthermore, the Raman spectrum (Figure III.15a - red) and X-ray diffraction pattern (Figure III.15b - red) of the film grown in non-oxidizing atmosphere show no distinct peaks, in contrast to the well-defined signatures observed for Co_3O_4 films synthesized in open air (Figure III.15 - blue). This absence of peaks suggests that the limited oxygen availability under non-oxidizing conditions hinders the formation of crystalline CoO_x phases.

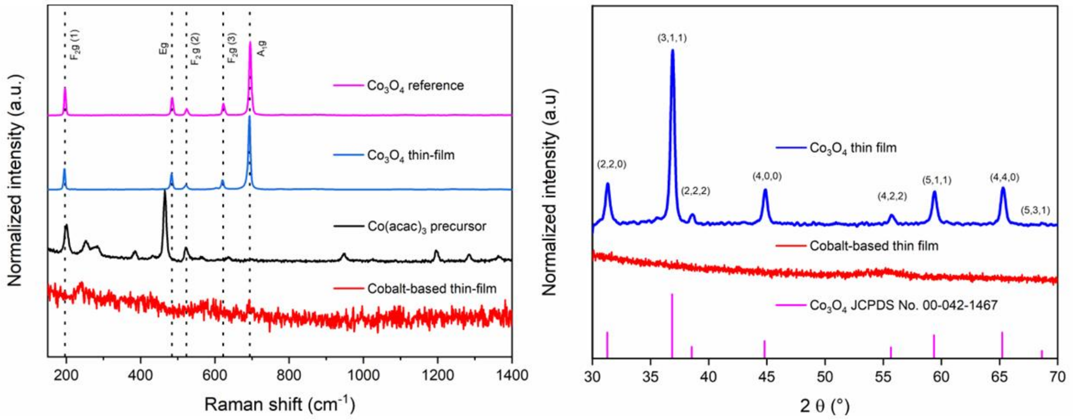

Figure III. 15 - a) Raman spectra of the thin films prepared by AP-PECVD under open-air conditions at 250°C and 40% O_2 in the carrier gas (Co_3O_4 thin film - blue) and in non-oxidizing atmosphere (Cobalt-based thin film - red). The Raman spectra of the reference Co_3O_4 sample (Co_3O_4 reference - magenta), fabricated from the oxidation of a pure metallic cobalt sample, and the raw cobalt precursor (Co(acac)$_3$ precursor - black) are provided for comparison. b) X-ray diffractograms of the cobalt-based thin films prepared by AP-PECVD under open-air conditions at 250°C and 40% O_2 (Co_3O_4 thin film - blue) and under non-oxidizing atmosphere (Cobalt-based thin film - red). The Co_3O_4 reference (magenta) No. 00-042-1467 from the JCPDS database is provided for comparison.

Chemical composition analyses of the thin films prepared under non-oxidizing atmosphere were carried out by ToF-SIMS depth-profiling (Figure III.8 and III.16) and XPS (Figure III.17) and compared with the thin films prepared under open-air conditions (250 °C, 40 % O_2). Figure III.17 shows the chemical composition obtained by XPS for the cobalt precursor, and the films prepared under non-oxidizing and open-air conditions. The films were analyzed near the surface and in the bulk.

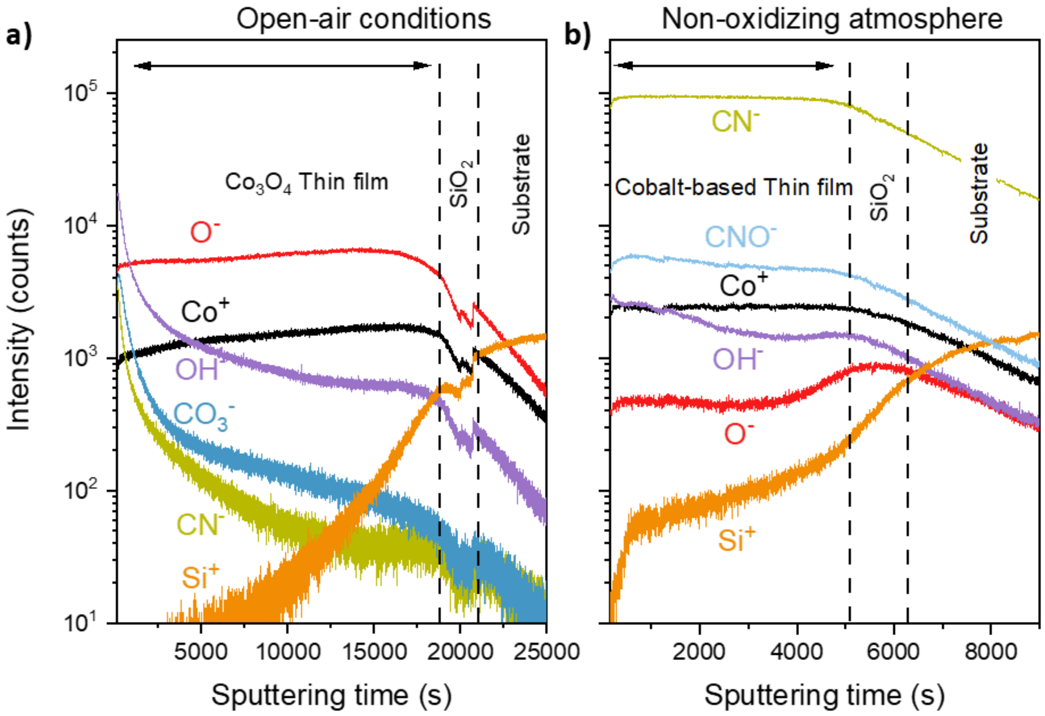

Figure III. 16 - ToF-SIMS profile of the thin films prepared by AP-PECVD under open-air conditions at 250°C (Co_3O_4 thin film) in a) and under non-oxidizing atmosphere (Cobalt-based thin film) in b) without addition of O_2 in the carrier gas. The interface thin film/SiO_2 native layer was identified by the variation of the inflection point from the different elements observed in the profile.

The thin film synthesized in non-oxidizing conditions shows higher carbon contamination than in open-air environment, both in the surface and in the bulk. Indeed, while carbon concentration determined by XPS is ~ 2 at.% in the bulk of the thin film produced in open-air, it reaches ~43 at.% for the thin film produced under non-oxidizing atmosphere. The absence of O_2 also leads to the incorporation of nitrogen moieties highlighted by the 17 at.% buildup in the film prepared under non-oxidizing conditions. ToF-SIMS analyses converge to the same conclusion, revealing significant presence of contaminants (CN^-, CNO^-, CO_3^-, OH^-, etc.) along the thin film. The CO_3^- and OH^- ions are very likely residues from the acac rings while CN^- and CNO^- are by-products from the precursor fragmentation by the plasma species (*e.g.,* N_2 metastables). The nitrogen-rich ions are consistently observed throughout the cobalt-based thin film depth (non-oxidizing conditions). Figure III.8a evidences the non-effective carbon elimination under non-oxidizing atmosphere by comparing the O^-/CO_3^- ratio to thin films produced in open-air atmosphere. A 10-fold ratio decrease was observed for non-oxidizing conditions even without considering the CN^- and CNO^- ions.

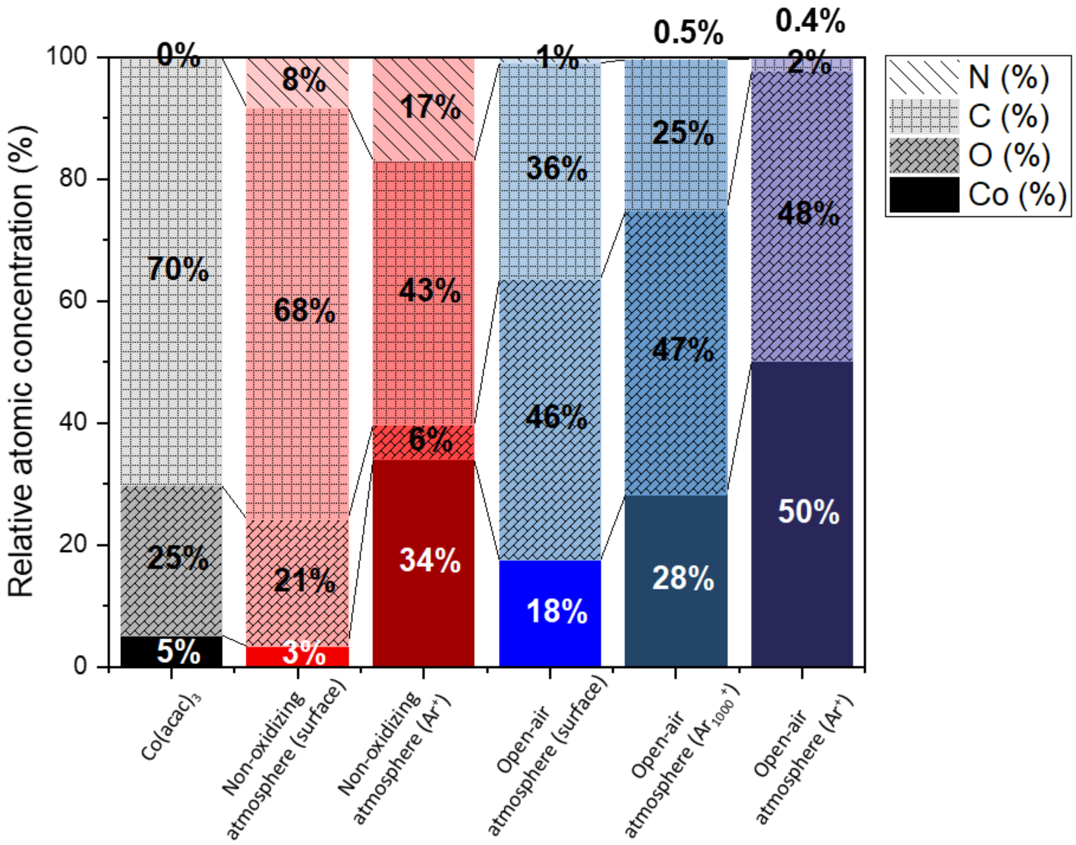

Figure III. 17 - Relative atomic composition of the Co_3O_4 thin films produced by AP-PECVD under open-air conditions (250°C and 40% O_2) and the cobalt-based thin film produced by AP-PECVD under non-oxidizing atmosphere conditions. XPS measurements were performed at the surface of the samples, after 900 s of Ar_{1000}^+ cluster sputtering and after 900 s of Ar^+ sputtering.

Thus, the lack of O_2 in the environment reduces the elimination of carbon-containing moieties from the precursor and possibly from the solvent and allows the incorporation of nitrogen[271]. N atoms and excited N_2 species are expected pathways for nitrogen adsorption on the film[194]. Without oxygen-bearing molecules, volatile nitrogen molecules, *e.g.*, N_yO_x, are not formed[272,273], increasing the nitrogen buildup. Similarly, carbonaceous species rely on the interaction with oxygen-bearing molecules to form volatile carbon species, *e.g.,* CO_x. $NO^•$ and its parent species have very high oxidizing potential[170], and likely contribute to the formation of these volatile species in open-air environment.

The thin film formed under non-oxidizing atmosphere conditions contains cobalt but very low oxygen, which differs with the thin film formed in open air. The Co^+ and O^- intensities observed by ToF-SIMS (Figure III.16) confirm the reduced oxygen concentration throughout the thin films produced in non-oxidizing atmosphere compared to the one produced in open air atmosphere. The O^-/Co^+ ratio determined from ToF-SIMS is significantly lower for the thin film produced in non-oxidizing atmosphere when compared to the one for the films formed in open air atmosphere and where Co_3O_4 was produced. Equally, the Co/O concentration ratio calculated from the XPS results (Figure III.17) highlights a similar difference between the films. The Co/O concentration ratio drops from about 6 for the thin film formed in a non-oxidizing atmosphere to 1 under open-air atmosphere. The higher value for Co/O concentration ratio suggests that cobalt is present in a phase other than oxide. Interestingly, the precursor presents a much lower Co/O concentration ratio (1/5), indicating that former oxygen content from the precursor molecules was preferentially subtracted to cobalt. Likely, the plasma species fragment the Co-O bond of $Co(acac)_3$ during the AP-PECVD process, as shown in R1. This fragmentation will depend on the bond dissociation energies (BDE) of the precursor. Previous works[19,206] proposed a BDE for the cobalt-oxygen bond to be close to the one of C-O (*ca.* 3.8 eV), much lower than the one of C=O (*ca.* 7.8 eV), also present in the acac rings. Therefore, the Co-O bond is expected to deplete faster, explaining the strong increase in the Co/O concentration ratio when compared to $Co(acac)_3$ precursor.

A similar trend is observed in the Co/C concentration ratio. This ratio increases significantly in the thin films compared to the $Co(acac)_3$ precursor, rising from 0.07 in the precursor to 0.78 under non-oxidizing conditions and up to 25 in open-air environments. Under open-air conditions, the substantial carbon depletion likely follows the previously proposed mechanisms (R1–R3), involving fragmentation of $Co(acac)_3$ precursor into carbon-rich intermediates that further react with reactive oxygen and nitrogen species (RONS).

In contrast, under non-oxidizing conditions, the mechanism appears to differ. Excited nitrogen species may initiate precursor fragmentation, as described in R1, leading to partial removal of both carbon and oxygen. Thermal decomposition may also contribute to this reduction, as suggested by Lalancette[219]. Additionally, interactions between plasma-generated species and precursor-derived radicals may further reduce carbon and oxygen content. These reactions likely produce volatile byproducts, but some carbon and nitrogen-containing fragments, such as CN^- and CNO^-, are incorporated into the film structure.

4. Main takeaways

This chapter aimed on synthesizing Co_3O_4 films on Si wafers by the AP-PECVD technique. In addition, the influence of the substrate temperature (due to substrate heating temperature or by changing the plasma-substrate distance) and O_2 concentration (in the carrier gas or in the environment) was investigated. The key takeaways are :

1. Stoichiometric and crystalline Co_3O_4 films were successfully synthesized by AP-PECVD technique. Overall, the Co_3O_4 films were dense, with excellent adhesion to the substrate and exhibited minor carbon contamination (despite being higher near the surface) as desired for protective interconnects coatings.
2. The stoichiometric and inorganic character of the Co_3O_4 coatings disappeared as the precursor injection is moved away from the plasma. Based on Raman spectroscopy, close to stoichiometric Co_3O_4 spinel oxide was deposited for precursor injection below 25 mm of distance from the plasma jet outlet. Further distance implied stronger retention of organic groups from the precursor. This reduction was suggested to be related to decrease in temperature, but mainly to the reduction of concentration of plasma species (necessary for fragmentation and oxidation reactions).
3. The use of heating plate (up to 300 °C) and O_2 addition in the carrier gas was evaluated. No major variations were observed, which was ascribed to the high temperatures already reached by the plasma gas near the surface (~ 700 K) and by the high amount of O_2 already available at the environment.
4. Thin film with low oxygen concentration and high carbon concentration were synthetized under non-oxidizing atmosphere. From this experiment, it is proposed that energetic plasma species fragment the precursor forming radicals, which react with oxygen-rich species produced in plasma (*i.e.*, RONS) to form Co_3O_4 films and eliminate residual impurities.

Based on the observations from Chapter III, we retained that heating the substrate or adding O_2 in the carrier gas are not fundamental parameters for producing high-quality films. The formation of Co_3O_4 films seems to be mainly related with the energy given by the plasma species and oxidation reactions led by reactive oxygen-rich species, *e.g.*, NO radicals. Therefore, the configuration comprising the plasma jet outlet-precursor distance of 15 mm was retained for the Co_3O_4 coatings produced on AISI 441 substrates, which will be discussed in Chapter IV, and presented in Chapters IV and V.

Chapter IV – Performance of Co_3O_4 Thin Films under SOEC Operating Conditions

1. Introduction

In this chapter, the performances of the Co_3O_4 coatings under SOC working conditions were evaluated. In such conditions, the coatings must provide a performance enhancement compared to their uncoated counterparts. In particular, the main objective is to extend the lifetime of AISI 441 interconnects under SOEC conditions, especially by reducing the Cr evaporation rate, the oxidation kinetics, and consequently the ASR increasing rate. These properties were evaluated for two distinct approaches comprising four Co_3O_4 coating thickness (from 400 to 2000 nm) and compared to uncoated AISI 441 substrates. In addition, elemental diffusion in Co_3O_4 (Mn and Cr) was evaluated for these different coatings during short and long-term annealing times. Finally, the effect of the coating on the oxidation growth was evaluated.

2. Methodology

The studied Co_3O_4 coatings were prepared from the AP-PECVD method described in Chapter III. To ensure a complete coverage of the substrate, the plasma jet was displaced horizontally, as shown in Figure IV.1a, with the deposition zone exceeding the substrate dimensions by 2.5 mm on each of the four sides. Figure IV.1b illustrates the path followed during one deposition scan. The plasma jet moves linearly from A0 to A0’, then shifts in the y-direction by an increment Δy to A1’, continues to A1, and so on, until the scan ends (marked by the red circle). The value of Δy was selected based on visual inspection, which indicated improved coating homogeneity with decreasing the increment (data not shown). The lateral deposition region was estimated to extend approximately 0.6 mm on each side of the scan line. Maurau *et al.*[158], using the same equipment, reported that a homogeneous coating is obtained within 0.8 mm, and the thickness decreases significantly beyond that. Based on this lateral coverage, Δy was set to 0.8 mm. As a result, the regions at the edges of each scan are expected to be influenced by two overlapping passes.

Table IV.1 summarizes the parameters used for the coating deposition. The AISI 441 substrate was not heated and O_2 was not added to the carrier gas since they did not induce any improvement as already discussed in chapter III. The plasma jet-precursor injection was set at 15 mm and the substrate position set at 1 mm below the injection point.

The Co_3O_4 coatings were produced using two different sequence strategies, which consisted of varying the displacement speed and the number of scans (Table IV.1). For the samples of batch 1 (named B1), the displacement speed was set at 0.5 mm·s^{-1}, which was observed to produce 150 to 250 nm thick coatings after 1 scan (based on cross-sectional SEM observations). Noticing that the precursor injection is not homogeneous during the whole deposition, after each scan, the sample was rotated by 90° prior to the following scan. Other two 90° rotations were performed, completing 4 total scans, to enhance homogeneity of deposition.

Table IV. 1 – Deposition conditions used for the two batches B1 and B2 used for the oxidation experiments.

Parameters	Batch 1 (B1)	Batch 2 (B2)
Dilution gas	Nitrogen (50 L·min^{-1})	
Plasma power	1000 W	
Atomising gas	N_2 (2 L·min^{-1})	
Carrier gas	N_2 (2 L·min^{-1})	
Precursor concentration	10 mM	
Precursor injection rate	400 µL·min^{-1}	
Displacement speed	0.5 mm·s^{-1}	5 mm·s^{-1}
Number of scans	4	Varied with thickness (150 for 2000 nm)
Coating thickness (nm)	700	400/1000/2000
Deposition time (min·cm^{-2})	100	65/160/330
Substrate heating temperature	No heating	
Plasma nozzle-injection distance	15 mm	
Injection-substrate distance	1 mm	

The rotation strategy is not the ideal procedure since it required the operator to stop the experiment after each scan, increasing the total deposition time.

For the samples of batch 2 (named B2), another strategy was evaluated to enhance homogeneity and make the coating procedure easier. Instead of rotating the samples after each scan, the displacement speed and the number of scans were increased. This strategy focused on the observation that precursor injection varied during the coating deposition due to atomisation limitations (Venturi). By increasing the number of times the plasma jet was passing over a point X, an increase of Co_3O_4 coating homogeneity was observed. The displacement rate was set at 5 mm·s^{-1}, a 10-fold increase compared to what as used for B1, and the number of scans varied with the desired thickness.

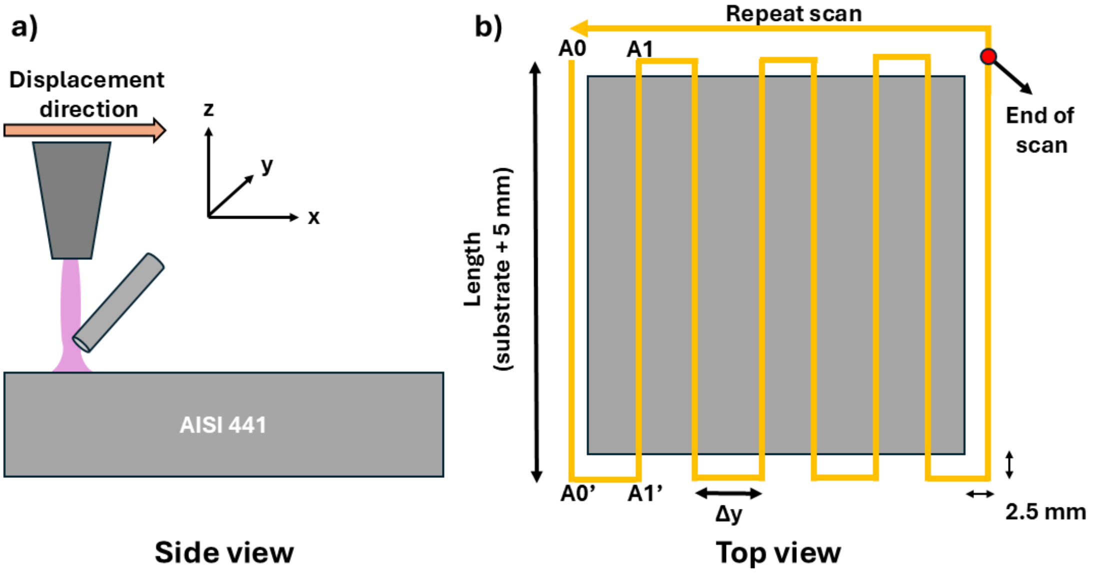

Figure IV. 1 – Scheme indicating the side view (a) and top view (b) of the AP-PECVD deposition on the AISI 441 substrates.

Besides the two different sequence strategies (B1 and B2), four different thickness were tested. For B1, the Co_3O_4 coatings were approximately 700 nm thick while for B2, three thickness were achieved: 400, 1000 and 2000 nm. It is important to note that, although describing the Co_3O_4 coatings with a specific thickness, e.g., B1-700 nm, the Co_3O_4 coatings are not expected to have a homogeneous thickness throughout the substrate. Therefore, the specified thickness rather corresponds to the average Co_3O_4 coating thickness (*th, in cm*), which was calculated from the mass gain values after deposition using the formula:

$$th = \frac{\Delta m}{\rho_{Co_3O_4} \times A} \qquad equation\ IV.1$$

With Δm, the mass gain (g), ρ, the density of Co_3O_4 (6,1 g·cm^{-3})[274] and A, the substrate area (cm^2). The mass gain values were used to confirm the extrapolation made from SEM measurements for a single scan.

The present work evaluated the behaviour of the coated and uncoated AISI 441 substrates by oxidation kinetics (thermogravimetric and discontinuous experiments), long-term annealing and Cr-evaporation experiments, as shown in Table IV.2. The interaction and diffusion mechanisms were studied by SEM and TEM imaging, EDS, SIMS, NanoSIMS, GD-OES for the chemical composition and XRD and Raman for structural analysis. ICP-OES analysis was performed to measure the Cr-volatilisation of the samples. The oxidation growth direction was evaluated using a sequential isotopic oxidation ($^{16}O_2/^{18}O_2$) experiment and evaluated by SIMS.

Table IV. 2 – Description of the experiments performed for each set of conditions.

Experiment	Annealing temperature	Annealing time	Samples
Oxidation kinetics (Thermogravimetric experiments)	800 °C	200 hours	Uncoated and B2 (400/1000/2000 nm)
		500 hours	Uncoated and B1 700 nm
Oxidation kinetics (discontinuous)	850 °C	1, 24, 48 and 120 hours	Uncoated and B1 700 nm
Long-term annealing	800 °C	2500 and 5000 hours	B1 700 nm
Cr-evaporation	800 °C	2000 hours	Uncoated and B2 (400/1000/2000 nm)
Two-stages oxidation test in $^{16}O_2/^{18}O_2$	800 °C	72 hours using $^{16}O_2$ followed by 168 hours using $^{18}O_2$	Uncoated and B2-1000 nm

3. Results

3.1. Description of the "as-deposited" coatings

The morphology and chemical composition of the Co_3O_4 coatings produced under B1 and B2 strategies were evaluated using SEM, confocal microscopy, and Raman spectroscopy. To enable a fair comparison, an additional B2 coating was deposited with the same target thickness as B1 (700 nm). Figure IV.2 presents SEM top-view images at different magnifications. The B1 coating displays lower homogeneity at both macroscopic and microscopic levels, with the presence of large clusters clearly visible on the surface. In contrast, the B2 coating appears much more uniform across the substrate. While similar clusters are also present in B2, they are more evenly distributed and show homogeneous coverage.

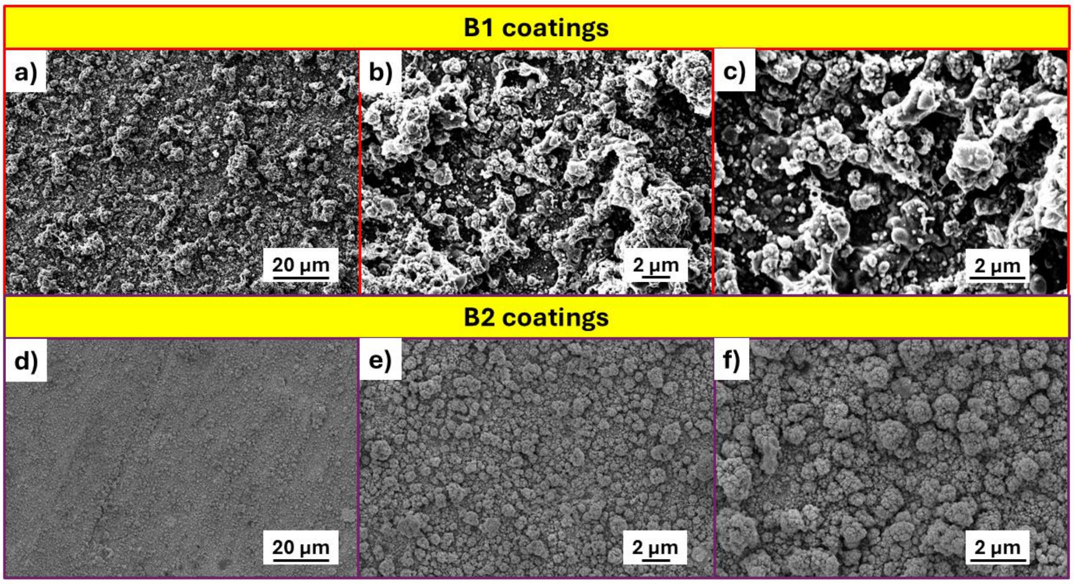

Figure IV. 2 – SEM top-view images from Co_3O_4 coatings produced following batch 1 (a, b and c) and batch 2 (d, e and f). The micrographs were obtained at a magnification of 1000x (a and d), 5000x (b and e) and 10000x (c and f). For a better comparison, the same coating thickness (700 nm) was prepared.

These topological differences are further confirmed by confocal microscopy (Figure IV.3), which reveals the formation of distinct cluster-like islands in the B1 sample, while B2 shows a more even surface profile. The results highlight the impact of displacement speed and the number of scans on the surface topography. In B1, the higher local precursor delivery and slower scan speed promote rapid growth in certain areas, resulting in the formation of clusters and significant local variations in thickness. In B2, the faster displacement speed lowers the precursor input per unit area and reduces the growth rate per scan. Therefore, yielding a smoother and more homogeneous coating.

Figure IV.4 presents the cross-sectional micrographs of the B1 (a) and B2 (b) coatings. Both coatings exhibit excellent adhesion to the AISI 441 substrate, consistent with previous observations on Si wafers (Chapter III). A relatively dense Co_3O_4 layer forms atop the substrate, although a few pores are visible within the coating on both cases. The measured thickness ranges approximately from 300 to 800 nm, within the target value of 700 nm. The B2 samples presented a coating thickness closer to the desired one, with a smaller thickness dispersion. It should be noted, however, that these cross-sections were obtained using FIB-SEM, which provides localized measurements and may not accurately represent the overall thickness distribution across the entire coating.

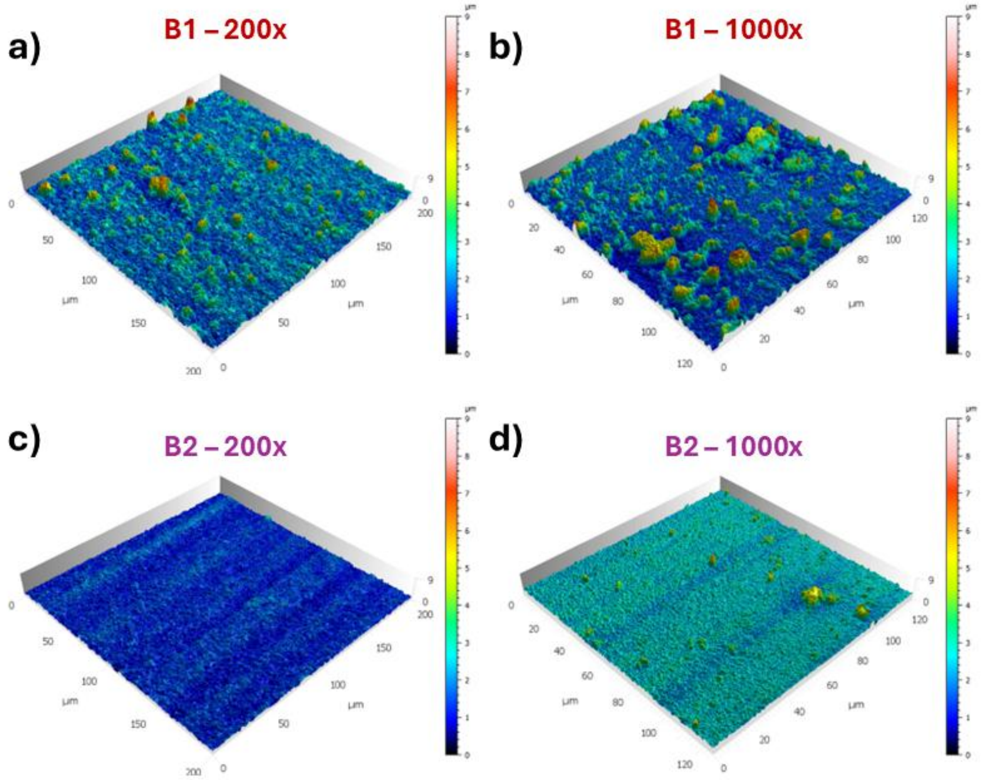

Figure IV. 3 – Surface topography images obtained for B1 (a and b) and B2 (c and d) coatings. The z scale was homogenized in all cases irrespective of the magnification.

Figure IV.5 presents the Raman spectra of the coatings deposited on AISI 441 (B1 and B2) and, for reference, on a Si substrate using a slower displacement speed, as shown in chapter III. All coatings exhibit the five characteristic peaks of the Co_3O_4 phase. Slight variations were observed in the position and width of the main A_1g peak. Specifically, the peak shifts from 688 cm^{-1} in B1 to 690 cm^{-1} in B2, approaching the value observed for the coating on silicon (692 cm^{-1}). The full width at half maximum (FWHM) also narrows in B2, aligning more closely with the reference sample.

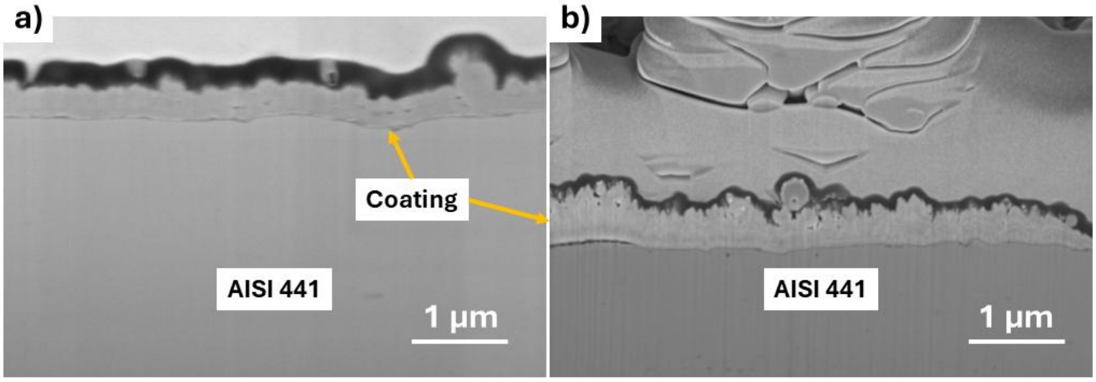

Figure IV. 4 – FIB-SEM cross-section from B1 (a) and B2 (b) 700 nm thick coatings.

These subtle differences are likely influenced by the processing conditions. The peak shift to lower wavenumber may indicate increased lattice strain or the presence of oxygen vacancies[244] in B1, while the sharper peaks in B2 suggest larger or more well-defined crystallites[241]. The improved spectral match in B2 likely results from a more uniform and prolonged energy input during deposition, promoting better quality coatings.

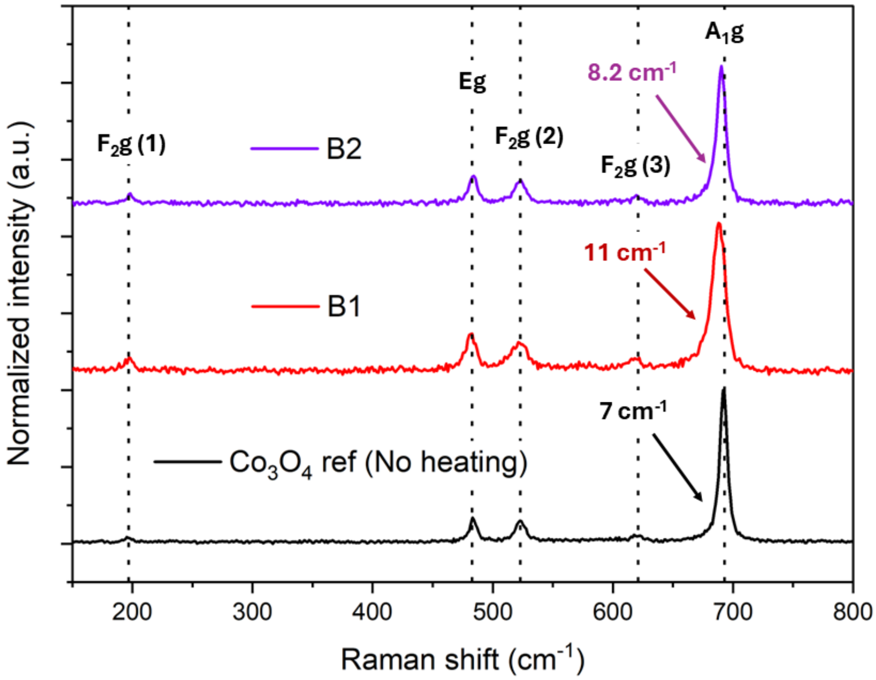

Figure IV. 5 – Raman spectra of coatings produced at 0.05 mm·s^{-1} (Chapter III, black), 0.5 mm·s^{-1} (B1, red) and 5 mm·s^{-1} (B2, violet). The FWHM of the A1g peak of each condition is displayed in the graph.

3.2. Oxidation performance of B1-700 nm sample

3.2.1. Oxidation kinetics at 800 and 850 °C

Figure IV.6 compares the mass gain per area unit as a function of time of the B1 and uncoated AISI 441 substrates at 800 °C and 850 °C. At 800 °C, thermogravimetric experiments (TGA) were carried in flowing dry air (1 L·min^{-1}) while at 850 °C, discontinuous oxidation experiments were conducted using static laboratory air. The mass gain results indicate that coated and uncoated AISI 441 substrates follow a parabolic oxidation behaviour irrespective of the temperature, suggesting the growth of compact and protective oxides controlled by diffusion through it.

The final mass gain area per unit area for coated and uncoated AISI 441 substrates is very similar for both temperatures. Yet, it is possible to observe a few differences, such as the stronger initial mass gain for the coated sample at 800 °C. The mass gain rate, then, slows down, so that the mass gain of the B1 and uncoated AISI 441 samples are roughly the same after 500 h of exposure. The parabolic rate constant (k_p) is used to evaluate the oxidation rate of the samples. k_p is calculated by plotting $\left(\frac{\Delta m}{A}\right)^2 = k_p \times t$, where $\left(\frac{\Delta m}{A}\right)^2$ refers to the square of mass gain per area unit (g^2·cm^{-4}), and t is the time in seconds. k_p is determined by the slope of the plot.

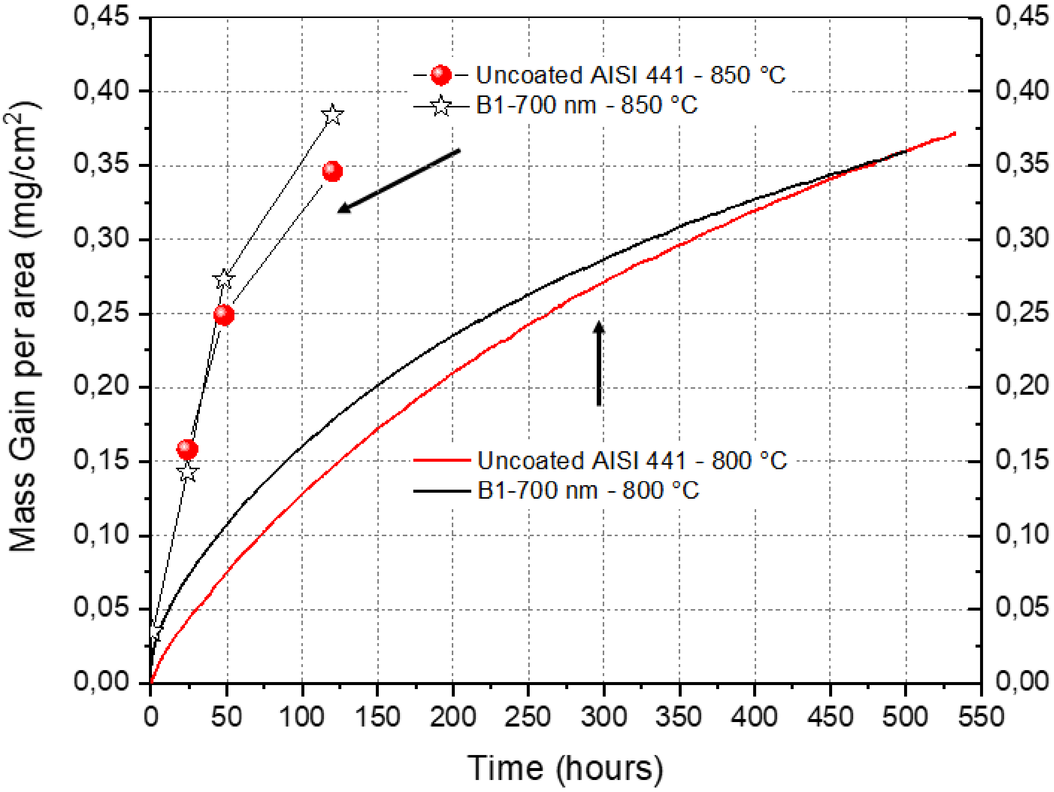

Figure IV. 6 - Evolution of the mass gain per area unit as a function of time for uncoated and coated samples at 800 and 850 °C. At 800 °C, the values were obtained using thermogravimetric (TGA) measurements under dry air while at 850 °C, discontinuous mass gain experiments were carried out under laboratory air.

Table IV.3 presents the k_p values for both coated and uncoated AISI 441 substrates at 800 °C and 850 °C, obtained by fitting the entire oxidation curve and, at 800 °C, for the last 100 h of exposure separately. The k_p values for the uncoated samples at 800 and 850 °C are consistent with those reported in literature for the same substrate[83]. In particular, Spotorno *et al.*[132] measured 25 × 10^{-14} $g^2 \cdot cm^{-4} \cdot s^{-1}$ for uncoated AISI 441. At 800 °C, the k_p values from the full-curve fit are similar for both B1 coated and uncoated AISI 441 substrates. However, when considering only the final 100 h, the coated sample shows a slightly lower k_p, indicating a modest reduction in oxidation kinetics due to the coating over time. At 850 °C, the k_p values are slightly higher for the coated sample compared to the uncoated one. The measured values are in line with those reported by Magrasó *et al.*[92] for Co coatings deposited by PVD on Sanergy™ HT (40 × 10^{-14} $g^2 \cdot cm^{-4} \cdot s^{-1}$), and higher than those for Ce-Co coatings (10 × 10^{-14} $g^2 \cdot cm^{-4} \cdot s^{-1}$).

Table IV. 3 - Parabolic rate constant (k_p) of uncoated and coated AISI 441 substrates at 800 and 850 °C. The k_p values of the AISI 441 substrates oxidized at 800 °C (TGA measurements) were also evaluated in the last 100 h.

	k_p ($g^2cm^{-4}s^{-1}$) $\times 10^{-14}$	k_p (of the last 100 h) ($g^2cm^{-4}s^{-1}$) $\times 10^{-14}$
AISI 441 - 800 °C	7.6	7.5
B1 - 800 °C	7.2	6.1
AISI 441 - 850 °C	29	
B1 - 850 °C	34	

3.2.2. Characterization of the oxide scale at 800 °C

Uncoated AISI 441 substrates

Figure IV.7 shows the SEM cross-section of the uncoated AISI 441 sample after 530 hours exposure to dry air at 800 °C (TGA experiment). The corresponding chemical composition of the oxide scale is presented in Figure IV.7c. A two-layer oxide scale developed: a dense and uniform inner layer of Cr_2O_3 and a non-uniform external layer identified as $MnCr_2O_4$ spinel. While the Cr_2O_3 layer maintains a relatively constant thickness, the $MnCr_2O_4$ spinel oxide shows significant variation due to its polyhedral growth morphology, as reported elsewhere[134,275,276]. The dark spots indicated by the yellow arrows correspond to titanium oxide precipitates, generally reported as Ti_2O_3 or Ti_3O_5[132,277]. Ti oxide precipitates are also observed below the oxide scale within the substrate, indicating internal oxidation. In that case, they are rather TiO_2 precipitates. The internal oxidation is consistent with the high oxygen affinity of Ti, even at low oxygen partial pressures. SiO_2 precipitates were also detected at the alloy/oxide interface, as shown by the Si profile (Figure IV.7c – green triangle). However, a continuous silica layer was not formed. A bright region near the Cr_2O_3/alloy interface corresponds to the formation of the Laves phase (Fe_2Nb), resulting from the presence of Nb in the substrate. This phase is known to sequester silicon[278,279], limiting excessive SiO_2 growth at the oxide/metal interface. This effect is beneficial since SiO_2 has low thermal expansion coefficient and poor electrical conductivity[11]. These features are widely reported in literature for AISI 441[48,83,132,275].

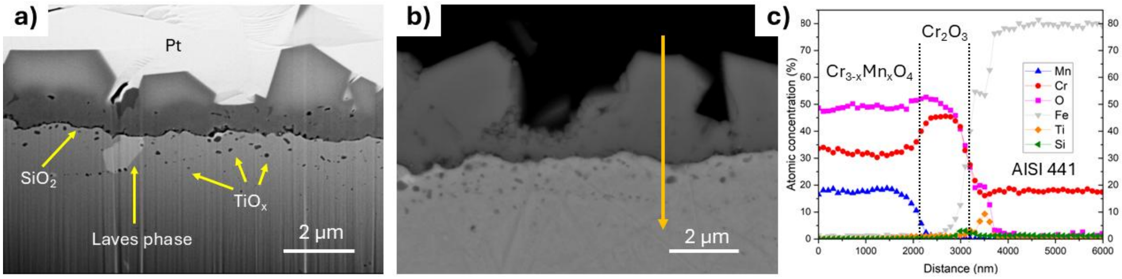

Figure IV. 7 – Uncoated AISI 441 sample oxidized under dry air for 530 h at 800 °C. a) FIB-SEM cross-sectional micrograph highlighting the duplex layer formed atop the AISI 441 substrate and additional features observed after oxidation. b) SEM cross-sectional micrograph. Orange line illustrates the zone analyzed by EDS profiling (c).

<u>B1-700 nm coated sample</u>

Figure IV.8a shows the top-view micrograph of the oxidized B1 sample after exposure at 800 °C for 500 hours. The micrograph highlights the presence of pyramidal grains at the surface, measuring approximately 2 µm. Figure IV.8b and c confirm these pyramidal features in the cross-section view. Furthermore, the backscattered electron (BSE) image reveals the chemical contrast enabling the identification of two phases above the alloy. The composition of theses phases was determined by EDS analysis (Figure IV.8d). The inner oxide layer is very likely Cr_2O_3 and the outer one is the initial Co-oxide coating with significant Mn incorporation. Both layers are compact and cover the totality of the substrate. Pores are visible near the alloy/oxide scale interface in a few regions of the sample. The presence of pores likely relates to the fast outwards diffusion of species from the substrate which creates metallic vacancies in the substrate and then pores[71]. Additionally, the Laves phases highlight the grain boundaries within the alloy, indicating higher concentration of them a few micrometres away from the oxide scale. Titanium oxide precipitates, and SiO_2 were also observed at the alloy/Cr_2O_3 interface (Figure IV.8c).

In addition to the above mentioned phases, very small white precipitates appeared close to the Cr_2O_3/Co-coating interface. These precipitates are identified as HfO_2, which were formed, unintentionally, during the atmospheric plasma deposition process. Indeed, Hafnium, which composes the high voltage electrode material from the plasma jet equipment, is possibly etched by the arc discharge. The formed HfO_2 nanoparticles subsequently reach the surface and end-up randomly dispersed across the coating (Figure IV.8c). The Cr_2O_3 layer thickness is observed to strongly vary throughout the sample, between 1.1 and 2.1 µm, with an average of 1.7 µm, calculated considering several measurements on five cross-sectional micrographs.

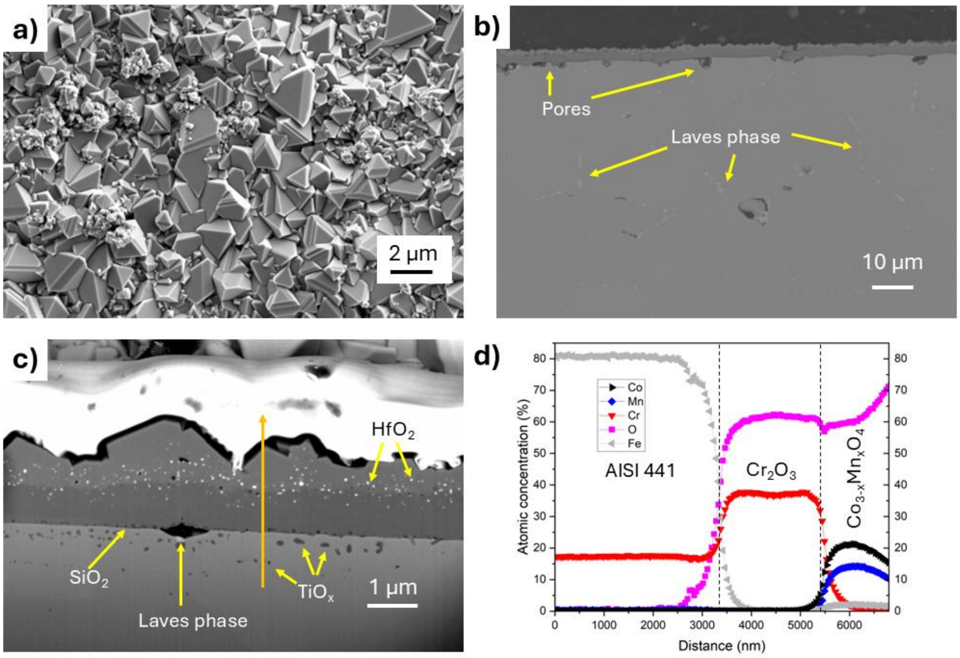

Figure IV. 8 – Co_3O_4 coated AISI 441 sample oxidized under dry air for 500 h at 800 °C. a) Top-view image showing the polyhedral shape of the scale grains. SEM (b) and FIB-SEM (c) cross-sectional micrographs show the various features observed in the micrographs at low and high magnification, respectively. Orange line illustrates the zone analyzed by EDS profiling (d).

Line scan EDS analysis (Figure IV.8d) was performed from the AISI 441 substrate to the external layer such as depicted by the orange arrow on Figure IV.8c). For the sake of clarity, only the major elements are shown in the profile, which reveals the presence of well-defined phases: Cr_2O_3 and Co-Mn oxide. The Mn presence in the coating highlights the diffusion of Mn from the AISI 441 substrate to the coating during the oxidation test. From a Mn/Co concentration ratio of 0.7, the Co-Mn phase was suggested to be a spinel with this stoichiometry: $Co_{1.8}Mn_{1.2}O_4$. Only Co and Mn were reported in the phase notation since only minor concentrations of Cr and Fe, below 2 at.%, were observed.

3.2.3. Characterization of the oxide scale at 850 °C

Figure IV.9 presents SEM cross-sections of coated and uncoated AISI 441 substrates oxidized at 850 °C for varying durations. Compared to uncoated AISI 441 substrates oxidized at 800 °C, the oxide scale at 850 °C appears more homogeneous, with a reduced presence of large Mn–Cr spinel grains (Figure IV.9a,c,e). Other features are consistent with those observed previously, including internal Ti oxidation, formation of the Laves phase, and the development of a two-layer oxide structure above the substrate. Although not well evidenced by the contrast in the SEM images, the Mn-Cr spinel was consistently observed in uncoated AISI 441 substrates, as shown by the EDS profile (Figure 9g). A Cr_2O_3 layer was formed in-between the alloy and the external spinel layer for coated and uncoated AISI 441 substrates. The uncoated AISI 441 substrates exhibited a composition for the external layer of $Mn_{1.35}Cr_{1.65}O_4$ after 120 h annealing, which slightly deviates from the $MnCr_2O_4$ stoichiometry formed for shorter annealing times (24 and 48 h). The external spinel oxide layer showed again a Mn-enrichment with the formation of $Mn_{1.0}Co_{2.0}O_4$, with Cr and Fe concentrations below 2 at.% after 120 h at 850 °C (Figure IV.9h). The Mn-enrichment of this layer seems to increase over time, as shown in Table IV.4. The chemical composition and thickness of the internal and external layers for coated and uncoated AISI 441 substrates after annealing at 800 and 850 °C are shown in Table IV.4. With time, the internal and external layers grow for coated and uncoated AISI 441 substrates (discussed in section 3.2.4).

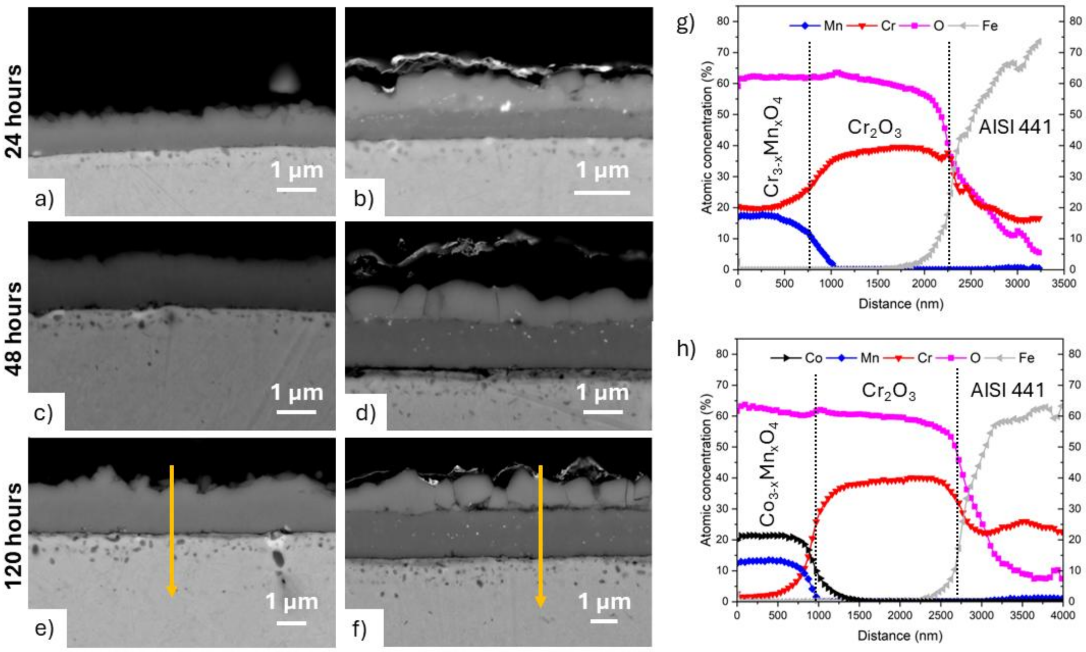

Figure IV. 9 - SEM cross-sectional micrographs showing uncoated (a, c and e) and B1 coated (b, d, f) AISI 441 substrates oxidized for 24 h (a and b), 48 h (c and d) and 120 h (e and f). EDS profiles from uncoated (g) and B1 coated (h) samples after 120 h of exposure at 850 °C are shown.

In the coated samples, bright HfO_2 particles originated from the etching of the high voltage electrode of the atmospheric plasma jet are again present. Interestingly, their position varies over annealing time. After 24 h, HfO_2 is mostly located within the coating layer, whereas after 120 h, it appears predominantly within the Cr_2O_3 layer. Due to their negligible mobility, HfO_2 particles could be considered as inert markers during the oxidation[41,45,46,280].

Their position shift into the Cr_2O_3 layer suggests that the chromia layer grows outwardly during oxidation. The outward growth aligns with previous studies on bare AISI 441[275,281], and it is consistent with the well-established outward-growth mechanism for chromia-forming alloys[48].

Figure IV.10 shows a TEM cross-section of the coated sample oxidized for 120 h at 850 °C. The bright-field image reveals fine equiaxed chromia grains homogeneously distributed, and large columnar Co–Mn spinel grains in the external layer. Elemental mapping confirms the distinct layered structure. It also clarifies the presence of a SiO_2 layer at the alloy/Cr_2O_3 interface and Ti oxide precipitates within the alloy matrix.

GD-OES (Appendix IV.1) analysis were performed to evaluate the presence of minor elements on coated (24, 48 and 120 h) and uncoated (120 h) samples. Coated and uncoated samples annealed for 48 h were also analysed by SIMS (Appendix IV.2). Overall, in coated and uncoated AISI 441 substrates, the concentration of Fe, Nb and Si was negligible in the chromia layer while a small Ti concentration (< 0.5 at.%) was observed. A slight concentration increase was detected in the external spinel layer for Fe, Nb and Ti for the uncoated AISI 441 substrates. From these elements, only Fe was detected in the external spinel layer of coated samples. Interestingly, the concentration of iron decreases with increasing oxidation time, from ~ 1 at.% after 24 h to ~ 0.5 at.% after 120 h. This Fe reduction likely results from Fe diffusing into the oxide scale only at the early stages before the formation of a continuous Cr_2O_3 oxide layer[282]. After the Cr_2O_3 formation, Fe concentration reduces due to continuous Mn enrichment of the spinel layer which dilutes Fe.

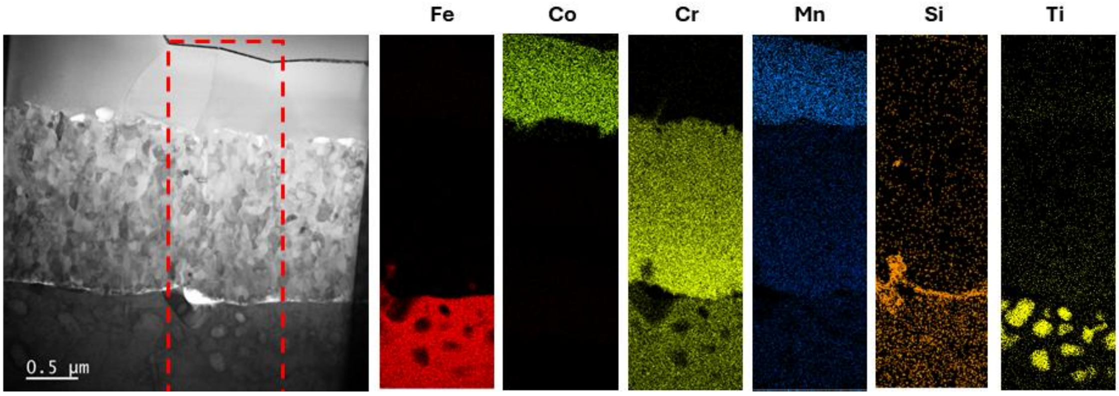

Figure IV. 10 – STEM-EDS mapping from B1 samples oxidized under laboratory air for 120 h at 850 °C.

3.2.4. Mn-diffusion in the external spinel oxide at 800 and 850 °C

Table IV.4 presents the evolution of the composition of the external spinel layer with time for coated and uncoated AISI 441 substrates after exposure at 800 °C or 850 °C. Uncoated AISI 441 substrates showed, with the exception of the sample oxidized for 120 h at 850 °C, the stoichiometric $MnCr_2O_4$ composition. The coated samples showed a continuous increase in Mn content over time, confirming an increase of Mn/Co concentration ratio in the spinel layer with time. It is important to note that the diffusion is much faster at 850 °C compared to 800 °C, such as expressed by the faster Mn-enrichment.

Table IV. 4 – Chemical composition of the inner and external layer formed during oxidation at 800 and 850 °C of coated and uncoated AISI 441 substrates. The thickness (ImageJ) and the chemical composition (EDS) of the chromia and spinel layers were obtained from the average measurements performed on at least five micrographs.

	Chromia layer thickness (µm)	Spinel composition	Spinel thickness (µm)
B1-800°C-500h	1.7 ± 0.3	**$Co_{1.8}Mn_{1.2}O_4$**	**1.1** ± 0.3
AISI 441-800°C-530h	0.8 ± 0.2	$MnCr_2O_4$	1.3 ± 0.4
B1-850°C-1h	0.3 ± 0.1	**$Co_{2.8}Mn_{0.2}O_4$**	**0.5** ± 0.2
B1-850°C-24h	0.7 ± 0.2	**$Co_{2.45}Mn_{0.55}O_4$**	**0.5** ± 0.1
AISI 441-850°C-24h	0.6 ± 0.2	$MnCr_2O_4$	0.4 ± 0.1
B1-850°C-48h	1.1 ± 0.1	**$Co_{2.35}Mn_{0.65}O_4$**	**0.9** ± 0.1
AISI 441-850°C-48h	0.8 ± 0.1	$MnCr_2O_4$	0.5 ± 0.1
B1-850°C-120h	1.7 ± 0.1	**$Co_{2.0}Mn_{1.0}O_4$**	**1.2** ± 0.2
AISI 441-850°C-120h	1.3 ± 0.3	$Mn_{1.35}Cr_{1.65}O_4$	0.9 ± 0.3

Raman spectroscopy was performed to follow the structural evolution of the phases formed during oxidation for coated and uncoated AISI 441 samples over time. Figure IV.11a compares the spectra of the as-received substrate and those oxidized at 850 °C for 24, 48, and 120 h with a Cr_2O_3 reference (*RRUF ID R060892*). No peaks are observed in the unoxidized uncoated AISI 441 substrate, as expected for the pristine AISI 441 metallic substrates.

The oxidized uncoated AISI 441 substrates showed prominent peaks at ~ 558, 645, and 685 cm^{-1} for all annealing times. These peaks closely match the Cr_2O_3 reference, which presents strong bands at 550, 649, and 687 cm^{-1}, despite the minor shifts, which could be attributed to doping effects, from substrate elements diffusing into the chromia layer or to another phase. Indeed, as observed by EDS measurements, a Mn-Cr rich phase was formed in the external layer. Only a study from Dutta *et al.* was found on $MnCr_2O_4$ spinel using Raman spectroscopy[283]. In the study, prominent peaks appear at 512 and 669 cm^{-1}, in contrast to peak positions observed here. Nonetheless, several studies explored other chromate spinels using Raman spectroscopy[284–286]. Overall, these chromate spinels exhibit a strong A_1g mode near 680 cm^{-1}. The octahedral sites of ACr_2O_4 chromates (A = cations in tetrahedral sites) are fully occupied by Cr cations[285,287,288], and the variation of the tetrahedral cation led to only minor peak shifts. Therefore, the peak observed at 685 cm^{-1} could be assigned to $MnCr_2O_4$, considering the Mn cation should occupy the tetrahedral position. The large peak broadening around 685 cm^{-1} could likely be explained by the overlap of peaks from $MnCr_2O_4$ and Cr_2O_3.

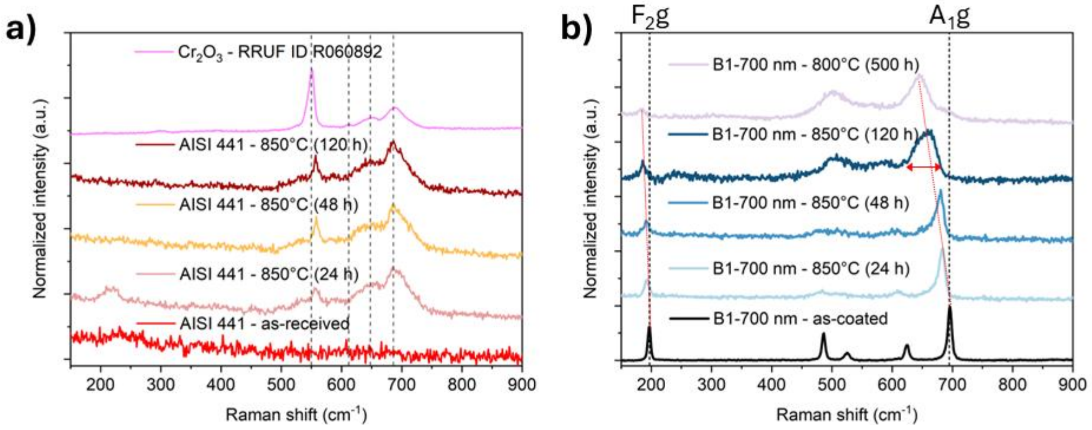

Figure IV. 11 - Raman spectra from uncoated (a) and B1 coated (b) samples at various oxidation conditions. Samples were compared with a Cr_2O_3 reference spectrum (a) and with the as-coated sample (b). Reference lines were used to highlight the peak positions from the Cr_2O_3 reference (a) and F_2g (1) and A_1g lines from the initial Co_3O_4 spinel. Dotted red lines show the peak shift and the red arrow, the broadening of the peaks.

Figure IV.11b evidenced the increase of Mn concentration in the Co_3O_4 with exposure time. The Mn content increase creates a shift and broadening of the Raman active modes. The spectral broadening complicates the identification of certain modes, particularly the Eg, F_2g (2) and F_2g (3) bands, at longer oxidation durations. Nevertheless, the A_1g and F_2g (1) modes remain discernible and can serve as reliable indicators of Mn incorporation into the spinel lattice.

Mn cations have larger ionic radii than Co cations which leads to lattice expansion. Thus, Mn incorporation in the Co rich spinel is expected to cause a peak shift to lower wavenumbers[289]. As discussed in chapter III, the A_1g and F_2g (1) modes relate mainly to vibrations on the octahedra (BO_6) and tetrahedra (AO_4), respectively[240]. Both modes showed a shift to lower wavenumbers, with a bigger variation of the A_1g mode. The peak width (FWHM) is also largely influenced by the increase in Mn content. Similar trends were reported by Bahlawane *et al.* for Fe-doped cobalt spinels[290], where peak broadening and the peak shift to lower wavenumbers were attributed to lattice distortion, higher degree of structural disorder and reduced bond strength. The increase in structural disorder is expected with Mn incorporation due to the strong valence variability of Mn[98,110] and likely increase in configurational entropy[289]. Liao *et al.* further associated such broadening with a decrease in bond strength and packing density[291].

3.2.5. Coating influence on Mn and Cr oxidation rate at 850 °C

To accurately understand the influence of the coating on the oxidation kinetics of AISI 441, the amounts of oxidized Cr and Mn from the substrate were calculated. For that purpose, the oxide thickness of the Cr-rich phases, comprising Cr_2O_3 and $MnCr_2O_4$, formed on coated and uncoated AISI 441 substrates was, first, assessed by measuring their thicknesses on various micrographs with the ImageJ software[292]. Then, by measuring the chemical composition by EDS analysis, the amount of Cr and Mn oxidized was calculated using the following equation

$$N_i = \frac{2 \times x_i \times th_O \times \rho_O}{M_O \times 10^7} \qquad (\mathrm{IV.2})$$

where N_i is the oxidized amount of Cr or Mn in mol·cm^{-2}, x_i is the Cr or Mn stoichiometric content in the oxide phase, th_O is the oxide thickness, ρ is the density and M is the molar mass of the oxide. The molar mass for each compound was calculated based on the Mn content and the density was considered to be 5.22, 4.94 and 5.56 g·cm^{-3} for Cr_2O_3, $Cr_{3-x}Mn_xO_4$ and $Co_{3-x}Mn_xO_4$, respectively. The densities of the mixed oxides were considered for x equal 1 irrespective of the value of x.

Figure IV.12 presents the oxidized amount of Mn and Cr in mol·cm^{-2} (a) and the evolution of the square thickness of the Cr-rich oxide scale (Cr_2O_3 and $Cr_{3-x}Mn_xO_4$) (b) as a function of time at 850 °C. Figure IV.12a indicates that the oxidized amount of Cr and Mn are closely related for coated and uncoated samples. These results are not surprising considering that the mass gains per unit area were also very similar (Figure IV.6). The graph confirms the parabolic-type behaviour of Cr oxidation but suggests that the amount of oxidized Mn increases linearly for both coated and uncoated AISI 441 substrates. The linear increase of the square thickness of the Cr-rich oxide layers in Figure IV.12b confirms their parabolic growth. Nonetheless, the slope is much less pronounced for the coated samples which indicates a reduced growth of Cr-rich oxides. The reduction in the formation rate of Cr-rich oxides in coated samples is related to the formation of a Co-Mn rich spinel instead of Cr-Mn spinel oxides.

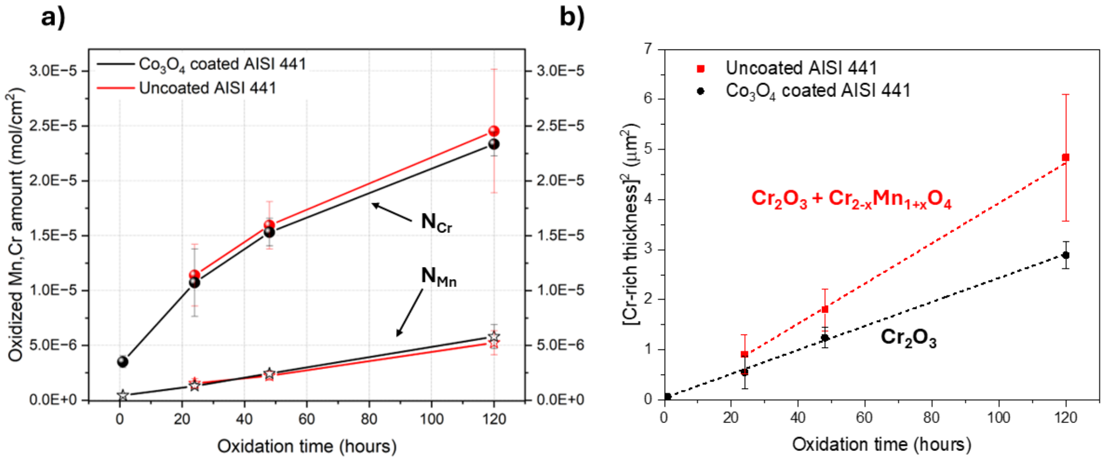

Figure IV. 12 - a) Amount of oxidized Cr (sphere) and Mn (star) over time, in mol·cm^{-2}, for the uncoated (red) and coated (black) samples oxidized at 850 °C under laboratory air. b) The square thickness of the layers showing a Cr-rich phase for the uncoated (red) and coated (black) samples.

3.2.6. Formation of a Co-Mn-Cr Reactive layer (RL) between Cr_2O_3 and the Co-Mn spinel layer

Outwards Cr diffusion was also evaluated for coated AISI 441 substrates. While uncoated AISI 441 substrates have shown the formation of Cr-Mn spinel oxide layer externally, the presence of the Co_3O_4 coatings seems to limit the Cr-enrichment of the external spinel layer. GD-OES analysis (Appendix IV.1) indicated a concentration below 0,1 at.% of Cr close to the oxide surface for coated samples annealed at 850 °C for 120 h. To better understand how the Co_3O_4 coatings inhibit this enrichment, the cross-section of the B1-700 nm sample oxidized at 850 °C for 120 h was analyzed using NanoSIMS. Figure IV.13 a,b,c indicates the mapping of the cross-section of the sample for Mn, Cr and Co, respectively. The intensity profile is displayed in Figure IV.13d, indicating the presence of four distinct phases: AISI 441, Cr_2O_3, a mix Co-Mn-Cr phase and the Co-Mn spinel oxide. This mix phase was not clearly observed previously from other techniques, likely due to its relatively low thickness. This phase is also known as Reactive Layer (RL): it consists of the formation of spinel oxide layer composed of Cr, Mn and Co. This RL was produced between chromia and spinel oxides.

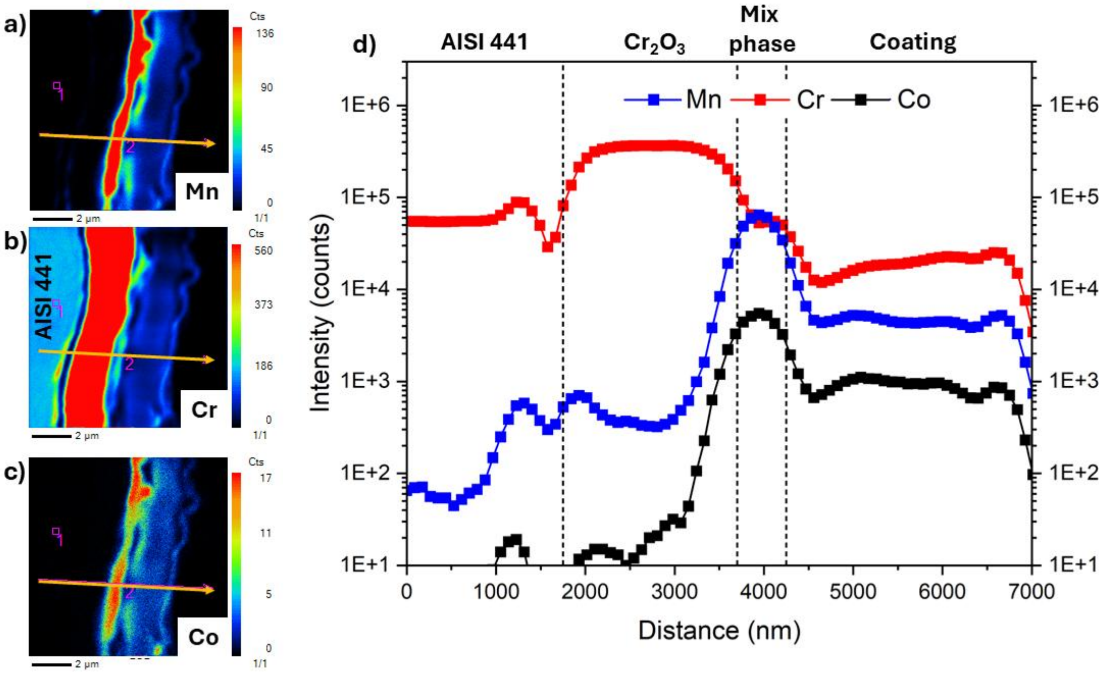

Figure IV. 13 - NanoSIMS analysis of the cross-section of B1 coated AISI 441 substrate annealed at 850 °C for 120 hours. Elemental mapping is shown for Mn (a), Cr (b) and Co (c). The elemental profile is shown in (d).

STEM-EDS results (Figure IV.14) performed on the same sample (B1-700 nm) exposed in laboratory air for 120 hours at 850 °C confirm the formation of this RL between chromia and spinel oxides. Figures IV.14c,d,e,f indicate the elemental mapping of Cr, Co and Mn altogether and separately, respectively. The dotted line highlights the interface of the Co mapping. Interestingly, this interface does not match the Cr and Mn interfaces, with particularly Cr and Co overlapping near the chromia/Co-Mn spinel interface. This overlapping confirms the formation of a RL spanning over few nanometres between the chromia and Co-Mn spinel. Moreover, a horizontal profile was traced within the Co-Mn spinel layer comprising two grain boundaries (Figure IV.14b). The profile indicates minimal Cr concentration inside the spinel grain but reveals a higher Cr concentration in the grain boundaries, suggesting a pathway for Cr-diffusion. This observation is in agreement with Kim *et al.*'s study where they suggested that Cr diffusion occurs via grain boundary diffusion in the Co-Mn spinel layer supplying Cr to the Co-Mn grain, and possibly to the surface[276]. In our work, the coated samples displayed a very low Cr concentration near the surface, suggesting that GB diffusion of Cr did not occur up to the surface for the used temperature and exposure time conditions (Figure IV.14d).

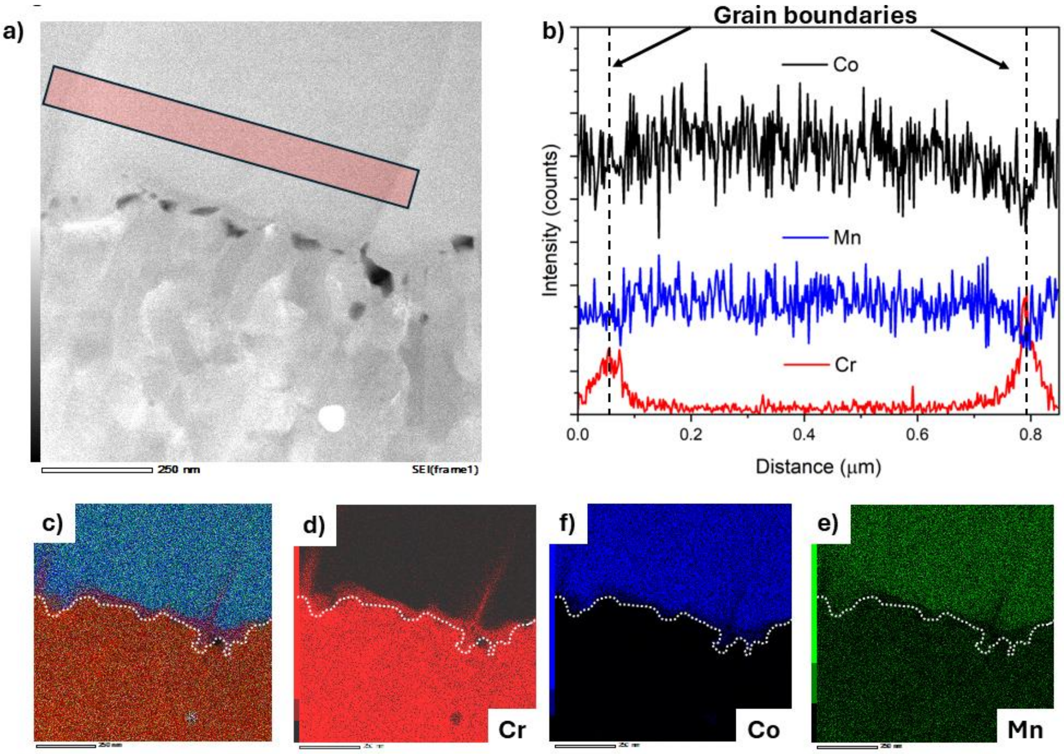

Figure IV. 14 – TEM analysis of the B1 coated sample annealed at 850 °C for 120 hours. a) STEM cross section showing the chromia scale (down) and Co-Mn spinel (up). The red rectangle indicates the region analyzed by EDS (b). c) Represents the elemental mapping of Cr (d), Co (e), and Mn (f) altogether.

3.2.7. Long-term exposure of B1-700 nm coatings

The long-term stability of the B1-700nm Co_3O_4 coatings was assessed after thermal exposure at 800 °C for 2500 and 5000 hours in laboratory air. Figure IV.16a and c shows the SEM cross-section of the B1 samples after 2500 and 5000 h, respectively. Over time, the presence and size of pores increased. The pores were mainly present near the alloy/chromia interface but also internally on the substrate. These pores are likely created by the accumulation of metallic vacancies, originated from the Cr and Mn diffusion for the oxide scale formation[278].

EDS profiles were carried out through the different oxide layers formed above the alloy (Figure IV.16b and d). The chemical profiles indicate a mild Mn enrichment near the alloy/Cr_2O_3 interface, particularly after 5000 h (Figure IV.15d). This Mn enrichment was observed previously at 850 °C using NanoSIMS analysis (Appendix IV.3) and indicates the formation of a Mn-Cr-rich phase in this region. However, the Mn concentration rapidly decreases away from the interface in the upper part of the Cr_2O_3 layer. Above the Cr_2O_3 layer, the initially Co-Mn-rich layer becomes rich in Cr after 2500 h of exposure. The Cr concentration at the spinel/gas interface is about 10 at%. Thus the so-called reactive layer (RL)[121,141] considerably grew compared to short exposure time and Cr is found throughout the whole spinel layer. These observations indicates that the coating efficiency against outwards Cr diffusion reduces over time. Within this RL, the chemical profile of Cr and Mn strongly varies. Cr concentration reduces towards the surface while Mn concentration increases. Interestingly, Co concentration remains relatively stable across the entire RL irrespective of the exposure time.

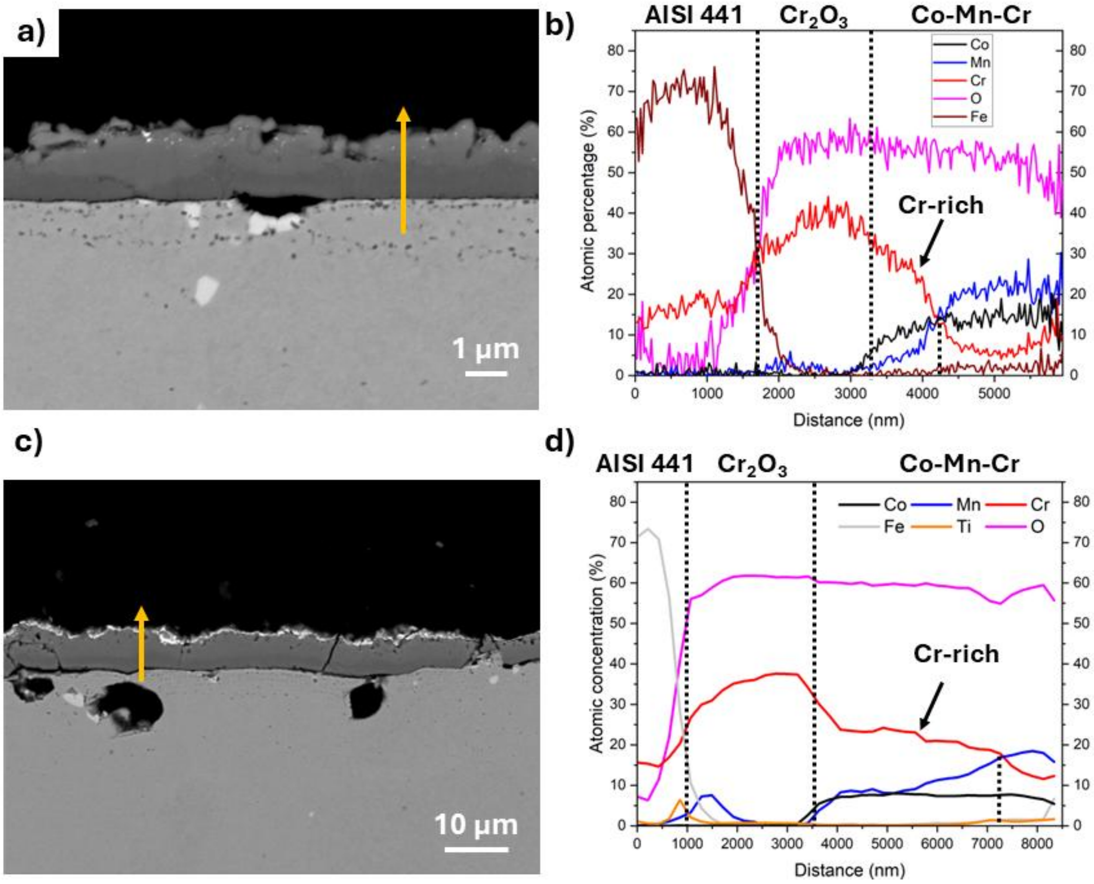

Figure IV. 15 – SEM cross-sections (a,c) and EDS profiles (b,d) of B1 coated samples annealed at 800 °C for 2500 h under laboratory air (a,b) and 5000 h (c,d) under an O_2 atmosphere. The dotted lines are used to highlight each layer of the chemical profile. The small-dotted line separates the Cr-rich sublayer (indicated by the region where Cr content is higher than Mn) and the Mn-rich sublayer (higher Mn content).

These compositional evolution features were further confirmed by XPS depth profiling (Figure IV.16a). In the profile, only the metallic Mn, Cr and Co elements were followed, and the results are presented in relative atomic concentration. The depth profiling was finished before reaching the Cr-rich part of the Reactive Layer. Due the strong variation of the chemical profile, the RL was stratified into two regions: a Cr-rich and a Mn-rich sublayers.

The Mn-rich layer was defined to start when Mn content becomes superior to the Cr content.

Raman spectroscopy was performed on the sample oxidized for 2500 h and compared to the initial Co_3O_4 coating and to the oxidized uncoated AISI 441 substrates (Figure IV.16b). Significant changes were observed compared to previously analyzed samples (Figure IV.11). The peaks showed significant broadening, and a new intense peak emerged at ~ 572 cm^{-1}. Additionally, the $F_{2g}(1)$ mode appeared at approximately 180 cm^{-1}, while the A_1g peak appeared at 665 cm^{-1} and developed a shoulder near 625 cm^{-1}, not previously observed. The spectral features now closely resemble those of the oxidized uncoated AISI 441 substrates (magenta) although slightly shifted to lower wavenumbers, as indicated in Figure IV.18b. These features corroborate with the substantial Cr incorporation into the spinel lattice. The shift to lower wavenumbers compared to the uncoated AISI 441 substrates likely arises from the partial occupation of Mn cations on the octahedral sites compared to a fully Cr occupied octahedra in $MnCr_2O_4$. Moreover, the observed peak broadening is slightly more pronounced than in Co-Mn spinels with high Mn content (Figure IV.11). This broadening is expected due to the increased structural complexity of the lattice. In this case, octahedral sites may be simultaneously occupied by Cr^{3+}, and different cation valences of Mn and Co, contributing to the disorder and resulting spectral features (Figure IV.16b). These features will be discussed in detail in section 3.3.4.

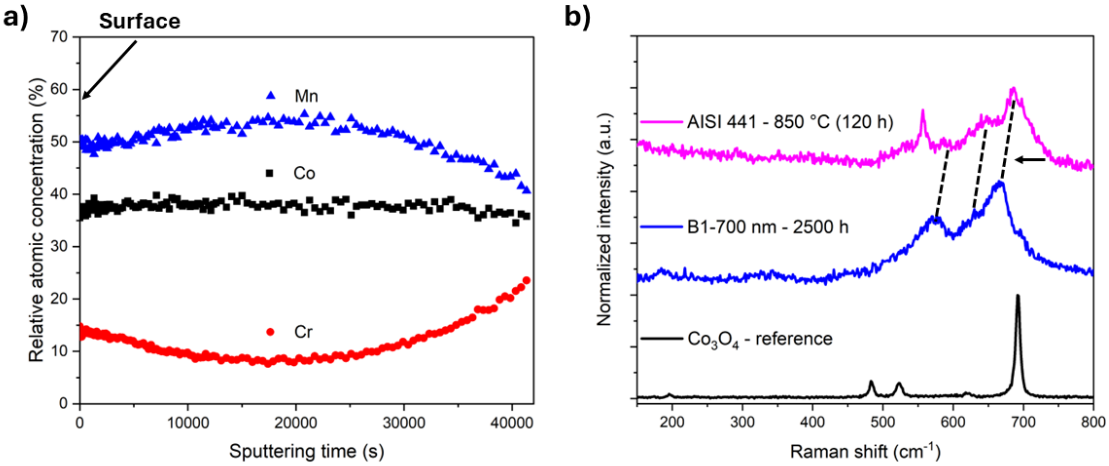

Figure IV. 16 – XPS analysis (a) and Raman spectra (b) of the B1 coated samples annealed at 800 °C for 2500 h under laboratory air. XPS analysis shows the relative atomic concentration of Mn, Co and Cr over the sputtering time. The XPS profile is performed from the surface to the oxide Oxygen was not considered in the measurements. The Raman spectrum of the B1 coated sample (blue) is compared to an unoxidized Co_3O_4 reference sample (black) and oxidized AISI 441 (magenta).

From the EDS profiles and the Raman analyses, it can be proposed that Mn and Cr atoms are in competition for the same crystallographic sites in the RL. This point will be discussed in the Discussion part.

The evolution of the thickness and composition of all oxide layers with exposure time were also analysed carefully. Interestingly, the Cr_2O_3 layer thickness did not increase between 500 and 2500 h (about 1.7 µm) and only slightly increased to 2.0 µm after 5000 h. In contrast, the external spinel oxide layer, more than doubled in thickness, from 1.1 µm (500 h) to 2.1 µm (2500 h) and to 3.0 µm (5000 h). The reduced Cr_2O_3 growth seems to relate with the increased growth of the external spinel layer. This relation is explained by the high Cr concentration in the external spinel layer, which indicates that the diffusing Cr was mainly incorporated to this layer. This relation will be discussed in detail in section 4.2 and 4.3.

The formed outer spinel oxide layers are mixed spinels of $Co_{3-x}Mn_{x-y}Cr_yO_4$ type. Table IV.5 presents the Cr and Mn-rich layers composition, their thickness and the thickness proportion of both layers. The inner Cr-rich spinel sublayer thickness increases over time, almost doubling between 2500 h (1.1 µm) and 5000 h (1.85 µm). On the other hand, the Mn-rich sublayer maintains a similar thickness (~ 1.1 µm) and roughly the same concentration. Co concentration is reduced in the external Mn-rich sublayer which is expected if the whole spinel layer (the Cr-rich and the Mn-rich sublayers) grows since all Co comes from the initial Co_3O_4 coating and no other Co source from the substrate is available.

Table IV. 5 – Thickness values of the chromia and spinel layers and the composition of the spinel sublayers for B1 coated samples at 800 °C for 2500 and 5000 h. The ratio of each sublayer is also displayed.

	Cr_2O_3 thickness (µm)	Total Spinel thickness (µm)	Inner spinel layer (Cr-rich)	External spinel layer (Mn-rich)	Inner/External spinel thickness ratio
2500 h	1.7 ± 0.5	2.1 ± 0.4	$Co_{0.7}Mn_{0.6}Cr_{1.7}O_4$	$Co_{0.9}Mn_{1.2}Cr_{0.9}O_4$	0.5/0.5
5000 h	2.0 ± 0.5	3.0 ± 0.7	$Co_{0.7}Mn_{0.6}Cr_{1.7}O_4$	$Co_{0.6}Mn_{1.4}Cr_{1.0}O_4$	0.6/0.4

The external Mn-rich sublayer shows a high Mn/Co concentration ratio, which is above unity, 1.3 and 2.3 after 2500 and 5000 h of exposure, respectively. Considering the whole spinel layer, the Mn/Co concentration ratio was also high: 1.0 and 1.3 after the 2500 and 5000 h of exposure time, respectively. Such observation demonstrates that the Mn concentration and, in consequence, the Mn/Co concentration ratio increases with exposure time in the outer spinel layer.

3.2.8. Preliminary discussion

Our results demonstrate that Mn diffuses progressively into the initial Co_3O_4 spinel layer which increases the Mn/Co concentration ratio in the outer spinel layer with exposure time. Overall, the B1 coating effectively avoided Cr diffusion initially but Cr diffusion barrier degrades over time which is evidenced by the fast growth of the Reactive Layer and, eventually, the increase of the Cr concentration at the oxide/gas interface. Interestingly, the progressive loss of the Cr diffusion barrier ability of the spinel coatings coincides with an increasing Mn/Co concentration ratio in it. This observation is in good agreement with previous reports which suggests that a high Mn/Co concentration ratio in Co-Mn spinel enhances outwards Cr diffusion[110,117].

To go further in that understanding, more studies were carried out in the next section. In these studies, the Co_3O_4 coating thickness was varied and the effect of the thickness on the oxidation performance and RL formation rate was evaluated. From the preliminary discussion, it is expected that a thicker Co-oxide coating which provides a larger reservoir of Co will delay the increase of the Mn/Co concentration ratio and, in consequence, will decrease the outwards Cr diffusion rate and RL growth rate. This work is carried out on the more homogeneous coatings prepared from the second deposition procedure (B2).

3.3. Oxidation performance of B2 coated samples

3.3.1. Oxidation kinetics

Figure IV.17 compares the mass gain per area unit over time of the uncoated and B2 coated AISI 441 substrates. The graph displays the results from the thermogravimetric measurements, conducted in dry air at 800 °C for 200 h (B2 coated samples) and 530 h (uncoated AISI 441 substrate). From these results, the parabolic rate constant (k_p) was calculated for each sample, and the values extrapolated to 2000 h. This extrapolation was performed to compare the expected mass gain per area unit with the experimental data obtained after discontinuous oxidation experiments performed for 2000 h under static laboratory air at the same temperature. These last values are displayed as full symbols in the graph while the empty symbols represent the mass gains per area unit that would have been expected if Cr volatilization did not occur. The significance of this correction will be discussed later.

The B2 coated samples show an improved oxidation kinetics compared to uncoated AISI 441 and B1 coated samples irrespective of the coating thickness. Table IV.6 presents the k_p values for the three B2 coated samples and compared to the uncoated and B1 coated samples. The results indicate a 2 to 3-fold decrease of the k_p compared to the bare AISI 441.

Table IV. 6 – Parabolic rate constant (k_p) values obtained from thermogravimetric experiments for 200 h for B2 coated samples and 530 h for uncoated AISI 441. B1-700 nm k_p is shown for comparison.

	Uncoated AISI 441	B1-700 nm	B2-400 nm	B2-1000 nm	B2-2000 nm
k_p ($g^2cm^{-4}s^{-1}$) $\times 10^{-14}$	7.6	7.2	3.5	2.5	3.0

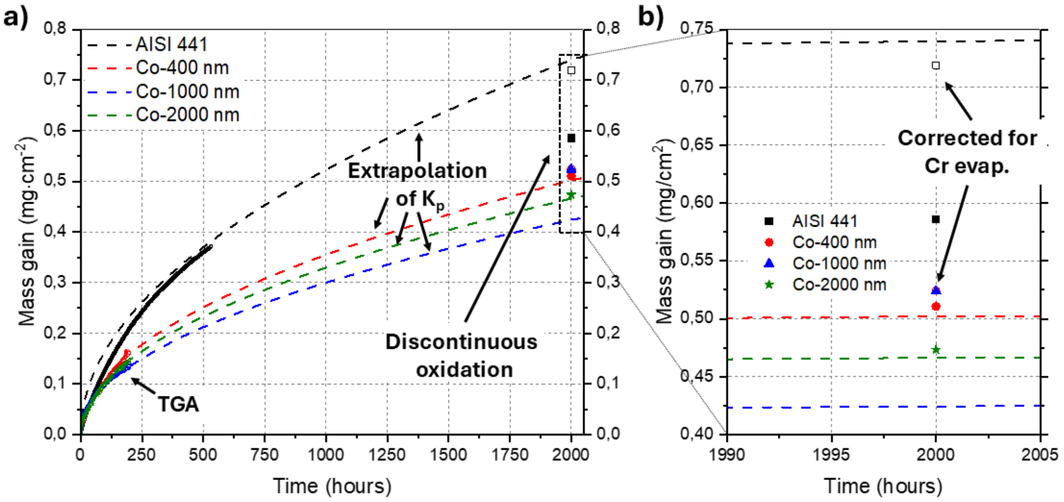

Figure IV. 17 - – Mass gain per unit area in function of time at 800 °C. The thermogravimetric experiments were conducted in dry air for 200 h for coated samples and 530 h for uncoated AISI 441. From these experiments, k_p values were calculated, and mass gain values were extrapolated to 2000 h. Discontinuous experiments were performed for 2000 h at 800 °C under laboratory air. Empty symbols refer to values corrected for Cr evaporation.

For the B2 coated AISI 441 substrates, the expected mass gain per area unit after 2000 h of exposure calculated from the k_p value are in excellent agreement with the measured mass gain per area unit after exposure in laboratory air for 2000 h. For the uncoated AISI 441 substrate, it is also the case if the measured mass gain per area unit is corrected by the mass loss due to Cr volatilization. This correction was performed since, for this experiment, the mass of Cr volatilized was partly trapped in a LSM powder. The amount of Cr retained in the LSM powder was recovered, dissolved using an acidic solution and analyzed by ICP-OES experiments. The calculation to obtain the mass loss as mass per area unit is explained in the experimental section by equation II.1 and equation II.2. The values obtained were added to the mass gain per area unit. From the B2 coated samples, only B2-400 nm samples were corrected for Cr volatilization, which is explained by the fact that this phenomenon is extremely low for the other coated samples as it will be demonstrated later (see section 3.3.5).

The oxidation kinetics is lower for the B2 than B1 coated samples. The improvement was noticed even for coatings thinner than in B1 (B2-400 nm), suggesting that such effect is linked to the atmospheric plasma deposition process. However, for the B2 samples, no clear effect on the oxidation kinetics was observed regarding the thickness increase.

3.3.2. Influence of the coating thickness on the short-term oxidation behaviour

Figure IV.18 displays the cross-section (a, b and c) of the B2 coated samples and their EDS profiles (d, e and f) after 200 h at 800 °C. The pores, previously observed on the B1 samples, were rarely observed for this batch of samples. Pores are generally formed from the outwards diffusion of substrate elements, which create metallic vacancies and finally coalesce to form pores. The fewer number of pores in the substrate of the B2 coated samples than the B1 coated samples confirms their reduced oxidation rate. Other features observed on the B1 samples, however, are still present: formation of Laves phase (white spots in the alloy), internal Ti oxidation (black dots) near the alloy/Cr_2O_3 interface and presence of HfO_2 precipitates dispersed along the coating and the chromia layer.

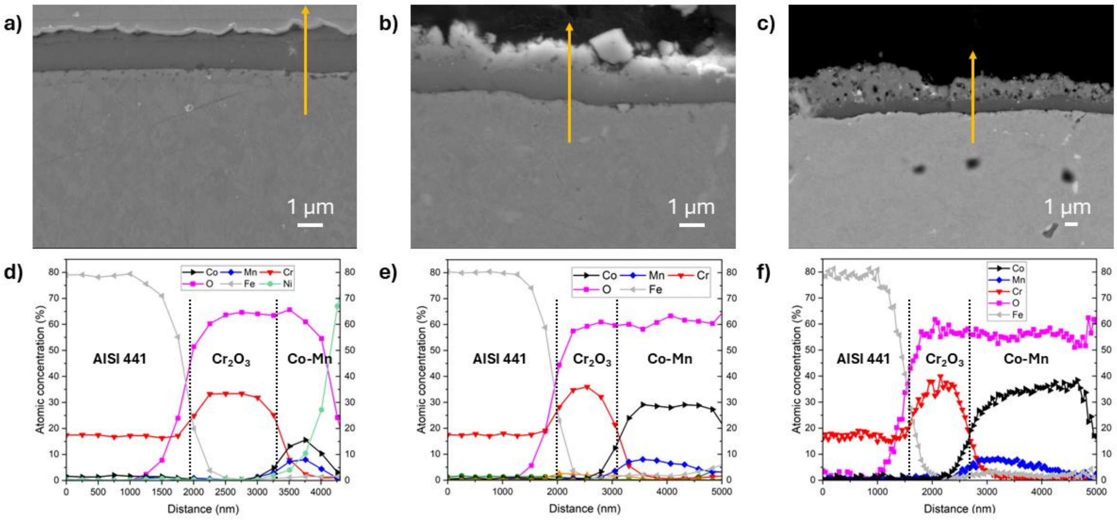

Figure IV. 18 - SEM cross-sections (a,b,c) and EDS profiles (d,e,f) of B2 coated samples annealed at 800 °C for 200 h under dry air. Figures (a) and (d) represent the sample B2-400 nm, (b) and (e) the sample B2-1000 nm, and (c) and (f) the sample B2-2000 nm. The dotted lines are used to highlight each layer of the chemical profile.

The Cr_2O_3 layer thickness was not constant over the surface of all B2 coated samples and an average thickness with its dispersion was indicated in Table IV.7. On one hand, it is observed that the average chromia thickness reduced with increasing Co_3O_4 thickness from 1.15 to 0.85 µm. The decreased Cr_2O_3 thickness points out a positive influence of increasing Co_3O_4 coating thickness regarding the Cr_2O_3 growth rate. On the other hand, the external Co-Mn spinel layer displayed a strong thickness increase with the coating thickness increase (from 0.7 to 2.1 µm). This increase is linked, of course, to the initial coating thickness but also to the growth of Mn oxide in the Co-rich spinel layer.

Table IV. 7 – Chemical composition of the spinel layer for each of the coated samples obtained by EDS analysis, and the thickness values for the chromia and spinel oxide layers. Samples were annealed at 800 °C for 200 h under dry air.

	B2-400 nm	**B2-1000 nm**	**B2-2000 nm**
Spinel phase	$Co_{1.9}Mn_{1.1}O_4$	$Co_{2.4}Mn_{0.6}O_4$	$Co_{2.6}Mn_{0.4}O_4$
Chromia layer thickness (µm)	1.15 ± 0.05	0.9 ± 0.1	0.85 ± 0.20
Spinel layer thickness (µm)	0.7 ± 0.1	1.2 ± 0.25	2.1 ± 0.6

The EDS analyses display the chemical profiles of the layers in each condition. The external layer is mostly composed of Co and Mn, although traces of Fe and Cr are also observed. The Mn concentration in the external layer decreases with increasing the Co_3O_4 coating thickness. The chemical composition, shown in Table IV.7, indicates that the Mn/Co concentration ratio considerably decreases with increasing initial Co_3O_4 thickness, reducing from 0.60 for the B2-400 nm coated sample to 0.15 for the B2-2000 nm coated sample. The decreased Mn/Co concentration ratio for thicker coatings confirms that increasing the Co_3O_4 thickness delays Mn-enrichment due to the larger initial Co reservoir. EDS profiles (Figure IV.18) from B2-1000 nm and B2-2000 nm show that Mn is not homogeneously distributed in the external layer. For B2-400 nm, Co and Mn follow the same profile shape in the external layer. In contrast, a Mn gradient is observed for the other two samples, particularly the thicker one (B2-2000 nm), with the Mn concentration reducing towards the surface.

3.3.3. Influence of the coating thickness on the long-term oxidation behaviour

<u>B2-400 nm coated sample:</u>

Figure IV.19 presents the SEM cross-section and corresponding EDS chemical profile of the B2-400 nm coated sample after 2000 h of exposure at 800 °C in laboratory air. The prolonged exposure reveals significant Cr diffusion throughout the entire external layer, very similar to what was observed for the B1-700 nm coated sample after 2500 and 5000 h in the same condition. Similar to the B1 coated sample, there is an accumulation of Mn close to the alloy/Cr_2O_3 interface forming a Mn-Cr oxide phase (Figure IV.15a,c). The Cr_2O_3 and the Mn-Cr-rich oxide layer, grows from 1.15 µm (200 h of exposure) to 1.65 µm (2000 h of exposure). The external spinel layer thickens to an average of 2.1 µm indicating a strong increase from the initial 400 nm Co_3O_4 coating. It highlights the strong Cr and Mn oxidation then diffusion into the outer spinel layer.

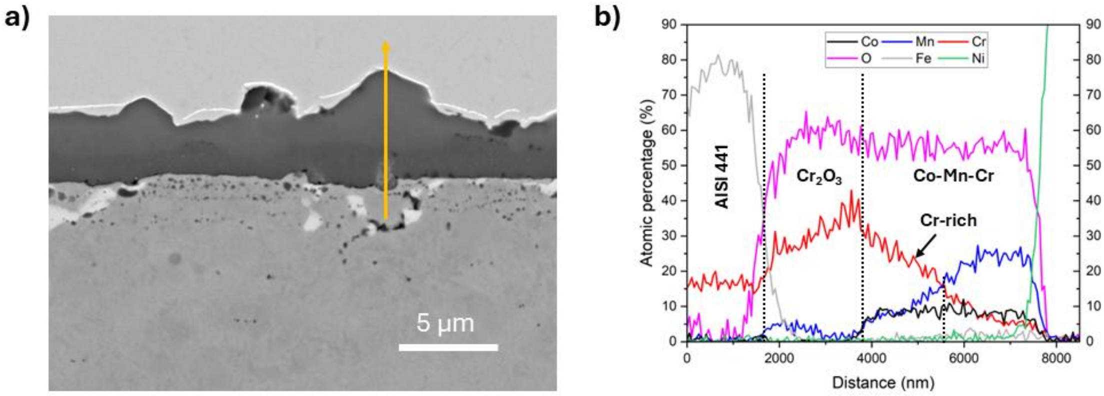

Figure IV. 19 - SEM cross-section (a) and EDS profiles (b) of B2-400 nm sample, annealed at 800 °C for 2000 h under laboratory air. The dotted lines are used to highlight each layer of the chemical profile. The small-dotted line separates the Cr-rich sublayer (indicated by the region where Cr content is higher than Mn) and the Mn-rich sublayer (higher Mn content). Sample was coated with Nickel prior to SEM observations.

The chemical profile of the B2-400 nm coated AISI 441 substrate after 2000 h of exposure at 800 °C reveals again the formation of the Reactive Layer (divided into Cr-rich and Mn-rich). The composition and thickness of the Cr-rich and Mn-rich sublayers of the outer spinel layer of the B2-400 nm AISI 441 substrate are presented in Table IV.8. Each sublayer corresponds to approximately half of the spinel, with about 1.1 µm of Cr-rich Reactive Layer and about 1.0 µm of Mn-rich sublayer. Again, very low Co variation is observed across the whole spinel layer, and Cr and Mn follow an inverse concentration profile. After 2000 h, Mn has noticeably enriched the most external layer, significantly raising the Mn/Co concentration ratio to approximately 2.4 within the Mn-rich layer, and 2.0 total (Table IV.9).

It is important to note that the total Cr-rich oxide layer present on all B2 coated samples is thinner than the Cr-rich oxide scale formed on uncoated AISI 441 substrates (Appendix IV.4), which is about thick 4.5 µm (comprising Cr_2O_3 and Mn-Cr spinel).

Table IV. 8 - Chemical composition of the spinel sublayers of the B2-400 nm coated AISI 441 substrate obtained by EDS analysis, and the thickness values for the chromia and spinel oxide layers. Samples were annealed for 2000 h at 800 °C under laboratory air.

B2-400 nm				
Cr_2O_3 thickness (µm)	Cr-rich RL	Cr-rich RL (µm)	Mn-rich RL	Mn-rich RL (µm)
1.65 ± 0.3	$Co_{0.6}Mn_{0.7}Cr_{1.7}O_4$	1.1 ± 0.3	$Co_{0.6}Mn_{1.5}Cr_{0.9}O_4$	1.0 ± 0.4

B2-1000 nm and 2000 nm coated samples:

Although no spallation was observed for the samples B2-1000 nm and B2-2000 nm after the experiment, a substantial portion of the coating was detached when cutting the sample for the cross-section preparation. Since cutting strongly damaged the sample, a TEM lamella was prepared using FIB, thus avoiding preparation drawbacks. The TEM analysis allows the clear observation of the film. However, it consists of a localized technique reducing the representability of the sample.

Figure IV.20 and Figure IV.21 show the bright field TEM cross-section view of the B2-1000 nm and B2-2000 nm coated samples, respectively, after 2000 h of exposure at 800 °C under laboratory air. The samples show the formation of a Cr_2O_3 layer with equiaxial grains, and a Co-Mn spinel layer on top of this layer. The microstructure of the spinel layer shifts from columnar grains (from the chromia/spinel interface to the surface in B2-1000 nm, Figure IV.20a) to large equiaxial grains in B2-2000 nm (Figure IV.21a). In both cases, the spinel structure was identified using Single Area Electron Diffraction (SAED) to be cubic, closely matching the $MnCo_2O_4$ reference obtained from JCPDS card No. 00-023-1237 (Figure IV.20c and Figure IV.20e).

Table IV. 9 - Chemical composition of the total external spinel layer for each of the coated samples obtained by EDS analysis, and the thickness values for the chromia and spinel oxide layers. Samples were annealed for 2000 h at 800 °C under laboratory air.

	B2-400 nm	**B2-1000 nm***	**B2-2000 nm***
Spinel phase	$Co_{0.6}Mn_{1.2}Cr_{1.2}O_4$	$Co_{1.7}Mn_{1.3}O_4$	$Co_{2.2}Mn_{0.9}O_4$
Chromia thickness (µm)	1.65 ± 0.3	2.4 ± 0.3	2.3 ± 0.3
Spinel thickness (µm)	2.1 ± 0.65	1.4 ± 0.4	2.0 ± 0.5

*Values were obtained from a TEM analysis and are not representative of the whole sample

Moreover, a $MnCr_2O_4$ layer was suggested by STEM-EDS (Figure IV.21g,h,i,j) and confirmed using SAED analysis (Figure IV.21f) in-between the alloy and the chromia layer. The cubic $MnCr_2O_4$ phase was identified using the *Materials Project* database (*mp-28226*)[293–295]. This phase ranged from 250-500 nm but was solely identified in the B2-2000 nm coated sample. Low concentration of Si was also observed below and in-between two $MnCr_2O_4$ layers.

The chemical composition and thickness of each layer were obtained by STEM-EDS profiling and from the micrographs and are reported in Table IV.9. The obtained thickness was averaged from two cross-section images for each sample. Interestingly, the chromia thickness is considerably higher for B2-1000 nm and B2-2000 nm in comparison to B2-400 nm. However, both thickness and chemical composition values should be taken with cautious since only a small region of the sample was analyzed.

In contrast to the EDS profiles from the B2-400 nm coated sample, the STEM-EDS profiles do not show the formation of a pronounced Cr-rich Reactive Layer. The RL extended over approximately 0.5 µm (Figure IV.20b) and 0.4 µm (Figure IV.21d) for B2-1000 nm and B2-2000 nm, respectively. It is important to note that the thickness of this RL seems to vary from grain to grain, as indicated in Figure IV.21c where the RL is minimal.

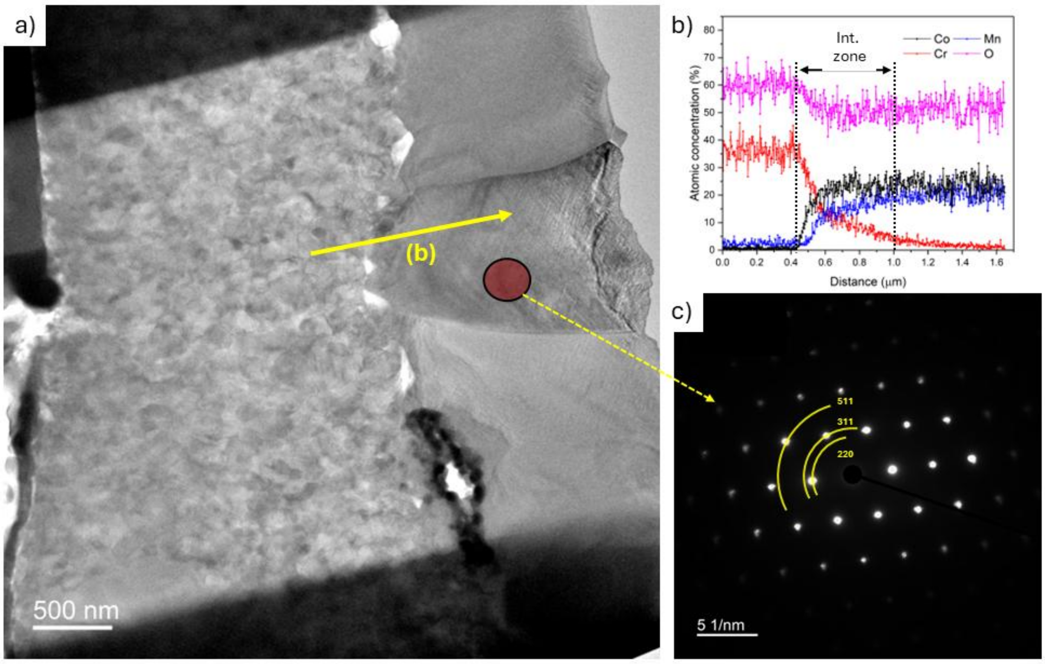

Figure IV. 20 - TEM bright field cross-section of the B2-1000 nm sample (a). Yellow arrow indicates the region where the EDS profile (b) was taken, and the red circle indicates the region where SAED analysis was performed.

Both B2-1000 nm and 2000 nm samples have shown a minimal Cr concentration over the remnant portion of the spinel layer and this concentration is negligible at the oxide surface. The concentration profile of Mn is slightly shifted in comparison to the Co profile in Figure IV.20b and Figure IV.21d. This shift, as discussed in section 3.2.7, refers to the crystallographic competition of Cr and Mn for the same sites. It is important to highlight that the thicker coatings, B2-1000 nm and B2-2000 nm, promoted a more effective Cr barrier, avoiding the extensive formation of the RL. Interestingly, much lower Mn/Co concentration ratios were observed for B2-1000 nm and B2-2000 nm in comparison to B2-400 nm where a large RL was formed.

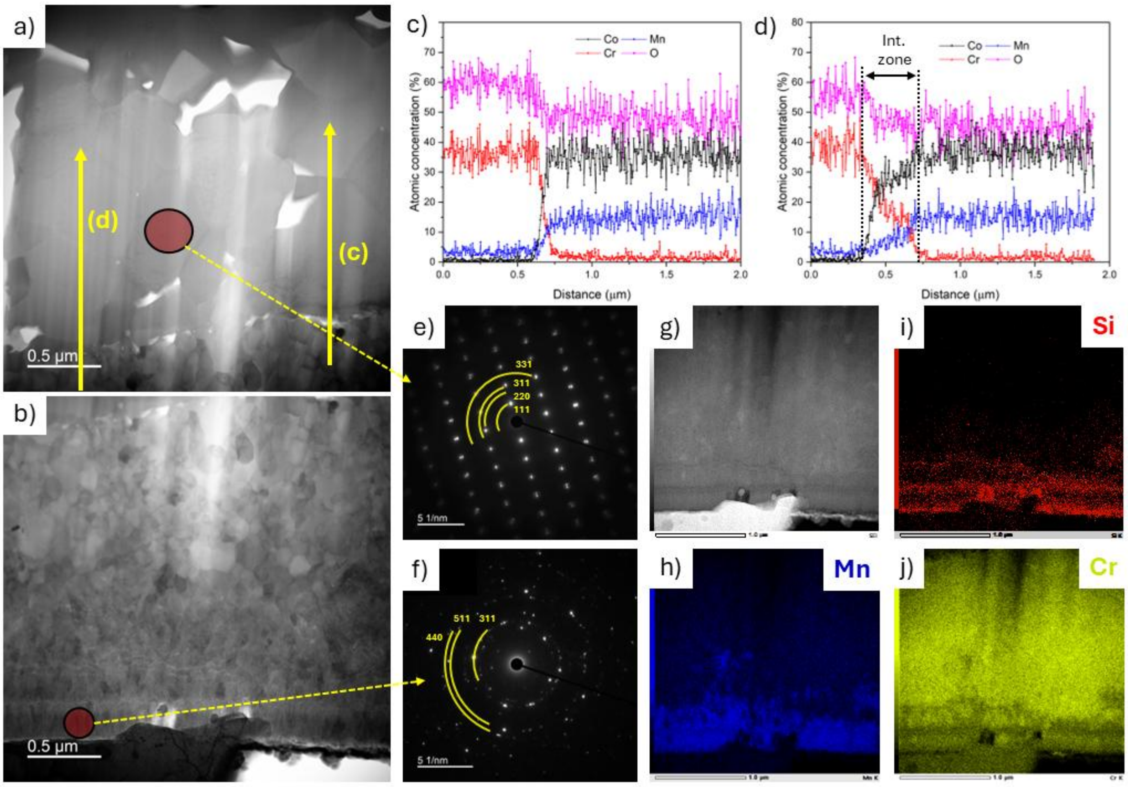

Figure IV. 21 - TEM bright field cross-section of the B2-2000 nm sample, showing the Co-Mn spinel layer (a), and the chromia layer (b). Yellow arrows indicate the regions where the EDS profiles (c,d) were taken, and the red circles indicate the regions where SAED analyses were performed. From (g), a STEM-EDS mapping was performed, showing Mn (h), Si (i) and Cr (j).

3.3.4. Extensive study of the spinel layer formed on B1 and B2 coated samples by Raman spectroscopy : link between Raman shift and chemical composition

Due to its highly localized nature, TEM analysis provides information limited to specific regions of the sample. Since the B2-1000 nm and B2-2000 nm coated AISI 441 substrates after 2000 h of exposure at 800 °C could not be evaluated by SEM/EDS analysis – due to destruction of the oxide scale after metallographic preparation-, Raman spectroscopy was employed to assess the chemical composition, particularly of the external spinel layer. In previous Raman spectroscopy analysis, a constant shift and broadening was observed in the peaks of Co-Mn spinel, with these features being more pronounced when more Mn was incorporated (Figure IV.11b). The spectra from B1 and B2 samples were analyzed, focusing on the F_2g (1) and A_1g vibrational modes by examining the peak position and broadening, and compared with the chemical composition obtained by EDS analysis. The trend observed was used to infer on the composition of the spinel formed on B2-1000 nm and B2-2000 nm coated AISI 441 substrates after 2000 h of exposure at 800 °C. A likewise approach was used by Bahlawane *et al.*[290] to evaluate the composition and structure of $Co_{3-x}Fe_xO_4$ spinels, and by Giovanelli *et al.*[289] for $Co_{3-x}Mn_xO_4$ spinel. The chosen peaks are sensitive to cation occupancy: F_2g (1) is mainly influenced by the occupancy of the tetrahedral sites while A_1g is influenced by the occupancy of the octahedral sites.

Figure IV.22 shows the evolution of the (a) F_2g (1) and (b) A_1g peak positions and their FWHM as a function of Mn incorporation. A clear trend is observed with both peaks shifting to lower wavenumbers with increasing Mn content. The shift is followed by a significant broadening (A_1g), particularly for $x > 0.6$ in the $Co_{3-x}Mn_xO_4$ spinel. This shift towards lower wave numbers correlates with the substitution of smaller Co ions by larger Mn ions, which can also be explained by a reduction of the bond strength[296,297]. Indeed, the increase in Mn content is related to increased bond length[104]; associated to reduced bond strength[296].

The Raman-based model was applied to verify the chemical composition of the spinel layer formed on the B2-2000 nm and B2-1000 nm coated samples after 2000 h of exposure at 800 °C. Several regions of the B2 coated AISI 441 substrates were evaluated, and the average values are represented by a red triangle (B2-1000 nm) and black star (B2-2000 nm). The error bars were used to enhance the representativity of the measurement. These values were then compared with the trend line indicated by the dotted lines. The black (peak position) and red (FWHM) squares represent the scatter of the measured values compared with the trend line. The values overlapping between peak position and FWHM indicate the x values of the $Co_{3-x}Mn_xO_4$ spinel. The Mn content of the B2-2000 nm (violet star) was estimated to be $x = 0.85–0.95$, based on the peak position and broadening for F_2g (1) and A_1g peaks. This result agrees well with STEM-EDS measurements.

However, the spinel layer formed on B2-1000 nm sample, with a higher Mn content ($x = 1.33$ from STEM-EDS), lies outside the range of the developed Raman model. For this sample, only the A_1g mode was deconvoluted, as the F_2g (1) mode was too broad to resolve clearly. The A_1g peak appears at 649 cm^{-1} with a broadening of approximately 56 cm^{-1} (shown in the graph as brown triangles). Additional features included a peak at ~ 500 cm^{-1} and a shoulder near ~ 560 cm^{-1}. The peak position deviates from the trend observed in the model. This discrepancy can be attributed to the coexistence of cubic and tetragonal phases at high Mn content ($x = 1.33$)[99,298], which was confirmed by XRD (Appendix IV.5). Yet, by extrapolating the values from the model, the broadening supports a high Mn content with the trend pointing to a x value between 1.3 and 1.4 (Figure IV.22b). Indeed, Giovanelli *et al.* indicated that FWHM of the Co-Mn spinel phase tends to increase until reaching its maximum at x = 1.5[289]. This broadening increase relates to an increase in configurational entropy, which represents an increase of cation pairs (Co^{2+}/Co^{3+}, Mn^{3+}/Mn^{4+}) in the octahedral sites[104].

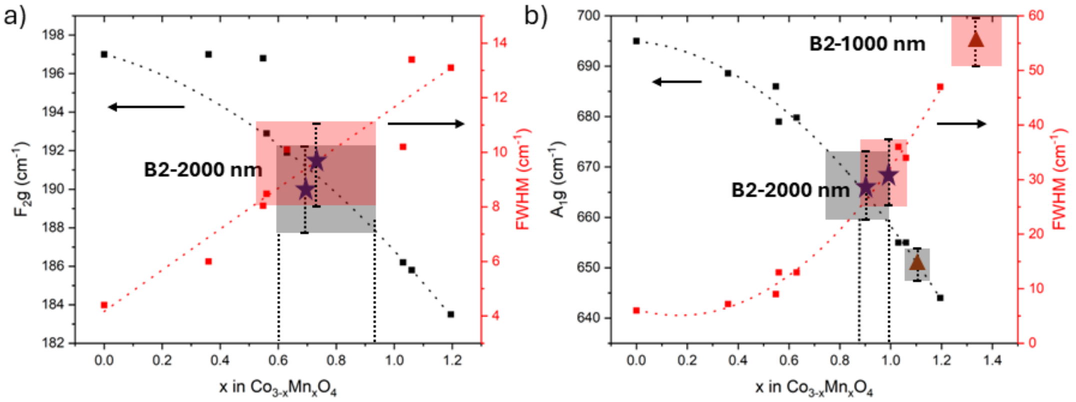

Figure IV. 22 - Raman model developed for the F_2g (1) (a) and the A_1g (b) vibration modes using data obtained by EDS analyses for various samples. Peak position (black) and broadening (red) are presented in function of Mn content in the Co-Mn spinel.

In conclusion, the proposed Raman model presented a good fit with the results obtained by EDS analyses within the stoichiometric range studied. Further experimental data is necessary to increase the robustness of the model, particularly for higher Mn concentration (x > 1.2). Moreover, our Raman analyses combined to chemical composition analyses of the spinel layer indicate that the Mn incorporation clearly influences both octahedral and tetrahedral sites, as previously observed by Giovanelli *et al.*[289] Mn ions, due to their higher crystal field stabilization energy (CFSE), preferentially occupy octahedral sites when entering into the initial Co_3O_4 coating. Previous works, using neutron diffraction characterisation of $(Co,Mn)_3O_4$, confirmed that Co^{2+} predominantly resides in tetrahedral positions, with Mn occupying octahedral sites[104,109]. Despite the minimal Mn presence in tetrahedral sites, a considerable peak displacement and broadening was still observed. The Mn influence on tetrahedral sites could be explained by the increase in AO_4 bond distance with the Mn incorporation. This AO_4 bond distance increase occurs despite Mn occupying octahedral sites[104].

3.3.5. Chromium evaporation

Chromium evaporation experiments were performed for the B2 coated samples for all thicknesses and for the uncoated AISI 441 substrate. The samples were annealed for 2000 h at 800 °C in laboratory air and the Cr evaporation rate was evaluated, indirectly, by the amount of Cr trapped in the LSM powder which is below the samples but not in contact with them. It is important to note that this method is semi-quantitative since the LSM powder will not completely trap the Cr volatile species. A more quantitative experiment procedure is proposed in literature but has the disadvantage to be done on a single sample only[299,300]. In consequence, the experimental procedure proposed in literature is less efficient to do fast “screening test” of many samples. The formation of Cr-volatile species occurs by reaction of Cr_2O_3 with O_2(g) and its rate is increased by the addition of H_2O(g) in air[69,73]:

$$2\ Cr_2O_{3(s)} + 3\ O_{2(g)} \rightarrow 4\ CrO_{3(g)}$$

$$2\ Cr_2O_{3(s)} + 4\ H_2O_{(g)} + 3\ O_{2(g)} \rightarrow 4\ CrO_2(OH)_{2(g)}$$

The amount of Cr trapped by LSM was obtained after dissolution of the LSM powder in acid solution then analysis of the Cr concentration in solution by ICP-OES. These values were used to calculate the Cr evaporation rate (equation IV.3) and compared to literature.

$$Cr_{evap-rate} = \frac{m_{Cr-evap.}}{A_{sub} \times t} \quad (IV.3)$$

where $m_{Cr\text{-}evap.}$ represents the amount of Cr trapped in the LSM powder, A_{sub} is the substrate area and *t* the time in seconds. A linear rate was assumed as shown in previous works[48,301]. Table IV.10 presents the Cr evaporation rates for both coated and uncoated samples and evaporation rate values of coated and uncoated AISI 441 substrates from literature. The uncoated AISI 441 substrate showed a Cr evaporation rate of 2.6×10^{-8} mg·cm^{-2}·s^{-1}, which, despite coming from a semi-quantitative method, correlates well with reported values for AISI 441 and other ferritic stainless steels in literature[48].

The B2 coated samples decreased drastically the volatilization rate of Cr compared to what was observed for the uncoated sample. For instance, the B2–400 nm sample showed a 10-fold decrease, while for the thicker coatings, the Cr evaporation rate falls below the detection limit of the analysis ($< 2 \times 10^{-10}$ mg·cm^{-2}·s^{-1}). This significant reduction is not surprising considering that the thicker coatings did not show any Cr at the oxide/gas interface. In this case, the formation of Cr volatile species was largely avoided. The low Cr evaporation rate relies in the same order of magnitude of other values found for coated samples in literature (Table IV.10).

Table IV. 10 - Comparison of Chromium evaporation rates of coated and uncoated AISI 441 substrates (this work) after exposure in laboratory air at 800 °C for 2000 h. Values for various ferritic stainless steels (FSS) exposed at 800 °C for different times and atmospheric conditions found in literature are added (italic).

Substrate	**Coating**	**Temperature (°C)**	**Time (h)**	**Details**	**Rate of Cr evaporation (10^{-10} mg cm^{-2}s^{-1})**
AISI 441[2]	-	800	2000	Laboratory air	261
AISI 441[2]	B2-400 nm	800	2000	Laboratory air	25.3
AISI 441[2]	B2-1000 nm	800	2000	Laboratory air	≤2
AISI 441[2]	B2-2000 nm	800	2000	Laboratory air	≤2
AISI 441[1]	-	*800*	*500*	*Air + 3%* H_2O	*660*
AISI 441[1]	-	*800*	*24-96*	*Air + 7%* H_2O	*250*
AISI 441[1]	*CeCo*	*800*	*1000*	*Air + 3%* H_2O	*7*
Crofer 22 APU[1]	-	*800*	*1000*	*Air + 1.88%* H_2O	*400*
Crofer 22 APU[1]	-	*800*	*500*	*Air + 3%* H_2O	*110*
Crofer 22 APU[1]	-	*800*	*500*	*Air + 3%* H_2O	*505*
Crofer 22 APU[1]	-	*800*	*1000*	*Air + 2%* H_2O	*170*
Crofer 22 APU[1]	*MCO*	*800*	*500*	*Air + 3%* H_2O	*25*
Crofer 22 APU[1]	*CeCo*	*800*	*1000*	*Air + 3%* H_2O	*7.1*

[1] Adapted from Reddy *et al.*[15]
[2] This work

These Cr-evaporation values were used to correct the mass gain measurements for the uncoated and B2–400 nm samples oxidized at 800 °C for 2000 h (Figure IV.17). After correction, the mass gain values for the uncoated AISI 441 showed better agreement with the predicted values, extrapolated from the parabolic rate constant (k_p). This good correlation suggests that the LSM powder trapped nearly all the evaporated Cr, providing a reliable estimate of total Cr loss.

3.4. Sequential Isotopic Tracer Experiment

Several isotopic and marker studies were performed on ferritic stainless steel (chromia-forming alloys), such as AISI 441, to understand its mechanism of oxidation. It has been proposed that the oxide scale grows by outward diffusion of the substrate elements, mainly Cr and Mn[48,275,281]. However, fewer studies evaluated the oxide scale growth on coated ferritic stainless steel samples. In this work, outward Cr diffusion was suggested from the presence of Hf precipitates in the chromia layer. Studies from Horita *et al.* investigated the diffusivity of oxygen at various temperatures (600 - 800 °C) for $MnCo_2O_4$ (prepared by RF sputtering) coated ZMG232 alloys. They showed that oxygen diffusion occurs rapidly through the coating but slows down close to the coating/chromia interface[59]. This result points out to poor oxygen barrier properties of the Co-Mn spinel layer and suggests that Cr_2O_3 growth occurs by the reaction with oxygen from air. Nevertheless, the fast oxygen diffusion could also represent a poor quality of the coatings. Guillou evaluated the chromia growth on AISI 441 at 800 °C after the formation of a dense and continuous Cr-Mn spinel atop the chromia[275]. The growth of chromia was reported to happen at the Cr_2O_3/Cr-Mn spinel interface by the outwards diffusion of Cr and the destruction of the spinel lattice.

To better understand the influence of the protective Co_3O_4 coatings developed by AP-PECVD on the formation of the oxide scale, sequential isotopic experiments in $^{16}O_2$ then $^{18}O_2$ were conducted. In this experiment, B2-1000 nm coating (only on one face) was first exposed to $^{16}O_2$ then to $^{18}O_2$ atmospheres. The oxidation time was chosen from the parabolic rate constant considerations of the B2-1000 nm coated sample. After each step, a 500 nm Cr_2O_3 oxide is expected to be formed, achieved after a 1st oxidation step ($^{16}O_2$) of 72 h and a 2nd oxidation step ($^{18}O_2$) of 168 h. One face of the sample was coated (B2-1000 nm), and the other face was uncoated. This sample preparation allowed to compare the oxidation mechanism for uncoated and coated AISI 441 substrate. The profiles of ^{16}O and ^{18}O in the oxide scale were then measured by SIMS.

Two scenarios were considered for the growth of the oxide scale from the previous observations made on the evolution in composition and thickness of the oxide scale. The two scenarios are depicted in Figure IV.23:

- Scenario 1: The spinel layer grows outwardly and chromia grows at the spinel/chromia interface by fast diffusion of oxygen through the spinel layer.

This last event was proposed by Horita *et al.*[59] and would represent an ^{18}O accumulation, detected by SIMS, at the spinel surface AND at the chromia/spinel interface.

- Scenario 2: The spinel layer grows outwardly and chromia grows at the spinel/chromia interface by consuming oxygen from the spinel layer. In that case, chromia is built with ^{16}O belonging to the former spinel layer and ^{18}O enrichment is only detected at the spinel surface. This scenario is the one proposed by Guillou for uncoated AISI 441[275].

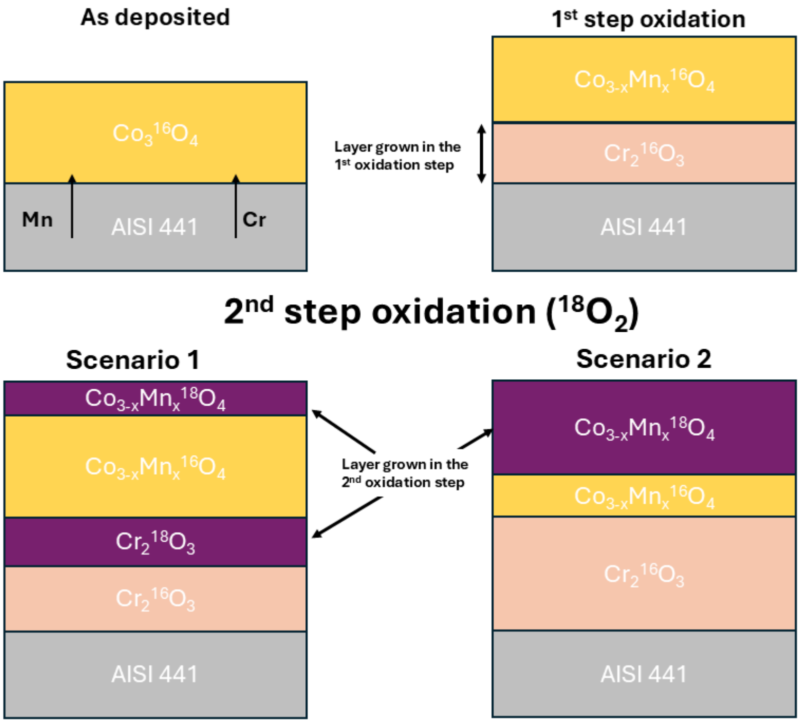

Figure IV. 23 – Schematic description of the two possible scenarios for the formation of the oxide scale. The scheme highlights the initial as-deposited material, and the oxide formed after the first oxidation step using $^{16}O_2$, hypothesizing on the formation of a chromia oxide and Mn-enrichment to the spinel. The two scenarios relate to the second oxidation step using $^{86}O_2$, and the layers grown during this stage are shown in purple.

Figure IV.24 displays the composition profile obtained by SIMS analysis after isotopic labelling with $^{16}O/^{18}O$ for the uncoated (a) and B2-1000 nm coated (b) samples.

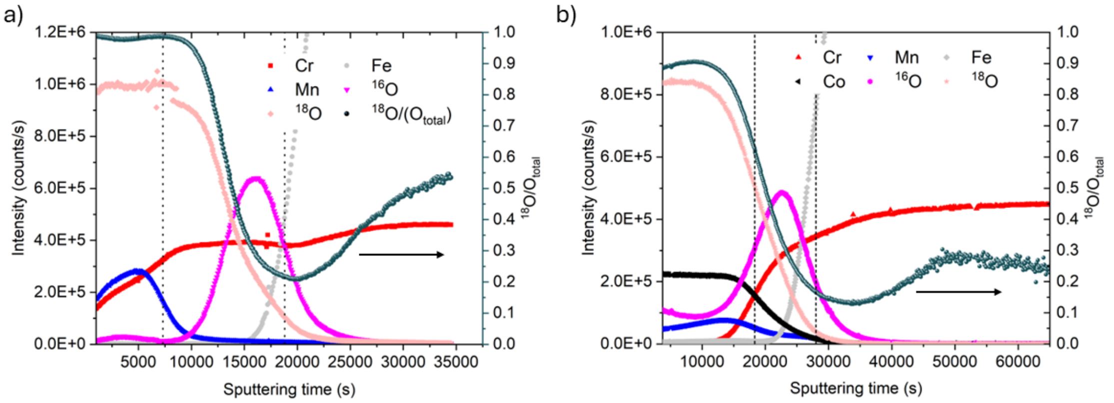

Figure IV. 24 – SIMS intensity profiles of uncoated (a) and B2-1000 nm coated (b) AISI 441 in function of sputtering time. The right axis indicates the intensity fraction of ^{18}O over the total oxygen intensity (^{16}O+^{18}O). The dotted lines indicate the spinel/chromia and chromia/alloy interfaces.

The alloy/chromia and chromia/spinel oxide interfaces are located at the inflection point of the chromium elemental profile. The intensity profiles (left axis) and the $^{18}O/^{18}O+^{16}O$ intensity ratio (right axis) are plotted in function of sputtering time. The same ^{18}O profile is observed for the uncoated and coated sample. ^{18}O is mainly present at the external part of the oxide layer. Moreover, a ^{18}O plateau with a $^{18}O/O_{total}$ ratio close to 1 are clearly observed which demonstrates the outwards growth of oxide. Then, the ^{18}O signal decreases considerably toward the inner part, before reaching the Cr_2O_3 layer. No strong ^{18}O accumulation is observed at the spinel/Cr_2O_3 interface which suggests that no fast diffusion of ^{18}O through the spinel layer to form Cr_2O_3 occurs. Such observations of the ^{18}O profile suggests that it is scenario 2 that occurs, in agreement with Guillou[275]:

- The external spinel oxide layer grows outwardly by outwards diffusion of metallic cations, Co and Mn mainly.
- The internal chromia layer grows at the spinel/chromia interface by consuming oxygen from the spinel layer mainly.

The point defect that are involved in the outwards diffusion of cations in chromia and the spinel layer are either vacancy or interstitial. Guillou proposed that the chromia scale grows at the spinel/chromia interface by Cr interstitial creation and diffusion[275]. This process will be discussed in the following part.

4. Discussion

All the results exposed previously on the oxide scale formation on the coated samples and the factors that has strong effect such as the initial coating thickness or the coating procedure (B1 or B2) is discussed below.

4.1. Oxide scale growth mechanism

The $^{18}O/(^{18}O+^{16}O)$ profile for the coated and uncoated AISI 441 substrates has shown that the growth on both cases is external (Figure IV.24a,b). Considering this behaviour, it is expected that the oxide growth happens in a similar manner in both uncoated and coated samples. For uncoated AISI 441 substrates, Guillou *et al.*[275] suggested that the chromia layer in contact with the substrate grows by the destruction of the Cr-Mn spinel phase which lays above it. A similar oxide growth mechanism is proposed for the coated sample with Co_3O_4 with the same formalism as proposed by Guillou[275]. The oxide growth mechanism for the coated sample is illustrated in Figure IV.25. Chromia grows outwardly by the Cr enrichment of the Co/Mn/Cr spinel lattice (Reaction Layer, RL), and the spinel grows outwardly by reacting with the atmospheric oxygen. The oxide scale growth follows the defect equilibrium, as shown in the scheme in Figure I.8, indicating a counter diffusion of electrons, defects and ions. The defect equilibrium expressions follow certain assumptions, such as conservation of mass and charge and site neutrality. By convention, equilibria are written in the direction of defect formation, and defects are defined for their highest ionization state. Defects in the chromia lattice are named (*c*), those in the spinel lattice as (*s*), and those generated in the Reactive Layer at the chromia/spinel interface as (*rl*). The notation A is used for atoms in the alloy matrix.

The defect type was not evaluated in this work. However, Guillou *et al.*[275] observed a predominance of interstitial type defects, which are expected for Cr_2O_3 at low oxygen partial pressures[302]. Mn was also considered in interstitial position. Other cations from the steel diffuse, such as Ti and Nb, but were not considered here for the sake of simplicity. The point defects may be described using the Kröger–Vink notation[303]. For the sake of clarity, the initial system will be considered when a continuous Cr_2O_3 layer is already formed, as described in Figure IV.25a, being alloy/chromia/spinel. At the metal/chromia interface, Cr and Mn atoms will be oxidized and form point defects, following the defect formation equilibria

$$Mn_{Mn}^{x}\,(A) \;=\; Mn_i^{\bullet\bullet}\,(c) \;+\; 2e^-$$

$$Cr_{Cr}^{x}\,(A) \;=\; Cr_i^{\bullet\bullet\bullet}\,(c) \;+\; 3e^-$$

The point defects formed diffuse through the chromia towards the Cr_2O_3/spinel interface. The Mn diffusion was shown to happen faster than Cr in chromia through the bulk[304] and grain boundaries[305].

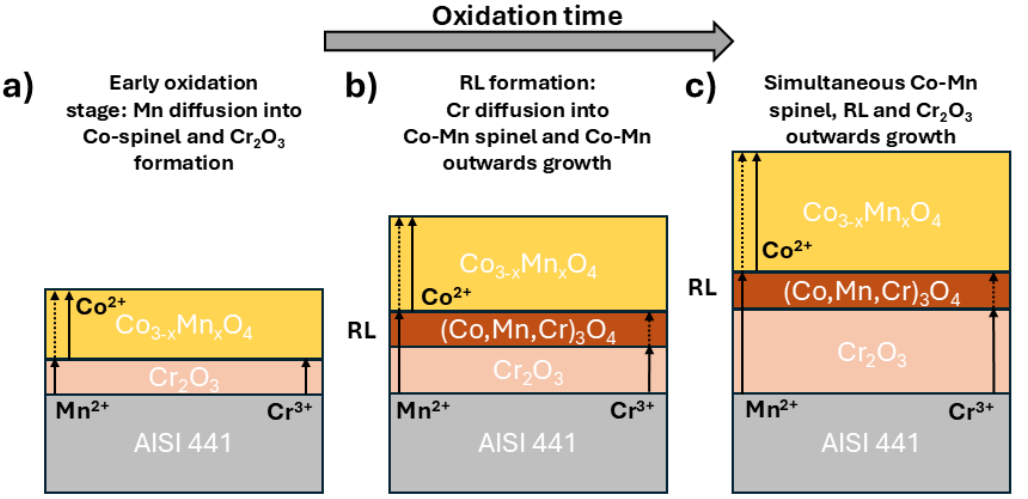

Figure IV. 25 – Evolution of the oxide scale with the oxidation time. a) Schematic representation of the oxide scale at the early oxidation stages: Mn diffusion into Co-spinel and Cr_2O_3 formation. b) Initial diffusion of Cr into the external spinel oxide resulting in the formation of the Reactive Layer (RL). The Co-Mn spinel grows outwards. c) Continuous Cr diffusion leads to Cr-enrichment of RL and thus formation of Cr_2O_3. All oxide layers grow outwards.

Chromia/Spinel Interface

The Mn diffusing ions are assumed to diffuse through the chromia and reach the interface with the spinel. These ions are expected to start the growth of the $Co_{3-x}Mn_xO_4$ spinel phase, and subsequent Mn enrichment of this phase. The growth of the Co-Mn spinel should start near the chromia/spinel interface, as suggested by the SIMS profile (Figure IV.24b). In consequence, it is expected that the Mn ions react with the initial Co-spinel, as follows:

$$x\,Mn_i^{\bullet\bullet}(c) + 3\,Co_{Co}^{x}(s) + 4\,O_O^{x}(s) \leftrightarrow x\,Mn_{Mn}^{x}(s) + (3-x)Co_{Co}^{x}(s) + 4\,O_O^{x}(s) + x\,Co_i^{\bullet\bullet}\,(s)$$

The introduction of Mn ions to the spinel creates additional point defects ($Co_i^{\bullet\bullet}\,(s)$). Alternatively, the diffusing Cr ions would lead to the Reactive Layer, and thus chromia formation. Considering that oxygen anions does not reach this interface, as shown by the isotopic sequential experiments, Cr ions will diffuse as $Cr_i^{\bullet\bullet\bullet}(c)$ to the spinel lattice. Cr ions are expected to occupy octahedral sites of the $Co_{3-x}Mn_xO_4$ spinel oxide[118], which possess a large number of empty sites[94]. The chemical profiles at the Cr_2O_3/RL/spinel interfaces (Figure IV.19b) evidenced an inverse behaviour for Cr and Mn, indicating that Mn is primarily displaced with the incorporation of Cr cations. The Cr diffusion into the spinel can be described as follows:

$$\begin{aligned} y\, Cr_i^{\bullet\bullet\bullet}(c) + x\, Mn_{Mn}^{x}(s) + (3-x)Co_{Co}^{x}(s) + 4\, O_O^{x}(s) \\ \leftrightarrow\ y\, Cr_{Cr}^{x}(rl) + (3-x)Co_{Co}^{x}(rl) + (x-y)\, Mn_{Mn}^{x}(rl) + 4\, O_O^{x}(rl) \\ +\ (y)\, Mn_i^{\bullet\bullet}(s) \end{aligned}$$

This reaction leads to the formation of new defects in the spinel layer: $Mn_i^{\bullet\bullet}(s)$ as shown here. The phase formed corresponds to the RL shown in Figure IV.25b, likely a $Co_{3-x}Mn_{x-y}Cr_yO_4$. With the continuous diffusion of Cr to this layer, Cr concentration increases in this Reactive Layer leading at the end to the chromia formation. This reaction is facilitated by the higher chromia thermodynamic stability compared to the $MnCo_2O_4$ spinel[89,306] and to mixed Co-Mn-Cr spinels[119]. Therefore, the chromia growth occurs at the expense of the spinel lattice (from the RL), which happens as follows:

$$\begin{aligned} (8-3y)\, Cr_i^{\bullet\bullet\bullet}(c) + 3\, y\, Cr_{Cr}^{x}(rl) + 3(3-x)Co_{Co}^{x}(rl) + 3(x-y)\, Mn_{Mn}^{x}(rl) + 12\, O_O^{x}(rl) \\ \leftrightarrow\ 8\, Cr_{Cr}^{x}(c) + 12\, O_O^{x}(c) + 3(3-x)\, Co_i^{\bullet\bullet}(s) + 3(x-y)\, Mn_i^{\bullet\bullet\bullet}(s) \end{aligned}$$

The point defects (interstitials here) created by the destruction of the spinel lattice with the Cr diffusion will diffuse towards the oxide/gas interface. The Co interstitial concentration will equal the amount of Co released by the spinel destruction (chromia/RL formation) and from Mn incorporation. The Mn flux diffusing towards the surface corresponds to the Mn interstitials released from the Cr diffusion.

These reactions, represented in Figure IV.25b,c, indicate that the Reactive Layer has to be primarily formed to enable the formation of a chromia layer. Such scenario predicts a competition for the growth of both layers. It will be discussed later.

Oxide/Gas Interface

At the oxide/gas interface, oxygen can adsorb onto surface sites s according to the non-dissociative sorption equilibrium:

$$s + O_2 \leftrightarrow 2\, O_{ads}^{x}$$

Mn and Co defects reaching this interface can react with the adsorbed oxygen to form $Co_{3-x}Mn_xO_4$ spinels. The following equation is shown, as example, for the formation of $MnCo_2O_4$ spinel:

$$Co_i^{\bullet\bullet}(s) + Co_i^{\bullet\bullet\bullet}(s) + Mn_i^{\bullet\bullet\bullet}(s) + 4\,O_{ads}^{x} + 8\,e' \\ \leftrightarrow Mn_{Mn}^{x}(s) + 2\,Co_{Co}^{x}(s) + 4\,O_{O}^{x}(s) + 4\,s$$

4.1.1.Comparison of the Reaction Layer formation formed on growing oxide scale with results from diffusion couple experiments in literature

Furthermore, these results suggest distinct mechanisms of reactive layer (RL) formation between coated samples and diffusion couple experiments. In diffusion couples, the RL is typically reported to grow through the counter-diffusion of Co and Mn ions inwards and Cr ions outwards, with a stronger tendency for the former [110,121,141,307]. In contrast, the Co_3O_4 coated samples from our work exhibited Cr diffusion outwards, similar to the conclusion reached by Talic *et al.*[123]. Likewise, the growth of the RL also seems to vary from these two cases. Wang *et al.*[121] measured the growth rate of the RL using $Mn_{1.5}Co_{1.5}O_4/Cr_2O_3$ diffusion couple and Pt markers. At 800 °C, a growth rate of 2.2×10^{-5} µm·s^{-1} was measured, which would translate into the formation of a 14 µm RL after 2500 h, and 19.9 µm after 5000 h. These values are significantly higher than the 2.1 and 3.0 µm obtained here after 2500 and 5000 h, respectively. Similar thinner RLs were reported by Talic *et al.*[123] and Magdefrau *et al.*[141] for MCO coatings on Crofer 22 APU confirming slower growth on coated ferritic stainless steel than in diffusion couples. Another strong variation can be observed in chemical profiles from diffusion couples and coated samples. While diffusion couples presented a single homogeneous region with a $(Co,Mn)Cr_2O_4$ phase[117,121,307], coated samples showed a gradient profile for Cr (decreasing) and Mn (increasing) towards the surface, and a stable composition of Co. This gradient can be attributed to the replacement of Mn cations by Cr as previously discussed. Overall, Cr concentration was lower in RL formed on FSS than in diffusion couples[123,148] as shown in RLs produced in this work (Figure IV.15 and Figure IV.19). These variations are likely related to varying driving forces for cation diffusion. While the driving force for diffusion, in diffusion couples, is the chemical potential gradient between the two oxides, the driving force for an oxide scale which grows is strongly influenced by the creation and consumption of point defects induced by the oxygen potential gradient through the oxide layers.

4.2. Competitive growth of Cr_2O_3 and Reaction Layer

The competitive growth of chromia and RL can be compared by analysing the thickness of both layers after short and long-term exposure at 800 °C. Let's first consider the samples presenting a fast growth of the Reactive Layer (B2-400 nm and B1-700 nm). In both cases, after long-term exposure, the RL extends to the surface, completely consuming the Co-Mn spinel. For thicker samples (B2-1000 nm and B2-2000 nm), a very thin reactive layer is formed, with Cr concentration rapidly dropping in the spinel layer. Interestingly, the coatings that formed a thin RL exhibit a much thicker Cr_2O_3 layer. Table IV.11 and Table IV.12 summarize the Cr_2O_3 and RL thicknesses observed over time for the B2 and B1 coated samples, respectively, at 800 °C. The results indicate that for the thin initial coatings (B2-400 nm and B1-700 nm), after the short-term exposure (200 and 500 h), the RL is the main growing layer. For these samples, Cr_2O_3 is thinner. For example, for the B1-700 nm coated sample, the chromia layer growth is minimal from 500 to 5000 h, only 0.3 µm, suggesting that nearly all diffusing Cr is incorporated to the reactive layer. On the contrary, for the thick initial coatings (B2-1000 nm and B2-2000 nm), it is Cr_2O_3 that mainly grows and the RL is much thinner.

Table IV. 11 – Thickness evolution of Cr_2O_3 and RL over time for B2 coated samples.

Sample	Cr_2O_3 (200 h)	RL (200 h)	Cr_2O_3 (2000 h)	RL (2000 h)
B2-400 nm	1.2 ± 0.1	Not observed (very thin)	1.7 ± 0.3	2.1 ± 0.7
B2-1000 nm	0.9 ± 0.2		2.4 ± 0.3	0.5 (max. observed)
B2-2000 nm	0.9 ± 0.2		2.3 ± 0.3	0.3 (max. observed)

These results confirm the competitive growth between Cr_2O_3 and the (Co,Mn,Cr) Reaction Layer. The Cr diffusion for RL formation instead of chromia formation was previously indicated by Talic *et al.*[123]. using $MnCo_2O_4$ and Fe or Cu-doped MCO coatings produced by Electrophoretic deposition (EPD) on Crofer 22 APU, exposed over 4000 h at 800 °C. Post-mortem analysis indicated that a 0.6 µm chromia oxide scale (similar to the as-prepared sample) formed, with all Cr having diffused to the reactive layer.

Table IV. 12 – Thickness evolution of Cr_2O_3 and RL over time for B2 coated samples

Oxidation time (h)	Cr_2O_3 (µm)	RL (µm)
500	1.7 ± 0.4	Not observed (very thin)
2500	1.7 ± 0.5	2.1 ± 0.4
5000	2.0 ± 0.5	2.95 ± 0.7

4.3. Impact of the Mn/Co concentration ratio in the outer spinel layer

4.3.1. Influence on the oxide scale formation

The main factor distinguishing samples with high and low RL formation is the Mn/Co concentration ratio in the external spinel layer. A lower Mn/Co concentration ratio proved favourable for slowing down RL growth, as shown by the thicker coatings (B2-1000 nm and B2-2000 nm). Even after 2000 h of annealing at 800 °C, only small amounts of Cr were detected in the Co–Mn layer of these samples and far from the external surface. In contrast, thinner coatings (B1-700 nm and B2-400 nm) exhibited high Mn/Co concentration ratio in the spinel layer and more extensive RL growth and Cr diffusion to the gas interface. Figure IV.26 illustrates this effect of the Mn/Co concentration ratio on the competitive growth rate of Cr_2O_3 and the RL. It highlights a preferential growth of chromia for low Mn/Co concentration ratio and preferential growth of RL for high Mn/Co concentration ratio.

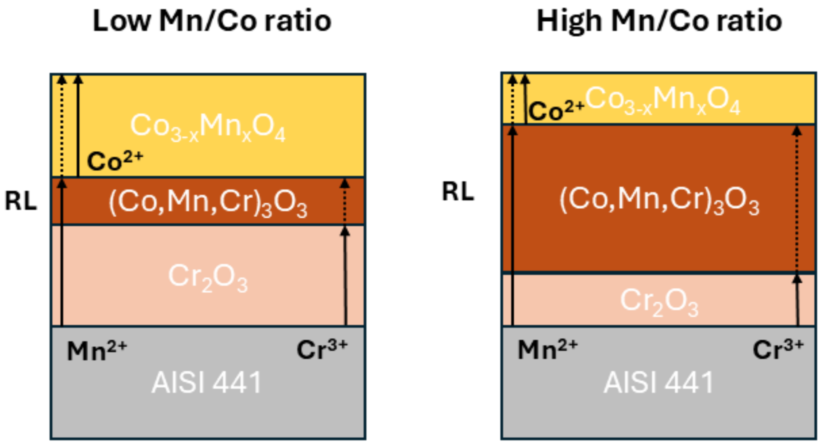

Figure IV. 26 – Schematic representation of the influence of Mn/Co concentration ratio on the growth rate of chromia and the RL.

Thus, the increase of the Mn/Co concentration ratio increases the diffusion of Cr into the spinel. Gao *et al.* studied the oxidation of $Mn_{1.5}Co_{1.5}O_4$ and $MnCo_2O_4$ coated Crofer 22 H samples (prepared by slurry deposition) in air at 800 °C for varying exposure times[110]. The samples with lower Mn/Co concentration ratio exhibited better protection against outwards Cr diffusion. The increase of Cr diffusion in spinel with high Mn/Co concentration ratio was attributed to the cation distribution (high Mn^{3+} occupation of octahedral sites) and strong Mn valence variability. Chesson *et al.*[117] studied $Co_{3-x}Mn_xO_4/Cr_2O_3$ diffusion couples for x = 1.0, 1.2, 1.35 and 1.5, and evaluated the influence of Mn content on the Reactive Layer formation rate at 900 °C. A strong influence of Mn concentration was observed, with RL growth rate being reduced at lower Mn/Co concentration ratios.

Thus, our results and literature confirmed a direct relationship between high Mn/Co concentration ratio in spinel and increased Cr diffusion and formation rate of the Reactive Layer. However, the physical reasons behind the influence of Mn are not that obvious. Several possible explanations for such behaviour could be proposed.

First of all, the Mn enrichment in the Co-Mn spinel increases the cation vacancy concentration[119,308], which could facilitate the Cr diffusion into the spinel.

The effect of Mn incorporation on the crystallographic structure of Co_3O_4 and on the cation distribution is shown in Figure IV.27a and Figure IV.27b, respectively. The phase diagram and cation distribution at 800 °C were performed using thermodynamic calculations for the $Co_{3-x}Mn_xO_4$ phase with varying x with the software Thermo-Calc[309]. Figure IV.27a shows that Co^{3+} and Co^{2+} occupy both tetrahedral and octahedral sites. By increasing x (thus Mn in Co-Mn spinel), Co^{3+} concentration decreases in tetrahedral and octahedral sites being replaced mainly by Mn^{3+} and Mn^{4+} on the octahedral sites and Co^{2+} in tetrahedral sites. For $x > 1$, Mn^{2+} cations also occupy the tetrahedral and octahedral sites. The Mn^{2+} and Mn^{3+} cations are larger (0.83 Å and 0.65 Å) than the Co^{3+} cations (0.61 Å) in octahedral position[253]. Previous works reported a strong correlation between ionic radius and lattice deformation, attributing the strain to the larger ions[310]. In addition, the Mn^{3+} cation is associated with the Jahn-Teller (JT) effect because it possesses a partially filled, degenerate electronic state in its octahedral coordination environment[311]. This degeneracy induces a local lattice distortion to lift the electronic instability and lower the system's energy. At low Mn^{3+} concentrations, these distortions remain localized[311,312]. However, if the Mn^{3+} concentration on octahedral sites reaches approximately 0.6-0.65 of the cation fraction, a cooperative Jahn-Teller effect may occur in the Co-Mn spinel[97], which consist into a cubic-tetragonal lattice deformation[313]. This distortion can be observed, by the yellow dotted line shown in Figure IV.27b, to occur at ≈ 0.66 of Mn cation occupation (x = 2 in $Co_{3-x}Mn_xO_4$) at 800 °C.

Other works observed this transition experimentally at around x =1.7 - 1.8 at 800 °C[112,298]. At lower temperatures the JT distortion occurs for lower x values of $Co_{3-x}Mn_xO_4$ spinels ($x \approx 1.3$ at room temperature)[99,104] due the variation of cation distribution with the temperature[111].

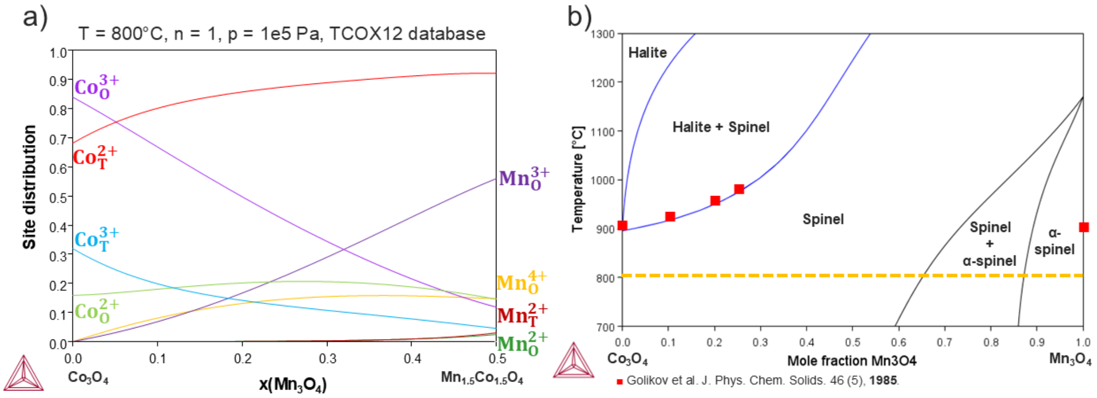

Figure IV. 27 - Thermodynamic calculations of the (a) cation distribution at 800 °C and (b) phase diagram for $Co_{3-x}Mn_xO_4$ spinels obtained using the software Thermo-Calc[309]. Data was obtained from Golikov et al.[314]

It is quite difficult to identify the exact physical reason for this relation between Mn/Co concentration ratio and Cr diffusion. However, it is likely related to lattice variation with increasing Mn concentration in the spinel phase. From our results, a composition of $Co_{1.7}Mn_{1.3}O_4$ (Mn/Co concentration ratio = 0.8) restricted the Cr diffusion outwards, while a Mn/Co concentration ratio of approximately 1 (stoichiometry being $Co_{1.5}Mn_{1.5}O_4$) exhibited fast outward diffusion of Cr. This last stoichiometry exhibits a lower Mn concentration than the one required for the cooperative JT lattice distortion at 800 °C[112,298], which indicates that the fast Cr diffusion into the spinel is not related directly to an abrupt lattice distortion from cubic to tetragonal structure. Instead, a gradual distortion led by the incorporation of Mn atoms and increased localized JT distortion is more likely.

It is proposed that this continuous lattice deformation by progressive Mn incorporation (lattice distortion by JT effect to be more precise) interferes on the diffusion path of Cr and accelerate it. To understand this assumption, let first explain what is usually proposed for cation diffusion in spinel. Overall, the diffusion path in spinels was assessed by Azaroff[315,316]: the fastest diffusion path for cations is to jump from octahedral to tetrahedral sites and back to another octahedral vacant site. This diffusion kinetics was described by Cox et al.[135] to follow

$$D = D_0 \exp\left[-(E_s + E_p)/RT\right]$$

where E_S is defined by the elastic energy penalty associated with the diffusing cation moving from octahedral to tetrahedral sites and E_p refers to the Octahedral Site Preference Energy (OSPE). Due to strong octahedral preference, Cr ions struggle to perform the path through tetrahedral sites[136,276]. Sun *et al.* suggested that, instead, Cr ions are more likely to diffuse by jumping from one octahedral site directly to another[136]. This direct diffusion could only happen if a significant amount of lattice strain was produced, since this requires an increase in the distance between two oxygen atoms to allow the Cr atom to pass between them[8,76,77]. Therefore, Cr diffusion into the spinel struggles to occur for close to ideal cases. However, this scenario may vary with a deviation from the ideal spinel case, which happens, for instance, when the oxygen parameter (*u*) value differs from 0.25[94]. Bordeneuve *et al.* showed that *u* values largely increase with Mn addition to the Co_3O_4 spinel oxide[104]. The increase of *u* values will affect the distances between cations and their neighbouring cation vacancies, which could facilitate the diffusion through the direct pathway (oct-oct). Most importantly, the replacement of Co ions by the larger Mn ions leads to a positive strain energy[288]. Similar strain is promoted by the Mn^{3+} through the local JT distortions. Therefore, the lattice is already deformed, which makes more space for cations to move and less extra E_S required for the diffusing Cr cation.

In conclusion, the addition of Mn cations, particularly Mn^{3+} cations, increases lattice deformation due their size and from the JT effect. This lattice deformation reduces the energy required for cations to diffuse, facilitating the diffusion. Overall, it seems that to maintain a low RL growth rate and limit Cr diffusion into the spinel, the Mn/Co concentration ratios should be lower than ≈ 0.8 for the conditions studied in this chapter (800 °C).

4.3.2. Prediction of the long-term Mn/Co concentration ratio in the outer spinel layer from initial coating thickness

The amount of oxidized Cr and Mn at 850 °C suggested a parabolic and linear oxidation behaviour for Cr and Mn, respectively (Figure IV.12a). A similar evaluation (eq. IV.2) can be made for the oxidation at 800 °C by considering various oxidation times (200, 500, 2000, 2500 and 5000 h) for B1 and B2 samples. Considering that the oxidized Cr amount strongly varies due to the different oxidation kinetics of B1 and B2 samples, only the amount of Mn oxidized was evaluated. The thickness values of the external spinel oxide layer were obtained using the ImageJ software and multiple micrographs for each sample[292], while the concentration was obtained from the average of, at least three EDS profiles. Results are reported in $mol\cdot cm^{-2}$ over time and shown in Figure IV.28a. The dotted line represents the total Mn available in the alloy, calculated by using the approach from Chanson *et al.*[317], which considers the equation IV.4, a 0.4 at.% Mn concentration in the alloy and a 0.2 mm-thick substrate.

$$n_{Mn} = \frac{\rho_A x_{Mn} th_A}{M_A} \quad (IV.4)$$

where ρ_A, M_A and th_A are the alloy density, molar mass and thickness, respectively, and x_{Mn} the atomic concentration of Mn in the alloy.

Figure IV.28a indicates that the amount of Mn oxidized has a steep initial rise, but ceases to increase at 2000 h. The values at 2000 h coincide with the Mn amount present in the alloy, suggesting the alloy reached complete Mn depletion: all Mn is oxidized. The values remain steady until the maximum duration investigated in this work (5000 h), further confirming the depletion hypothesis. Interestingly, the values at 200 and 2000 h (B2 samples) matched closely the values obtained for uncoated AISI 441 substrates. It suggests that, despite reducing Cr oxidation, the B2 coated samples do not reduce Mn oxidation and outwards diffusion.

The pink squares indicate the total amount of Mn in the spinel layer for the coated samples with additional 50 µm thick Lanthanum-Strontium-Manganese (LSM) coating. These values will be described later in Chapter V.

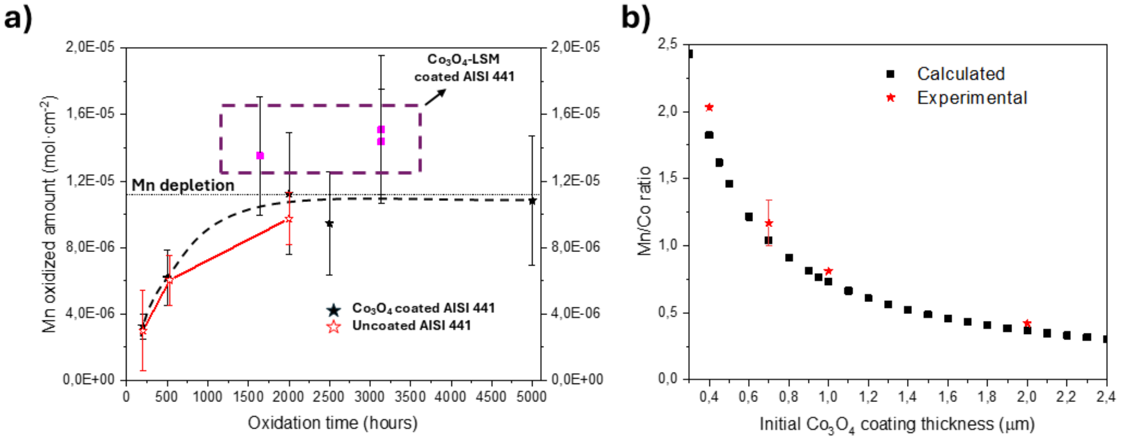

Figure IV. 28 - a) Amount of oxidized Mn in function of time at 800 °C. Red empty and black stars represent coated and uncoated samples respectively. The horizontal line represents the maximum amount of Mn in the AISI 441 alloy, calculated from equation IV.4. The dotted line is a guide to the eye, representing the amount of Mn oxidized over time. Pink squares indicate coated samples with an extra LSM layer. b) Mn content in the Co-Mn spinel, calculated from equation IV.5, in function of the initial Co_3O_4 coating thickness. The dotted lines correspond to the Co_3O_4 initial coating thicknesses used in this work (400, 700, 1000 and 2000 nm).

Understanding the Mn behaviour in the steel is a key point when developing the coatings because the amount of Mn diffusing over time will influence the stoichiometry of the oxide scales formed, and thus their diffusion (and electrical) properties. Considering that Mn diffuses mainly to the external spinel layer over time, it is possible to approximate the composition of the oxide layer after Mn depletion, in systems without LSM addition. Such prediction would help to prevent the formation of a spinel phase with high Mn/Co concentration ratio, shown to reduce Cr-barrier protection. Figure IV.28b compares the Mn/Co concentration ratio value in the spinel phase as a function of the initial Co_3O_4 coating thickness. The Mn/Co concentration ratio was calculated using

$$^{Mn}/_{Co} = \frac{n_{Mn}}{2n_{Co}} \quad (IV.5)$$

where n_{Mn}corresponds to the total amount of Mn in the alloy (1.11×10^{-5} mol·cm^{-2}) and $n_{Co}$to the amount of Co of one coating side, which varies with the thickness increase. n_{Co} was obtained using equation IV.2. Calculated points are shown by the black squares. Using the samples where Mn has been completely depleted in the alloy (exposed at 800 °C for more than 2000 h), one can relate the experimental measured Mn/Co concentration ratio with the calculated value from the initial coatings. There is a very good agreement between the experimental and calculated values, indicating that it is possible to predict the long-term Mn/Co concentration ratio of spinel oxides. The value can, then, be compared to the critical value (Mn/Co = 0.8) to evaluate if the outwards Cr diffusion will at least be fast in the spinel layer.

4.4. Co_3O_4 coating influence on AISI 441 oxidation kinetics

4.4.1. Influence of the atmospheric pressure plasma procedure on the oxidation performance

The B2 coated samples showed a significant improvement in the oxidation performance when compared to the B1 samples. This improvement was not directly related to the coating thickness since even the thin coating (B2-400 nm) displayed a two-fold reduction compared to the 700 nm from the B1 sample. Nonetheless, the benefit observed for B2 coatings seems to be a result of the methodology chosen for batch B2.

The B1 samples were coated after only four scans at a displacement speed of 0.5 mm·s^{-1}, representing, on average a ~ 175 nm layer per scan. Conversely, the B2 samples were coated at a displacement speed ten times faster, but under multiple scans, resulting in a ~ 14 nm layer per scan. This variation clearly rendered the production of more homogeneous coatings in B2, as shown in Figure IV.2 and Figure IV.3, which could indeed explain the strong oxidation reduction. Despite these variations, the cross-section of both approaches (Figure IV.4) exhibited compact coatings, particularly close to the alloy. Similarly, Co_3O_4 was obtained through both methodologies (Figure IV.5), with some variations as peak shift to lower wavenumbers and broadening from B2 to B1. This variation could represent a deviation from stoichiometry and the broadening a reduction of the crystallite size.

Persson *et al.*[119] suggested that a few parameters influence the oxidation kinetics of the coated sample, namely: the chemical potential gradient (1) and diffusion coefficients (2) of the diffusing species throughout the scale, the density (3) and number of grain boundaries (4) of the coating, and the reactivity (5) of the coating with the diffusing ions (Mn and Cr). Since the phase produced is the same, the (1) and (5) should not largely vary. The density and number of GBs will be strongly influenced by the process. B2 samples produced more homogeneous coatings compared to B1 samples, which showed strong thickness variation and formation of large clusters. However, the density of the coatings was not evaluated in this work. Regarding the grain boundaries, it was indicated by Raman spectroscopy the presence of larger crystallites, which would represent less grain boundaries in the coating. GBs offer a faster diffusion path and could largely influence the oxidation kinetics[305,318].

Another alternative is related to the presence of Hf precipitates throughout the coating. Hf is a reactive element (RE), and these elements are known to reduce the oxidation kinetics by blocking GBs and thus decreasing the diffusivity of cations (2)[41,43,319]. Hf particles were observed in both conditions but the faster displacement in B2 and multiple scans could facilitate a more homogeneous distribution of these Hf precipitates throughout the coating. More specifically, considering that only a thin layer is coated per scan, and that Hf precipitates are coated within these scans, Hf precipitates would be closer to the alloy. The Hf presence close to the alloy/coating interface could be beneficial to reduce the diffusivity of the Cr cations. Nonetheless, this hypothesis is difficult to prove since Hf precipitates were observed to be randomly distributed in both conditions. Although no conclusive evidence was observed, the better homogeneity, larger crystallites and possible Hf dispersion of B2 samples offers a reasonable explanation for the improved oxidation performance.

4.4.2. Coating thickness influence

No clear effect of the coating thickness on the oxidation kinetics was observed between 400 and 2000 nm. However, a strong effect on the Cr volatilization rate was identified. The increase in Co_3O_4 coating thickness offered a larger Co reservoir, delaying the increase of the Mn/Co concentration ratio. The lower Mn/Co concentration ratio for B2-1000 nm and B2-2000 nm reduced the formation of the RL and avoided the presence of Cr at the oxide/gas interface. The absence of Cr at the surface prevented Cr volatilization. In contrast, the thin B2-400 nm layers exhibit Cr (between 5 and 10 at.%) at the surface, resulting in Cr volatilization Nonetheless, a 10-fold reduction in comparison to uncoated samples was observed. The reduction observed likely relates to i) delayed Cr diffusion to the surface and ii) low Cr activity[77] in comparison to $MnCr_2O_4$, generally observed externally for uncoated samples.

4.4.3. Expected influence of coatings to the electrical performance from our previous observations

The application of protective coatings proved highly beneficial in improving the oxidation resistance of AISI 441 substrates and in drastically reducing chromium evaporation. However, it is equally important to assess how the resulting oxide scales influence the electrical performance of the interconnects under operating conditions.

From literature, it is well known that the electrical properties of the oxide scale decrease with the increase of the thickness of Cr-rich oxide scale (both Cr_2O_3 and Cr rich spinel oxide). Our results demonstrate that the use of coatings reduced this thickness. For instance, the Cr-rich oxide layer (considering Cr_2O_3 and Cr rich spinel oxide) reduced from 4.5 µm for the uncoated AISI 441 substrate to 3.8 µm (B2-400 nm) and less than 3.0 µm for B2-1000 nm and B2-2000 nm after 2000 h of exposure at 800 °C. Moreover, these thickness values for coated samples consider the formed RL thickness which has not always high Cr concentrations. Chromia and Cr-Mn spinel, oxides formed on the uncoated AISI 441 substrate have high Cr concentration (with all Cr atoms located in the octahedral sites for Cr-Mn spinel) and, in consequence, have low electrical conductivity (between 0.001-0.05 $S \cdot cm^{-1}$). The conductivity of the RL formed in the spinel layer largely depends on its Cr concentration. Indeed, low conductivity values (0.007 $S \cdot cm^{-1}$) were obtained for RLs with high Cr stoichiometry ($Cr/(Cr+Mn+Co) \approx 2/3$), whereas higher conductivities were measured for RLs with lower Cr concentrations[118]. The Cr concentration for B1-700 nm and B2-400 nm after long-term exposure was 1.7/3 or below, which is reported[118] to represent a conductivity of approximately 0.05 S·cm^{-1}. Such values start to have a negative impact in electrical performance. B2-1000 nm and B2-2000 nm showed much lower Cr concentrations. Thus their electrical performances are expected to be much better.

The formation of Cr-rich phases was found to depend strongly on the Mn/Co concentration ratio on coated samples: lower ratios favoured the formation of chromia, while higher ratios promoted the growth of the reactive layer (RL). Consequently, thinner coatings (e.g., B2–400 nm) were observed to form thinner chromia layers but thicker, Cr-enriched RLs during long-term exposure. It is thus expected that the thinner coatings exhibit an initial benefit to the ASR values by reducing Cr_2O_3 formation. However, over time, the continuous Cr incorporation to the RL is expected to decrease the overall conductivity and increase ASR values. Moreover, Cr may eventually reach the oxide/gas interface, as observed for the B2–400 nm coating. The direct exposure of Cr to the gas phase promotes Cr evaporation reactions, and further degradation of the electrical performance.

4.5. Influence of additional LSM coating on the oxidation kinetics of Co_3O_4 coated samples and effect on oxide scale composition

In SOC operation, an LSM contact layer is commonly applied to enhance electrical contact between the interconnects and the electrodes. Therefore, understanding the formation of the oxide scale on the coated samples with LSM as well and then, the effect of the formed oxide scale on the overall electrical behavior is essential. The influence of the LSM contact layer on the oxidation behavior of AISI 441 was examined through thermogravimetric analyses at 700, 800, and 850 °C for B1–700 nm coated samples covered with an additional ~ 50 µm LSM coating (Figure IV.29a). The addition of LSM clearly reduced the parabolic oxidation rate constant by approximately a factor higher than two at 800 and 850 °C compared with coated samples without LSM (Figure IV.29b), like the trend observed for uncoated AISI 441 substrates (CEA results). This reduction suggests that the LSM layer significantly reduces the formation rate of poorly conducting oxides and thus maintains better electrical performance for the SOC interconnects. This reduction was suggested to be related to a reduction of the oxygen partial pressure at the coating/LSM interface[320].

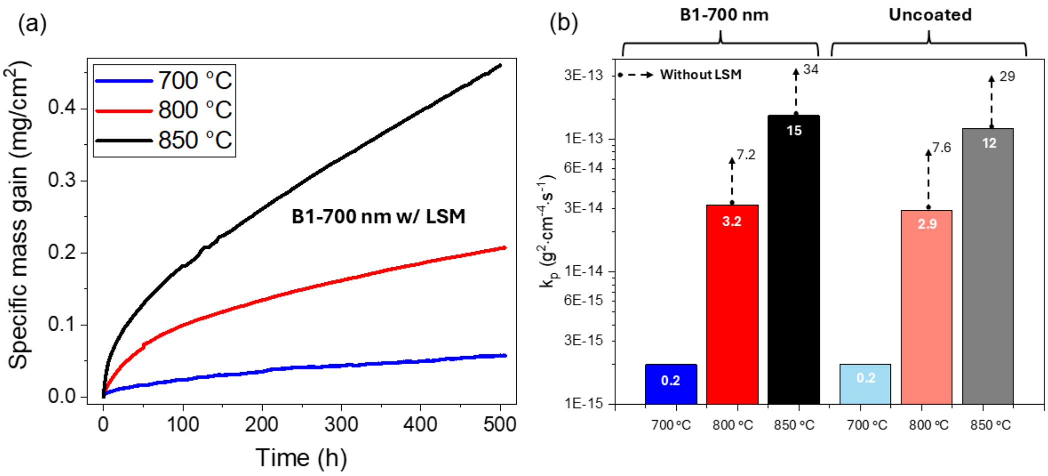

Figure IV. 29 - a) Mass gain over time for B1-700 nm coated samples with the addition of a LSM layer using TGA measurements. Samples were oxidized at 700, 800 and 850 °C for 500, 450 and 170 h, respectively. The k_p values are highlighted in (b).

Cross-sectional observations of the alloy/Co_3O_4/LSM samples revealed that the LSM layer exhibited a high porosity and only partial contact with the oxide surface (Figure IV.30). EDS analyses confirmed the formation of the chromia layer and the incorporation of Mn into the outer Co–Mn spinel. Considering the importance of Mn amount on the Mn/Co concentration ratio and thus on the scale growth, it is important to assess the influence of the addition of a Mn-rich layer (LSM) to the AISI 441 coated substrates. Notably, as shown in Figure IV.27a, the presence of the LSM layer increased the amount of Mn in the external spinel oxide during long-term exposure compared to what happened without additional LSM coating. It suggests that Mn diffuses from the LSM layer into the Co-Mn spinel.

The following chapter (Chapter V) will focus on the evaluation of the electrical performance of coated and uncoated AISI 441 substrates using deposited LSM contact layers.

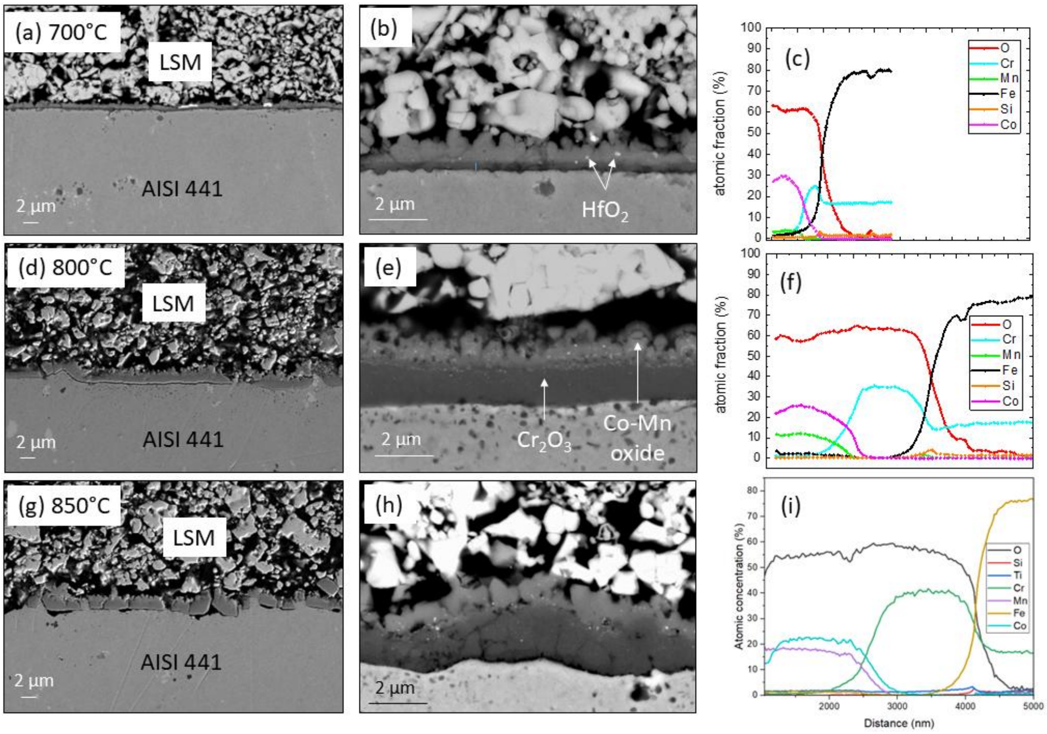

Figure IV. 30 – SEM cross-sections and EDS chemical profiles of the B1-700 nm coated samples with the addition of a LSM layer oxidized at 700 (a,b,c), 800 (d,e,f) and 850 °C (g,h,i).

5. Main takeaways

In Chapter IV, the Co_3O_4 coatings were deposited on AISI 441 substrates using two different deposition strategies. The aim of Chapter IV was to evaluate the protective character of Co_3O_4 coatings produced by AP-PECVD. The oxidation behaviour of the films was investigated by evaluating the oxidation kinetics, Cr evaporation and oxide scale growth air between 700 and 850 °C. In addition, the oxidation growth mechanism of the scale was studied on Co_3O_4 coated and uncoated AISI 441 substrates. The key takeaways are:

1. Using a fast displacement speed (5 $mm \cdot s^{-1}$) and a high number of scans (B2 strategy) produced more homogeneous coatings, which proved positive to reduce the oxidation kinetics of AISI 441 substrates. Co_3O_4 coatings produced at low displacement speed (B1 strategy) did not clearly affect the oxidation kinetics behaviour.
2. An inner Cr_2O_3 layer and an outer Co/Mn spinel layer are formed on the coated samples. A Reactive Layer (RL) made of Cr-rich Co/Mn spinel layer were formed between Cr_2O_3 and the external Co-Mn spinel oxide.
3. Using sequential oxidation tests with labelled O_2 molecules, it is demonstrated that the Co/Mn spinel layer grows outwardly and the Cr_2O_3 grows at the RL/ Cr_2O_3 interface by consuming the spinel layer. The RL was shown to grow from the diffusion of Cr into the spinel, which converted into Cr_2O_3 by the Cr enrichment of this RL.
4. Competitive growth between Cr_2O_3 and RL was observed and related to the Mn/Co concentration ratio in the external Co-Mn spinel oxide: high Mn/Co concentration ratios favour the diffusion of Cr and, thus, the growth rate of Cr-rich Reactive Layers.
5. Mn diffuses into the external Co-spinel, with the Mn/Co concentration ratio increasing over time. The Mn/Co concentration ratio also increased faster for thinner coatings.
6. The Co_3O_4 coating thickness was also varied for B2 samples, from 400 to 2000 nm. The thicker Co_3O_4 coatings (B2-1000 nm and B2-2000 nm) exhibited lower Mn/Co concentration ratio than B1-700 nm and B2-400 nm even after long term exposure at 800 °C. Interestingly, these two samples (B2-1000 nm and B2-2000 nm) exhibited larger Cr_2O_3 oxide layers but minimal formation of a RL, and thus negligible Cr

concentration at the oxide/gas interface. B2 coated AISI 441 substrates hindered by at least ten times the Cr evaporation in comparison to uncoated AISI 441 substrate.

7. The Mn amount was shown to be depleted from the AISI 441 (0.2 mm) after 2000 h of exposure at 800 °C. Therefore, the Mn/Co concentration ratio on the external spinel oxide after long-term exposure can be predicted by considering the initial Co_3O_4 coating thickness and the amount of Mn present in the alloy. This prediction is important since it enables the control of the Mn/Co concentration ratio, and thus the oxide scale growth.
8. Overall, the Co_3O_4 coated AISI 441 substrates reduced the formation of low electrically conductive Cr-rich phases by avoiding the formation of Cr-Mn spinel that is observed for uncoated AISI 441.
9. Finally, Chapter IV also evaluated the influence of Lanthanum Strontium Manganate (LSM) layers, used as contact layer to improve electrical contact, on top of the coated AISI 441 substrates. It was shown that oxidation kinetics drastically reduces for coated and uncoated AISI 441 substrates. Moreover, it was shown that using an LSM layer increases the amount of Mn in the external spinel oxide, which will vary the Mn/Co concentration ratio over time.

B1-700 nm, B2-400 nm and B2-2000 nm coated AISI 441 substrates will be evaluated regarding their electrical performance via ASR measurements in Chapter V.

Chapter V – Electrical performance of the Co_3O_4 coated and uncoated AISI 441 substrates

1. Introduction

Metallic interconnects must provide excellent electrical connection between cathode and anode, which can be negatively affected upon excessive chromia formation over time. Moreover, metallic interconnects are known to release Cr volatile species during oxidation at high temperatures, which may redeposit at the electrode and degrade the electrochemical performance[11–13]. Co_3O_4 coatings are used to address such issues. The electrical performance of the substrate-coating couple can be evaluated by the Area Specific Resistance (ASR) experiment[11–13,83]. This experiment measures the electrical performance of materials for SOCs applications, with the ASR value representing the sum of the resistances of each layer of the cell.

The sum of these values should remain as low as possible, with target values ranging from 50[12] to 100[13] $m\Omega \cdot cm^2$, with the lower limit resistance values being more desirable in the present work. The ASR measurement experiment can be operated in both SOEC and SOFC mode, which is defined by the direction the electrons flow[83]. ASR measurements in SOEC and SOFC modes are both important since these modes do not yield the same mechanisms, particularly regarding the redeposition of Cr volatile species. This Cr redeposition is more pronounced under SOFC mode[321] and sharply raises the ASR values.

The experiments performed in Chapter V simulate the operating conditions. In brief, the experiments consisted of *in-situ* ASR measurements, performed during several isotherms at 700, 800 and 850 °C for various duration. The isotherms performed during experiments 1 and 2 are displayed in Figure V.1. Prior to the first isotherm at 700 °C, the samples were heated up to 850 °C during 1 h to ensure densification of the contact layer (made in Lanthanum Strontium Manganate perovskite, LSM) on the sample surface and the platinum electrode to enhanced electrical contact. This step is also performed prior to SOEC operation to ensure the ideal sealing of glass and interconnect components.

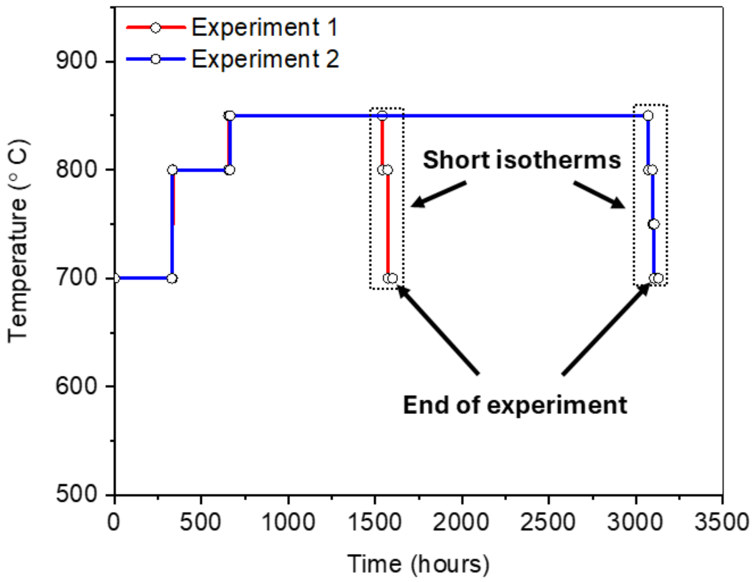

Figure V. 1 - Heating profiles (Experiments 1 & 2) for the evaluation of the ASR values of the uncoated AISI substate (Experiments 1 & 2) and the B1-700 nm (Experiment 1), B2-400 nm (Experiment 2) and B2-2000 nm (Experiment 2) coated AISI substates.

The objective of the ASR test is to accelerate the ASR increase kinetics by working at temperatures between 700 °C up to 850 °C with the latter being higher than the expected maximum temperature reached in SOC. This chapter aims at understanding the relationship between the ASR data with the sample characteristics observed at the end of the experiment. The influence of the Co_3O_4 coatings, and their initial characteristics (thickness and morphology) on the electrical performance were also assessed for the samples from batches B1 and B2. In chapter IV, we showed that B2 samples exhibited better coating homogeneity and significantly reduced oxidation kinetics. Moreover, the coating thickness was shown to be critical for further reducing Cr evaporation combined and the formation of a Cr-rich Reactive Layer (RL).

The samples from batches B1 (700 nm) and B2 (400 and 2000 nm) were studied for the ASR experiments and compared with the uncoated AISI 441 samples. All samples were covered by a 50 µm-thick LSM coating on both sides as the electrical contact layer. After the ASR experiment, the post-mortem samples were characterized by SEM and EDS, and the Pt electrode/LSM interface were characterized by XPS chemical analysis.

2. Results

2.1. Electrical performance of the uncoated and B1-700 nm coated AISI 441 substrates

2.1.1. Area Specific Resistance (ASR)

Figure V.2 shows the evolution of the ASR for the B1-700 nm coated sample and the uncoated AISI 441 substrate. The curves shown here describe the SOEC and SOFC behaviours of the B1-700 nm sample separately, while the curve of the uncoated sample represents the totality of the sample, accounting for the ASR average of both SOFC and SOEC values. The first isotherm was performed at 700 °C and maintained for 333 h. The ASR values remained stable for the uncoated sample (5.3 mΩ·cm^2). On the other hand, the B1-700 nm coated sample showed a continuous increase ASR value until stabilizing after approximately 180 h to reach 23 mΩ·cm^2 (SOEC mode) and 16 mΩ·cm^2 (SOFC mode). These values are much higher than the ASR value reached for the uncoated AISI 441 substrate.

The second isotherm was performed for 320 h at 800 °C. After the temperature increase, at 1 °C·min^{-1}, a sudden and large drop in the ASR values was observed for the B1-700 nm coated AISI 441 substrate. The ASR value for the SOEC mode reach roughly the same value as the one observed for the uncoated AISI 441 substrate, about 5 mΩ·cm^2. This ASR drop relates to the improved semiconducting properties of the oxide[322,323]. Indeed, the increase in temperature favours the charge carrier mobility[11]. The ASR of the uncoated AISI 441 substrate decreased also but was almost not detectable on Figure V.2. Then, the ASR values for the B1-700 nm coated AISI 441 substrate remained quite stable or slightly increasing whereas the uncoated AISI 441 substrate values sharply increased.

The third isotherm was performed at 850 °C for 880 h. Again, the ASR values dropped for all samples, although the drop was much less pronounced and is hardly visible in Figure V.2. At the 850 °C isotherm, the ASR of the uncoated sample increased at a faster rate than at 800 °C. After 1200 h of exposure, a drastic increase of the ASR rate is observed for the uncoated AISI 441 substrate which stops only with the current inversion, shown by the magenta spheres (this experimental procedure and the reason to do it will be explained later). At 850 °C, the ASR of the B1-700 nm coated AISI 441 substrate increases also (at a higher rate than at 800 °C) but at a rate much lower than for the uncoated AISI 441 substrate.

Applying a linear regression model over the entire third isotherm period (uncoated AISI 441 did not exhibit linear behaviour during the whole isotherm and was sectioned between 700-1000 h and 1280-1340 h), the ASR increasing rate was calculated for all samples at 850 °C. The values are given in Table V.1: the ASR increasing rate is about 3 (SOFC) to 4 times (SOEC) lower for the B1-700 nm coated AISI 441 substrate than for the uncoated AISI 441 substrate during the first period of exposure at 850 °C. Very important, no drastic ASR increase occurs for the B1-700 nm coated AISI 441 substrate as it was the case for the uncoated AISI 441 substrate after 1200 h of exposure (Figure V.2).

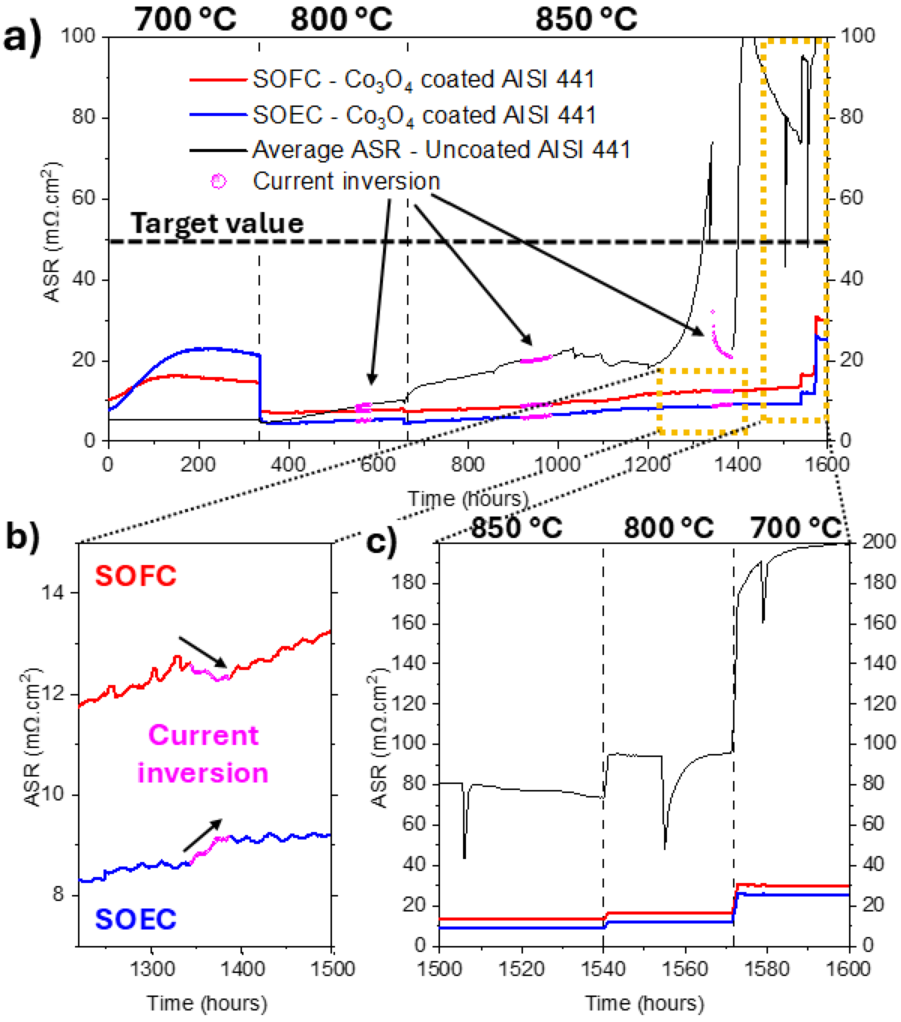

Figure V. 2 - (a) Area Specific Resistance (ASR) experiment evolution as a function of time. The experiment was conducted under 5 L·h^{-1} flow of synthetic air at 700 °C for 333 h, 800 °C for 320 h and 850 °C for 890 h. The average ASR values of uncoated AISI 441 sample (black) and the ASR values of the B1-700 nm under SOFC (red) and SOEC (blue) mode were followed. Current inversion periods (magenta spheres) were conducted during the experiment. The third current inversion period is highlighted in (b) for SOEC/SOFC modes of the B1-700 nm sample. At the end of the experiment, short additional isotherms were conducted at 800 and 700 °C, zoom in (c).

After 1540 h of exposure, the temperature was lowered to 800 °C (and maintained for 30 h) then to 700 °C (and maintained for 30 h) (Figure V.2c). This procedure was carried out to determine the activation energy of the ASR for all samples (presented in section 2.3). Much lower ASR values were obtained for the B1-700 nm coated AISI 441 substrate in comparison to the uncoated AISI 441 substrate at all temperatures. Notably, the ASR values of the B1-700 nm coated AISI 441 substrate remained much below the target values of 50 $m\Omega\cdot cm^2$ over the whole temperature range while the uncoated AISI 441 substrate exceeded such number.

Table V. 1 – ASR values for the B1-700 nm (both SOC modes) and uncoated (average) AISI 441 substrates at the end of the experiment at 700, 800 and 850 °C. The increasing rate was obtained from the linear regression during the isotherm at 850 °C. The values in parenthesis for uncoated sample highlights the increasing rate during the steep ASR rise occurring from 1200 h of exposure.

Sample	**ASR at 850 °C ($m\Omega\cdot cm^2$)**	**ASR at 800 °C ($m\Omega\cdot cm^2$)**	**ASR at 700 °C ($m\Omega\cdot cm^2$)**	**Linear increasing rate at 850 °C ($m\Omega\cdot cm^2\cdot 1000h^{-1}$)**
Uncoated AISI 441	74	95	198	23 (76)
B1-700 nm (SOFC)	14	16	30	8
B1-700 nm (SOEC)	9	12	25	6

2.1.2. Current inversion

The steep ASR increase for the uncoated AISI 441 substrate starting after 1200 h of exposure suggests the rapid formation of poorly conductive oxide phases. In previous test carried out at CEA[83], it has been shown that this drastic ASR increase, in fact, occurs exclusively on the face working in SOFC mode. Unfortunately, such observation could not be performed in our test configuration since the ASR value for the uncoated AISI 441 substrate was including both surfaces (SOEC and SOFC). The fact that the current direction has an effect on the ASR kinetics suggests strongly that this phenomenon is electrochemically driven. It has been proposed that this drastic ASR increase is due to evaporation/redeposition of Cr rich oxide in LSM or at the Pt/LSM interface[69,81,83]. The proposed scenario is that Cr_2O_3 (Cr^{+3}) evaporates to form CrO_3(g) (Cr^{VI}) by reaction with O_2(g). Subsequently, Cr^{VI} in CrO_3(g) is reduced to form chromium rich oxide (Cr^{+3}) somewhere in LSM or most likely at the Pt/LSM interface by trapping coming electrons. By this mechanism, the Cr redeposition depends strongly on the current direction since the electrochemical reduction of volatile species (Cr^{VI}) governs the process. Consequently, the effect is more pronounced in SOFC mode, where electrons flow in the same direction as the Cr species. Interestingly, Zhu *et al.* showed that the ASR induced by this phenomenon could be partially reversed by operating the cell in SOEC mode[324], providing thus an electrochemical cleaning of the electrode[83,321,324]. Using the approach from Zhu *et al.*[324], Bouvier *et al.* [unpublished CEA study] developed a method to detect Cr redeposition events[83]. The technique consists of switching the operational mode by inverting the current, here referred to as current inversion. This procedure not only enables the electrochemical cleaning of the electrode but also to verify if the observed ASR increase originates mainly from Cr volatilization/redeposition.

Figure V.2 shows that three current inversion events (magenta spheres) were performed during the experiment. The first inversion was carried out at 800 °C after 550 h of exposure. No effect could be observed on the ASR value and increasing kinetics, neither for the uncoated nor for the coated samples. The second inversion was applied at 850 °C after 920 h of exposure. Again, no effect was observed. Such observations demonstrate that the Cr volatilization/redeposition was not involved in the measured ASR values.

Finally, a last inversion was carried out at 850 °C after 1340 h of exposure when the ASR of the uncoated AISI 441 substrate had significantly increased and had reached about 73 $m\Omega\cdot cm^2$. This time, a large effect of current inversion was observed: the ASR of the uncoated AISI 441 substrate dropped rapidly initially and then more slowly to reach about 20 $m\Omega\cdot cm^2$ after 42 h of inverted current (Figure V.2a). Such ASR decrease by current inversion is explained by the “electrochemical cleaning effect”: the Cr rich oxide deposit in LSM or more likely at the Pt/LSM interface would be volatilized again since they are only stabilized electrochemically. By switching back to the initial current direction, the ASR values drastically increase once more demonstrating that this “cleaning effect” was only transitory. This observation could be due to the fact that the CrO_3 species that were generated by the “cleaning effect” were still localized and not evacuated in the bulk gas phase. In consequence, they rapidly redeposited. The redeposition process will be discussed in section V.3.4.

For the B1-700 nm coated AISI 441 substrate, only minor ASR variations were observed after 1340 h, with the drop from 12.6 to 12.3 $m\Omega\cdot cm^2$ for the SOFC mode, and the slight ASR increase from 8.6 to 9.2 $m\Omega\cdot cm^2$ for the SOEC mode over 42 h (Figure V.2b)). Such observations demonstrates that the large ASR increase for the uncoated AISI 441 substrate was due to the electrochemically driven Cr volatilization/redeposition phenomenon. Such event did not occur for the B1-700 nm coated AISI 441 substrate.

2.2. Electrical performance of the uncoated, B2-400 nm and B2-2000 nm coated AISI 441 substrates

2.2.1. ASR (experiment 2)

Figure V.3 shows the ASR curves of the B2 coated AISI 441 substrate (400 and 2000 nm) and the uncoated AISI 441 substrate. In this experiment, the ASR value of the SOEC and SOFC modes for both samples was not distinguished. Indeed, the sample potential was not measured, and the ASR value was measured only between the two platinum electrodes. In consequence, the ASR value represents the mean value of both SOC modes. Like the previous experiment, three sequential isotherms were performed at 700, 800 and 850 °C. Samples were maintained for 330 h at 700 °C then at 800 °C. The isotherm at 850 °C lasted approximately 2400 h in which a thermal cycling event which lasted around 70 h occurred after 2120 h of exposure.

At 700 °C, the same fast ASR increase as already evidenced in Fig V.2 occurs for the B2 coated AISI 441 substrates. This ASR increase seems to relate with the coating thickness. The B2-2000 nm coated AISI 441 substrate (42 $m\Omega \cdot cm^2$) showed a value two times higher at its peak than the B2-400 nm AISI 441 substrate (21 $m\Omega \cdot cm^2$). The uncoated AISI 441 substrate, on the other hand, showed again a stable ASR value (5 $m\Omega \cdot cm^2$) during the isotherm at 700 °C. The high values observed at 700 °C for coated samples will be discussed in detail in Appendix V.

A substantial ASR drop was again observed for the B2 coated AISI 441 substrates after increasing the temperature to 800 °C. For the B2-400 nm coated AISI 441 substrate, it decreased to 3 $m\Omega \cdot cm^2$ which is lower than the uncoated AISI 441 substrate. For the B2-2000 nm coated AISI 441 substrate, the final value at 800 °C is 9 $m\Omega \cdot cm^2$, slightly higher than the ASR measured for the uncoated AISI 441 substrate, 4 $m\Omega \cdot cm^2$. During the isotherm at 800 °C, the ASR of the B2 coated AISI 441 substrates decreased, particularly for the B2-2000 nm sample whereas the ASR for the uncoated AISI 441 substrate slightly increased. This ASR evolution was exactly what was observed in the previous ASR test in Figure V.2.

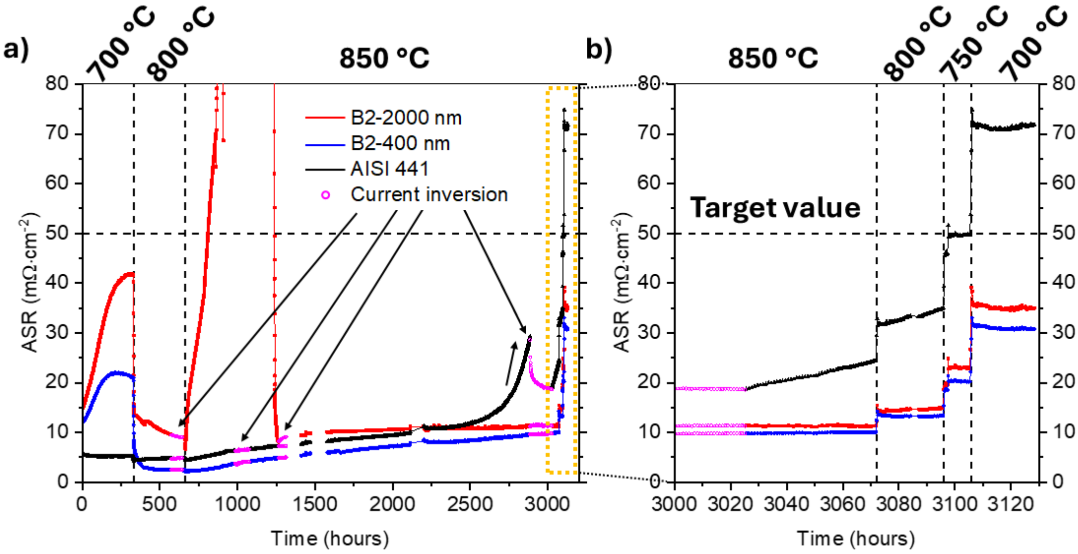

Figure V. 3 - (a) Area specific resistance (ASR) experiment evolution in function of time. The experiment was conducted under 5 L·h^{-1} flow of synthetic air at 700 °C for 330 h, 800 °C for 330 h and 850 °C for approximately 2400 h. The average ASR values of uncoated (black), B2-400 nm (blue) and B2-2000 nm (red) AISI 441 substrates were followed. Current inversion periods (magenta spheres) were conducted during the experiment. At the end of the experiment, short additional isotherms were conducted at 800, 750 and 700 °C (b).

When the temperature was increased to 850 °C, a further small ASR drop is observed, followed by a continuous ASR increase rate for the uncoated (~ 3 mΩ·cm^2·kh^{-1}) and B2-400 nm (~ 3 mΩ·cm^2·kh^{-1}) AISI 441 substrates until the thermal cycling event (2120 h). The B2-2000 nm AISI 441 substrate showed a significant ASR increase after transitioning to 850 °C followed by an abrupt ASR drop to values close to the ones measured for the other samples after 1270 h. As it will be demonstrated later, this increase was not due to volatilization/redeposition of Cr. Another explanation is needed for this abnormal evolution. One possibility is that the formed oxide layer on the B2-2000 coated AISI 441 exhibited poor electrical contact in one of its interfaces when switching to 850 °C and that a good contact was re-established at 1270 h. After 1270 h, the ASR for the B2-2000 nm coated AISI 441 substrate remained slightly higher than for the B2-400 nm and the uncoated AISI 441 up to the thermal cycling event. However, the ASR increasing rate of B2-2000 nm was much lower than for the other samples (1 mΩ·cm^2·kh^{-1}) between 1600 and 2120 h.

After the thermal cycling, the ASR curve of the uncoated AISI 441 showed a strong increase starting from 2500 h. In contrast, B2 coated AISI 441 substrates did not exhibit such ASR increase. The stability of the B2 coated samples is confirmed by the ASR increasing rates. These values were estimated in two stages: from 1600 to 2120 h and from 2200 to 3100 h.

For the uncoated AISI 441 substrate, this second stage considered solely the very strong ASR increase observed at 2750-2900 h. The values are summarized in Table V.2 and indicate a good consistency of ASR increasing rate for B2 coated AISI 441 substrates on both stages. In addition, it also shows that the ASR increasing rate for B2-2000 nm is much lower.

Table V. 2 – Average ASR values for the B2-2000 nm, B2-400 nm and uncoated samples at the end of the experiment at 700, 800 and 850 °C. The increasing rate was obtained from the linear regression during the isotherm at 850 °C. Values obtained from 1600 to 2120 h are shown in the left, and from 2200 to 3100 h are shown in the right. The values in right for uncoated sample highlight the increasing rate during the steep ASR rise (2750-2900 h). Values from experiment 1 are given for comparison (orange). Values in parentheses represent the SOFC mode while the SOEC values are shown on the right for B1-700 nm sample.

Sample	**ASR 850 °C**	**ASR 800 °C**	**ASR 700 °C**	**Increasing rate at 850 °C ($m\Omega\cdot cm^2\cdot 1000h^{-1}$)**
AISI 441 (1600 h)	74	95	198	23/76
AISI 441 (3120 h)	24	35	71	3/99
B1-700 nm (1600 h)	(14) 9	(16) 12	(30) 25	(8) 6
B2-400 nm (3120 h)	10	13	31	3/3
B2-2000 nm (3120 h)	11	15	35	1/1

At the end of the experiment, further isotherms were performed at 800, 750 and 700 °C. As for the previous ASR test (Figure V.2), it is assumed that the oxide scale at 800, 750 and 700 °C is the one obtained at higher temperature, 850 °C, in term of composition and thickness. In consequence, the measured ASR value for the four temperatures is for the same oxide scale. This oxide scale will be analysed in the next part. The final ASR values are reported at each temperature in Table V.2. Both B2 coated samples showed ASR values at least two times lower than the uncoated AISI 441 substrate over the 700-850 °C temperature range. In addition, these values are below the ASR target values (50 $m\Omega\cdot cm^{-2}$) over the whole temperature range for B2-400 nm and B2-2000 nm AISI 441 substrates. Despite being acceptable over 800 °C, the ASR curve of the uncoated AISI 441 substrate showed signs of Cr evaporation/redeposition (revealed by the strong ASR increase between 2750 and 2900 h of exposure).

2.2.2. Current inversion

Four current inversions events were performed for this experiment: a first one for 70 h at 800 °C and three times at 850 °C (for 100, 70 and 45 h in that order). Despite presenting a strong ASR increase when switching the temperature from 800 to 850 °C, the B2-2000 nm AISI 441 substrate did not show a strong ASR reduction during the current inversion periods. This result confirms that this increase was not related to Cr evaporation/redeposition, that could have been the case, but more likely the transitory degradation of the electrical contact, as proposed previously. For this sample, no significant ASR variation was noticed on the last current inversion (2880-3025 h), which confirms the benefits of the coating against Cr volatilization. Similarly, the B2-400 nm sample ASR behaviour was not affected during the current inversion events.

Conversely, the uncoated AISI 441 substrate showed a significant ASR increase at 2750 h, followed by a rapid decrease to similar ASR values when the current was inversed. The sudden ASR decrease confirms that Cr species poisoned the LSM and/or Pt electrode. Despite being effective to electrochemically clean the electrode, the ASR values rise again as soon as the current is reversed as for the previous test (Figure V.2).

2.3. Activation energy

The ASR temperature dependence was assessed between 850 and 700 °C for all samples using the ASR values obtained at the end of the experiment through the isothermal steps. Figure V.4 confirms that all samples followed an Arrhenius-like behaviour over the temperature range, showing a good fit with the small polaron hopping conduction formula. The activation energies were calculated from the slope of the curves as follows:

$$\frac{ASR}{T} = A \cdot exp\left(\frac{E_a}{k_b T}\right) \qquad equation\, V.3$$

Where A is the pre-exponential factor ($\Omega \cdot cm^2 K^{-1}$), E_a is the activation energy ($kJ \cdot mol^{-1}$) and k_b is the Boltzmann constant ($eV \cdot K^{-1}$). Table V.3 summarizes the activation energy values obtained for samples from experiment 1 (Figure V.2) and 2 (Figure V.3). The displayed activation energy represents the average values obtained from the variation of ASR during heating and cooling step. Minimal variation was observed between the two values.

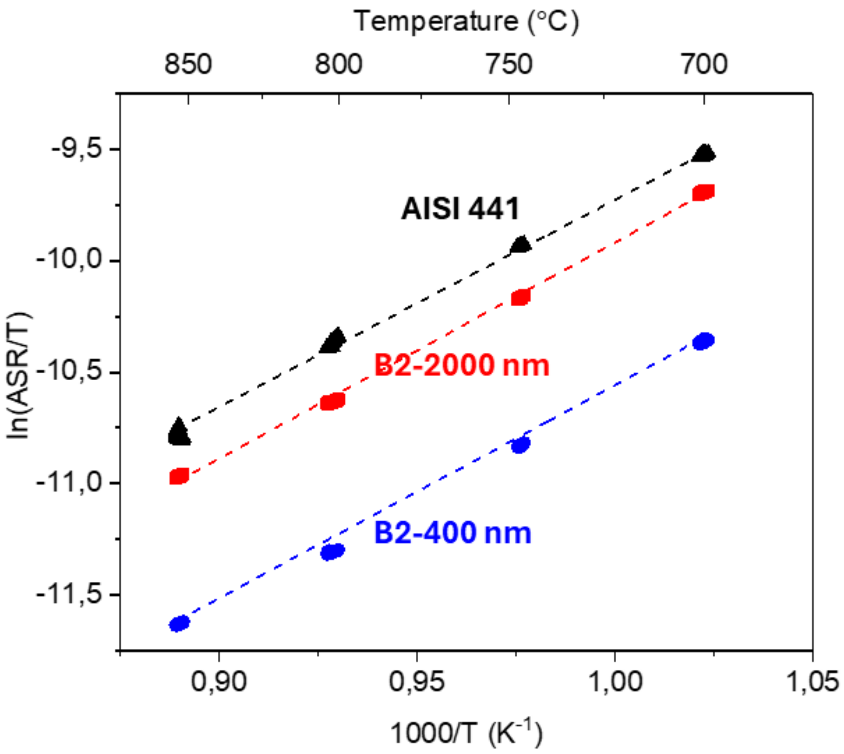

Figure V. 4 – ASR values in function of temperature determined during stepwise cooling at the end of experiment 2.

Samples from experiment 2 exhibited higher activation energy values compared to samples from experiment 1, both coated and uncoated. In experiment 2, the two B2 coated samples showed nearly identical activation energies (~ 0.82 eV), both slightly higher than the uncoated sample (~ 0.77 eV). The B1-700 nm sample was evaluated at both SOFC and SOEC modes, showing a 0.1 eV higher value in SOEC mode. Their average value (0.69 eV), however, matched well with the uncoated AISI 441 sample (0.69 eV). All these values will be discussed in Discussion section.

Table V. 3 – Activation energy values obtained from the small polaron hopping conduction equation for samples from experiments 1 and 2 (bold). The activation energies from SOFC (left) and SOEC (right) were calculated for the B1-700 nm sample. Average value is shown in parenthesis. The activation energy shown here is the average value from the activation energy obtained during a cooling and a heating step.

	AISI 441 (1600 h)	**AISI 441 (3130 h)**	B1-700 nm (1600 h)	**B2-400 nm (3130 h)**	**B2-2000 nm (3130 h)**
Activation energy (eV)	0.69	**0.77**	0.64/0.74 (0.69)	**0.83**	**0.82**

2.4. Microstructural characterization of the oxide scale

Figure V.5 and V.7 show the cross-section (a) and chemical profile (b) of the uncoated AISI 441 substrates after the ASR test (experiment 1 and 2 respectively). After experiment 1, the uncoated AISI 441 substrate shows an oxide scale made of a Cr_2O_3 layer and a $Cr_{2-x}Mn_{1+x}O_4$ layer with varying composition. The spinel composition at the LSM interface is $Mn_{1.5}Cr_{1.5}O_4$ and is richer in Cr near Cr_2O_3 with a stoichiometry that can be approximated to $MnCr_2O_4$. Moreover, the chemical profile indicates the formation of Si-rich oxide phases at the oxide/alloy interface but not continuous throughout the sample. The same observation is made for the uncoated sample after experiment 2. The oxide scale is made of Cr_2O_3 and a Mn/Cr rich spinel layer. From the measured composition, the following stoichiometry can be proposed for the outer spinel layer: $Mn_{1.2}Cr_{1.8}O_4$.

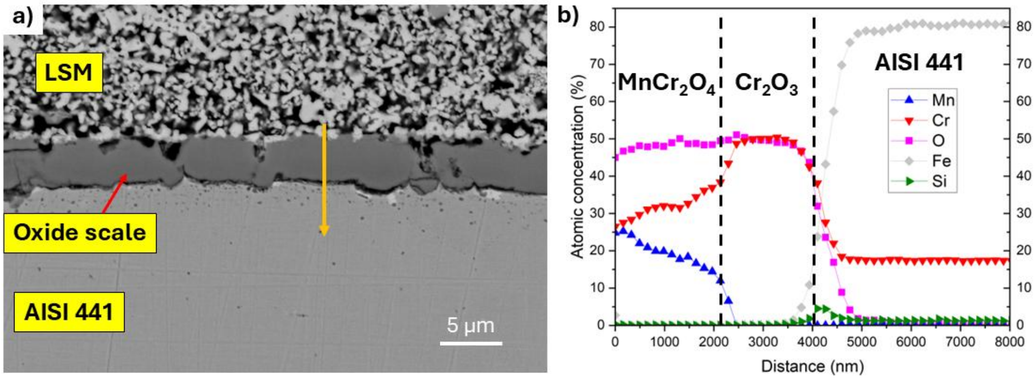

Figure V. 5 – SEM cross-section (a) and EDS analysis (b) of the uncoated sample after the ASR experiment 1. The orange arrow highlights the position of the EDS measurement.

The cross-section and EDS analyses of the coated B1-700 nm sample after experiment 1 and the coated B2-400 nm and B2-2000 nm samples after experiment 2 are shown in Figure V.6 and Figure V.7, respectively. The samples were composed of two oxide layers: an inner chromia layer and a (Co,Mn,Cr) rich outer spinel layer.

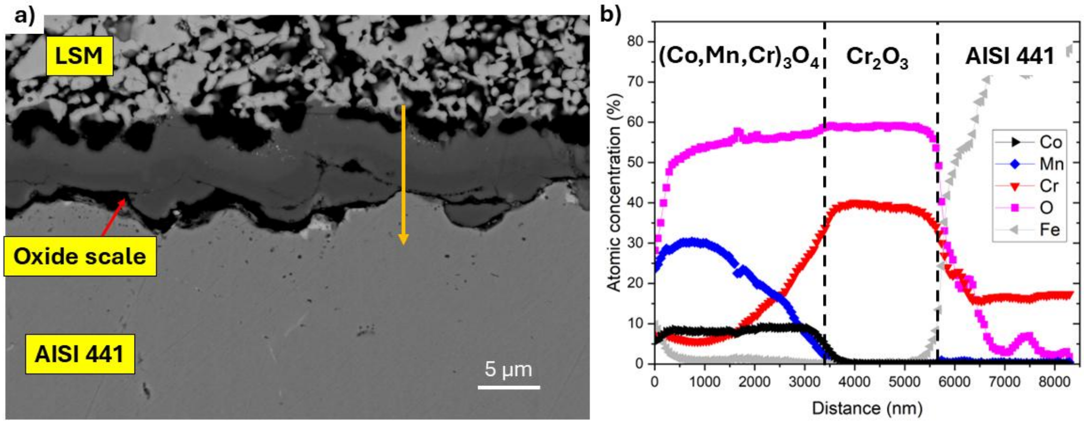

Figure V. 6 - SEM cross-section (a) and EDS analysis (b) of the B1-700 nm sample after the ASR experiment.

Table V.4 summarizes the average chemical composition of the oxide layer and their respective thickness for both the uncoated and coated sample after experiment 1 and 2. The thickness and chemical composition of this outer layer strongly varied in different regions of the sample. Thus, the chemical composition was averaged from five EDS chemical profile, resulting in $Co_{0.5}Mn_1Cr_{1.5}O_4$. The Cr concentration is very high close to the interface with chromia but decreases close to the oxide/LSM interface.

Table V. 4 - Average thickness of chromia and spinel layers from experiment 1 (highlighted in orange) and 2 obtained from five micrographs and measured using the software imageJ. The chemical composition from the spinel layer was obtained from the average of five EDS analysis.

Sample	Cr_2O_3 thickness (µm)	Spinel composition	Spinel thickness (µm)
Uncoated	2.1 ± 0.4	$MnCr_2O_4$	2.5 ± 0.5
B1-700 nm	2.9 ± 0.9	$Co_{0.5}Mn_{0.1}Cr_{1.5}O_4$	3.1 ± 0.5
Uncoated	2.3 ± 0.4	$Mn_{1.2}Cr_{1.8}O_4$	2.6 ± 0.5
B2-400 nm	3.2 ± 1.1	$Co_{0.4}Mn_{1.0}Cr_{1.6}O_4$	3.2 ± 1.0
B2-2000 nm	3.6 ± 1.3	$Co_{1.3}Mn_{0.8}Cr_{0.9}O_4$	3.9 ± 0.9

From Table V.4, both the Cr_2O_3 and the spinel layer thickness increases in the following order (experiment 2): uncoated > B2-400 nm > B2-2000 nm. The thicker spinel oxide layer for the coated samples is, of course, mainly due the initial coating thickness. But it is interesting to note that:

- The thicker is the initial Co_3O_4 coating, the thicker is the Cr_2O_3 layer formed below it.
- The Mn/Co concentration ratio in the outer Co-Mn rich spinel layer increases with the decrease of the initial Co_3O_4 coating.
- The Cr concentration of the outer Co-Mn rich spinel layer increases when the Mn/Co concentration ratio increases. The Cr concentration at the spinel/LSM interface is about 14 at% for B2-400 nm sample (Mn/Co concentration ratio = 2.5) whereas it is < 2 at% for B2-2000 nm sample (Mn/Co ratio = 0.6).

All these observations are in excellent agreement with the observations from chapter IV: higher Cr_2O_3 growth rate is combined with a slower growth rate of Cr-rich Reactive Layer (RL) in the outer spinel layer, which is induced by a lower Mn/Co concentration ratio in the outer spinel phase.

Finally, for both heating profiles, a much better adhesion between oxide and LSM contact layer was observed for the uncoated AISI 441 substrates with most of the sample in direct contact. On the other hand, the coated AISI 441 substrates showed only a few contact points between oxide and LSM, particularly for the B2-2000 nm sample. The alloy/oxide interface showed a good adhesion, although a few cracks were observed near the alloy/oxide interface on the coated samples. These cracks could, however, have originated during the metallographic preparation of the samples.

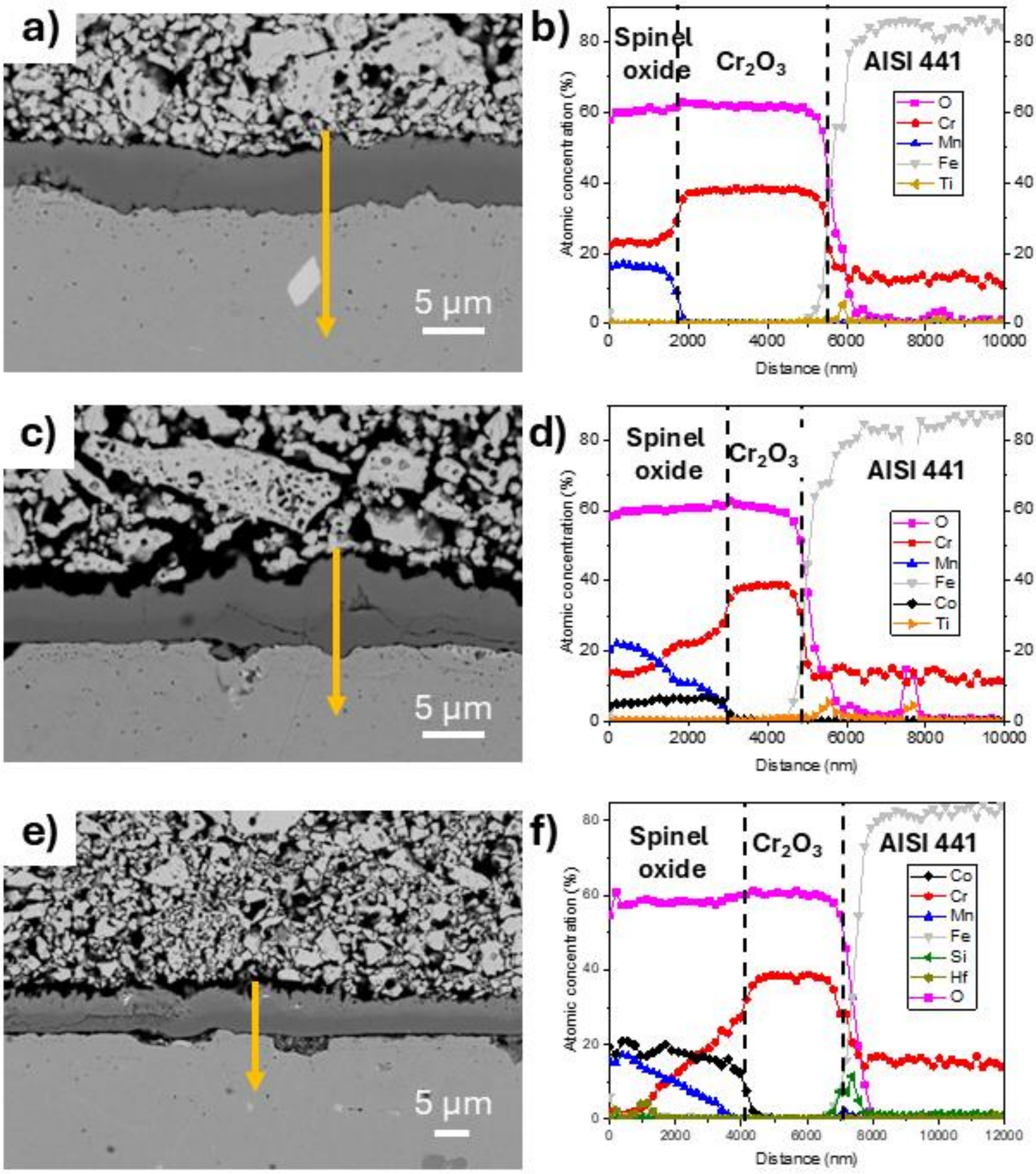

Figure V. 7 - SEM cross-sections (a, c and e) and EDS analyses (b, d and f) of the uncoated (a, b), B2-400 nm (c, d) and B2-2000 nm (e, f) samples after the ASR experiment. The orange arrow highlights the position of the EDS measurement.

2.5. Chromium poisoning

The transfer of Cr in LSM and near the LSM/Pt electrode interface was analyzed for the samples after experiment 1 and experiment 2.

First, the cross-section micrographs for both uncoated and B1-700 nm coated samples after experiment 1 revealed Cr-rich regions in the LSM contact layer. Some of these regions are highlighted on the cross-sections by yellow circles shown in Figure V.8. They could be identified by the chemical contrast observed on the images and were confirmed by the EDS mapping of the same region (Figure V.8a) and by EDS analysis of region 2 in Figure V.8b (see Table V.5).

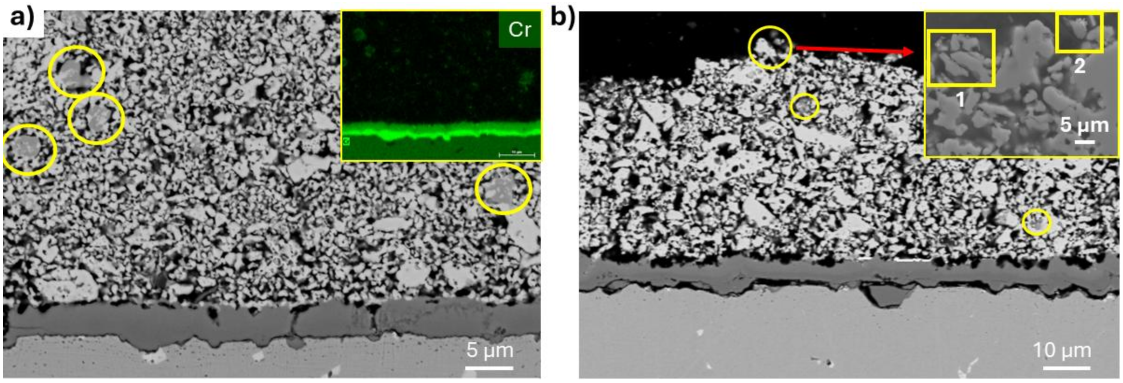

Figure V. 8 - SEM cross-sections of the uncoated (a) and B1-700 nm coated (b) samples after the ASR experiment. The yellow circles indicate regions with higher Cr concentration highlighted by the chemical contrast on the measurement. In (a), the Cr chemical mapping is shown for comparison. In (b), the square represents the region in the yellow circle close to the Pt electrode. The EDS analysis are shown in Table V.5.

Table V. 5 – Chemical composition (% at.) of regions 1 and 2 highlighted by the yellow squares in Figure V.8b. The other element is oxygen.

	Cr (%)	**La (%)**	**Sr (%)**	**Mn (%)**
Region 1	0.2	16.1	6.9	19.5
Region 2	4.8	7.1	3.9	14.5

EDS results confirm that Cr species migrate from the alloy into the LSM contact layer, particularly for the uncoated AISI 441 substrate where the Cr amount is higher. In addition to the EDS analysis in the LSM contact layer, the composition of the LSM/Pt electrode interface on the surface working in the SOFC mode (where the strong ASR increase was observed in Figure V.2 for the uncoated sample) was also evaluated by XPS measurements (Table V.6). The XPS results indicate a 2-fold higher concentration of Cr, and a 3-fold higher Mn concentration on the Pt electrode surface for the uncoated AISI 441 than for the B1-700 nm coated sample. At the LSM contact layer, the difference was less pronounced with only a mild difference in the Cr concentration in this region. These results suggests that the Cr species reached the Pt electrode surface and partially deposit on it for the uncoated AISI 441, and to a minor extent for the B1-700 nm coated AISI 441 substrates. This higher Cr concentration at the LSM/Pt interface likely explains the strong increase of the ASR value at

850 °C for the surface of the uncoated sample working in SOFC mode. The ASR increase was much lower for the coated sample in agreement with a lower Cr concentration in LSM and at the LSM/Pt electrode interface.

Table V. 6 - XPS measurements obtained at the LSM and Pt side of the surface of the uncoated and B1-700 nm coated samples working in SOFC mode. After the experiment, the cell was disassembled, separating the alloy/LSM couple from the Pt electrode. The measurements were conducted at the LSM and Pt electrode surfaces.

Sample	Position	Cr (%)	Mn (%)	Pt (%)	La (%)	Sr (%)
Uncoated	Pt electrode	8	22	68	-	-
	LSM	12	37	-	40	11
B1-700 nm	Pt electrode	4	8	85	-	-
	LSM	10	31	-	47	10

Similar analyses were carried out for the uncoated and B2 coated AISI 441 substrates after experiment 2. Figure V.9a shows the cross-section of the B2-2000 nm sample, comprising the alloy/oxide/LSM. EDS analyses were carried out on the yellow rectangles (from 1 to 12), shown in Figure V.9a. The same procedure was carried out for the uncoated and B2-400 nm samples, with rectangle 1 representing a region close to the oxide scale and rectangle 12 a region close to the Pt electrode. Figure V.9b displays the mass concentration of Cr (star) and Co (square) in function of the distance from the oxide scale for all samples. Only SOEC is shown here, but SOFC exhibited a similar trend.

No Cr was detected in LSM by EDS for the sample B2-2000 nm whereas it was detected in few zones for B2-400 nm. Around 1.5 at% of Cr was detected through the whole thickness of LSM for the uncoated AISI 441, except at the point closer to the Pt electrode (for SOFC side Cr was also observed at the furthest point). Overall, much less Cr was detected over the LSM contact layer if a coating was applied. An additional information is that Co seems to migrate from the coating towards the LSM contact layer, particularly for the thicker coating, with larger Co reservoir. Co was detected up to 20 µm within the LSM layer.

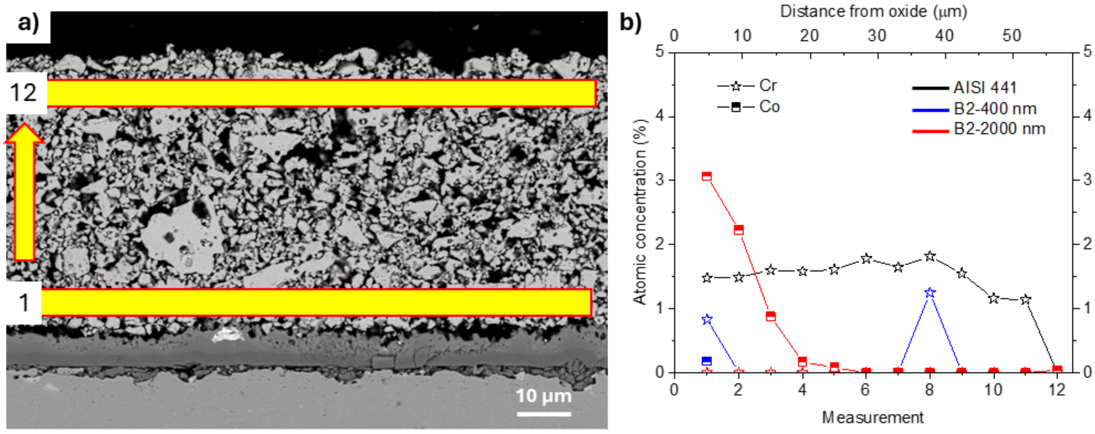

Figure V. 9 - SEM cross-section (a) of the B2-2000 nm AISI 441 substrate after the ASR experiment working in SOEC mode. The yellow rectangles highlight the region where the EDS measurements were performed. 12 regions in the LSM layer were analyzed, with region 1 representing the region closer to the oxide and 12, the region closer to the Pt electrode. (b) Atomic concentration of Cr (star) and Co (square) are presented in function of the measurement (distance from the oxide) within the LSM layer.

In conclusion, from these analyses, the Co_3O_4 coating clearly decreases the Cr volatilization rate which decreases, then, the Cr transfer into LSM. Such effect is directly linked to the Cr concentration at the LSM/oxide interface which is strongly linked to the Mn/Co concentration ratio in the coating and thus its initial thickness (as demonstrated previously).

3. Discussion

The ASR experiments aimed to evaluate the electrical performance of Co_3O_4 coated and uncoated AISI 441 substrates. In the results shown previously, all coated samples showed lower ASR values after the “accelerated” ASR test and, above all, avoided the strong ASR increase observed for uncoated samples at 850 °C over time. This ASR rise in uncoated samples is likely linked to Cr poisoning, as indicated by chemical analyses (XPS and EDS) of LSM and the surface of the Pt electrode, and suggested by the beneficial effect of current inversion periods. The presence of a coating mitigates this effect by promoting the formation of a Co–Mn-rich spinel over Cr_2O_3 which decrease drastically the Cr concentration in contact with the oxidizing atmosphere. For the B2-2000 nm sample, Cr concentration was minimal at the surface, which also reflected in the absence of Cr in the LSM layer.

All samples displayed at the end of the test semiconducting behaviour at all tested temperature, 700 °C, 800 °C and 850 °C. The values obtained here range from 0.69 to 0.83 eV. Overall, the activation energies obtained from ASR measurements for chromia forming alloys are generally ranges between 0.65 and 0.9 eV[83,92,123,325,326]. These values are generally attributed to Cr_2O_3 and Cr-Mn spinel but are also in the range of Co-Mn-Cr spinels with high Cr concentration[118]. It is hard to conclude which exact phase governs the ASR values, but it likely refers to a Cr-rich oxide phase.

The following discussion compares the measured ASR values at the end of the test with reference coatings from literature and tries to understand the contribution of each observed oxide layer to the ASR value. In addition, the discussion focuses on the influence of coatings on the oxide-scale evolution (Cr_2O_3 growth rate and Cr enrichment of the spinel layer in particular) and the suppression of Cr evaporation.

3.1. Uncoated AISI 441

The uncoated AISI 441 have shown a steady ASR increase without abnormal variations except when the Cr evaporation/redeposition phenomena became pronounced at 1200 h and 2400 h in experiment 1 and 2 (Figures V.2 and V.3), respectively. ASR values represent the sum of the resistances of each layer of the cell, being described as:

$$ASR = ASR_{AISI\ 441} + ASR_{oxide\ 1} + ASR_{oxide\ 2} + ASR_{CL} + ASR_{interfaces} \qquad equation\ V.1$$

where oxide 1 and 2 represent the chromia oxide scale formed during oxidation and the spinel oxide (in this case $Mn_{1+x}Cr_{2-x}O_4$), respectively, CL represents the LSM contact layer, and the interfaces corresponds to the sum of resistances over each interface (alloy/oxide 1, oxide 1/oxide 2, oxide 2/LSM and LSM/Pt electrode). The ASR of each layer can be defined as:

$$ASR = \frac{th}{\sigma} \qquad equation\ V.2$$

where *th* refers to the layer thickness (cm) and σ to its electrical conductivity ($S{\cdot}cm^{-1}$). Therefore, ASR values should increase with increasing layer thickness and strongly depend on the electrical conductivity of each layer and their interfaces. Overall, the ASR values from the alloy and LSM contact layer can be considered negligible due their remarkably high electrical conductivity[83]. The ASR coming from the interfaces are considered here as taking part of the overall ASR value of each oxide layer since they are not known independently. Both chromia and manganese chromite spinel have relatively low electrical conductivity values. However, these values vary considerably in literature, ranging from 0.001 to 0.05

S·cm^{-1} at 800 °C[83,327] for chromia and 0.001 to 0.4 S·cm^{-1} for the $Mn_{1+x}Cr_{2-x}O_4$[89,152,153], with values increasing with the Mn content. The conductivity variation observed on these two oxides relates to multiple factors, such as conductivity measurements on many different substrates (i.e., sintered Cr_2O_3 with varying purity concentrations or thermally grown Cr_2O_3 (TGO) formed on different metallic substrates) and the use of different experimental configurations (with different electrical contact layer for example)[144,145,147,150,328–330]. Using ASR ex-situ measurements on AISI 441 coated with Ce-Co at 800 °C, Goebel *et al.* tried to correlate the measured ASR values at different exposure times (7000, 23000 and 35000 h) with the Cr_2O_3 thickness[90]. Using upper and lower Cr_2O_3 conductivity values proposed in literature and previously mentioned, they calculated the ASR values and compared them to the experimental ones. The upper chromia conductivity values exhibited a much better fit with the experimental data[90].

Regarding the large scatter of the conductivity values of chromia in literature, it is quite impossible to determine the ASR of the oxide scale which grows on the uncoated AISI 441 sample from these values and the measured chromia scale. Thus, it is fundamental to proceed differently. Our approach was rather to determine the chromia electrical conductivity of our sample (using equation V.2) by using the ASR experimental data measured at the end of the experiment (mainly the ASR value at 800 °C) and the total oxide scale thickness values (by considering the error bars) measured by SEM on cross section at the end of the test. To use such approach, a few considerations were applied:

- only uncoated AISI 441 sample from experiment 2 was considered due to the strong influence from Cr redeposition in experiment 1
- the total ASR was attributed to the oxide scale (despite a fraction of it likely coming from the interfacial resistance, such as observed from the ASR raise due to Cr evaporation/redeposition),
- from the widespread chromia and manganese chromite conductivity values observed in literature, the conductivities of chromia and of the Cr-Mn spinel oxide layer were considered to be quite similar. Thus, the conductivity of the entire chromium rich oxide scale (Cr_2O_3 and $Mn_{1+x}Cr_{2-x}O_4$) was determined instead of each phase separately.
- the average oxide thickness was applied to equation V.2 with the error bars being calculated from the standard deviation of the thickness values.

From these considerations, the conductivity of the entire Cr-rich oxide scale was calculated to be 0.015 ± 0.003 S·cm^{-1}. From a similar experiment, Bouvier *et al.* [unpublished work at CEA] found a conductivity value of 0.018 ± 0.003 S·cm^{-1}, very close to our result. This conductivity value matches the order of magnitude of chromia and manganese chromite conductivity values found in literature, and closer to the upper limit as found by Goebel *et al.*[90] previously. Moreover, it is possible that real conductivity of the oxide scale is slightly higher since Cr evaporation/redeposition occurred in that test. In consequence, the measured ASR is not only due to the Cr rich oxide scale as assumed in our calculation. In conclusion, the conductivity value that has been calculated here is a minimum value.

Knowing the conductivity values of the oxide scale is fundamental to determine long-term ASR evolution. Figure V.10 displays the ASR values at 800 °C as a function of the oxide layer thickness for different nature of Cr rich oxides. The ASR values are calculated using the electrical conductivity data from literature. For chromia, three values of conductivities were considered: the lower and upper conductivity values from literature and the value obtained in our work (0.015 S·cm^{-1}). The graph shows the strong influence of the electrical conductivity values to the ASR values. For example, while the ASR target value (50 mΩ·cm^{2}) is reached for a 0.5 μm chromia layer when considering the lower conductivity limit (0.001 S·cm$^{-1)}$, it only reached after approximately 8 μm with the conductivity value measured in the present work.

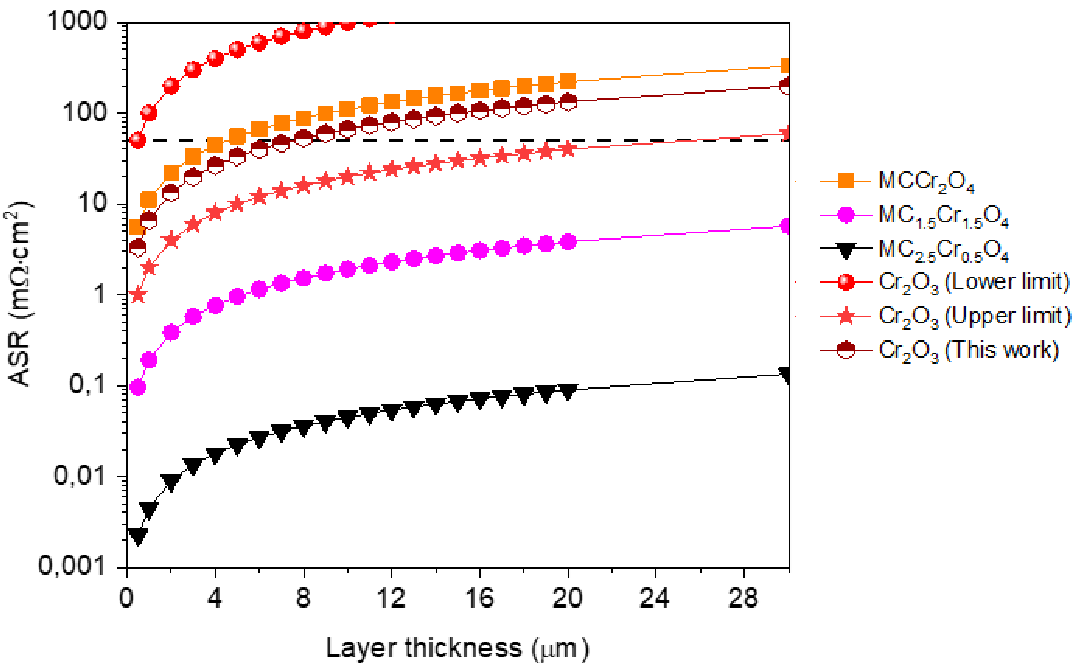

Figure V. 10 – Calculated ASR values in function of the layer thickness (μm). The ASR values were calculated from equation V.2, and the electrical conductivity data was obtained from Liu et al.[118] for the Co-Mn spinels with different Cr contents (MC$_{3-x}$Cr$_x$O$_4$), while the chromia values were obtained from the lower[151] and upper[144,145] chromia conductivity values in literature, and from the values obtained in our work (hexagon filled in the upper part).

3.2. B1 and B2 coated AISI 441

Chromia and Co-Mn spinels with different Cr contents forms on the coated sample surface. Figure V.10 presents the influence of Cr content in the Co-Mn spinels on the ASR values. The electrical conductivity data was obtained from Liu *et al.*[118] at 800 °C, acquired by measurements on $Co_{1.5-x}Mn_{1.5-x}Cr_{2x}O_4$ (for x = 0.0, 0.25, 0.50 ,0.75 and 1.0) spinel oxides. They observed a strong conductivity reduction with the Cr content increase, particularly for very high Cr (x approaching 1). Indeed, considering the conductivity being dependent on the formation of cation pairs in the octahedral sites, the Cr incorporation should drastically reduce the number of cation pairs, and thus the small polaron hopping effect[118,142]. Figure V.10 indicates a very low contribution to ASR values for $Co_{1.5-x}Mn_{1.5-x}Cr_{2x}O_4$ spinels with $x \leq 0.75$. With x = 1, the Co rich spinel conductivity (0.009 $S \cdot cm^{-1}$) decreases considerably. For this composition, ASR values become even higher than that of the uncoated AISI 441, formed exclusively by Cr_2O_3 and $Mn_{1+x}Cr_{2-x}O_4$, at same oxide thickness.

As for the uncoated sample, the composition and thickness of the total oxide scale was used to explain the ASR values obtained at the end of the ASR experiment for all the coated samples.

The conductivities of the outer spinel layer observed for the coated samples were approximated from its average chemical composition and the conductivity values of the Co-Mn-Cr rich oxide spinel published in literature[118] (Table V.7). The B2-2000 nm sample exhibited a low Cr-content on the external spinel oxide, which results in a small contribution to the ASR values. In contrast, the thinner counterparts, particularly B2-400 nm showed higher Cr-content (~ 1.6 as stoichiometric coefficient on Cr) resulting in a noticeable ASR contribution (~ 2 $m\Omega \cdot cm^2$). However, this ASR values represent only a small portion of the total ASR value measured at 800 °C at the end of the test (13 $m\Omega \cdot cm^2$). Therefore, it can be considered that the measured ASR values for all coated samples can be mainly attributed to Cr_2O_3.

The electrical conductivity of the chromia layer formed on the coated samples was calculated using the ASR values at 800 °C after subtracting the ASR values corresponding to the spinel (Table V.7) and applying the result to the equation V.2. The values are presented in Table V.8.

Table V. 7 – Calculated ASR values for the spinel phase using the spinel thickness measured and the electrical conductivity values from literature[118].

Sample	**Spinel phase**	**Spinel thickness (µm)**	**Electrical conductivity (S·cm^{-1})**	**ASR values (mΩ·cm^2)**
B1-700 nm	$Co_{0.53}Mn_{0.96}Cr_{1.51}O_4$	3.1 ± 0.6	0.5	0.6 ± 0.1
B2-400 nm	$Co_{0.35}Mn_{1.04}Cr_{1.61}O_4$	3.2 ± 0.9	0.2	2.0 ± 0.6
B2-2000 nm	$Co_{1.3}Mn_{0.82}Cr_{0.88}O_4$	3.9 ± 0.9	2.5	0.2 ± 0.1

The three $\sigma_{Cr_2O_3}$ obtained from the average chromia thickness (0.022 ± 0.007, 0.024 ± 0.008 and 0.028 S·cm^{-1} ± 0.01) shows a good consistency overall. These values are in quite good agreement with the value obtained previously on the uncoated sample (0.015 ± 0.003 S·cm^{-1}) and with values obtained from our group on uncoated AISI 441 operated solely on SOEC mode (0.018 ± 0.003 S·cm^{-1}), and from Stevenson *et al.* (0.030 S·cm^{-1}) for Co-Mn coated AISI 441[148]. The slightly lower values obtained for the uncoated sample could be justified by an additional contribution to the ASR, suggested by the strong ASR increase likely related to Cr evaporation/redeposition event.

Table V. 8 – Chromia electrical conductivity values calculated from the ASR values and Cr_2O_3 thickness for coated and uncoated samples at 800 °C.

Sample	**Chromia electrical conductivity (S·cm^{-1})**
B1-700 nm	0.022 ± 0.007
B2-400 nm	0.028 ± 0.010
B2-2000 nm	0.024 ± 0.008
AISI 441 (Exp. 2)	0.015 ± 0.003

3.3. Long-term electrical performance prediction

The ASR evolution with time is a valuable data since it can be used to predict the long-term electrical performance of interconnect[117,123]. The SOCs lifetime is expected to surpass 40 000 h, which comprises maintaining ASR values below target values (< 50 mΩ·cm^2) upon this period[11]. The increasing rate of the ASR is driven by the formation rate of the oxide phases with low electrical conductivity (chromia, manganese chromite and Co-Mn with high Cr content) and by the rate of Cr volatilization then redeposition at the Pt electrode.

In chapter IV, we observed that B2 samples, particularly B2-2000 nm, significantly reduced the oxidation rate and thus the formation of poorly conducting layers (Cr_2O_3, $Cr_{2-x}Mn_{1+x}O_4$ and the RL if rich in Cr) in comparison to uncoated AISI 441 and to B1-700 nm coated samples. In addition, they reduced Cr evaporation by at least 10 times in comparison to the uncoated AISI 441. The improved properties were partly related to the coating quality but also related to the coating thickness. As discussed in chapter IV, there was a competitive growth in coated samples between chromia and RL. It was shown (Table IV.11) that this growth was related to the Mn/Co concentration ratio, with high ratios favouring the formation of the RL due to the fast Cr diffusion, as in B2-400 nm and B1-700 nm, and low ratios favouring the formation of Cr_2O_3, as in B2-2000 nm. On one side, increasing the formation of RL is beneficial due to the decrease in Cr_2O_3 formation. On the other side, with the continuous Cr incorporation over time, the RL will become Cr-rich and thus poorly conducting (Figure V.10). Moreover, in thin coatings (B1-700 nm and B2-400 nm), Cr has reached the surface, which could instigate Cr evaporation.

The benefit of keeping a low Mn/Co ratio in the external spinel layer are confirmed by the ASR experiments. The lower ASR increasing rates were obtained for sample B2-2000 nm, which can thus be explained by the much lower Cr content on the Reactive layer (RL) and lower RL formation rate (Table V.7). Finally, the large ASR increasing rate observed for the uncoated samples in both experiments is mainly linked with the Cr poisoning effect and not only the growth rate of the chromium rich oxide scale (Cr_2O_3 and manganese chromite spinel).

Using the ASR values obtained at the end of the experiment at 850 °C, and the increasing rates obtained from a linear regression (Table V.1 and Table V.2), one can extrapolate the ASR over time, and estimate roughly when the ASR target value will be reached (50 mΩ·cm^2) using:

$$t - t_{exp_{850\,°C}} = \frac{(ASR_{target\,value} - final\ ASR_{850\,°C})}{ASR_{increasing\ rate}} \quad equation\ V.3$$

Only coated samples were evaluated here since the ASR target value was already overcame or close to by the uncoated samples. The exposure time at which the ASR is expected to reach 50 mΩ·cm^2 at 850 °C is presented in Table V.9 for all coated samples.

The coated samples from batch 2 (400 and 2000 nm) have considerably increased the lifetime of interconnects compared to B1-700 nm sample at 850 °C. In addition, the thicker Co_3O_4 coatings (B2-2000 nm sample) provides a large increase in the lifetime expectancy, more than three times compared to B2-400 nm at 850 °C. Importantly, the lifetime obtained for the B2-2000 nm (5.8 years) surpasses the 40,000 h (4.5 years) expectancy for SOC operation, placing the thicker B2 coating as a good candidate for interconnect protective coating.

Table V. 9 – Predicted lifetime values at 850 °C for coated AISI 441 samples estimated from equation V.3.

	B1 - SOFC	**B1 - SOEC**	**B2-400 nm**	**B2-2000 nm**
Predicted Lifetime (hours)	5,500	7,800	16,100	51,200

Nonetheless, these results should be taken with a lot of caution. First, such approach implies that the increasing rate remains stable over time. But at least two phenomena are expected to modify the ASR increasing rate. First, the Cr concentration in the outer Co-Mn spinel layer is expected to increase with time because of the progressive Mn diffusion in the spinel phase, from the LSM layer (Figure IV.27a). This Mn diffusion will modify the Mn/Co ratio of the spinel phase, which if high enough can accelerate Cr diffusion into the spinel layer (RL formation). The higher Cr concentration in the spinel will decrease the spinel conductivity. Moreover, as the Cr concentration at the spinel surface increases, Cr evaporation and redeposition become more significant [77]. This last effect is expected to induce ASR increase mainly in SOFC mode[83]. Lower effect is expected in SOEC mode.

Yet, the ASR values were estimated from the upper operational temperature in SOCs. Overall, the SOCs operational temperature fluctuates between 650 and 850 °C[32,331]. Operating at lower temperatures signifies lower oxide scale growth rates, but also much lower electrical conductivity values. Considering that the oxidation kinetics was accelerated in our experiment, one can expect smaller increasing rates at lower temperatures.

3.4. Cr evaporation

Cr poisoning was confirmed for the uncoated samples in both experiments. The strong ASR increase, observed solely on SOFC mode, was suggested to relate to the Cr deposition at the Pt electrode. Indeed, the electrochemical cleaning performed during the current inversion periods (Figures V.2 and 3) and identification of Cr (Figure V.8a, Figure V.9b and Table V.5) at the LSM and near the LSM/Pt electrode interface suggest that this increase is related to Cr species.

Nevertheless, a few considerations are necessary. The strong ASR increase was only noticeable after 1200 and 2500 h in experiment 1 and 2, respectively. Yet, Cr evaporation is expected to occur at a continuous rate in uncoated AISI 441 since the same phase (Cr-Mn spinel) is in direct contact with the gas interface during the whole experiment[15,78,123,299]. Similarly, no major changes were detected by the initial current inversion periods, implying that Cr poisoning did not impact in the ASR values. These facts indicate that the strong ASR growth seems to occur only after a certain Cr threshold is reached.

Previous studies observed a similar continuous ASR growth followed by a plateau (CEA results not shown here). The growth was explained by the increased coverage of Cr-rich oxide on the Pt electrode, with the plateau representing the instant of complete coverage of the Pt electrode[16]. Considering this phenomena and supposing that the oxide produced is a Cr_2O_3 or $MnCr_2O_4$, one can estimate the thickness of this layer formed near the Pt electrode. In our approach, the ASR values at the end of experiment 1 at 800 °C (98 mΩ·cm^2) were used by subtracting the values implied for the presence of oxide scale (~ 20 mΩ·cm^2) and by applying the Cr_2O_3 conductivity values obtained in this work or from literature (equation V.2). The calculated thicknesses are reported in Table V.10.

Table V. 10 – Calculated required thickness for the Cr-rich oxide redeposited at the Pt/electrode interface. The thickness values were calculated using the chromia conductivity values from literature and from this work, and the ASR obtained at the end of experiment 1 at 800 °C.

$\sigma_{Cr_2O_3}$ (S·cm^{-1})	ASR at 800 °C (mΩ·cm^2)	Calculated thickness (µm)
0.001	98 – 20 = **78**	0.8
0.025		20
0.050		40

Using the values from this work would imply the formation of a 20 µm-thick oxide near the Pt electrode. Considering the lower conductivity limit (0.001 S·cm^{-1}), a 0.8 µm-thick oxide is necessary to be formed. These values are unrealistically high, as no evidence of such a thick continuous Cr-rich oxide layer was observed experimentally. The rapid ASR increase instead suggests either the formation of a very thin continuous and very resistive oxide layer, or a decrease in the conductivity of another phase due to Cr incorporation. If the ASR growth were solely caused by the formation of a thin continuous oxide layer, it would require an oxide with a conductivity several times lower than the minimal values reported for Cr_2O_3 or $MnCr_2O_4$, which is unlikely. The second alternative could relate to an increase Cr concentration of the LSM layer (50 µm), which could lead to a reduction in the LSM conductivity. Indeed, EDS measurements (Figure V.9b) indicated a homogeneous Cr concentration across the LSM layer, which could explain the increase. However, similar Cr concentration values were obtained in both SOEC and SOFC modes, despite the ASR increase being noticed only on SOFC mode. In conclusion, the assumptions proposed to explain the strong increase in ASR on the SOFC side remain inconclusive. Further studies are required to clarify this phenomenon.

4. Main takeaways

In chapter V, the electrical performance of B1-700 nm, B2-400 nm and B2-2000 nm coated AISI 441 substrates were investigated through in-situ ASR measurements and compared with uncoated AISI 441. The experiments were performed with a series of isotherms at 700, 800 and 850 °C. The long isotherm was performed at 850 °C to accelerate the oxidation kinetics process. It was concluded that:

1. At the end of the experiment, Co_3O_4 coated AISI 441 substrates exhibited much lower ASR values in comparison to uncoated AISI 441, irrespective of the temperature. Moreover, the ASR increasing rate was lower for Co_3O_4 coated AISI 441 substrates, particularly for the B2-2000 nm samples. Higher values observed for uncoated AISI 441 were attributed to the faster formation of Cr-rich oxides, possessing low conductivity, and to the stronger Cr evaporation/redeposition.
2. Regarding the Co_3O_4 coated AISI 441 substrates, the reduction observed for B2-2000 nm was attributed to the lower Mn/Co concentration ratio of the external spinel oxide, which reduced the formation of poorly conducting layers (e.g., Cr_2O_3 and Cr-rich RL).
3. The Cr-rich oxides (Cr_2O_3 and Cr-Mn spinel) were the main phases governing the ASR values in both Co_3O_4 coated and uncoated AISI 441 substrates. A conductivity value was calculated by using the measured thickness of the Cr-rich oxides and the measured ASR value at the end of the test. The values for Co_3O_4 coated AISI 441 substrates range from 0.022 ± 0.007 to 0.028 ± 0.01 $S \cdot cm^{-1}$ and were around 0.015 ± 0.003 $S \cdot cm^{-1}$ for uncoated AISI 441 substrate. The values were in line with previous reports.
4. Moreover, a strong ASR increase was observed for uncoated AISI 441 substrates and was attributed to the Cr evaporation/redeposition process. Although the exact mechanism is not fully understood, the phenomena was suggested to be Cr-related by the current inversion periods and by the high concentration of Cr at the LSM and LSM/Pt electrode interface.
5. Finally, the time to reach the ASR target value (50 $m\Omega \cdot cm^2$) was predicted for all Co_3O_4 coated AISI 441 substrates. The B2-2000 nm samples presented the longer expected time at 850 °C (≈ 5.8 years), considering that the ASR increasing is maintained stable, and no oxide spallation occurs. This value is superior to the

attended lifetime requirements (≈ 4.5 years) and, at least, three times higher than the other Co_3O_4 coated AISI 441 substrates evaluated in Chapter V.

Conclusions

The present PhD work focused on the understanding of the mechanisms driving i) the AP-PECVD formation of dense Co_3O_4 coatings and ii) the efficient protection of AISI 441 substrates by Co_3O_4 coatings in the perspective of their integration as interconnect materials for SOCs application. Protection of interconnect materials for SOCs application requires the formation of high density coatings with low impurity levels.

In chapter III, the AP-PECVD parameters enabling the formation of crystalline and low impurity Co_3O_4 coatings were successfully elucidated. In addition, the Co_3O_4 coatings exhibited a stoichiometry close to Co_3O_4 alongside a low porosity and excellent adhesion to the studied substrates. The Co_3O_4 coatings composition and structure were shown to be mainly determined by the energy given by the plasma process, *i.e.*, energetic species and thermal energy, since minimal influence of substrate temperature was observed. A strong correlation between reactive oxygen nitrogen species (RONS), *e.g.*, NO, and the formation of pure cobalt oxides was disclosed. Specifically, when operating under open-air atmosphere conditions, NO compounds were abundantly observed in the plasma afterglow. Experiments conducted in a non-oxidizing atmosphere, *i.e.*, reduced concentration of RONS, yielded a high retention of carbonaceous species in the films that differ strongly from the composition expected for any cobalt oxide.

In the second part of this work, described in chapters IV and V, the developed Co_3O_4 coatings were deposited on AISI 441 substrates and their behaviour as protective coating was studied. Two AP-PECVD strategies were selected for the AP-PECVD application of the Co_3O_4 coatings on the AISI 441 substrate. The first (named B1) used a low displacement speed and only four deposition cycles, while the second (named B2) used a ten times faster displacement speed and involved multiple deposition cycles to reach thicknesses ranging from 400 to 2000 nm. The second strategy was demonstrated to produce more homogeneous Co_3O_4 coatings and strongly reduce the oxidation kinetics of AISI 441 substrates. Three Co_3O_4 coating thicknesses (400, 1000 and 2000 nm) were evaluated in B2 strategy. No clear effect on oxidation kinetics was observed with Co_3O_4 thickness variation. However, a slight benefit was observed for Cr evaporation. Nonetheless, all B2 coated AISI 441 substrates were beneficial for preventing the Cr evaporation rate as they reduced by at least ten times the rates in comparison to the uncoated AISI 441. Moreover, both strategies (B1 and B2) promoted the reduction of the formation of Cr-rich oxide phases. Co_3O_4 coated AISI 441 substrates formed a three-layer oxide scale, composed by Cr_2O_3, a Co-Mn-Cr rich layer, called Reactive Layer (RL) and an external Co-Mn spinel from bulk to the surface. The composition of the Co-Mn spinel oxide was determined by EDS analysis and confirmed using a Raman model, developed in base of the variation of position and broadening of peaks $F_2g(1)$ and A_1g. The composition of the Co-Mn spinel varied over time and relied significantly on the initial Co_3O_4 coating thickness, with Mn/Co concentration ratio increasing faster for thinner Co_3O_4 coatings.

Sequential isotopic tracer experiments enabled to understand that the oxide scale grows outwardly in a similar way as for the uncoated AISI 441 substrate. Based on similar reasoning performed by Guillou[275], a mechanism for the oxide scale formation was proposed. The RL grows due to the continuous diffusion of Cr atoms from the AISI 441 alloy into the Co-Mn spinel oxide. The continuous diffusion is responsible for an increase of the Cr concentration up to a point where the Cr_2O_3 phase becomes more stable than the mix Co-Mn-Cr spinel (RL). Competitive growth of Cr_2O_3 and RL is observed and is function of the composition of the external spinel oxide. The preferential growth of Cr_2O_3 was observed to occur for low Mn/Co concentration ratios (in the external spinel layer), while the growth of RL is favored for high Mn/Co concentration ratios. Such observation is explained by the variation of the chromium diffusion coefficient with the Mn/Co concentration ratio: the chromium diffusion increases in spinel with the increase of the Mn/Co concentration ratios. It is attributed to the lattice deformation led by the incorporation of larger Mn cations (namely Mn^{2+} and Mn^{3+}) than Co cations.

In Chapter V, *in-situ* Area Specific Resistance (ASR) measurements were performed to investigate the electrical performance of coated and uncoated AISI 441substrates at 700, 800, and 850 °C. Overall, all coated AISI 441 substrates exhibited significantly lower ASR values compared to uncoated AISI 441 substrates, particularly after long-term exposures. The uncoated AISI 441 substrates exhibited a strong ASR increase after long-term exposure, which was attributed to the Cr vaporization/redeposition process. No such behavior was observed for the coated samples. Several Co_3O_4 coating thickness were investigated regarding the electrical performance, which ranged from 400 nm to 2000 nm. The best performance was achieved for the B2-2000 nm coated AISI 441 substrate, which confirms the beneficial effect of higher coating quality and thicker thickness (leading to lower Mn/Co concentration ratio), on the electrical performance. The Cr-rich oxides (Cr_2O_3 and Cr-Mn spinel) were identified as the main phases influencing the ASR values, on both coated and uncoated AISI 441 substrates. Conductivity values for the Cr-rich oxide were estimated by the correlation of the thickness measurements with the ASR values. The conductivity of Cr_2O_3 was estimated to be between $0.022 \pm 0.007\ S\cdot cm^{-1}$ and $0.028 \pm 0.010\ S\cdot cm^{-1}$ for coated AISI 441 substrates, and the conductivity of the Cr-rich oxide to be around 0.015 ± 0.003

S·cm^{-1} for uncoated AISI 441 substrate. The conductivity values from the RL varies considerably with the Cr concentration. Negligible influence on the ASR values was observed for the RL from the B2-2000 nm coated AISI 441 substrate. However, for thin initial coatings (B1-700 nm and B2-400 nm), a non-negligible ASR value was obtained. The ASR of the RL is predicted to increase with exposure time due to continuous Cr enrichment.

The major conclusion of that work is to propose that the electrical performance of Co_3O_4 coated sample is controlled by the growth rate of the Cr-rich oxide scale composed of Cr_2O_3 and $(Mn,Co)Cr_2O_4$.

Outlook

This PhD work demonstrated that the AP-PECVD process is effective for synthesizing protective Co_3O_4 coatings and provided new insights into Co–Mn spinel/alloy interactions, particularly regarding oxide scale formation. Nevertheless, several aspects merit further investigation. The following perspectives are organized into three main categories: (i) further comprehension studies, (ii) continuation of the current work, and (iii) technological improvements in coating and processing.

Further comprehension studies

Some mechanisms identified during this PhD work require deeper understanding. For instance, the Cr evaporation/redeposition process observed in Chapter V merits detailed analysis. Although Cr was significantly observed in the LSM contact layer and near the LSM/Pt electrode interface, the ASR increase was too high to be solely attributed to Cr-rich oxide formation. Microstructural and phase characterization of the LSM/Pt electrode interface would help clarify these mechanisms. Moreover, results suggest the existence of a threshold beyond which ASR growth accelerates. Identifying this threshold could allow prediction of electrode degradation times.

The ASR experiments from chapter V have exhibited an abnormal ASR rise for the Co_3O_4 coated AISI 441 substrates at 700 °C. A few hypotheses were proposed in Appendix V.1 but more studies should be carried out to investigate the mechanisms behind it. In particular, longer isotherms at 700 °C should be performed to evaluate if ASR values remain high over time or if they decrease to the level measured for uncoated AISI 441 substrates.

The Mn/Co concentration ratio in the outer spinel layer was shown to govern oxide scale formation. This ratio can be approximated for coated AISI 441 substrates over time, once Mn depletion from the substrate occurs. However, the presence of the LSM contact layer introduces an additional Mn source, leading to further enrichment of the external spinel oxide and complicating the analysis. Future studies should quantify Mn diffusion from LSM into external spinel oxide to better assess its impact during long-term exposure.

Continuation of the work

Predictive studies initiated during this PhD work could be further developed. In Chapter V, ASR evolution over time was modelled to estimate the time required to reach the 50 $m\Omega\cdot cm^2$ ASR target. However, the model accounted that the electrical behaviour grows steadily over time. Complementary simulations, such as those initiated at CEA based on parabolic rate constants (k_p), could be extended to Co_3O_4 coated AISI 441 substrates, provided the oxide scale evolution is better understood. In particular, separating the contribution of chromia and RL growth to the total scale thickness could enable more accurate lifetime predictions.

Technological improvements

From a technological standpoint, the AP-PECVD technique has proven capable of depositing dense and high quality Co_3O_4 coatings and can potentially be extended to more complex architectures, such as multilayers (e.g., CeO_2/ Co_3O_4) or doped films (e.g., Fe- or Ti-doped Co_3O_4). CeO_2 interlayers are known to enhance scale adhesion and significantly reduce oxidation kinetics, and preliminary experiments not reported in this work confirmed that CeO_2 can be synthesized via AP-PECVD. Similarly, Fe and Ti doping could further improve Cr-barrier properties.

Despite these promising results, deposition rates remain modest (330 $min\cdot cm^{-2}$ to produce a 2000 nm Co_3O_4 coating), limiting large-scale applicability. Several strategies could enhance process efficiency:

i. Precursor design: In Chapter III, attempts to increase the injection rate were limited by the atomization system, which could not efficiently handle higher liquid precursor solution flow rates. The Co-based precursor was dissolved into an acetone solvent to produce the solution, which limits the precursor amount to its solubility in the solvent. Designing a precursor solution better fitted for such atomization system should be beneficial.

ii. Alternative injection/atomization systems: A variation in the atomization system could also be evaluated, for instance, through the heated nebulization system.

iii. Process optimization: Finally, the deposition rate could be increased by increasing the efficiency of the AP-PECVD process. In the framework of this PhD work, several experiments were performed using HMDSO (model precursor) using different AP-

PECVD configurations. Two main strategies were used: (i) injecting the precursor inside the plasma jet outlet nozzle, prior to its interaction with ambient air, and (ii) introducing a quartz confinement tube to retain the precursor within the plasma plume, thereby minimizing losses to the exhaust and secondary particle formation outside the deposition zone. A sixfold growth rate increase was observed when injecting the precursor inside the plasma jet nozzle, which was attributed to strong fragmentation of the precursor using such strategy. Despite the strong fragmentation, coatings were smooth and close to SiO_2 stoichiometry with minimal impurity content. The same approach could be used to increase the deposition rate of Co_3O_4 coatings. The findings of this study were discussed in detail in a journal article [*Preparing for submission*].

References

(1) IPCC. *Global Warming of 1.5°C*; Cambridge University Press, 2022. https://doi.org/10.1017/9781009157940.

(2) Chaar, Z.; Rouault, B.; Schuller, A. *Hydrogène Bas-Carbone: Quels Usages Pertinents à Moyen Terme Dans Un Monde Décarboné*; 2022.

(3) Energy Agency, I. *Global Hydrogen Review 2024*; 2024. www.iea.org.

(4) Académie des Sciences. *Hydrogène Aujourd’hui et Demain*; 2024.

(5) Liu, H.; Yu, M.; Tong, X.; Wang, Q.; Chen, M. High Temperature Solid Oxide Electrolysis for Green Hydrogen Production. *Chemical Reviews*. American Chemical Society September 25, 2024, pp 10509–10576. https://doi.org/10.1021/acs.chemrev.3c00795.

(6) Ebbesen, S. D.; Jensen, S. H.; Hauch, A.; Mogensen, M. B. High Temperature Electrolysis in Alkaline Cells, Solid Proton Conducting Cells, and Solid Oxide Cells. *Chemical Reviews*. American Chemical Society November 12, 2014, pp 10697–10734. https://doi.org/10.1021/cr5000865.

(7) Zhang, H.; Miyamoto, A.; Suzuki, A.; Wang, H.; Williams, M. C. Thermal Behavior and Performance Trajectories of Electrolysers. *ECS Trans.* 2018, *83* (1), 211–224. https://doi.org/10.1149/08301.0211ecst.

(8) Mougin, J.; Chatroux, A.; Couturier, K.; Petitjean, M.; Reytier, M.; Gousseau, G.; Lefebvre-Joud, F. High Temperature Steam Electrolysis Stack with Enhanced Performance and Durability. In *Energy Procedia*; Elsevier Ltd, 2012; Vol. 29, pp 445–454. https://doi.org/10.1016/j.egypro.2012.09.052.

(9) Hansen, J. B. Solid Oxide Electrolysis - a Key Enabling Technology for Sustainable Energy Scenarios. *Faraday Discuss.* 2015, *182*, 9–48. https://doi.org/10.1039/c5fd90071a.

(10) Xu, Y.; Cai, S.; Chi, B.; Tu, Z. Technological Limitations and Recent Developments in a Solid Oxide Electrolyzer Cell: A Review. *International Journal of Hydrogen Energy*. Elsevier Ltd January 2, 2024, pp 548–591. https://doi.org/10.1016/j.ijhydene.2023.08.314.

(11) Talic, B. Metallic Interconnects for Solid Oxide Fuel Cells High Temperature Corrosion and Protective Spinel Coatings.

(12) Fergus, J. W. Metallic Interconnects for Solid Oxide Fuel Cells. *Materials Science and Engineering: A* 2005, *397* (1–2), 271–283. https://doi.org/10.1016/j.msea.2005.02.047.

(13) Zhu, W. Z.; Deevi, S. C. Opportunity of Metallic Interconnects for Solid Oxide Fuel Cells: A Status on Contact Resistance. *Mater. Res. Bull.* 2003, *38* (6), 957–972. https://doi.org/10.1016/S0025-5408(03)00076-X.

(14) Zhu, J. H.; Chesson, D. A.; Yu, Y. T. Review-(Mn,Co)3O4-Based Spinels for SOFC Interconnect Coating Application. *J. Electrochem. Soc.* 2021.

(15) Reddy, M. J.; Kamecki, B.; Talic, B.; Zanchi, E.; Smeacetto, F.; Hardy, J. S.; Choi, J. P.; Mazur, L.; Vaßen, R.; Basu, S. N.; Brylewski, T.; Svensson, J. E.; Froitzheim, J. Experimental Review of the Performances of Protective Coatings for Interconnects in Solid Oxide Fuel Cells. *J. Power Sources* 2023, *568*. https://doi.org/10.1016/j.jpowsour.2023.232831.

(16) Dejob, T. DÉPÔT DE COUCHES MINCES MULTIÉLÉMENTS PAR PULVERISATION HIPIMS RÉACTIVE POUR LA PROTECTION D'INTERCONNECTEURS D'EHT, Université de Technologie de Troyes, 2024.

(17) Boccaccini, L. Elaboration de Revêtements Pour Interconnecteurs d'EHT Par Voie Humide, La Rochelle Université, 2025.

(18) Massines, F.; Sarra-Bournet, C.; Fanelli, F.; Naudé, N.; Gherardi, N. Atmospheric Pressure Low Temperature Direct Plasma Technology: Status and Challenges for Thin Film Deposition. *Plasma Process. Polym.* December 2012, pp 1041–1073. https://doi.org/10.1002/ppap.201200029.

(19) Merche, D.; Vandencasteele, N.; Reniers, F. Atmospheric Plasmas for Thin Film Deposition: A Critical Review. *Thin Solid Films*. April 30, 2012, pp 4219–4236. https://doi.org/10.1016/j.tsf.2012.01.026.

(20) Fanelli, F.; Fracassi, F. Atmospheric Pressure Non-Equilibrium Plasma Jet Technology: General Features, Specificities and Applications in Surface Processing of Materials. *Surf. Coat. Technol.* 2017, *322*, 174–201. https://doi.org/10.1016/j.surfcoat.2017.05.027.

(21) Snyders, R.; Hegemann, D.; Thiry, D.; Zabeida, O.; Klemberg-Sapieha, J.; Martinu, L. Foundations of Plasma Enhanced Chemical Vapor Deposition of Functional Coatings. *Plasma Sources Sci. Technol.* 2023, *32* (7). https://doi.org/10.1088/1361-6595/acdabc.

(22) MANN, M. E. *Our Fragile Moment: How Lessons from Earth's Past Can Help Us Survive the Climate Crisis*; Hachette, UK, 2023.

(23) Hawken, P. *Drawdown: The Most Comprehensive Plan Ever Proposed to Reverse Global Warming*; Penguin, 2017.

(24) IPCC. *Global Warming of 1.5°C*; Cambridge University Press, 2022. https://doi.org/10.1017/9781009157940.

(25) *World Energy Outlook 2024*. www.iea.org/terms.

(26) - International Energy Agency, I. *Global Energy and Climate Model Documentation 2024*; 2024. www.iea.org.

(27) Mansilla, C.; Bourasseau, C.; Cany, C.; Guinot, B.; Duigou, A. Le; Lucchese, P. Hydrogen Applications: Overview of the Key Economic Issues and Perspectives. In *Hydrogen Supply Chain: Design, Deployment and Operation*; Elsevier, 2018; pp 271–292. https://doi.org/10.1016/B978-0-12-811197-0.00007-5.

(28) Mansilla, C.; Bourasseau, C.; Cany, C.; Guinot, B.; Duigou, A. Le; Lucchese, P. Hydrogen Applications: Overview of the Key Economic Issues and Perspectives. In *Hydrogen Supply Chain: Design, Deployment and Operation*; Elsevier, 2018; pp 271–292. https://doi.org/10.1016/B978-0-12-811197-0.00007-5.

(29) International Renewable Energy Agency, T. *SHAPING SUSTAINABLE INTERNATIONAL HYDROGEN VALUE CHAINS*; 2024.

(30) *CLIMATE CHANGE : SCIENCE AND SOLUTIONS HYDROGEN AND AMMONIA 1 CLIMATE CHANGE : SCIENCE AND SOLUTIONS | BRIEFING 4*.

(31) Jain, R.; Panwar, N. L.; Chitranjan Agarwal; Gupta, T. A Comprehensive Review on Unleashing the Power of Hydrogen: Revolutionizing Energy Systems for a Sustainable Future. *Environmental Science and Pollution Research* 2025, *32* (22), 13329–13359. https://doi.org/10.1007/s11356-024-33541-1.

(32) Hauch, A.; Küngas, R.; Blennow, P.; Hansen, A. B.; Hansen, J. B.; Mathiesen, B. V.; Mogensen, M. B. Recent Advances in Solid Oxide Cell Technology for Electrolysis. *Science (1979)*. 2020, *370* (6513). https://doi.org/10.1126/science.aba6118.

(33) Pandiyan, A.; Uthayakumar, A.; Subrayan, R.; Cha, S. W.; Moorthy, S. B. K. Review of Solid Oxide Electrolysis Cells: A Clean Energy Strategy for Hydrogen Generation. *Nanomaterials and Energy* 2019, *8* (1). https://doi.org/10.1680/jnaen.18.00009.

(34) Min, G.; Choi, S.; Hong, J. A Review of Solid Oxide Steam-Electrolysis Cell Systems: Thermodynamics and Thermal Integration. *Applied Energy*. Elsevier Ltd December 15, 2022. https://doi.org/10.1016/j.apenergy.2022.120145.

(35) Mougin, J. Hydrogen Production by High-Temperature Steam Electrolysis. In *Compendium of Hydrogen Energy: Hydrogen Production and Purification: Volume 1*; Elsevier, 2015; Vol. 1, pp 225–253. https://doi.org/10.1016/B978-1-78242-361-4.00008-X.

(36) Xu, Y.; Cai, S.; Chi, B.; Tu, Z. Technological Limitations and Recent Developments in a Solid Oxide Electrolyzer Cell: A Review. *International Journal of Hydrogen Energy*. Elsevier Ltd January 2, 2024, pp 548–591. https://doi.org/10.1016/j.ijhydene.2023.08.314.

(37) Ni, M.; Leung, M. K. H.; Leung, D. Y. C. Technological Development of Hydrogen Production by Solid Oxide Electrolyzer Cell (SOEC). *International Journal of Hydrogen Energy*. May 2008, pp 2337–2354. https://doi.org/10.1016/j.ijhydene.2008.02.048.

(38) Mahato, N.; Banerjee, A.; Gupta, A.; Omar, S.; Balani, K. Progress in Material Selection for Solid Oxide Fuel Cell Technology: A Review. *Progress in Materials Science*. Elsevier Ltd July 28, 2015, pp 141–337. https://doi.org/10.1016/j.pmatsci.2015.01.001.

(39) Reddy, M. J. *THESIS FOR THE DEGREE OF LICENTIATE OF ENGINEERING Metallic Materials in Solid Oxide Fuel Cells: Oxidation and Chromium Evaporation Properties*.

(40) Puranen, J. *Protective Spinel Coatings for Solid Oxide Fuel Cell Interconnectors by Thermal Spray Processes From Conventional Dry Powder to Novel Solution Precursor Thermal Spraying*; 2015; Vol. 1.

(41) Hou, P. Y. The Reactive Element Effect - Past, Present and Future. In *Materials Science Forum*; Trans Tech Publications Ltd, 2011; Vol. 696, pp 39–44. https://doi.org/10.4028/www.scientific.net/MSF.696.39.

(42) Chen, X.; Hou, P. Y.; Jacobson, C. P. *Title Protective Coating on Stainless Steel Interconnect for SOFCs: Oxidation Kinetics and Electrical Properties Permalink Https://Escholarship.Org/Uc/Item/5pc2b46r Publication Date*. https://escholarship.org/uc/item/5pc2b46r.

(43) Naumenko, D.; Pint, B. A.; Quadakkers, W. J. Current Thoughts on Reactive Element Effects in Alumina-Forming Systems: In Memory of John Stringer. *Oxidation of Metals*. Springer New York LLC August 1, 2016. https://doi.org/10.1007/s11085-016-9625-0.

(44) Pint, B. A. Progress in Understanding the Reactive Element Effect Since the Whittle and Stringer Literature Review. In *John Stringer Symposium on High Temperature Corrosion*; 2001.

(45) Stringer, J. *The Reactive Element Effect in High-Temperature Corrosion**; 1989; Vol. 20.

(46) Whittle, D. P.; Stringer, J.; Whittlet, D. P. *Improvements in High Temperature Oxidation Resistance by Additions of Reactive Elements or Oxide Dispersions VIII. IMPROVEMENT IN PROPERTIES: ADDITIVES IN OXIDATION RESISTANCE Improvements in High Temperature Oxidation Resistance by Additions of Reactive Elements or Oxide Dispersions*; 1980; Vol. 295.

(47) Reddy, M. J.; Svensson, J. E.; Froitzheim, J. Evaluating Candidate Materials for Balance of Plant Components in SOFC: Oxidation and Cr Evaporation Properties. *Corros. Sci.* 2021, *190*. https://doi.org/10.1016/j.corsci.2021.109671.

(48) Reddy, M. J.; Chausson, T. E.; Svensson, J. E.; Froitzheim, J. 11–23% Cr Steels for Solid Oxide Fuel Cell Interconnect Applications at 800 °C – How the Coating Determines Oxidation Kinetics. *Int. J. Hydrogen Energy* 2023, *48* (34), 12893–12904. https://doi.org/10.1016/j.ijhydene.2022.11.326.

(49) Fang, Q.; Frey, C. E.; Menzler, N. H.; Blum, L. Electrochemical Performance and Preliminary Post-Mortem Analysis of a Solid Oxide Cell Stack with 20,000 h of

Operation. *J. Electrochem. Soc.* 2018, *165* (2), F38–F45. https://doi.org/10.1149/2.0541802jes.

(50) Kofstad, P. *High Temperature Corrosion*; Elsevier: Amsterdam, 1988.

(51) Neil Birks, Gerald H. Meier, Frederick S. Pettit - Introduction to the High-Temperature Oxidation of Metals-Cambridge University Press (2006).

(52) Hauffe, K. *Oxidation of Metals*; Springer US: Boston, MA, 1995. https://doi.org/10.1007/978-1-4684-8920-0.

(53) Atkinson, A. *Transport Processes during the Growth of Oxide Films at Elevated Temperature*; 1985.

(54) Wagner, C. *Oxidation of Alloys Involving Noble Metals*.

(55) Wagner, C. Theoretical Analysis of the Diffusion Processes Determining the Oxidation Rate of Alloys ’. *J. Electrochem. Soc.* 1952.

(56) Quadakkers2003.

(57) Hagel, W. C.; Seyboldt, A. U. Cation Diffusion in Cr 2 O 3. *J. Electrochem. Soc.* 1961.

(58) Tsaï, S. C.; Huntz, A. M.; Philibert, J. Diffusion Of54Cr And18O in Cr2O 3 Scales and Growth Mechanism. *Defect and Diffusion Forum* 1997, *143–147*, 1195–1200. https://doi.org/10.4028/www.scientific.net/DDF.143-147.1195.

(59) Horita, T.; Kishimoto, H.; Yamaji, K.; Xiong, Y.; Brito, M. E.; Yokokawa, H.; Baba, Y.; Ogasawara, K.; Kameda, H.; Matsuzaki, Y.; Yamashita, S.; Yasuda, N.; Uehara, T. Diffusion of Oxygen in the Scales of Fe-Cr Alloy Interconnects and Oxide Coating Layer for Solid Oxide Fuel Cells. *Solid State Ion.* 2008, *179* (38), 2216–2221. https://doi.org/10.1016/j.ssi.2008.07.024.

(60) Sabioni, A. C. S.; Huntz, A. M.; Philibert, J.; Lesage, B.; Monty, C. *Relation between the Oxidation Growth Rate of Chromia Scales and Self-Diffusion in Cr203*; 1992; Vol. 27.

(61) Tsai, S. C.; Huntz, A. M.; Dolin, C.; onty, C. M. Study by SIMS of the 54Cr and 18 0 Diffusion in Cr 203 and in Cr 2 0 3 Scales. 1996, *13*, 587–595.

(62) Molin, S.; Chen, M.; Hendriksen, P. V. Oxidation Study of Coated Crofer 22 APU Steel in Dry Oxygen. *J. Power Sources* 2014, *251*, 488–495. https://doi.org/10.1016/j.jpowsour.2013.09.100.

(63) Palcut, M.; Mikkelsen, L.; Neufeld, K.; Chen, M.; Knibbe, R.; Hendriksen, P. V. Corrosion Stability of Ferritic Stainless Steels for Solid Oxide Electrolyser Cell Interconnects. *Corros. Sci.* 2010, *52* (10), 3309–3320. https://doi.org/10.1016/j.corsci.2010.06.006.

(64) Fontana, S.; Amendola, R.; Chevalier, S.; Piccardo, P.; Caboche, G.; Viviani, M.; Molins, R.; Sennour, M. Metallic Interconnects for SOFC: Characterisation of Corrosion Resistance and Conductivity Evaluation at Operating Temperature of Differently Coated Alloys. *J. Power Sources* 2007, *171* (2), 652–662. https://doi.org/10.1016/j.jpowsour.2007.06.255.

(65) Brylewski, T.; Nanko, M.; Maruyama, T.; Przybylski, K. *Application of Fe-16Cr Ferritic Alloy to Interconnector for a Solid Oxide Fuel Cell*; 2001; Vol. 143. www.elsevier.comrlocaterssi.

(66) Quadakkers, W. J.; Bongartz, K. The Prediction of Breakaway Oxidation for Alumina Forming ODS Alloys Using Oxidation Diagrams. *Materials and Corrosion* 1994, *45* (4), 232–241. https://doi.org/10.1002/maco.19940450404.

(67) Huczkowski, P.; Christiansen, N.; Shemet, V.; Piron-Abellan, J.; Singheiser, L.; Quadakkers, W. J. Oxidation Limited Life Times of Chromia Forming Ferritic Steels. *Materials and Corrosion* 2004, *55* (11), 825–830. https://doi.org/10.1002/maco.200303798.

(68) Uehara, T.; Yasuda, N.; Okamoto, M.; Baba, Y. Effect of Mn-Co Spinel Coating for Fe-Cr Ferritic Alloys ZMG232L and 232J3 for Solid Oxide Fuel Cell Interconnects on Oxidation Behavior and Cr-Evaporation. In *Journal of Power Sources*; 2011; Vol. 196, pp 7251–7256. https://doi.org/10.1016/j.jpowsour.2010.11.078.

(69) Hilpert, K.; Das, D.; Miller, M.; Peck, D. H.; Weiss, R. Chromium Vapor Species over Solid Oxide Fuel Interconnect Materials and Their Potential for Degradation Processes. *J. Electrochem. Soc* 1996, *143*, 3642.

(70) Froitzheim, J.; Canovic, S.; Nikumaa, M.; Sachitanand, R.; Johansson, L. G.; Svensson, J. E. Long Term Study of Cr Evaporation and High Temperature Corrosion

Behaviour of Co Coated Ferritic Steel for Solid Oxide Fuel Cell Interconnects. *J. Power Sources* 2012, *220*, 217–227. https://doi.org/10.1016/j.jpowsour.2012.06.092.

(71) Burstein, T.; Young, D. J. *ELSEVIER CORROSION SERIES*.

(72) Opila, E. J.; Jacobson, N. S.; Myers, D. L.; Copland Evan H. Predicting Oxide Stability in High-Temperature Water Vapor. *High Temperature Protection* 2006.

(73) Fergus, J. W. Effect of Cathode and Electrolyte Transport Properties on Chromium Poisoning in Solid Oxide Fuel Cells. *Int. J. Hydrogen Energy* 2007, *32* (16), 3664–3671. https://doi.org/10.1016/j.ijhydene.2006.08.005.

(74) Holcomb, G. R. *Calculation of Reactive-Evaporation Rates of Chromia*.

(75) Wongpromrat, P.; Galerie, A.; Thublaor, T.; Chandra-ambhorn, W.; Ponpo, P.; Watasuntornpong, P.; Yamanaka, K.; Chiba, A.; Tunthawiroon, P.; Siripongsakul, T.; Chandra-ambhorn, S.; Ruangtrakoon, N. Evidence for Chromium, Cobalt and Molybdenum Volatilisations during High Temperature Oxidation of Co-27Cr-6Mo Alloy. *Corros. Sci.* 2022, *202*. https://doi.org/10.1016/j.corsci.2022.110285.

(76) Stanislowski, M.; Froitzheim, J.; Niewolak, L.; Quadakkers, W. J.; Hilpert, K.; Markus, T.; Singheiser, L. Reduction of Chromium Vaporization from SOFC Interconnectors by Highly Effective Coatings. *J. Power Sources* 2007, *164* (2), 578–589. https://doi.org/10.1016/j.jpowsour.2006.08.013.

(77) Holcomb, G. R.; Alman, D. E. Effect of Manganese Addition on Reactive Evaporation of Chromium in Ni-Cr Alloys. *J. Mater. Eng. Perform.* 2006, *15* (4), 394–398. https://doi.org/10.1361/105994906X117170.

(78) Sachitanand, R.; Sattari, M.; Svensson, J. E.; Froitzheim, J. Evaluation of the Oxidation and Cr Evaporation Properties of Selected FeCr Alloys Used as SOFC Interconnects. *Int. J. Hydrogen Energy* 2013, *38* (35), 15328–15334. https://doi.org/10.1016/j.ijhydene.2013.09.044.

(79) Yokokawa, H.; Horita, T.; Sakai, N.; Yamaji, K.; Brito, M. E.; Xiong, Y. P.; Kishimoto, H. Thermodynamic Considerations on Cr Poisoning in SOFC Cathodes. *Solid State Ion.* 2006, *177* (35–36), 3193–3198. https://doi.org/10.1016/j.ssi.2006.07.055.

(80) Wang, T.; Yan, S.; Zhao, M.; Yang, T.; Liu, J. Mechanisms of Chromium Poisoning in Solid Oxide Cell Air Electrodes and Research Advances in Enhancing Chromium-

Resistivity. *Huagong Xuebao/CIESC Journal*. Materials China June 25, 2024, pp 2091–2108. https://doi.org/10.11949/0438-1157.20240130.

(81) Jiang, S. P.; Chen, X. Chromium Deposition and Poisoning of Cathodes of Solid Oxide Fuel Cells - A Review. *International Journal of Hydrogen Energy*. Elsevier Ltd January 2, 2014, pp 505–531. https://doi.org/10.1016/j.ijhydene.2013.10.042.

(82) Li, J.; Zhang, Y.; Zhao, K.; Jiang, S. P.; Chen, M. An Investigation of Cr Vaporization from SUS430 Metallic Interconnect and Deposition on (La,Sr)MnO3 Cathode of Intermediate Temperature Solid Oxide Fuel Cells. *J. Power Sources* 2023, *579*. https://doi.org/10.1016/j.jpowsour.2023.233285.

(83) Bouvier, M.; Casadebaigt, A.; Dejob, T.; Bosonnet, S.; Couturier, K.; Rouillard, F. *Long-Term Oxidation and Electrical Performance of Bare and Different CeO 2-Co Coated Ferritic 2 Stainless Steel in Air at High Temperature for SOC Interconnect Application*. https://ssrn.com/abstract=4906966.

(84) Chen, K.; Hyodo, J.; Dodd, A.; Ai, N.; Ishihara, T.; Jian, L.; Jiang, S. P. Chromium Deposition and Poisoning of La0.8Sr0.2MnO3 Oxygen Electrodes of Solid Oxide Electrolysis Cells. *Faraday Discuss.* 2015, *182*, 457–476. https://doi.org/10.1039/c5fd00010f.

(85) Hu, Y.; Li, D.; Guo, H.; Liu, S. H.; Meng, Y.; Ding, S.; Li, C. X. Recent Progress of High-Performance Interconnectors for SOFC: From Materials, Protective Coatings, Optimizing Strategies, towards the Real Stack Applications. *Chemical Engineering Journal*. Elsevier B.V. February 1, 2025. https://doi.org/10.1016/j.cej.2025.159321.

(86) Tan, K. H.; Rahman, H. A.; Taib, H. Coating Layer and Influence of Transition Metal for Ferritic Stainless Steel Interconnector Solid Oxide Fuel Cell: A Review. *Int. J. Hydrogen Energy* 2019, *44* (58), 30591–30605. https://doi.org/10.1016/j.ijhydene.2019.06.155.

(87) Shaigan, N.; Qu, W.; Ivey, D. G.; Chen, W. A Review of Recent Progress in Coatings, Surface Modifications and Alloy Developments for Solid Oxide Fuel Cell Ferritic Stainless Steel Interconnects. *Journal of Power Sources*. March 15, 2010, pp 1529–1542. https://doi.org/10.1016/j.jpowsour.2009.09.069.

(88) Mah, J. C. W.; Muchtar, A.; Somalu, M. R.; Ghazali, M. J. Metallic Interconnects for Solid Oxide Fuel Cell: A Review on Protective Coating and Deposition Techniques.

Int. J. Hydrogen Energy 2017, *42* (14), 9219–9229. https://doi.org/10.1016/j.ijhydene.2016.03.195.

(89) Petric, A.; Ling, H. Electrical Conductivity and Thermal Expansion of Spinels at Elevated Temperatures. *Journal of the American Ceramic Society* 2007, *90* (5), 1515–1520. https://doi.org/10.1111/j.1551-2916.2007.01522.x.

(90) Goebel, C.; Berger, R.; Bernuy-Lopez, C.; Westlinder, J.; Svensson, J. E.; Froitzheim, J. Long-Term (4 Year) Degradation Behavior of Coated Stainless Steel 441 Used for Solid Oxide Fuel Cell Interconnect Applications. *J. Power Sources* 2020, *449*. https://doi.org/10.1016/j.jpowsour.2019.227480.

(91) Grolig, J. G.; Froitzheim, J.; Svensson, J. E. Coated Stainless Steel 441 as Interconnect Material for Solid Oxide Fuel Cells: Oxidation Performance and Chromium Evaporation. *J. Power Sources* 2014, *248*, 1007–1013. https://doi.org/10.1016/j.jpowsour.2013.08.089.

(92) Magrasó, A.; Falk-Windisch, H.; Froitzheim, J.; Svensson, J. E.; Haugsrud, R. Reduced Long Term Electrical Resistance in Ce/Co-Coated Ferritic Stainless Steel for Solid Oxide Fuel Cell Metallic Interconnects. *Int. J. Hydrogen Energy* 2015, *40* (27), 8579–8585. https://doi.org/10.1016/j.ijhydene.2015.04.147.

(93) Hill, R. J.; Craig, J. R.; Gibbs, G. V. *PHYSICS I] CHEMISTRY MIHERALS Systematics of the Spinel Structure Type*; 1979; Vol. 4.

(94) Sickafus, K. E.; Wills, J. M.; Grimes, N. W. *Structure of Spinel*.

(95) Verwey, E. J.; Haayman, P. W.; Romeijn, F. C. Physical Properties and Cation Arrangement of Oxides with Spinel Structures II. Electronic Conductivity. *J. Chem. Phys.* 1947, *15* (4), 181–187. https://doi.org/10.1063/1.1746466.

(96) Navrotsky, A.; Kleppa, O. J. The Thermodynamics of Cation Distributions in Simple Spinels. *Journal of Inorganic and Nuclear Chemistry* 1967, *29* (11), 2701–2714. https://doi.org/10.1016/0022-1902(67)80008-3.

(97) Goodenough, J. B.; Loeb, A. L. Theory of Ionic Ordering, Crystal Distortion, and Magnetic Exchange Due to Covalent Forces in Spinels*. *Physical Review* 1955, *98* (2).

(98) Bordeneuve, H.; Rousset, A.; Tenailleau, C.; Guillemet-Fritsch, S. Cation Distribution in Manganese Cobaltite Spinels Co3-x Mn x O4 (0 ≤ x ≤ 1) Determined by Thermal

Analysis. In *Journal of Thermal Analysis and Calorimetry*; 2010; Vol. 101, pp 137–142. https://doi.org/10.1007/s10973-009-0557-7.

(99) Bordeneuve, H.; Rousset, A.; Tenailleau, C.; Guillemet-Fritsch, S. Cation Distribution in Manganese Cobaltite Spinels Co3-x Mn x O4 (0 ≤ x ≤ 1) Determined by Thermal Analysis. In *Journal of Thermal Analysis and Calorimetry*; 2010; Vol. 101, pp 137–142. https://doi.org/10.1007/s10973-009-0557-7.

(100) Naka, S.; Inagaki, M.; Tanaka, T. *On the Formation of Solid Solution in Co3_ M Nx04 System*; 1972; Vol. 7.

(101) O'Neill, H. St. C.; Navrotsky, A. Simple Spinels: Crystallographic Parameters, Cation Radii, Lattice Energies, and Cation Distribution. *American Mineralogist* 1983, *68*, 181–194.

(102) Chesson, D. A.; Zhu, J. H. *Effect of Off-Stoichiometry on Electrical Conductivity in Ni-Fe and Mn-Co Spinel Systems Effect of Off-Stoichiometry on Electrical Conductivity of (Ni,Fe)3O4 and (Mn,Co)3O4 Spinels*. https://mc04.manuscriptcentral.com/jes-ecshttps://mc04.manuscriptcentral.com/jes-ecs.

(103) Verwey, E. J. W.; Heilmann, E. L. Physical Properties and Cation Arrangement of Oxides with Spinel Structures I. Cation Arrangement in Spinels. *J. Chem. Phys.* 1947, *15* (4), 174–180. https://doi.org/10.1063/1.1746464.

(104) Bordeneuve, H.; Tenailleau, C.; Guillemet-Fritsch, S.; Smith, R.; Suard, E.; Rousset, A. Structural Variations and Cation Distributions in Mn3-XCoxO4 (0 ≤ x ≤ 3) Dense Ceramics Using Neutron Diffraction Data. *Solid State Sci.* 2010, *12* (3), 379–386. https://doi.org/10.1016/j.solidstatesciences.2009.11.018.

(105) Liu, Y.; Fergus, J. W.; Wang, K.; Dela Cruz, C. Crystal Structure, Chemical Stabilities and Electrical Conductivity of Fe-Doped Manganese Cobalt Spinel Oxides for SOFC Interconnect Coatings. *J. Electrochem. Soc.* 2013, *160* (11), F1316–F1321. https://doi.org/10.1149/2.114311jes.

(106) Mcclure, D. S. *THE DISTRIBUTION OF TRANSITION METAL CATIONS IN SPINELS*; 1957; Vol. 3.

(107) Pelton, A. D.; Schmalzried, H.; Sticher, J. Thermodynamics of Mn304-Co304, Fe304-Mn304, and Fe304,-Co304 Spinels by Phase Diagram Analysis. *Phys. Chem.* 1979, *83* (3), 241–252.

(108) Nakatsuka, A.; Ikeda, Y.; Yamasaki, Y.; Nakayama, N.; Mizota, T. Cation Distribution and Bond Lengths in CoAl2O4 Spinel. *Solid State Commun.* 2003, *128* (2–3), 85–90. https://doi.org/10.1016/S0038-1098(03)00652-5.

(109) Park, K. R.; Han, H. S.; Hou, D.; Jones, J. L.; Oh, N.; Ahn, C.; Lee, J.; Lee, S. H.; Mhin, S. Crystal Structures and Electrical Properties of Cobalt Manganese Spinel Oxides. *Mater. Today Commun.* 2020, *25*. https://doi.org/10.1016/j.mtcomm.2020.101298.

(110) Gao, J.; Si, X.; Wang, X.; Li, C.; Qi, J.; Cao, J. Exploring the Effects of Mn Content in the Mn-Co Spinel Coating on Its Formation and Slowing the Outward Cr Diffusion. *Corros. Sci.* 2023, *217*. https://doi.org/10.1016/j.corsci.2023.111158.

(111) Chen, M.; Hallstedt, B.; Gauckler, L. J. Thermodynamic Assessment of the Co-O System. *Journal of Phase Equilibria* 2003, *24* (3), 212–227. https://doi.org/10.1361/105497103770330514.

(112) Brylewski, T.; Kucza, W.; Adamczyk, A.; Kruk, A.; Stygar, M.; Bobruk, M.; Dąbrowa, J. Microstructure and Electrical Properties of Mn1+xCo 2-XO4 (0 ≤ x ≤ 1.5) Spinels Synthesized Using EDTA-Gel Processes. *Ceram. Int.* 2014, *40* (9 PART A), 13873–13882. https://doi.org/10.1016/j.ceramint.2014.05.106.

(113) Kale, G. M.; Pandit, S. S.; Jacob, K. T. *Thermodynamics of Cobalt (II, III) Oxide (Co3O4): Evidence of Phase Transition*; 1988; Vol. 29.

(114) Dunitz, J. D.; Orgel, L. E. *ELECTRONIC PROPERTIES OF OXIDES-II TRANSITION-METAL CATION DISTRIBUTION AMONGST OCTAHEDRAL AND TETRAHEDRAL SITES*; 1957; Vol. 3.

(115) Sarkar, A.; Eggert, B.; Witte, R.; Lill, J.; Velasco, L.; Wang, Q.; Sonar, J.; Ollefs, K.; Bhattacharya, S. S.; Brand, R. A.; Wende, H.; de Groot, F. M. F.; Clemens, O.; Hahn, H.; Kruk, R. Comprehensive Investigation of Crystallographic, Spin-Electronic and Magnetic Structure of (Co0.2Cr0.2Fe0.2Mn0.2Ni0.2)3O4: Unraveling the Suppression of Configuration Entropy in High Entropy Oxides. *Acta Mater.* 2022, *226*. https://doi.org/10.1016/j.actamat.2021.117581.

(116) Aukrust, E.; Muan, A. Phase Relations in the System Cobalt Oxide– Manganese Oxide in Air. *Journal of the American Ceramic Society* 1963, *46* (10), 511–511.

(117) Chesson, D. A.; Zhu, J. H. Effect of Spinel Stoichiometry on Reaction Layer Formation between (Mn,Co) 3 O 4 and Cr 2 O 3 . *J. Electrochem. Soc.* 2025, *172* (6), 064506. https://doi.org/10.1149/1945-7111/adde18.

(118) Liu, Y.; Fergus, J. W.; Cruz, C. Dela. Electrical Properties, Cation Distributions, and Thermal Expansion of Manganese Cobalt Chromite Spinel Oxides. *Journal of the American Ceramic Society* 2013, *96* (6), 1841–1846. https://doi.org/10.1111/jace.12254.

(119) Persson, A. H.; Mikkelsen, L.; Hendriksen, P. V.; Somers, M. A. J. Interaction Mechanisms between Slurry Coatings and Solid Oxide Fuel Cell Interconnect Alloys during High Temperature Oxidation. *J. Alloys Compd.* 2012, *521*, 16–29. https://doi.org/10.1016/j.jallcom.2011.12.095.

(120) Zhang, H.; Wu, J.; Liu, X.; Baker, A. Studies on Elements Diffusion of Mn/Co Coated Ferritic Stainless Steel for Solid Oxide Fuel Cell Interconnects Application. *Int. J. Hydrogen Energy* 2013, *38* (12), 5075–5083. https://doi.org/10.1016/j.ijhydene.2013.02.026.

(121) Wang, K.; Liu, Y.; Fergus, J. W. Interactions between SOFC Interconnect Coating Materials and Chromia. *Journal of the American Ceramic Society* 2011, *94* (12), 4490–4495. https://doi.org/10.1111/j.1551-2916.2011.04749.x.

(122) Dileep, K. C. J.; Liu, Y.; Ganley, J.; Tilson, W.; Dekich, A.; Fergus, J. Transition Metal Doping of Manganese Cobalt Spinel Oxides for Coating SOFC Interconnects. In *TMS Annual Meeting*; 2012; pp 305–311. https://doi.org/10.1149/2.054401jes.

(123) Talic, B.; Molin, S.; Wiik, K.; Hendriksen, P. V.; Lein, H. L. Comparison of Iron and Copper Doped Manganese Cobalt Spinel Oxides as Protective Coatings for Solid Oxide Fuel Cell Interconnects. *J. Power Sources* 2017, *372*, 145–156. https://doi.org/10.1016/j.jpowsour.2017.10.060.

(124) Yang, Z.; Xia, G. G.; Wang, C. M.; Nie, Z.; Templeton, J.; Stevenson, J. W.; Singh, P. Investigation of Iron-Chromium-Niobium-Titanium Ferritic Stainless Steel for Solid Oxide Fuel Cell Interconnect Applications. *J. Power Sources* 2008, *183* (2), 660–667. https://doi.org/10.1016/j.jpowsour.2008.05.037.

(125) Kurokawa, H.; Jacobson, C. P.; DeJonghe, L. C.; Visco, S. J. Chromium Vaporization of Bare and of Coated Iron-Chromium Alloys at 1073 K. *Solid State Ion*. 2007, *178* (3–4), 287–296. https://doi.org/10.1016/j.ssi.2006.12.010.

(126) Thorbjørn Krogsgaard, ©; Reddy, M.; Froitzheim, J. *Lifetime Model For FSS Interconnects Based On Chromium Content THORBJØRN KROGSGAARD*.

(127) Mazur, Ł.; Molin, S.; Dąbek, J.; Durczak, K.; Pyzalski, M.; Brylewski, T. Physicochemical Properties of Mn1.45Co1.45Cu0.1O4 Spinel Coating Deposited on the Crofer 22 H Ferritic Steel and Exposed to High-Temperature Oxidation under Thermal Cycling Conditions. *J. Therm. Anal. Calorim*. 2022, *147* (10), 5649–5666. https://doi.org/10.1007/s10973-021-10884-2.

(128) Kang Huai, T.; Lowrance, Y.; Farhana Abd Rahman, N.; Asyikin Yusop, U.; Abd Rahman, H.; Jaidi, Z.; Faizal Tukimon, M.; Saifulddin Mohd Azami, M. Mathematical Modeling and Experiment Verification for the Solid Oxide Fuel Cell Mn1.5Co1.5O4 Interconnect Coating. *Mater. Lett*. 2024, *358*. https://doi.org/10.1016/j.matlet.2023.135825.

(129) Cheng, F.; Yu, Y.; Lu, Y.; Wang, Z.; Ling, Y.; Jing, C.; Guan, C.; Wang, J. Performance of CoMnO Spinel Coating onto 441 SS for SOEC Interconnect Application. *Coatings* 2022, *12* (11). https://doi.org/10.3390/coatings12111723.

(130) Falk-Windisch, H.; Svensson, J. E.; Froitzheim, J. The Effect of Temperature on Chromium Vaporization and Oxide Scale Growth on Interconnect Steels for Solid Oxide Fuel Cells. *J. Power Sources* 2015, *287*, 25–35. https://doi.org/10.1016/j.jpowsour.2015.04.040.

(131) Jin, Y.; He, X.; Liu, Z.; Yue, X.; Zhang, G.; Wang, S.; Shang, L. Effect of Bias Voltage on High-Temperature Oxidation Resistance and Electrical Properties of Mn-Co Coating with Metal Interconnects for Solid Oxide Fuel Cell. *Surf. Topogr.* 2024, *12* (4). https://doi.org/10.1088/2051-672X/ad8a75.

(132) Spotorno, R.; Paravidino, D.; Delsante, S.; Piccardo, P. Volatilization of Chromium from AISI 441 Stainless Steel: Time and Temperature Dependence. *Surf. Coat. Technol.* 2022, *433*. https://doi.org/10.1016/j.surfcoat.2022.128125.

(133) Molin, S.; Sabato, A. G.; Bindi, M.; Leone, P.; Cempura, G.; Salvo, M.; Cabanas Polo, S.; Boccaccini, A. R.; Smeacetto, F. Microstructural and Electrical Characterization

of Mn-Co Spinel Protective Coatings for Solid Oxide Cell Interconnects. *J. Eur. Ceram. Soc.* 2017, *37* (15), 4781–4791. https://doi.org/10.1016/j.jeurceramsoc.2017.07.011.

(134) Gambino, L. V. Evaluation of Solid Oxide Fuel Cell Interconnect Coatings: Mechanisms Behind Structure and Property Change During Reaction Layer Formation, University of Connecticut, 2015. https://opencommons.uconn.edu/dissertations/1008.

(135) Cox M. G. C.; McEnaney B.; Scott V. D. A Chemical Diffusion Model for Partitioning of Transition Elements in Oxide Scales on Alloys. *Philosophical Magazine* 1972, *26*, 839–851. https://doi.org/10.1080/14786437208226960-Philosophical.

(136) Sun, R. Diffusion of Cobalt and Chromium in Chromite Spinel. *J. Chem. Phys.* 1958, *28* (2), 290–293. https://doi.org/10.1063/1.1744108.

(137) Lu, F.-H.; Dieckmann, R. Point Defects and Cation Tracer Diffusion in (CoxMn1-x) 3-ΔO4 Spinels. *Solid State Ionics* 1993, *67*, 145–155.

(138) Lu, F.-H.; Dieckmann, R. Point Defects and Cation Tracer Diffusion in (Co, Fe, Mn)3-ΔO4 Spinels: I. Mixed Spinels (Cox, Fe2y, Mny)3-ΔO4. *Solid State Ion.* 1992, 290–302.

(139) Lu, F.-H.; Tinkler, S.; Dieckmann, R. Point Defects and Cation Tracer Diffusion in (CoxFe1_x)3-ΔO4 Spinels. *Solid State Ion.* 1993, *62*, 39–52.

(140) Töpfer, J.; Aggarwal, S.; Dieckmann, R. Point Defects and Cation Tracer Diffusion in (Crx,Fe1-x) 3-ΔO4 Spinels. *Solid State Ion.* 1995, 251–266.

(141) Magdefrau, N. J.; Chen, L.; Sun, E. Y.; Yamanis, J.; Aindow, M. Formation of Spinel Reaction Layers in Manganese Cobaltite-Coated Crofer22 APU for Solid Oxide Fuel Cell Interconnects. *J. Power Sources* 2013, *227*, 318–326. https://doi.org/10.1016/j.jpowsour.2012.07.091.

(142) Lu, Z.; Zhu, J.; Andrew Payzant, E.; Paranthaman, M. P. Electrical Conductivity of the Manganese Chromite Spinel Solid Solution. *Journal of the American Ceramic Society* 2005, *88* (4), 1050–1053. https://doi.org/10.1111/j.1551-2916.2005.00205.x.

(143) Kofstad, P.; Norby, T. *Defect Chemistry and Reactions in Solids*; University of Oslo, 2007.

(144) Holt, A. Electrical Conductivity and Defect Structure of Cr2O3. II. Reduced Temperatures (< ~ 1000°C). *Solid State Ion.* 1994, *69*, 137–143.

(145) Holt, A. Electrical Conductivity and Defect Structure of Cr2O3. I. High Temperatures (> ~ 1000°C). *Solid State Ion.* 1994, *69*, 127–136.

(146) Holt, A.; Kofstad, P. Electrical Conductivity and Defect Structure of Mg-Doped Cr2O3. *Solid State Ion.* 1997, *100*, 201–209.

(147) Park, J.-H.; Natesan, K. *Electronic Transport in Thermally Grown Cr~O3*; 1990; Vol. 33.

(148) Stevenson, J. W.; Yang, Z. G.; Xia, G. G.; Nie, Z.; Templeton, J. D. Long-Term Oxidation Behavior of Spinel-Coated Ferritic Stainless Steel for Solid Oxide Fuel Cell Interconnect Applications. *J. Power Sources* 2013, *231*, 256–263. https://doi.org/10.1016/j.jpowsour.2013.01.033.

(149) KOUMOTO, K.; YANAGIDA, H. Electrical Conduction in Pure and Li-Substituted Co3O4. *Journal of the American Ceramic Society* 1981, *64* (11), C-156-C-157. https://doi.org/10.1111/j.1151-2916.1981.tb15878.x.

(150) Holt, A. Electrical Conductivity of Cr2O3 Doped with TiO2. *Solid State Ion.* 1999, *117*, 21–25.

(151) Crawford, J. A.; Vest, R. W. Electrical Conductivity of Single-Crystal Cr2O3. *J. Appl. Phys.* 1964, *35* (8), 2413–2418. https://doi.org/10.1063/1.1702871.

(152) Qu, W.; Jian, L.; Hill, J. M.; Ivey, D. G. Electrical and Microstructural Characterization of Spinel Phases as Potential Coatings for SOFC Metallic Interconnects. *J. Power Sources* 2006, *153* (1), 114–124. https://doi.org/10.1016/j.jpowsour.2005.03.137.

(153) Sakai, N.; Horita, T.; Xiong, Y. P.; Yamaji, K.; Kishimoto, H.; Brito, M. E.; Yokokawa, H.; Maruyama, T. Structure and Transport Property of Manganese-Chromium-Iron Oxide as a Main Compound in Oxide Scales of Alloy Interconnects for SOFCs. *Solid State Ion.* 2005, *176* (7–8), 681–686. https://doi.org/10.1016/j.ssi.2004.11.012.

(154) Goebel, C.; Fefekos, A. G.; Svensson, J. E.; Froitzheim, J. Does the Conductivity of Interconnect Coatings Matter for Solid Oxide Fuel Cell Applications? *J. Power Sources* 2018, *383*, 110–114. https://doi.org/10.1016/j.jpowsour.2018.02.060.

(155) Sachitanand, R.; Sattari, M.; Svensson, J. E.; Froitzheim, J. The Oxidation of Coated SOFC Interconnects in Fuel Side Environments. *Fuel Cells* 2016, *16* (1), 32–38. https://doi.org/10.1002/fuce.201500066.

(156) Premkumar, P. A.; Starostin, S. A.; De Vries, H.; Paffen, R. M. J.; Creatore, M.; Eijkemans, T. J.; Koenraad, P. M.; Van De Sanden, M. C. M. High Quality SiO2-like Layers by Large Area Atmospheric Pressure Plasma Enhanced CVD: Deposition Process Studies by Surface Analysis. *Plasma Processes and Polymers* 2009, *6* (10), 693–702. https://doi.org/10.1002/ppap.200900033.

(157) Hnilica, J.; Schäfer, J.; Foest, R.; Zajíčková, L.; Kudrle, V. PECVD of Nanostructured SiO2 in a Modulated Microwave Plasma Jet at Atmospheric Pressure. *J. Phys. D Appl. Phys.* 2013, *46* (33). https://doi.org/10.1088/0022-3727/46/33/335202.

(158) Maurau, R.; Boscher, N. D.; Olivier, S.; Bulou, S.; Belmonte, T.; Dutroncy, J. Ô.; Sindzingre, T.; Choquet, P. Atmospheric Pressure, Low Temperature Deposition of Photocatalytic TiOx Thin Films with a Blown Arc Discharge. *Surf. Coat. Technol.* 2013, *232*, 159–165. https://doi.org/10.1016/j.surfcoat.2013.05.001.

(159) Chemin, J. B.; Bulou, S.; Baba, K.; Fontaine, C.; Sindzingre, T.; Boscher, N. D.; Choquet, P. Transparent Anti-Fogging and Self-Cleaning TiO2/SiO2 Thin Films on Polymer Substrates Using Atmospheric Plasma. *Sci. Rep.* 2018, *8* (1). https://doi.org/10.1038/s41598-018-27526-7.

(160) Stauss, S.; Imanishi, Y.; Miyazoe, H.; Terashima, K. High Rate Deposition of ZnO Thin Films by a Small-Scale Inductively Coupled Argon Plasma Generated in Open Air. *J. Phys. D Appl. Phys.* 2010, *43* (15). https://doi.org/10.1088/0022-3727/43/15/155203.

(161) Acharya, K.; Bulou, S.; Gaulain, T.; Gérard, M.; Choquet, P. Site-Selective Atmospheric Pressure Plasma-Enhanced Chemical Vapor Deposition Process for Micrometric Deposition of Plasma-Polymerized Methyl Methacrylate. *Plasma Processes and Polymers* 2021, *18* (2). https://doi.org/10.1002/ppap.202000143.

(162) Niemczyk, E. M.; Gomez-Lopez, A.; Haler, J. R. N.; Frache, G.; Sardon, H.; Quintana, R. Insights on the Atmospheric-Pressure Plasma-Induced Free-Radical Polymerization of Allyl Ether Cyclic Carbonate Liquid Layers. *Polymers (Basel).* 2021, *13* (17). https://doi.org/10.3390/polym13172856.

(163) Uricchio, A.; Fanelli, F. Low-Temperature Atmospheric Pressure Plasma Processes for the Deposition of Nanocomposite Coatings. *Processes*. MDPI November 1, 2021. https://doi.org/10.3390/pr9112069.

(164) Huerta-Flores, A. M.; Usiobo, O. J.; Audinot, J.-N.; Heyberger, R.; Choquet, P.; Boscher, N. D.; Boscher, N. D.; Huerta-Flores, A. M. *Low Temperature Open-Air Plasma Deposition of SrTiO 3 Films for Solar Energy Harvesting: Impact of Precursors on the Properties and Performances*.

(165) Patel, D. K. ATMOSPHERIC PRESSURE PLASMA ASSISTED DEPOSITION OF ZIRCONIA/SILICA CONVERSION COATINGS, University of Illinois Urbana-Champaign, 2023.

(166) Fridman, A. A. . *Plasma Chemistry*; Cambridge University Press, 2012.

(167) Sivaram, S. *Chemical Vapor Deposition*; Springer US: Boston, MA, 1995. https://doi.org/10.1007/978-1-4757-4751-5.

(168) Hori, M. Radical-Controlled Plasma Processes. *Reviews of Modern Plasma Physics*. Springer December 1, 2022. https://doi.org/10.1007/s41614-022-00084-2.

(169) Takeda, K.; Ishikawa, K.; Tanaka, H.; Sekine, M.; Hori, M. Spatial Distributions of O, N, NO, OH and Vacuum Ultraviolet Light along Gas Flow Direction in an AC-Excited Atmospheric Pressure Ar Plasma Jet Generated in Open Air. *J. Phys. D Appl. Phys.* 2017, *50* (19). https://doi.org/10.1088/1361-6463/aa6555.

(170) Brisset, J. L.; Moussa, D.; Doubla, A.; Hnatiuc, E.; Hnatiuc, B.; Kamgang Youbi, G.; Herry, J. M.; Naïtali, M.; Bellon-Fontaine, M. N. Chemical Reactivity of Discharges and Temporal Post-Discharges in Plasma Treatment of Aqueous Media: Examples of Gliding Discharge Treated Solutions. *Industrial and Engineering Chemistry Research*. August 20, 2008, pp 5761–5781. https://doi.org/10.1021/ie701759y.

(171) Belmonte, T.; Henrion, G.; Gries, T. Nonequilibrium Atmospheric Plasma Deposition. *J. Therm. Spray Technol.* June 2011, pp 744–759. https://doi.org/10.1007/s11666-011-9642-0.

(172) Thiry, D.; Reniers, F.; Snyders, R. A Joint Mechanistic Description of Plasma Polymers Synthesized at Low and Atmospheric Pressure. In *Surface Modification of Polymers: Methods and Applications*; wiley, 2019; pp 67–106. https://doi.org/10.1002/9783527819249.ch3.

(173) Tendero, C.; Tixier, C.; Tristant, P.; Desmaison, J.; Leprince, P. Atmospheric Pressure Plasmas: A Review. *Spectrochimica Acta - Part B Atomic Spectroscopy*. Elsevier 2006, pp 2–30. https://doi.org/10.1016/j.sab.2005.10.003.

(174) Winter, J.; Brandenburg, R.; Weltmann, K. D. Atmospheric Pressure Plasma Jets: An Overview of Devices and New Directions. *Plasma Sources Sci. Technol.* 2015, *24* (6). https://doi.org/10.1088/0963-0252/24/6/064001.

(175) Mariotti, D.; Sankaran, R. M. Microplasmas for Nanomaterials Synthesis. *Journal of Physics D: Applied Physics*. August 18, 2010. https://doi.org/10.1088/0022-3727/43/32/323001.

(176) Bardos, L. Afterglow and Decaying Plasma CVD Systems. *Vacuum* 1988.

(177) Bhatt, S.; Pulpytel, J.; Krcma, F.; Mazankova, V.; Arefi-Khonsari, F. *POROUS SILICON & TITANIUM DIOXIDE COATINGS PREPARED BY ATMOSPHERIC PRESSURE PLASMA JET CHEMICAL VAPOUR DEPOSITION TECHNIQUE-A NOVEL COATING TECHNOLOGY FOR PHOTOVOLTAIC MODULES*; 2011; Vol. 3.

(178) Fakhouri, H.; Salem, D. Ben; Carton, O.; Pulpytel, J.; Arefi-Khonsari, F. Highly Efficient Photocatalytic TiO2 Coatings Deposited by Open Air Atmospheric Pressure Plasma Jet with Aerosolized TTIP Precursor. *J. Phys. D Appl. Phys.* 2014, *47* (26). https://doi.org/10.1088/0022-3727/47/26/265301.

(179) Liu, F.; Nie, L.; Lu, X.; Stephens, J.; Ostrikov, K. Atmospheric Plasma VUV Photon Emission. *Plasma Sources Sci. Technol.* 2020, *29* (6). https://doi.org/10.1088/1361-6595/ab8e4d.

(180) Kaneko, T.; Kato, H.; Yamada, H.; Yamamoto, M.; Yoshida, T.; Attri, P.; Koga, K.; Murakami, T.; Kuchitsu, K.; Ando, S.; Nishikawa, Y.; Tomita, K.; Ono, R.; Ito, T.; Ito, A. M.; Eriguchi, K.; Nozaki, T.; Tsutsumi, T.; Ishikawa, K. Functional Nitrogen Science Based on Plasma Processing: Quantum Devices, Photocatalysts and Activation of Plant Defense and Immune Systems. *Japanese Journal of Applied Physics*. IOP Publishing Ltd January 1, 2022. https://doi.org/10.35848/1347-4065/ac25dc.

(181) Olivier, S. *Réalisation d'un Dépôt Photocatalytique de Dioxyde de Titane à Basse Température Avec Une Torche Plasma à La Pression Atmosphérique*; 2018. http://www.culture.gouv.fr/culture/infos-pratiques/droits/protection.htm.

(182) Belmonte, T.; Arnoult, G.; Henrion, G.; Gries, T. Nanoscience with Non-Equilibrium Plasmas at Atmospheric Pressure. *Journal of Physics D: Applied Physics*. September 14, 2011. https://doi.org/10.1088/0022-3727/44/36/363001.

(183) Kouotou, P. M.; Tian, Z. Y.; Mundloch, U.; Bahlawane, N.; Kohse-Höinghaus, K. Controlled Synthesis of Co3O4 Spinel with Co(Acac)3 as Precursor. *RSC Adv.* 2012, *2* (29), 10809–10812. https://doi.org/10.1039/c2ra21277c.

(184) Hodgkinson, J. L.; Sheel, D. W. Advances in Atmospheric Pressure PECVD: The Influence of Plasma Parameters on Film Morphology. *Surf. Coat. Technol.* 2013, *230*, 73–76. https://doi.org/10.1016/j.surfcoat.2013.06.079.

(185) Sun, L.; Yuan, G.; Gao, L.; Yang, J.; Chhowalla, M.; Gharahcheshmeh, M. H.; Gleason, K. K.; Choi, Y. S.; Hong, B. H.; Liu, Z. Chemical Vapour Deposition. *Nature Reviews Methods Primers*. Springer Nature December 1, 2021. https://doi.org/10.1038/s43586-020-00005-y.

(186) Dutuit, O.; Carrasco, N.; Thissen, R.; Vuitton, V.; Alcaraz, C.; Pernot, P.; Balucani, N.; Casavecchia, P.; Canosa, A.; Picard, S. Le; Loison, J. C.; Herman, Z.; Zabka, J.; Ascenzi, D.; Tosi, P.; Franceschi, P.; Price, S. D.; Lavvas, P. Critical Review of N, N+, N+2, N ++, and N++2 Main Production Processes and Reactions of Relevance to Titan's Atmosphere. *Astrophysical Journal, Supplement Series*. February 2013. https://doi.org/10.1088/0067-0049/204/2/20.

(187) Ishikawa, K. Perspectives on Functional Nitrogen Science and Plasma-Based in Situ Functionalization. *Jpn. J. Appl. Phys.* 2022, *61* (SA). https://doi.org/10.35848/1347-4065/ac3558.

(188) Guerra, V.; Sá, P. A.; Loureiro, J. *Role Played by the N 2 (A 3 Σ u +) Metastable in Stationary N 2 and N 2-O 2 Discharges You May Also like Role Played by the N 2 (A 3 Σ + u) Metastable in Stationary N 2 and N 2-O 2 Discharges*; 2001; Vol. 34. www.iop.org/Journals/jdPII:S0022-3727.

(189) Ni, G.; Lin, Q.; Li, L.; Cheng, C.; Chen, L.; Shen, J.; Lan, Y.; Meng, Y. Alternating Current-Driven Non-Thermal Arc Plasma Torch Working with Air Medium at Atmospheric Pressure. *J. Phys. D Appl. Phys.* 2013, *46* (45). https://doi.org/10.1088/0022-3727/46/45/455204.

(190) Machida, M.; Canesqui, M. A.; Moshkalev, S. A. Comparison Between Conventional and Transferred DBD Plasma Jets for Processing of PDMS Surfaces. *IEEE Trans Plasma Sci* 2017, *45* (3), 346–355. https://doi.org/10.48550/arXiv.1606.07657.

(191) Pulpytel, J.; Kumar, V.; Peng, P.; Micheli, V.; Laidani, N.; Arefi-Khonsari, F. Deposition of Organosilicon Coatings by a Non-Equilibrium Atmospheric Pressure Plasma Jet: Design, Analysis and Macroscopic Scaling Law of the Process. *Plasma Processes and Polymers* 2011, *8* (7), 664–675. https://doi.org/10.1002/ppap.201000121.

(192) Gessel, A. F. H.; Bruggeman, &; Van Gessel, A.; Hrycak, B.; Jasí Nski, M.; Mizeraczyk, J.; Van Der Mullen, J.; Bruggeman, P. J. Temperature and NO Density Measurements by LIF and OES on an Atmospheric Pressure Plasma Jet Citation for Published Version (APA): Temperature and NO Density Measurements by LIF and OES on an Atmospheric Pressure Plasma Jet. *J. Phys. D Appl. Phys. 46* (9), 1. https://doi.org/10.1088/0022.

(193) Kubota, Y.; Ichiki, R.; Hara, T.; Yamaguchi, N.; Takemura, Y. *SPECTROSCOPIC ANALYSIS OF NITROGEN ATMOSPHERIC PLASMA JET*.

(194) Ghobeira, R.; Esbah Tabaei, P. S.; Nikiforov, A.; Morent, R.; De Geyter, N. Unraveling Exclusive In-Plasma Initiated Oxidation Processes Occurring at Polymeric Surfaces upon O2 Admixtures to Medium Pressure Ar and N2 DBD Treatments. *Polymers (Basel)*. 2023, *15* (14). https://doi.org/10.3390/polym15142978.

(195) Gorbanev, Y.; Privat-Maldonado, A.; Bogaerts, A. Analysis of Short-Lived Reactive Species in Plasma-Air-Water Systems: The Dos and the Do Nots. *Anal. Chem.* 2018, *90* (22), 13151–13158. https://doi.org/10.1021/acs.analchem.8b03336.

(196) Hilt, F.; Hovish, M. Q.; Rolston, N.; Brüning, K.; Tassone, C. J.; Dauskardt, R. H. *Rapid Route to Efficient, Scalable, and Robust Perovskite Photovoltaics in Air*; 2018.

(197) Pipa, A. V.; Reuter, S.; Foest, R.; Weltmann, K. D. Controlling the NO Production of an Atmospheric Pressure Plasma Jet. *J. Phys. D Appl. Phys.* 2012, *45* (8). https://doi.org/10.1088/0022-3727/45/8/085201.

(198) Gromov, M.; Leonova, K.; Britun, N.; De Geyter, N.; Morent, R.; Snyders, R.; Nikiforov, A. Plasma Nitrogen Fixation in the Presence of a Liquid Interface: Role of OH Radicals. *React. Chem. Eng.* 2022, *7* (5), 1047–1052. https://doi.org/10.1039/d2re00014h.

(199) Huber, K. P.; Herzberg, G. *Molecular Spectra and Molecular Structure*; Springer US, 1979. https://doi.org/10.1007/978-1-4757-0961-2.

(200) Park, S.; Choe, W.; Moon, S. Y.; Yoo, S. J. Electron Characterization in Weakly Ionized Collisional Plasmas: From Principles to Techniques. *Advances in Physics: X*. Taylor and Francis Ltd. January 1, 2019. https://doi.org/10.1080/23746149.2018.1526114.

(201) Hopfe, V.; Sheel, D. W. Atmospheric-Pressure Plasmas for Wide-Area Thin-Film Deposition and Etching. *Plasma Processes and Polymers* 2007, *4* (3), 253–265. https://doi.org/10.1002/ppap.200600202.

(202) Buddhadasa, M.; Vandenabeele, C. R.; Snyders, R.; Girard-Lauriault, P. L. Single Source Precursor vs. Precursor Mixture for N-Rich Plasma Polymer Deposition: Plasma Diagnostics and Thin Film Analyses. *Plasma Processes and Polymers* 2017, *14* (11). https://doi.org/10.1002/ppap.201700030.

(203) Parsons, G. N.; Tsu, D. V.; Lucovsky, G. Properties of Intrinsic and Doped a -Si:H Deposited by Remote Plasma Enhanced Chemical Vapor Deposition . *Journal of Vacuum Science & Technology A: Vacuum, Surfaces, and Films* 1988, *6* (3), 1912–1916. https://doi.org/10.1116/1.575244.

(204) Schäfer, J.; Foest, R.; Sigeneger, F.; Loffhagen, D.; Weltmann, K. D.; Martens, U.; Hippler, R. Study of Thin Film Formation From Silicon-Containing Precursors Produced by an RF Non-Thermal Plasma Jet at Atmospheric Pressure. *Contributions to Plasma Physics* 2012, *52* (10), 872–880. https://doi.org/10.1002/ctpp.201200043.

(205) Guruvenket, S.; Andrie, S.; Simon, M.; Johnson, K. W.; Sailer, R. A. Atmospheric-Pressure Plasma-Enhanced Chemical Vapor Deposition of a-SiCN:H Films: Role of Precursors on the Film Growth and Properties. *ACS Appl. Mater. Interfaces* 2012, *4* (10), 5293–5299. https://doi.org/10.1021/am301157p.

(206) Luo, Y.-R.; J. Alistair Kerr. Bond Dissociation Energies. In *CRC handbook of chemistry and physics*; 2012; Vol. 89.89, pp 65–98.

(207) Cui, L.; Ranade, A. N.; Matos, M. A.; Pingree, L. S.; Frot, T. J.; Dubois, G.; Dauskardt, R. H. Atmospheric Plasma Deposited Dense Silica Coatings on Plastics. *ACS Appl. Mater. Interfaces* 2012, *4* (12), 6587–6598. https://doi.org/10.1021/am301723d.

(208) Johnson, K. W.; Guruvenket, S.; Sailer, R. A.; Ahrenkiel, S. P.; Schulz, D. L. Atmospheric Pressure Plasma Enhanced Chemical Vapor Deposition of Zinc Oxide

and Aluminum Zinc Oxide. *Thin Solid Films* 2013, *548*, 210–219. https://doi.org/10.1016/j.tsf.2013.09.060.

(209) Alexandrov, S. E.; McSporran, N.; Hitchman, M. L. Remote AP-PECVD of Silicon Dioxide Films from Hexamethyldisiloxane (HMDSO). *Chemical Vapor Deposition* 2005, *11* (11–12), 481–490. https://doi.org/10.1002/cvde.200506385.

(210) Herbert, P. A. F.; O'Neill, L.; Jaroszýnska-Wolínska, J. Soft Plasma Polymerization of Gas State Precursors from an Atmospheric Pressure Corona Plasma Discharge. *Chemistry of Materials* 2009, *21* (19), 4401–4407. https://doi.org/10.1021/cm900816e.

(211) Reuter, R.; Rügner, K.; Ellerweg, D.; Arcos, T. de los; von Keudell, A.; Benedikt, J. The Role of Oxygen and Surface Reactions in the Deposition of Silicon Oxide like Films from HMDSO at Atmospheric Pressure. *Plasma Process. Polym.* 2012, No. 11-12, 1116–1124.

(212) Starostine, S.; Aldea, E.; de Vries, H.; Creatore, M.; van de Sanden, M. C. M. Atmospheric Pressure Barrier Discharge Deposition of Silica-like Films on Polymeric Substrates. In *Plasma Processes and Polymers*; 2007; Vol. 4. https://doi.org/10.1002/ppap.200731203.

(213) Morent, R.; De Geyter, N.; Van Vlierberghe, S.; Dubruel, P.; Leys, C.; Gengembre, L.; Schacht, E.; Payen, E. Deposition of HMDSO-Based Coatings on PET Substrates Using an Atmospheric Pressure Dielectric Barrier Discharge. *Prog. Org. Coat.* 2009, *64* (2–3), 304–310. https://doi.org/10.1016/j.porgcoat.2008.07.030.

(214) De Geyter, N.; Morent, R.; Van Vlierberghe, S.; Dubruel, P.; Leys, C.; Gengembre, L.; Schacht, E.; Payen, E. Deposition of Polymethyl Methacrylate on Polypropylene Substrates Using an Atmospheric Pressure Dielectric Barrier Discharge. *Prog. Org. Coat.* 2009, *64* (2–3), 230–237. https://doi.org/10.1016/j.porgcoat.2008.07.029.

(215) Sawada, Y.; Ogawat, S.; Kogoma, M. Synthesis of Plasma-Polymerized Tetraethoxysilane and Hexamethylsiloxane Films Prepared by Atmospheric Pressure Glow Discharge. *Journal of Physics D: Applied* 1995, *28*, 1661–1669.

(216) Benčina, M.; Junkar, I.; Zaplotnik, R.; Valant, M.; Iglič, A.; Mozetič, M. Plasma-Induced Crystallization of TiO 2 Nanotubes. *Materials* 2019, *12* (4). https://doi.org/10.3390/ma12040626.

(217) Kramer, N. J.; Anthony, R. J.; Mamunuru, M.; Aydil, E. S.; Kortshagen, U. R. Plasma-Induced Crystallization of Silicon Nanoparticles. *J. Phys. D Appl. Phys.* 2014, *47* (7). https://doi.org/10.1088/0022-3727/47/7/075202.

(218) Yasuda, H. Ki. Yasuda. *Plasma polymerization. Academic press* 2012.

(219) Lalancette, R. A.; Syzdek, D.; Grebowicz, J.; Arslan, E.; Bernal, I. The Thermal Decomposition and Analyses of Metal Tris-Acetylacetonates: Free Radical Formation from Al, Cr, Mn, Fe and Co Complexes. *J. Therm. Anal. Calorim.* 2019, *135* (6), 3463–3470. https://doi.org/10.1007/s10973-018-7598-8.

(220) Schubert, J. S.; Popovic, J.; Haselmann, G. M.; Nandan, S. P.; Wang, J.; Giesriegl, A.; Cherevan, A. S.; Eder, D. Immobilization of Co, Mn, Ni and Fe Oxide Co-Catalysts on TiO2 for Photocatalytic Water Splitting Reactions. *J. Mater. Chem. A Mater.* 2019, *7* (31), 18568–18579. https://doi.org/10.1039/c9ta05637h.

(221) Alema, F.; Osinsky, A.; Mukhopadhyay, P.; Schoenfeld, W. V. Epitaxial Growth of Co3O4 Thin Films Using Co(Dpm)3 by MOCVD. *J. Cryst. Growth* 2019, *525*. https://doi.org/10.1016/j.jcrysgro.2019.125207.

(222) Georgi, C.; Hildebrandt, A.; Tuchscherer, A.; Oswald, S.; Lang, H. Hexacarbonyl (Trimethylsilyl Ethyne) Dicobalt as MOCVD Precursor for Thin Cobalt Layer Formation. *Z. Anorg. Allg. Chem.* 2013, *639* (14), 2532–2535. https://doi.org/10.1002/zaac.201300292.

(223) Ehrhardt, C.; Gjikaj, M.; Brockner, W. Thermal Decomposition of Cobalt Nitrato Compounds: Preparation of Anhydrous Cobalt(II)Nitrate and Its Characterisation by Infrared and Raman Spectra. *Thermochim. Acta* 2005, *432* (1), 36–40. https://doi.org/10.1016/j.tca.2005.04.010.

(224) Luque, J. and D. R. C. LIFBASE: Database and Spectral Simulation Program (Version 1.5). 1999.

(225) Hadjiev, V. G.; Iliev, M. N.; Vergilov, I. V. *The Raman Spectra of Co3O4*; C: Solid State Phys. 21, 1988.

(226) Hansson, A. N.; Linderoth, S.; Mogensen, M.; Somers, M. A. J. Inter-Diffusion between Co3O4 Coatings and the Oxide Scale on Fe-22Cr. *J. Alloys Compd.* 2007, *433* (1–2), 193–201. https://doi.org/10.1016/j.jallcom.2006.06.086.

(227) Vennela, A. B.; Mangalaraj, D.; Muthukumarasamy, N.; Agilan, S.; Hemalatha, K. V. Structural and Optical Properties of Co3O4 Nanoparticles Prepared by Sol-Gel Technique for Photocatalytic Application. *Int. J. Electrochem. Sci.* 2019, *14* (4), 3535–3552. https://doi.org/10.20964/2019.04.40.

(228) Koza, J. A.; He, Z.; Miller, A. S.; Switzer, J. A. Electrodeposition of Crystalline Co 3O 4-A Catalyst for the Oxygen Evolution Reaction. *Chem. Mater.* 2012, *24* (18), 3567–3573. https://doi.org/10.1021/cm3012205.

(229) Rautiainen, A.; Lindblad, M.; Backman, L. B.; Puurunen, R. L. Preparation of Silica-Supported Cobalt Catalysts through Chemisorption of Cobalt(II) and Cobalt(III) Acetylacetonate. *Phys. Chem. Chem. Phys.* 2002, *4* (11), 2466–2472. https://doi.org/10.1039/b201168a.

(230) Backman, L. B.; Rautiainen, A.; Lindblad, M.; Jylhä, O.; Krause, A. O. I. *Characterisation of Co/SiO 2 Catalysts Prepared from Co(Acac) 3 by Gas Phase Deposition*; Applied Catalysis A: General 208.1-2, 2001; Vol. 208.

(231) Olejníček, J.; Šmíd, J.; Perekrestov, R.; Kšírová, P.; Rathouský, J.; Kohout, M.; Dvořáková, M.; Kment, Š.; Jurek, K.; Čada, M.; Hubička, Z. Co 3 O 4 Thin Films Prepared by Hollow Cathode Discharge. *Surf. Coat. Technol.* 2019, *366*, 303–310. https://doi.org/10.1016/j.surfcoat.2019.03.010.

(232) Prieto, P.; Marco, J. F.; Serrano, A.; Manso, M.; de la Figuera, J. Highly Oriented (111) CoO and Co3O4 Thin Films Grown by Ion Beam Sputtering. *J. Alloys Compd.* 2019, *810*. https://doi.org/10.1016/j.jallcom.2019.151912.

(233) Hansson, A. N.; Linderoth, S.; Mogensen, M.; Somers, M. A. J. Inter-Diffusion between Co3O4 Coatings and the Oxide Scale on Fe-22Cr. *J. Alloys Compd.* 2007, *433* (1–2), 193–201. https://doi.org/10.1016/j.jallcom.2006.06.086.

(234) Burriel, M.; Garcia, G.; Santiso, J.; Hansson, A. N.; Linderoth, S.; Figueras, A. Co3O4 Protective Coatings Prepared by Pulsed Injection Metal Organic Chemical Vapour Deposition. *Thin Solid Films* 2005, *473* (1), 98–103. https://doi.org/10.1016/j.tsf.2004.07.081.

(235) Mariotti, D.; Belmonte, T.; Benedikt, J.; Velusamy, T.; Jain, G.; Švrček, V. Low-Temperature Atmospheric Pressure Plasma Processes for "Green" Third Generation

Photovoltaics. *Plasma Process. Polym.* Wiley-VCH Verlag January 1, 2016, pp 70–90. https://doi.org/10.1002/ppap.201500187.

(236) Huerta-Flores, A. M.; Usiobo, O. J.; Audinot, J. N.; Heyberger, R.; Choquet, P.; Boscher, N. D. Low Temperature Open-Air Plasma Deposition of SrTiO3Films for Solar Energy Harvesting: Impact of Precursors on the Properties and Performances. *ACS Appl. Mater. Interfaces* 2022, *14* (6), 8527–8536. https://doi.org/10.1021/acsami.1c20792.

(237) Cai, Z.; Liu, B.; Zou, X.; Cheng, H. M. Chemical Vapor Deposition Growth and Applications of Two-Dimensional Materials and Their Heterostructures. *Chemical Reviews*. American Chemical Society July 11, 2018, pp 6091–6133. https://doi.org/10.1021/acs.chemrev.7b00536.

(238) Pedersen, H.; Elliott, S. D. Studying Chemical Vapor Deposition Processes with Theoretical Chemistry. *Theor. Chem. Acc.* 2014, *133* (5), 1–10. https://doi.org/10.1007/s00214-014-1476-7.

(239) Berry, A. D.; Gaskill, D. K.; Holm, R. T.; Cukauskas, E. J.; Kaplan, R.; Henry, R. L. Formation of High Tc Superconducting Films by Organometallic Chemical Vapor Deposition. *Appl. Phys. Lett.* 1988, *52* (20), 1743–1745. https://doi.org/10.1063/1.99719.

(240) Natarajan, K.; Munirathinam, E.; Yang, T. C. K. Operando Investigation of Structural and Chemical Origin of Co3O4Stability in Acid under Oxygen Evolution Reaction. *ACS Appl. Mater. Interfaces* 2021, *13* (23), 27140–27148. https://doi.org/10.1021/acsami.1c07267.

(241) Tyczkowski, J.; Kapica, R.; Łojewska, J. Thin Cobalt Oxide Films for Catalysis Deposited by Plasma-Enhanced Metal-Organic Chemical Vapor Deposition. *Thin Solid Films* 2007, *515* (16 SPEC. ISS.), 6590–6595. https://doi.org/10.1016/j.tsf.2006.11.056.

(242) Laguna-Bercero, M. A.; Sanjuán, M. L.; Merino, R. I. Raman Spectroscopic Study of Cation Disorder in Poly- and Single Crystals of the Nickel Aluminate Spinel. *Journal of Physics Condensed Matter* 2007, *19* (18). https://doi.org/10.1088/0953-8984/19/18/186217.

(243) Wu, M.; Chen, S.; Soomro, A.; Ma, S.; Zhu, M.; Hua, X.; Xiang, W. Investigation of Synergistic Effects and High Performance of La-Co Composite Oxides for Toluene Catalytic Oxidation at Low Temperature. *Environmental Science and Pollution Research* 2019, *26* (12), 12123–12135. https://doi.org/10.1007/s11356-019-04672-7.

(244) Gao, L.; Yalon, E.; Chew, A. R.; Deshmukh, S.; Salleo, A.; Pop, E.; Demkov, A. A. Effect of Oxygen Vacancies and Strain on the Phonon Spectrum of HfO2 Thin Films. *J. Appl. Phys.* 2017, *121* (22). https://doi.org/10.1063/1.4984833.

(245) Huang, J.; Sheng, H.; Ross, R. D.; Han, J.; Wang, X.; Song, B.; Jin, S. *Modifying Redox Properties and Local Bonding of Co3O4 by CeO2 Enhances Oxygen Evolution Catalysis in Acid*.

(246) Ferrari, A. C. Raman Spectroscopy of Graphene and Graphite: Disorder, Electron-Phonon Coupling, Doping and Nonadiabatic Effects. *Solid State Commun.* 2007, *143* (1–2), 47–57. https://doi.org/10.1016/j.ssc.2007.03.052.

(247) Ferrari, A. C.; Robertson, J. *Interpretation of Raman Spectra of Disordered and Amorphous Carbon*.

(248) Iliev, M. N.; Abrashev, M. V; Lee, H.-G.; Popov, V. N.; Sun, Y. Y.; Thomsen, C.; Meng, R. L.; Chu, C. W. *Raman Spectroscopy of Orthorhombic Perovskitelike YMnO 3 and LaMnO 3*; 1998.

(249) Muñoz-Ferreiro, C.; López-Pernía, C.; Gallardo-López, Á.; Poyato, R. Unravelling the Optimization of Few-Layer Graphene Crystallinity and Electrical Conductivity in Ceramic Composites by Raman Spectroscopy. *J. Eur. Ceram. Soc.* 2021, *41* (16), 290–298. https://doi.org/10.1016/j.jeurceramsoc.2021.09.025.

(250) Biesinger, M. C.; Payne, B. P.; Grosvenor, A. P.; Lau, L. W. M.; Gerson, A. R.; Smart, R. S. C. Resolving Surface Chemical States in XPS Analysis of First Row Transition Metals, Oxides and Hydroxides: Cr, Mn, Fe, Co and Ni. *Appl. Surf. Sci.* 2011, *257* (7), 2717–2730. https://doi.org/10.1016/j.apsusc.2010.10.051.

(251) Wu, J.; Xue, Y.; Yan, X.; Yan, W.; Cheng, Q.; Xie, Y. Co3O4 Nanocrystals on Single-Walled Carbon Nanotubes as a Highly Efficient Oxygen-Evolving Catalyst. *Nano Res.* 2012, *5* (8), 521–530. https://doi.org/10.1007/s12274-012-0237-y.

(252) Cardenas-Flechas, L. J.; Barba-Ortega, J. J.; Joya, M. R. Analysis and Evaluation of Structural Properties of Co3O4 Microparticles Obtained at Low Temperature.

Ceramica 2022, *68* (385), 52–59. https://doi.org/10.1590/0366-69132022683853152.

(253) Shannon, R. D. *Revised Effective Ionic Radii and Systematic Studies of Interatomie Distances in Halides and Chaleogenides*; 1976; Vol. 32.

(254) Pearse, R. W. B.; Gaydon, A. G. *The Identification of Molecular Spectra*, 4th ed.; Chapman and Hall, Ed.; John Wiley & Sons, Inc.: London, 1976; Vol. 297.

(255) Acharya, K.; Bulou, S.; Gaulain, T.; Choquet, P. AP-PACVD Plasma Printer: Investigating the Influence of Gas Flow Rates to Printing Resolution in Parallel with CFD Simulation. *J. Phys. D Appl. Phys.* 2021, *54* (48). https://doi.org/10.1088/1361-6463/ac2063.

(256) Kment, S.; Kluson, P.; Zabova, H.; Churpita, A.; Chichina, M.; Cada, M.; Gregora, I.; Krysa, J.; Hubicka, Z. Atmospheric Pressure Barrier Torch Discharge and Its Optimization for Flexible Deposition of TiO2 Thin Coatings on Various Surfaces. *Surf. Coat. Technol.* 2009, *204* (5), 667–675. https://doi.org/10.1016/j.surfcoat.2009.09.007.

(257) Sharma, M.; Austin, J. M.; Glumac, N. G.; Massa, L. NO and OH Spectroscopic Vibrational Temperature Measurements in a Postshock Relaxation Region. *AIAA Journal* 2010, *48* (7), 1434–1443. https://doi.org/10.2514/1.J050047.

(258) Lalancette, R. A.; Syzdek, D.; Grebowicz, J.; Arslan, E.; Bernal, I. The Thermal Decomposition and Analyses of Metal Tris-Acetylacetonates: Free Radical Formation from Al, Cr, Mn, Fe and Co Complexes. *J. Therm. Anal. Calorim.* 2019, *135* (6), 3463–3470. https://doi.org/10.1007/s10973-018-7598-8.

(259) Schubert, J. S.; Popovic, J.; Haselmann, G. M.; Nandan, S. P.; Wang, J.; Giesriegl, A.; Cherevan, A. S.; Eder, D. *Electronic Supplementary Information Immobilization of Co, Mn, Ni and Fe Oxide Co-Catalysts on TiO2 for Photocatalytic Water Splitting Reactions*; 2019.

(260) Lin, Z.; Han, D.; Li, S. Study on Thermal Decomposition of Copper(II) Acetate Monohydrate in Air. *J. Therm. Anal. Calorim.* 2012, *107* (2), 471–475. https://doi.org/10.1007/s10973-011-1454-4.

(261) Acharya, K.; Bulou, S.; Gaulain, T.; Gérard, M.; Choquet, P. Site-Selective Atmospheric Pressure Plasma-Enhanced Chemical Vapor Deposition Process for

Micrometric Deposition of Plasma-Polymerized Methyl Methacrylate. *Plasma Processes and Polymers* 2021, *18* (2). https://doi.org/10.1002/ppap.202000143.

(262) Qi, R.; Jones, D. L.; Liu, Q.; Liu, Q.; Li, Z.; Yan, C. Field Test on the Biodegradation of Poly(Butylene Adipate-Co-Terephthalate) Based Mulch Films in Soil. *Polym. Test.* 2021, *93*. https://doi.org/10.1016/j.polymertesting.2020.107009.

(263) Shmidt, F. K.; Nindakova, L. O.; Shainyan, B. A.; Saraev, V. V.; Chipanina, N. N.; Umanetz, V. A. Hydrogenation Catalysts Formation in the System AlEt3-Co(Acac) 2,3. *J. Mol. Catal. A Chem.* 2005, *235* (1–2), 161–172. https://doi.org/10.1016/j.molcata.2005.02.033.

(264) Shen, C.; Shaw, L. L. FTIR Analysis of the Hydrolysis Rate in the Sol-Gel Formation of Gadolinia-Doped Ceria with Acetylacetonate Precursors. *J. Solgel Sci. Technol.* 2010, *53* (3), 571–577. https://doi.org/10.1007/s10971-009-2133-9.

(265) Li, Y.; Qiu, W.; Qin, F.; Fang, H.; Hadjiev, V. G.; Litvinov, D.; Bao, J. Identification of Cobalt Oxides with Raman Scattering and Fourier Transform Infrared Spectroscopy. *Journal of Physical Chemistry C* 2016, *120* (8), 4511–4516. https://doi.org/10.1021/acs.jpcc.5b11185.

(266) Guerra, V.; Tejero-del-Caz, A.; Pintassilgo, C. D.; -, al; Qiao, J.-J.; Yang, Q.; Wang, L.-C.; Ono, R.; Oda, T. *Physics Ryo Ono and Tetsuji Oda*; 2002; Vol. 35.

(267) De Benedictis, S.; Dilecce, G. Rate Constants for Deactivation of N2(A) V=2-7 by O, O2, and NO. *Journal of Chemical Physics* 1997, *107* (16), 6219–6229. https://doi.org/10.1063/1.474287.

(268) Griem, H. R. *Principles of Plasma Spectroscopy*; 2005.

(269) Guerra, V.; Sá, P. A.; Loureiro, J. Role Played by the N 2 (A 3 Σ u +) Metastable in Stationary N 2 and N 2-O 2 Discharges You May Also like Role Played by the N 2 (A 3 Σ + u) Metastable in Stationary N 2 and N 2-O 2 Discharges. *J. Phys. D: Appl. Phys* 2001, *34*, 1745–1755.

(270) Abuyazid, N. H.; Üner, N. B.; Peyres, S. M.; Mohan Sankaran, R. Charge Decay in the Spatial Afterglow of Plasmas and Its Impact on Diffusion Regimes. *Nat. Commun.* 2023, *14* (1). https://doi.org/10.1038/s41467-023-42442-9.

(271) Fotouhiardakani, F.; Laurent, M.; Profili, J.; Ravichandran, S.; Dorairaju, G.; Laroche, G. Fragmentation Mechanism in a Nitrogen Dielectric Barrier Discharge Plasma on

Fluoropolymer Polymer Films. *Materials* 2023, *16* (3). https://doi.org/10.3390/ma16030942.

(272) Erme, K. The Effect of Catalysts in Plasma Oxidation of Nitrogen Oxides, University of Tartu, 2019.

(273) Norberg, S. A.; Johnsen, E.; Kushner, M. J. Formation of Reactive Oxygen and Nitrogen Species by Repetitive Negatively Pulsed Helium Atmospheric Pressure Plasma Jets Propagating into Humid Air. *Plasma Sources Sci. Technol.* 2015, *24* (3). https://doi.org/10.1088/0963-0252/24/3/035026.

(274) Lide, D. R. *Handbook of Chemistry and Physics* , 84th ed.; CRC, 2006.

(275) Guillou, S. UNIVERSITE DE BOURGOGNE COMMISSARIAT A L'ENERGIE ATOMIQUE de Saclay DEN/DPC/SCCME/Laboratoire d'Etude de La Corrosion Non Etude Du Comportement d Comme Matériau d'inter l'Electrolyse Etude Du Comportement d'un Alliage Chromino Comme Matériau d'interconnecteur Pour l'Electrolyse à Haute Température, Université de Bourgogne, 2011.

(276) Kim, B. K. Fundamental Study on the Mechanism of High Temperature Oxidation and Cr Behavior of SOFC Materials, Seoul National University, 2017.

(277) Froitzheim, J.; Meier, G. H.; Niewolak, L.; Ennis, P. J.; Hattendorf, H.; Singheiser, L.; Quadakkers, W. J. Development of High Strength Ferritic Steel for Interconnect Application in SOFCs. *J. Power Sources* 2008, *178* (1), 163–173. https://doi.org/10.1016/j.jpowsour.2007.12.028.

(278) Reddy, M. J. *THESIS FOR THE DEGREE OF DOCTOR OF PHILOSOPHY Metallic Materials for Solid Oxide Fuel Cells and Electrolysers Mitigating High Temperature Corrosion*.

(279) Physico-Chemical Investigations on Co-Mn-Oxide Spinels. https://doi.org/10.6100/IR332566.

(280) Pieraggi, B.; Rapp, R.; Rapp, R. A.; Pieraggi(', B. Novel Explanation of the "Reactive Element Effect" in Alloy Oxidation. *Journal de Physique IV Proceedings* 1993, *111* (C9), 3. https://doi.org/10.1051/jp4:1993926ï.

(281) Roy, T.; Latu-Romain, L.; Guillotte, I.; Latouche, B.; Wouters, Y. Modeling of Trilayered Oxide Thermally Grown on 441 Ferritic Stainless Steel at 900 °C in Synthetic Air.

Oxidation of Metals 2021, *96* (1–2), 31–41. https://doi.org/10.1007/s11085-021-10041-y.

(282) Falk-Windisch, H.; Claquesin, J.; Sattari, M.; Svensson, J. E.; Froitzheim, J. Co- and Ce/Co-Coated Ferritic Stainless Steel as Interconnect Material for Intermediate Temperature Solid Oxide Fuel Cells. *J. Power Sources* 2017, *343*, 1–10. https://doi.org/10.1016/j.jpowsour.2017.01.045.

(283) Dutta, B.; Pal, D. Absorption and Raman Spectroscopy: Ferrimagnet Spinel MnCr2O4. In *AIP Conference Proceedings*; American Institute of Physics Inc., 2019; Vol. 2115. https://doi.org/10.1063/1.5113208.

(284) Hosterman, B. D.; Raman, ". Raman Spectroscopic Study of Solid Solution Spinel Oxides Raman Spectroscopic Study of Solid Solution Spinel Oxides Repository Citation Repository Citation. 2011. https://doi.org/10.34917/2476131.

(285) D'Ippolito, V.; Andreozzi, G. B.; Bersani, D.; Lottici, P. P. Raman Fingerprint of Chromate, Aluminate and Ferrite Spinels. *Journal of Raman Spectroscopy* 2015, *46* (12), 1255–1264. https://doi.org/10.1002/jrs.4764.

(286) Malézieux, J.-M.; Piriou, B. Relation Entre La Composition Chimique et Le Comportement Vibrationnel de Spinelles de Synthèse et de Chromites Naturelles En Microspectrométrie Raman. *Bulletin de Minéralogie* 1988, *111* (6), 649–669. https://doi.org/10.3406/bulmi.1988.8110.

(287) Koc, N.; Timucin, M. Activity-Composition Relations in MnCr 2O 4-CoCr 2O 4 Solid Solutions and Stabilities of MnCr 2O 4 and CoCr 2O 4 at 1300°C. *Journal of the American Ceramic Society* 2005, *88* (9), 2578–2585. https://doi.org/10.1111/j.1551-2916.2005.00489.x.

(288) Jacob, K. T.; Fitzner, K. *Ion-Exchange Equilibria between (Mn, Co)O Solid Solution and (Mn, Co) Cr20 4 and (Mn, Co) Al O, Spinel Solid 9 Solutions at 1100* ~; 1977; Vol. 12.

(289) Giovannelli, F.; Marsteau, V.; Zaghrioui, M.; Autret, C.; Delorme, F. Low Temperature Synthesis of Co3O4 and (Co1−xMnx)3O4 Spinels Nanoparticles. *Advanced Powder Technology* 2017, *28* (5), 1325–1331. https://doi.org/10.1016/j.apt.2017.02.022.

(290) Bahlawane, N.; Ngamou, P. H. T.; Vannier, V.; Kottke, T.; Heberle, J.; Kohse-Höinghaus, K. Tailoring the Properties and the Reactivity of the Spinel Cobalt Oxide.

Physical Chemistry Chemical Physics 2009, *11* (40), 9224–9232. https://doi.org/10.1039/b910707j.

(291) Liao, Q.; Li, L. Structural Dependence of Microwave Dielectric Properties of Ixiolite Structured ZnTiNb 2O 8 Materials: Crystal Structure Refinement and Raman Spectra Study. *Dalton Transactions* 2012, *41* (23), 6963–6969. https://doi.org/10.1039/c2dt12451c.

(292) Image_Processing_with_ImageJ.

(293) Jirak, Z.; Vratislav, S.; Zajicek, J. Oxygen Parameters and Debye-Waller Factors in Mnx Cr3-x O4 Spinels. *Physica Status Solidi A - Applications and Materials* 1976, *37*, K47–K51.

(294) Jirak, Z.; Vratislav, S.; Novak, P. Study of Cubic and Tetragonal Structures in the System Mnx Cr3-x O4. *Physica Status Solidi A - Applications and Materials* 1978, *50*, K21–K24.

(295) Hastings, J. M.; Corliss, L. M. Magnetic Structure of Manganese Chromite. *Physical Review (1,1893-132,1963/141,1966-188,1969)* 1962, *126*, 556–565.

(296) Neese, F. *Lecture 5: Vibrational Spectroscopy*.

(297) Jimenez-Sandoval, S. *Micro-Raman Spectroscopy: A Powerful Technique for Materials Research*. www.elsevier.com/locate/mejo.

(298) Vila, E.; Rojas, R. M.; Martín De Vidales, J. L.; García-Martínez, O. Structural and Thermal Properties of the Tetragonal Cobalt Manganese Spinels Mn x Co 3-x O 4 (1.4 < x < 2.0). 1996.

(299) Froitzheim, J.; Svensson, J. E. Nanocoatings for SOFC Interconnects - Mitigating Chromium Volatilization and Improving Corrosion Properties. In *Materials Science Forum*; Trans Tech Publications Ltd, 2011; Vol. 696, pp 412–416. https://doi.org/10.4028/www.scientific.net/MSF.696.412.

(300) Froitzheim, J.; Svensson, J.-E. Multifunctional Nano-Coatings for SOFC Interconnects. *ECS Trans.* 2011, *35* (1), 2503–2508. https://doi.org/10.1149/1.3570248.

(301) Talic, B.; Falk-Windisch, H.; Venkatachalam, V.; Hendriksen, P. V.; Wiik, K.; Lein, H. L. Effect of Coating Density on Oxidation Resistance and Cr Vaporization from Solid

Oxide Fuel Cell Interconnects. *J. Power Sources* 2017, *354*, 57–67. https://doi.org/10.1016/j.jpowsour.2017.04.023.

(302) Kofstad, P. Defects and Transport Properties of Metal Oxides. *Oxidation of Metals* 1995, *44*.

(303) Kröger, F. A.; Vink, H. J. Relations between the Concentrations of Imperfections in Solids. *Phys. Chem. Solids Pergamon Press* 1958, *5*, 208–223.

(304) Gilewicz-Wolter, J.; Urek, Z. Z. ˙ ; Dudała, J.; Lis, J.; Homa, M.; Wolter, M. *Diffusion of Chromium, Manganese, and Iron in MnCr 2 O 4 Spinel*.

(305) Atkinson, A. *Solid State Lonics 28-30*; 1988.

(306) Thanedburapasup, S.; Wetchirarat, N.; Muengjai, A.; Tengprasert, W.; Wiman, P.; Thublaor, T.; Uawongsuwan, P.; Siripongsakul, T.; Chandra-ambhorn, S. Fabrication of Mn–Co Alloys Electrodeposited on AISI 430 Ferritic Stainless Steel for SOFC Interconnect Applications. *Metals (Basel)*. 2023, *13* (3). https://doi.org/10.3390/met13030612.

(307) Talic, B.; Hendriksen, P. V.; Wiik, K.; Lein, H. L. Diffusion Couple Study of the Interaction between Cr 2 O 3 and MnCo 2 O 4 Doped with Fe and Cu. *Solid State Ion.* 2019, *332*, 16–24. https://doi.org/10.1016/j.ssi.2019.01.008.

(308) Muhich, C. L.; Aston, V. J.; Trottier, R. M.; Weimer, A. W.; Musgrave, C. B. First-Principles Analysis of Cation Diffusion in Mixed Metal Ferrite Spinels. *Chemistry of Materials* 2016, *28* (1), 214–226. https://doi.org/10.1021/acs.chemmater.5b03911.

(309) Andersson, J.-O.; Helander, T.; Höglund, L.; Shi, P.; Sundman, B. THERMO-CALC & DICTRA, Computational Tools For Materials Science. *Calphad* 2002, *26* (2), 273–312.

(310) Lee, W.; Chen, S. Y.; Tseng, E.; Gloter, A.; Chen, C. L. Study of Defect Structure in Ferromagnetic Nanocrystalline CeO2: Effect of Ionic Radius. *Journal of Physical Chemistry C* 2016, *120* (27), 14874–14882. https://doi.org/10.1021/acs.jpcc.6b02817.

(311) Marianetti, C. A.; Ceder, G.; Morgan, D. First-Principles Investigation of the Cooperative Jahn-Teller Effect for Octahedrally Coordinated Transition-Metal Ions. *Phys. Rev. B Condens. Matter Mater. Phys.* 2001, *63* (22). https://doi.org/10.1103/PhysRevB.63.224304.

(312) Blanchet, M. D.; Matthews, B. E.; Spurgeon, S. R.; Heald, S. M.; Issacs-Smith, T.; Comes, R. B. *Jahn-Teller-Driven Phase Segregation in Mn x Co 3-x O4 Spinel Thin Films*.

(313) Rao, C. N. R.; Rao, G. V. S. Electrical Conduction in Metal Oxides. *Phys. Stat. Sol. (a)* 1970, *1* (597).

(314) Golikov, Y. V; Tubin, S. Y.; Barkhatov, V. P.; Balakirev, V. F. *PHASE DIAGRAMS OF THE Co-Mn-O SYSTEM IN AIR*; 1985; Vol. 46.

(315) Azároff, L. V. Role of Crystal Structure in Diffusion. II. Activation Energies for Diffusion in Closest-Packed Structures. *J. Appl. Phys.* 1961, *32* (9), 1663–1665. https://doi.org/10.1063/1.1728415.

(316) Azároff, L. V. Role of Crystal Structure in Diffusion. I. Diffusion Paths in Closest-Packed Crystals. *J. Appl. Phys.* 1961, *32* (9), 1658–1662. https://doi.org/10.1063/1.1728414.

(317) Chanson, R.; Bouvier, M.; Miserque, F.; Rouillard, F.; Schuster, F. *Influence of Cobalt and Cobalt-Manganese Oxide Coating Thickness Deposited by DLI-MOCVD as a Barrier against Cr Diffusion for SOC Interconnect*.

(318) Atkinson, A. *DIFFUSION ALONG GRAIN BOUNDARIES AND DISLOCATIONS IN OXIDES, ALKALI HALIDES AND CARBIDES*; 1984; Vol. 12.

(319) Hou, P. Y. Impurity Effects on Alumina Scale Growth * †. In *Science and Technology of Alumina*; 2002.

(320) Palcut, M.; Mikkelsen, L.; Neufeld, K.; Chen, M.; Knibbe, R.; Hendriksen, P. V. Efficient Dual Layer Interconnect Coating for High Temperature Electrochemical Devices. *Int. J. Hydrogen Energy* 2012, *37* (19), 14501–14510. https://doi.org/10.1016/j.ijhydene.2012.07.038.

(321) van Leeuwen, T. K.; Dowdy, R.; Guerrero, A.; Gannon, P. Reactive Evaporation and Condensation of Chromium: A Review. *Journal of Power Sources*. Elsevier B.V. July 15, 2023. https://doi.org/10.1016/j.jpowsour.2023.233065.

(322) Holstein, T. Studies of Polaron Motion Part II. The “Small” Polaron.

(323) Holstein, T. Studies of Polaron Motion Part I. The Molecular-Crystal Model.

(324) Zhu, Z.; Sugimoto, M.; Pal, U.; Gopalan, S.; Basu, S. Electrochemical Cleaning: An in-Situ Method to Reverse Chromium Poisoning in Solid Oxide Fuel Cell Cathodes. *J. Power Sources* 2020, *471*. https://doi.org/10.1016/j.jpowsour.2020.228474.

(325) Seo, H. S.; Jin, G.; Jun, J. H.; Kim, D. H.; Kim, K. Y. Effect of Reactive Elements on Oxidation Behaviour of Fe-22Cr-0.5Mn Ferritic Stainless Steel for a Solid Oxide Fuel Cell Interconnect. *J. Power Sources* 2008, *178* (1), 1–8. https://doi.org/10.1016/j.jpowsour.2007.12.026.

(326) Chevalier, S.; Caboche, G.; Przybylski, K.; Brylewski, T. Effect of Nano-Layered Ceramic Coatings on the Electrical Conductivity of Oxide Scale Grown on Ferritic Steels. In *Journal of Applied Electrochemistry*; 2009; Vol. 39, pp 529–534. https://doi.org/10.1007/s10800-008-9726-9.

(327) Goebel, C.; Berger, R.; Lundberg, M. W.; Westlinder, J.; Svensson, J.-E.; Froitzheim, J. Long Term (4 Years) Performance of Co/Ce Coated 441 for SOFC Interconnect Applications. *ECS Trans.* 2017, *78* (1), 1675–1679. https://doi.org/10.1149/07801.1675ecst.

(328) Liu, H.; Lyon, S. B.; Stack, M. M. The Partial Ionic and Electronic Conductivity of Y-Containing and Y-Free Chromia Scales. *Oxidation of Metals* 2001, *56*.

(329) Liu, H.; Stack, M. M.; Lyon, S. B. Reactive Element Effects on the Ionic Transport Processes in Cr2O3 Scales. *Solid State Ion.* 1998, *109*, 247–257.

(330) Halt, A. *Electrical Conductivity and Defect Structure of Mg-Doped Cr203*; 1997; Vol. 100.

(331) Wachsman, E. D.; Lee, K. T. Lowering the Temperature of Solid Fuel Cells. *Science (1979).* 2011, *334* (6058), 935–939. https://doi.org/10.1126/science.1212741.

(332) Yang, Z.; Xia, G.; Wang, C.; Nie, Z.; Templeton, J.; Stevenson, J.; Singh, P.; Manivannan, A.; Shultz, T.; Surdoval, W. *Investigation of AISI 441 Ferritic Stainless Steel and Development of Spinel Coatings for SOFC Interconnect Applications*; 2008. http://www.ntis.gov/ordering.htm.

(333) Falk-Windisch, H.; Svensson, J. E.; Froitzheim, J. The Effect of Temperature on Chromium Vaporization and Oxide Scale Growth on Interconnect Steels for Solid Oxide Fuel Cells. *J. Power Sources* 2015, *287*, 25–35. https://doi.org/10.1016/j.jpowsour.2015.04.040.

(334) Huang, K.; Hou, P. Y.; Goodenough, J. B. Characterization of Iron-Based Alloy Interconnects for Reduced Temperature Solid Oxide Fuel Cells. *Solid State Ion*. 2000, *129*, 237–250.

List of Appendices

Appendix I – State of the art

Appendix I. 1 - Parabolic rate constants (kp) obtained in the literature for coated and uncoated AISI 441, Crofer H, Crofer 22 APU and AISI 430. Coatings used, annealing temperature and conditions used are shown.

Substrate	Coating	Conditions	Temperature (°C)	Kp $[g^2 \cdot cm^{-4} \cdot s^{-1}]$ $(\times 10^{-14})$	Ref
AISI 441	-	Dry air	800	7.1	83
AISI 441	-	Air + 3% H_2O	800	6.5	132
AISI 441	-	Air + 3% H_2O	800	11	48
AISI 441	-	Lab air	800	6	332
AISI 430		Not specified	800	9	128
Crofer H		Lab air	800	4	127
Crofer 22 APU		Lab air	800	1.8	123
Crofer 22 APU		Air + 3% H_2O	800	7	333
AISI 441	Co	Dry air	800	6	83
AISI 441	CeCo	Dry air	800	3	83
AISI 441	CeCo	Air + 3% H_2O	800	7	48
AISI 441	CeCo	Air + 3% H_2O	800	8	126
AISI 441	CoMnO	Lab air	800	1.8	129
AISI 441	MCO	Lab air	800	2	332
AISI 430	MnCo	Not specified	800	3	128
Crofer H	MCO	Lab air	800	0.9	127
Crofer 22 APU	MC	Lab air	800	0.9	123
Crofer 22 APU	Co_3O_4 + LSM	Dry O_2	800	2.3	62
AISI 441		Air + 3% H_2O	850	25	132
AISI 441		Lab air	850	30	131
AISI 441		Lab air	850	23	129
Crofer 22 APU		Air + 3% H_2O	850	33	333

Crofer 22 APU		Air + 1% H_2O	850	34	[119]
AISI 441	CeCo	Air + 3% H_2O	850	14	[126]
AISI 441	MnCo	Lab air	850	12	[131]
Crofer 22 APU	Co_3O_4	Air + 1% H_2O	850	3	[119]
Crofer 22 APU	Co_3O_4 + LSM	Dry O_2	850	3.6	[62]
Crofer 22 APU	$MnCo_2O_4$	Air + 1% H_2O	850	14	[119]

Appendix III – Synthesis of Co_3O_4 by AP-PECVD technique: Growth Mechanisms

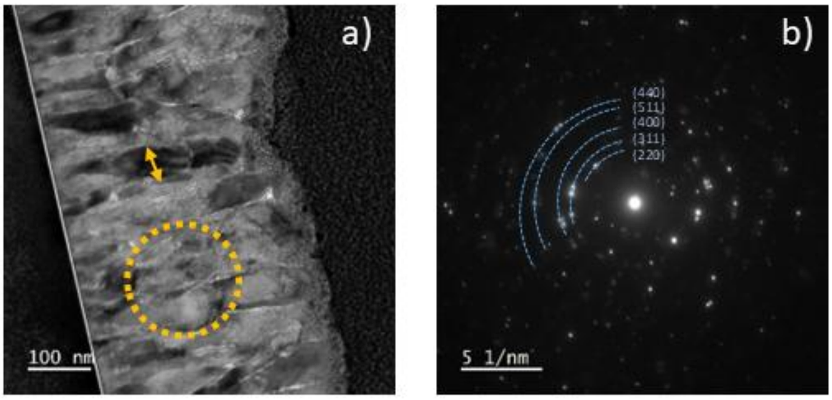

Appendix III. 1 - TEM cross section of the Co_3O_4 thin film (a). Selected area electron diffraction (SAED) image (b) corresponding to the region highlighted in the orange dotted circle. The SAED analysis confirms the formation of crystalline Co_3O_4. Peak positions are the same as found in XRD. There is a slight deviation from the theoretical value for Co_3O_4.

Appendix III. 2 - Peak positions, FWHM for the peaks F_2g (1) and A_1g, which refers to Co^{2+} and Co^{3+} respectively, and the peak ratio based on the intensity of these two peaks. Data was acquired from the Raman spectrum for all conditions and FWHM was calculated using a Lorentzian deconvolution from Origin software. The data was compared to a reference from literature (Hadjiev et al.[225]) and to a Co_3O_4 standard produced in the laboratory.

Sample	**F_2g (1) (cm^{-1})**	**FWHM (cm^{-1})**	**Peak ratio (F_2g /A_1g)**	**Eg (cm^{-1})**	**F_2g (2) (cm^{-1})**	**F_2g (3) (cm^{-1})**	**A_1g (cm^{-1})**	**FWHM (cm^{-1})**
Hadjiev et al.	194.4	4.9		482.4	521.6	618.4	691	6.2
No Heating – 40% O_2	195.5	4.5	0.36	483.8	522.6	621.2	693.3	6.7
200°C – 40% O_2	195.7	4.4	0.32	484	522.7	621.4	693.5	6.3
250°C – 40% O_2	195.2	4.3	0.29	483.5	522.2	620.8	693	6.15
300°C – 40% O_2	194.9	4.4	0.26	483.3	522.1	620.6	692.8	6.18

Co_3O_4 standard	**197**	**3.6**	**0.37**	**484.7**	**523.7**	**622.7**	**694.6**	**4.8**

Appendix IV - Performance of Co_3O_4 Thin Films under SOEC Operating Conditions

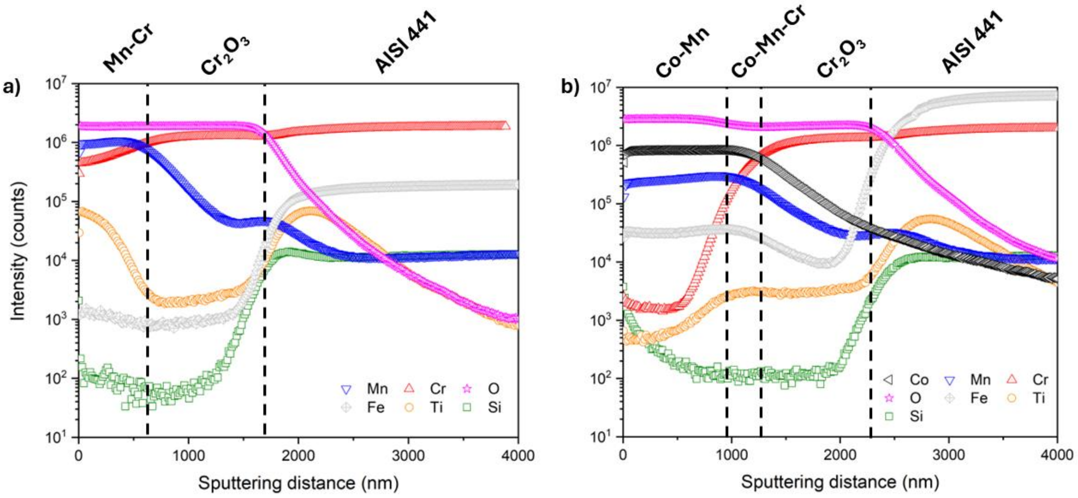

Appendix IV. 1 - SIMS profile of the uncoated (a) and B1 coated (b) samples annealed at 850 °C for 48 hours.

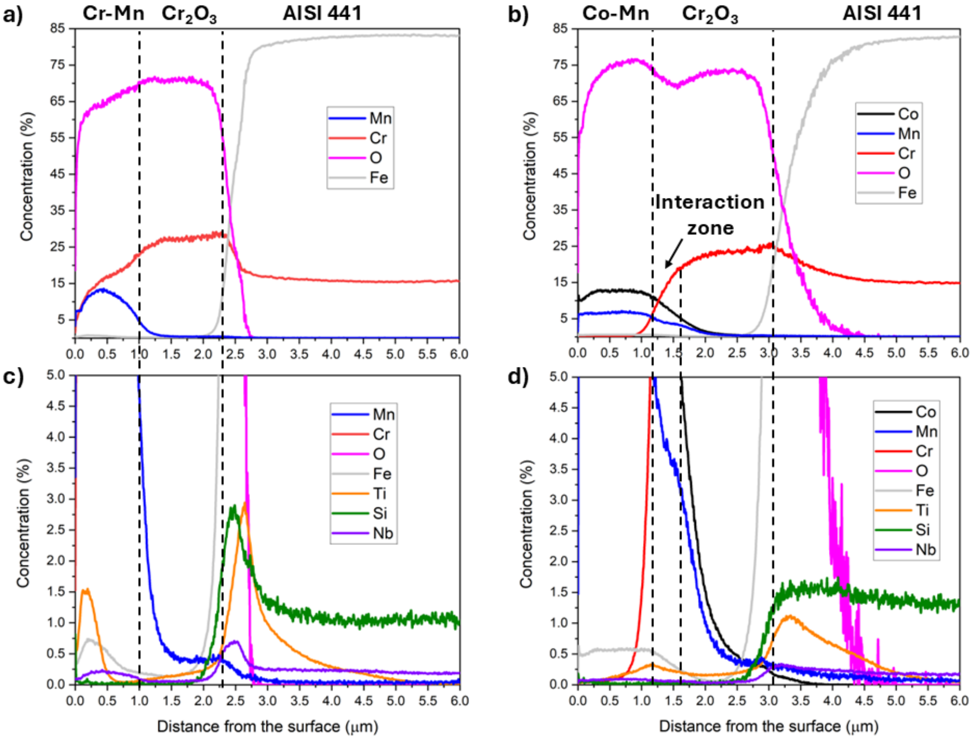

Appendix IV. 2 - GD-OES analysis of the uncoated (a, c) and coated (b, d) samples annealed at 850 °C for 120 hours. The (c) and (d) represent a zoomed region of the (a) and (b) images to highlight elements in minor concentration.

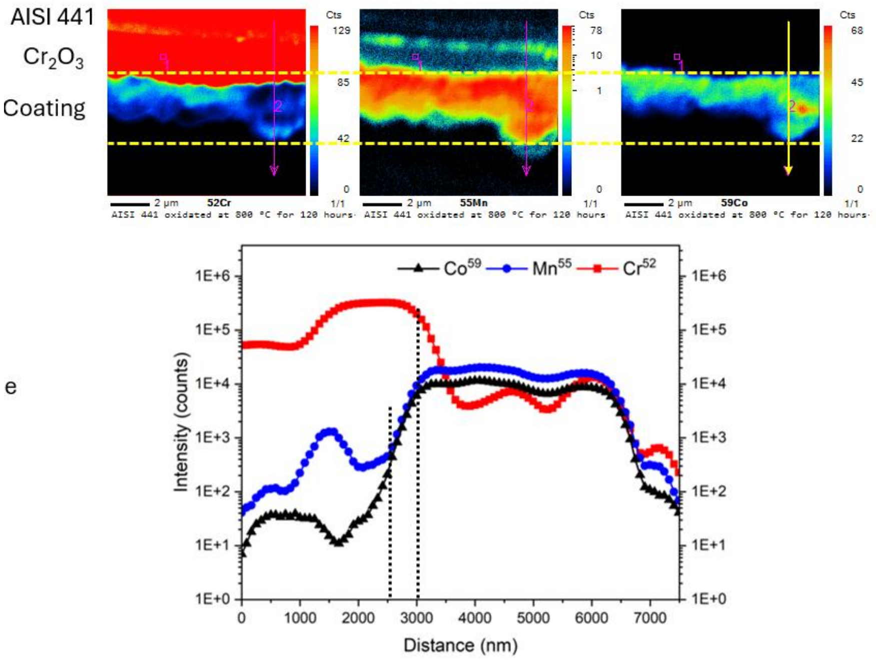

Appendix IV. 3 – NanoSIMS analysis with elemental mapping of Cr, Mn and Co. A Mn-Cr layer is observed between alloy and Cr_2O_3.

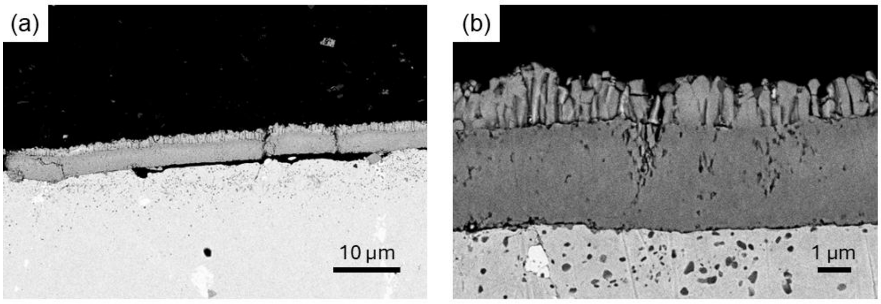

Appendix IV. 4 – Cross-section micrograph of the uncoated AISI 441 substrate after 2000 h of exposure at 800 °C. Average Cr-rich oxide layer thickness is 4.5 µm.

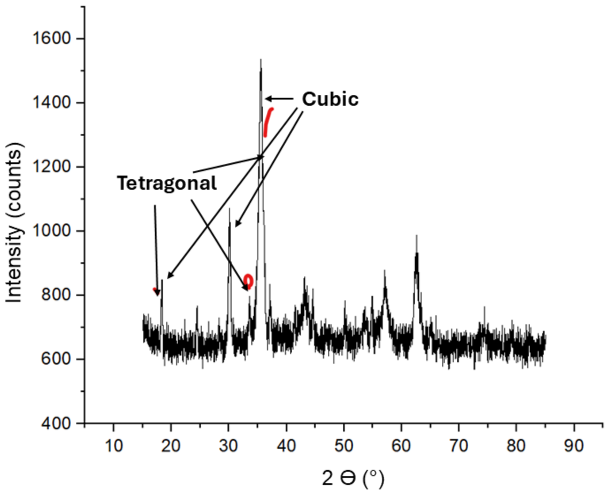

Appendix IV. 5 – X-ray diffraction analysis of B2-1000 nm after 2000 h of exposure at 800 °C. Shoulder peaks were referenced to the tetragonal phase.

Appendix V - Electrical performance of the Co_3O_4 coated and uncoated AISI 441 substrates

Appendix V.1 – Evolution of the oxide scale

Specific study of the ASR evolution at 700 °C

The evolution of the ASR for the B1 and B2 coated samples (Figure V.1 and V.2) revealed a curious ASR increase during the first oxidation step, at 700 °C followed by a rapid and strong ASR decrease when the temperature was increased to 800 °C. Meanwhile, the ASR of the uncoated AISI 441 remained relatively flat during the same step. The progressive ASR increase at 700 °C was more pronounced on the SOEC mode (Figure V.1) and seemed to be influenced by the Co_3O_4 coating thickness (Figure V.2), since the ASR values have doubled (21 to 42 $m\Omega \cdot cm^2$) for the thick sample (B2-2000 nm).

To better understand such behaviour, an additional ASR experiment (named experiment 3) was performed. The experiment was conducted in the same manner as previous experiments: with an initial 1-hour period performed at 850 °C to enhance electrical contact. The sample was cooled down to the first isotherm at 700 °C, and maintained for 167 h, which approximately corresponds to the time necessary to stabilize ASR values in the previous ASR experiments. The sample was then heated up to 800 °C (0.5 $°C \cdot min^{-1}$) maintained at such temperature for 1 h and cooled down again to 700 °C (1 $°C \cdot min^{-1}$). Appendix V.1a displays the evolution of ASR values over time.

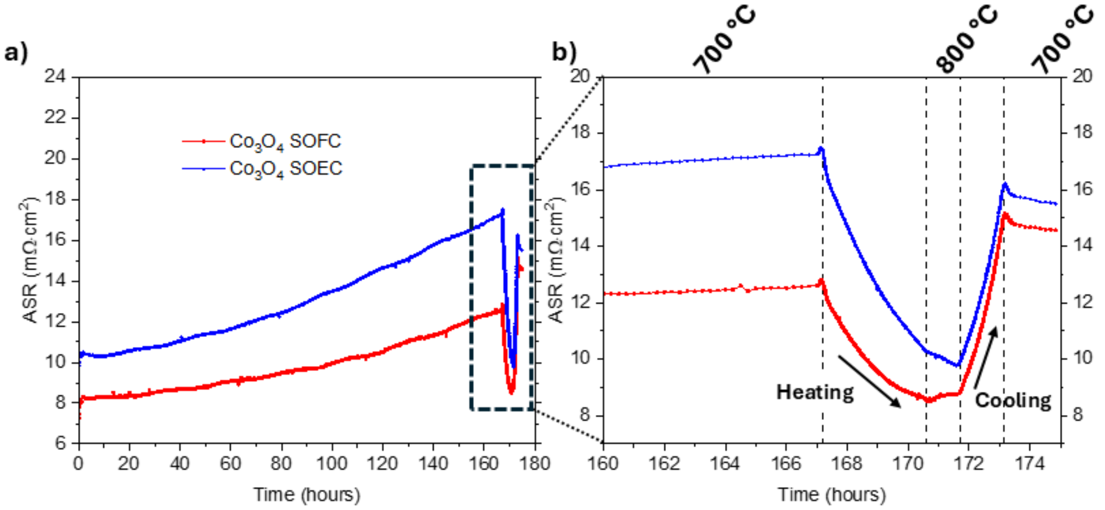

Appendix V. 1 - (a) ASR evolution as a function of time for the B1-700 nm sample operated in SOFC (red) and SOEC (blue) modes. (b) ASR evolution during heating and cooling at the end stage of the ASR experiment.

The coated sample shows a continuous ASR increase at 700 °C, which only decreased when the temperature was increased to 800 °C (with higher values in SOEC than SOFC mode). The ASR value at 800 °C dropped by almost half and raised again when the sample was cooled down to 700 °C. Curiously, after this heating and cooling steps, the values vary in comparison to values before the heating step, being 16 and 17 $m\Omega\cdot cm^2$ at the end of experiment, and before heating step, on SOEC mode and 15 and 12 $m\Omega\cdot cm^2$ at the end and before heating step on SOFC mode.

Appendix V.1b presents the evolution of ASR with temperature during heating and cooling. The activation energy was calculated during the heating and cooling steps in both modes, being 0.55 eV in SOEC mode in both steps, while in SOFC mode it ranged from 0.5 eV during heating to 0.6 eV during cooling. These values are noticeably lower than those obtained at the end of the previous experiments which were about 0.7-0.8 eV (Chapter V). Overall, activation energies obtained from ASR experiments using chromia forming alloys range from 0.65 to 0.9 eV[83,92,123,325,326]. However, activation energy obtained on thermally grown chromia oxide are approximately 0.6 eV[329], coherent with values obtained in experiment 3. Activation energy values rely on multiple factors, such as the concentration of doping elements, temperature in which the oxide scale is developed and the quality and type of interfaces. Thus, the activation energy (E_a) values refer to a contribution of the oxide governing the process but also from the interfaces (alloy/oxide, oxide/LSM and LSM/Pt) which represent the charge transfer from one oxide to another[334]. Huang *et al.* observed a variation on E_a values when varying the electrode in contact with the alloy and the temperature of oxide scale formation[334]. Considering that the substrate and electrode remain the same in all cases, the activation energy variation observed from uncoated and coated samples should rise from the phases formed during oxidation or from the difference of interfaces.

Microstructural characterization

The B1-700 nm sample oxidized during this experiment was analyzed by SEM and EDS for the SOEC (a, b) and SOFC (c, d) modes in Appendix V.2 in order understand such ASR behaviour. The composition of the spinel oxide layer ($Co_{2.5}Mn_{0.25}Fe_{0.25}O_4$) and the chromia thickness (~ 300 nm) is very similar in both modes. The presence of Fe in both spinel oxide layers is noticeable for this short-term experiment. Such presence was not observed in the spinel layer after the previous long-term experiments. Fe diffusion occurs mostly during the initial moments of oxidation before a continuous and sufficiently thick chromia layer is formed on the sample surface. Once such chromia layer is formed, iron diffusion in the spinel layer stops[282]. No signs of a continuous SiO_2 layer were observed and a fair adhesion between oxide and LSM was observed.

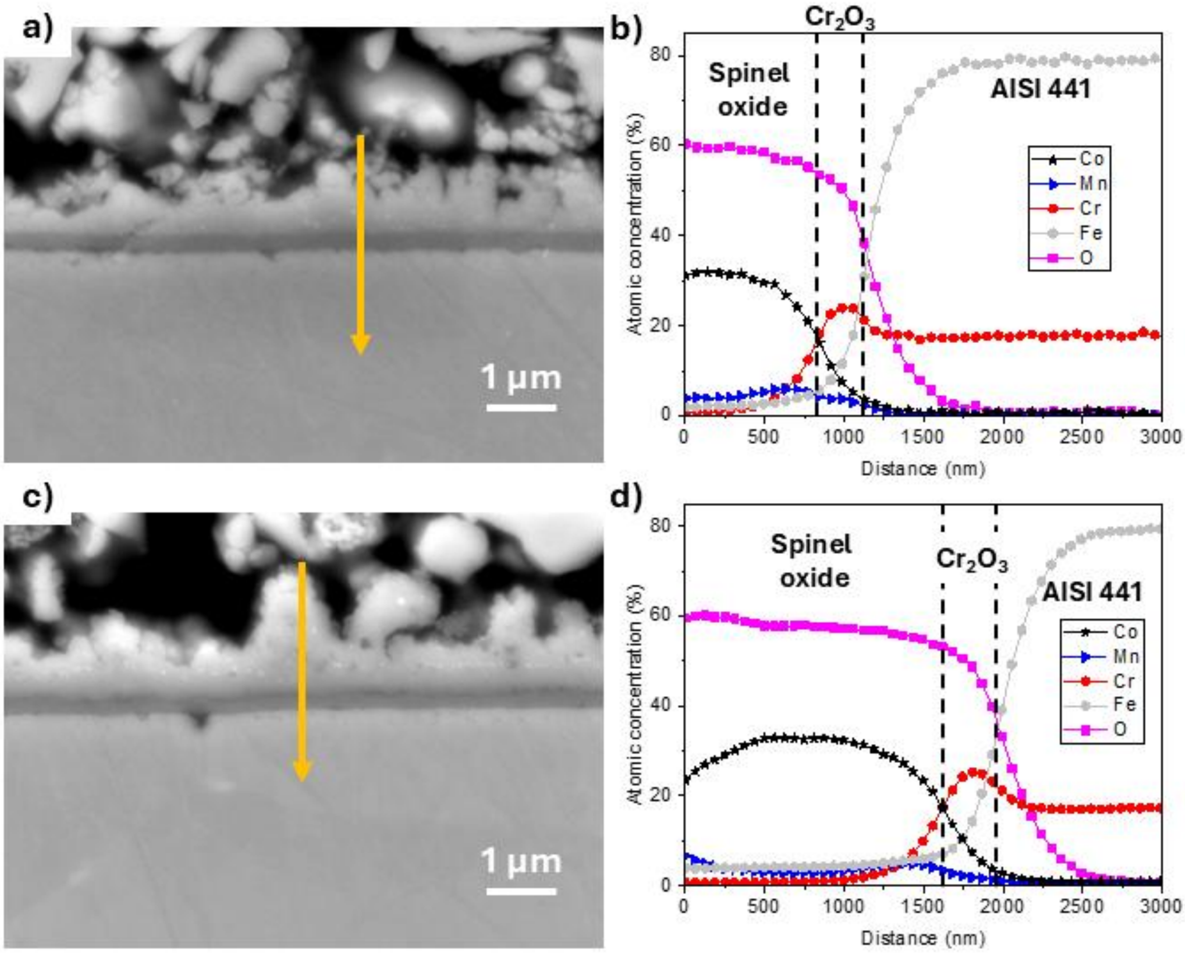

Appendix V. 2 - SEM cross-sections (a, c) and EDS analyses (b, d) of the B1-700 nm sample under SOEC (a, b) and SOFC (c, d) modes after the ASR experiment 3. The orange arrow highlights the position of the EDS measurement.

As previously shown in equation V.1, the ASR values from experimental data are a sum of the multiple layers and interfaces. The micrographs shown in Appendix V.2 indicate that the oxide/LSM interface exhibits few contact points. The poor contact at this interface could indeed provide an explanation to the higher ASR values. However, poor contact was also observed in previous coated samples (Figure V.7) oxidized for longer exposure times but that presented lower ASR values.

The oxide scale was formed by a chromia layer and a Co_3O_4 spinel oxide with minor Mn and Fe concentration. Co_3O_4 electrical conductivity ranges from 0.6[149] to 2.2[89] S·cm^{-1} at 700 °C.

The Mn incorporation to the lattice is expected to increase such values due to increase in the number of cation pairs[105]. In contrast, Fe addition was shown to slightly decrease the electrical conductivity of $MnCo_{2-x}Fe_xO_4$ spinels, with the effect being more pronounced for higher Fe content. Yet, Lee et al. reported conductivities in the range of 0.1 and 1 $S \cdot cm^{-1}$ for varying concentration of Co in the $Co_xFe_{3-x}O_4$ spinel. Taking the lowest conductivity reported at 700 °C (0.1 $S \cdot cm^{-1}$) and the phase thickness (~700 nm), the expected ASR from the spinel layer is 0,7 $m\Omega \cdot cm^2$. These values are much lower than the values obtained in experiment 3 and indicate that the ASR increase at 700 °C is not related to the spinel layer.

The lower ASR values from the spinel layer indicate that ASR values are mainly governed by the chromia layer. Applying the same approach used to calculate the chromia values at the end of the experiment (Table V.8), one can estimate the chromia electrical conductivity at 700 °C from experiment 3 and compare the chromia values at the end of long-term experiments (Chapter V). Values are summarized in Appendix V.3. With this approach, a value of 2.0×10^{-3} $S \cdot cm^{-1}$ was obtained for chromia from the short-term experiment while a value five times higher was obtained from the long-term experiments.

Appendix V. 3 - Chromia electrical conductivity calculated for coated samples from experiments 1-3. ASR values were taken from the values at the end of the experiment at 700 °C, and from the average values from SOC modes in experiment 3. The average chromia thickness was considered.

	Chromia thickness (nm)	$ASR_{Average}$ at 700 °C ($m\Omega \cdot cm^2$)	$\sigma_{Cr_2O_3}$ ($S \cdot cm^{-1}$)
B1-700 nm (Exp. 3)	**300**	**15.1**	$\mathbf{2.0 \times 10^{-3}}$
B1-700 nm (Ex. 1)	2900	25.2	1.15×10^{-2}
B2-400 nm (Exp. 2)	3165	30.7	1.03×10^{-2}
B2-2000 nm (Exp. 2)	3565	60.2	1.01×10^{-2}

In any case, the variation seems to be related to the Co_3O_4 coatings since uncoated AISI 441 substrates show minimal ASR variation. However, this variation is likely not related to a faster Cr-rich phases growth, which was shown to occur faster for uncoated samples. Interestingly, the ASR values for uncoated AISI 441 substrates at the 700 °C isotherm remains stable and below 6 $m\Omega \cdot cm^2$ (Figure V.2 and V.3).

Two main results were observed in experiment 3. First, the activation energy of Co_3O_4 coated samples is lower for samples oxidized at lower temperatures, suggesting evolution of Cr_2O_3 defect chemistry or in the interfaces. Indeed, Huang et al.[334] have observed varying activation energy values for oxide scale formed at different temperatures. Second, ASR values of Co_3O_4 coated samples are more negatively affected at 700 °C than uncoated AISI 441 samples, at least for short-term exposure. This negative effect of the coatings could not be well understood but it seems that it either influences the chromia electrical conductivity, lower in comparison to chromia formed at higher temperatures or it leads to other processes governing ASR values. The variation of electrical conductivity could be explained by a reduction of the oxygen partial pressure (p_{O_2}) at the chromia/spinel interface with the presence of Co_3O_4 coatings, as indicated in other works[14,119,320]. Several works have highlighted the influence of the p_{O_2} on chromia electrical conductivity[146,147], particularly at lower temperatures (<1000 °C) [144]. Overall, chromia is considered a p-type semiconductor[50,329], being negatively affected by the reduction of p_{O_2}[146,147]. Therefore, the higher values could indeed correspond to chromia defect chemistry being affected by the oxygen partial pressure. Moreover, thicker coatings (B2-2000 nm) are expected to have a stronger influence on the p_{O_2}, explaining the higher values obtained for this sample.

The improvement in electrical conductivity with temperature, observed for samples in chapter V, could relate to the increase of the doping effect since, at higher temperatures, it is expected that the solubility of different elements increases. This argument could also be used to explain the continuous ASR increase (Appendix V.1) during the isotherm at 700 °C. Considering that the chromia was initially formed at 850 °C, the chromia phase requires a certain amount of time to equilibrate its defect chemistry. Holt and Kofstad[146] and Park and Natesan[147] have observed that chromia defect chemistry requires long equilibration times to stabilize after switching oxidation conditions.